COMPREHENSIVE STUDY OF DENSE ARRAY CONCENTRATOR PHOTOVOLTAIC SYSTEM USING NON-IMAGING PLANAR CONCENTRATOR

SIAW FEI LU

DOCTOR OF PHILOSOPHY IN ENGINEERING

FACULTYOF ENGINEERING AND SCIENCE
UNIVERSITI TUNKU ABDUL RAHMAN
AUGUST 2014

COMPREHENSIVE STUDY OF DENSE ARRAY CONCENTRATOR PHOTOVOLTAIC SYSTEM USING NON-IMAGING PLANAR CONCENTRATOR

By

SIAW FEI LU

A thesis submitted to the Department of Electrical and Electronic Engineering,
Faculty of Engineering and Science,
Universiti Tunku Abdul Rahman,
in partial fulfilment of the requirements for the degree of
Doctor of Philosophy in Engineering
August 2014

ABSTRACT

COMPREHENSIVE STUDY OF DENSE ARRAY CONCENTRATOR PHOTOVOLTAIC SYSTEM USING NON-IMAGING PLANAR CONCENTRATOR

Siaw Fei Lu

Concentrator photovoltaic (CPV) system performance is affected when there is non-uniform illumination especially for densely packed CPV system. When a dense array is operating under nonuniform flux distribution, current mismatch will happen among the cells that are connected in series, causing degradation to output power. This is a crucial drawback because maximum output power of the array is considerably reduced when its current-voltage (*I*-*V*) curve has many mismatch steps that leads to lower fill factor and conversion efficiency. Addressing this matter, a comprehensive study to optimize the performance of dense-array using non-imaging planar concentrator (NIPC) system under non-uniform illumination is proposed. In the new systematic approach, a fast-prediction method (FPM) using three point model (TPM) is proposed to analyze large and complicated interconnection of dense array. It is an expeditious, efficient, cost-effective and reasonably accurate approach and is useful to optimize dense-array configuration for any new design of solar concentrator, before proceeding to a comprehensive *I*-*V* curve simulation. This method can optimize the performance of dense array via using the best interconnection for any concentrator such as parabola, Fresnel lens, nonimaging concentrator etc. with

the use of standard CPV cells in the market. Once initial dense-array design is completed, detailed computer simulations are carried out to verify the prediction. Comprehensive simulations using Matlab has verified the proposed FPM prediction. Last but not least, the modeling method had been successfully validated with a non-imaging planar concentrator prototype to achieve practical conversion efficiency of 29.80%. It was found that the measured *I-V* curve closely resembles simulated FPM prediction and measured maximum output power varies by only 1.34%.

ACKNOWLEDGEMENTS

This PhD thesis is the result of a challenging and rewarding journey, upon which so many people have contributed in and given their support. First and foremost, I would like to express my sincere appreciation and gratitude to my supervisor, Prof. Dr. Chong Kok Keong, and co-supervisor, Dr. Ng See Seng, for their guidance throughout this research journey as well as for being supportive along the road of publishing journal and conference papers.

I am also indebted to the project advisor, Dr. Philip Tan Chee Lin, for his constant support, insightful advice, and encouragement which made me understand and appreciate my journey.

Special gratitude is also expressed to the research team partners, Wong Chee Woon, Yew Tiong Keat, Chong Yee How, Tan Ming Gui, Tan Woei Chong and Lim Chuan Yang for the inspiring discussion, support and encouragement through the years.

I especially appreciate the understanding, faith, advice and indescribable support from parents, parents-in-law, siblings and family members. To my supportive husband, and adorable son, I will always be grateful for your love and trust in me.

APPROVAL SHEET

This dissertation/thesis entitled "**COMPREHENSIVE STUDY OF DENSE ARRAY CONCENTRATOR PHOTOVOLTAIC SYSTEM USING NON-IMAGING PLANAR CONCENTRATOR**" was prepared by SIAW FEI LU and submitted as partial fulfillment of the requirements for the degree of Doctor of Philosophy in Engineering at Universiti Tunku Abdul Rahman.

Approved by:

____
(Prof. Dr. Chong Kok Keong)
Date: ………………
Supervisor
Department of Electrical and Electronic Engineering
Faculty of Engineering and Science
Universiti Tunku Abdul Rahman

____
(Dr. Ng See Seng)
Date: ………………
Co-supervisor
Department of Mechanical and Material Engineering
Faculty of Engineering and Science
Universiti Tunku Abdul Rahman

FACULTY OF ENGINEERING AND SCIENCE

UNIVERSITI TUNKU ABDUL RAHMAN

Date: 14 August 2014

SUBMISSION OF THESIS

It is hereby certified that **SIAW FEI LU** (ID No: **07UED05808**) has completed this final year project/ dissertation/ thesis* entitled "**COMPREHENSIVE STUDY OF DENSE ARRAY CONCENTRATOR PHOTOVOLTAIC SYSTEM USING NON-IMAGING PLANAR CONCENTRATOR**" under the supervision of Prof. Dr. Chong Kok Keong (Supervisor) from the Department of Electrical and Electronic Engineering, Faculty of Engineering and Science, and Dr. Ng See Seng (Co-Supervisor) from the Department of Mechanical and Material Engineering, Faculty of Engineering and Science.

I understand that University will upload softcopy of my thesis in pdf format into UTAR Institutional Repository, which may be made accessible to UTAR community and public.

Yours truly,

____

Siaw Fei Lu

DECLARATION

I hereby declare that the dissertation is based on my original work except for quotations and citations which have been duly acknowledged. I also declare that it has not been previously or concurrently submitted for any other degree at UTAR or other institutions.

Name : Siaw Fei Lu

Date : 14 August 2014

TABLE OF CONTENTS

Page

LIST OF TABLES

LIST OF FIGURES

Figures		Page
2.9	A schematic presenting the architecture of (a) a CPV module; (b) a VMJ solar cell made from several vertical junctions that are connected in series internally; (c) a vertical junction and its segment of length *dx* (Segev and Kribus 2013)	27
2.10	A contour plot of concentrated solar flux distribution was acquired with an optical scanner (Siaw and Chong, 2013)	28
2.11	This bar chart shows packing configuration of an array with five series-connected strings at 0.07A current mismatch. (Siaw and Chong, 2013)	30
2.12	A diagram showing the complicated distribution of CPV cells from different strings across a dense-array. Solar cells that are from the same series string are presented with the same colour for easy reference (Siaw and Chong, 2013)	30
3.1	A non-imaging planar is formed using flat mirrors, whereby every mirror comprises a finite number of reflective points, and each reflective point is illuminated by a discrete number of sub-rays	32
3.2	The main coordinate system is (x, y, z), and is defined in the planer of the NIPC with its origin at the center of the concentrator. On the other hand, sub-coordinate system (*x'*, *y'*, *z'*) is defined at the local facet mirror	33
3.3	A representation of triple-junction solar cell that is simplified from three-current source in series model into a two-diode model. In this study, an equivalent of the two-diode model, which is a solar cell block in SimElectronics, Simulink is adopted as the basic block of our dense-array	37
3.4	Current-voltage (*I-V*) curve of triple-junction InGaP/InGaAs/Ge CPV cells from EMCORE 2008 datasheets, plotted at various solar concentration levels and temperature 25 ^{o}C.	39

Figures		Page

Figures		**Page**

LIST OF ABREVIATIONS

BF	Best Fit
BFD	Best Fit Decreasing
BL	Bridge-Link
BPP	Bin-Packing Problem
CFD	Computational Fluid Dynamic
CPV	Concentrator Photovoltaic
CTJ	Concentrating Triple Junction
DBC	Direct-Bond-Copper
DC	Direct Current
DNI	Direct Normal Irradiance
FF	Fill Factor
FPM	Fast-Prediction Method
I-V	Current-Voltage
NIPC	Non-Imaging Planar Concentrator
PV	Photovoltaic
PMMA	Polymethyl-Methacrylate
P-V	Power-Voltage
SOE	Secondary Optical Element
SP	Series-Parallel
STC	Standard Test Conditions
TCT	Total-Cross-Tied
UTAR	Universiti Tunku Abdul Rahman
VMJ	Vertical Multi-Junction

NOMENCLATURE

A_{pixel}	area of receiver pixel [m^2]
$A_{reflective}$	Area of reflective point [m^2]
A_{CPV}	Active area of dense-array assembly [m^2]
A_{image}	Image area on the cooling block [m^2]
A_r	Mirror area which reflects solar flux to the target [m^2]
C	Solar concentration ratio
d	Number of basic modules in each row of a dense array
f	Focal distance [m]
i	Row location of flat mirror
j	Column location of the concentrator
I	Output current of solar cell [A]
I_{o1}	Saturation current of the first diode [A]
I_{o2}	Saturation current of the second diode [A]
I_{mp}	Current of maximum power point [A]
I_{ph}	Solar-induced current [A]
I_{SC}	Short-circuit current [A]
$\mathrm{I_{SC,T}}$	Operating short-circuit current at the temperature T [K]
$\mathrm{I_{SC\text{-}STC}}$	Short-circuit current when operating at STC [A]
k	Boltzmann constant
k_{c}	Thermal conductivity [$Wm^{-1}K^{-1}$]
$k_{\mathrm{arctic\ silver}}$	Thermal conductivity of arctic silver layer [$Wm^{-1}K^{-1}$]
k_{CPV}	Thermal conductivity of CPV cell [$Wm^{-1}K^{-1}$]
k_{copper}	Thermal conductivity of copper cooling block [$Wm^{-1}K^{-1}$]

$k_{\text{DBC-copper}}$	Thermal conductivity of copper layer of direct bond copper (DBC) substrate [$\text{Wm}^{-1}\text{K}^{-1}$]
k_{solder}	Thermal conductivity of solder layer, $\text{Wm}^{-1}\text{K}^{-1}$
K_{i}	Short-circuit current coefficient [A/$^{\text{o}}$C]
K_{v}	open-circuit voltage coefficient [V/$^{\text{o}}$C]
l	Thickness of material [m]
N	Diode ideality factor
N_{cell}	Total number of solar cells in a row of a dense array
N_{C}	Total counts of sub-rays within a light cone
N_1	Diode ideality factor of the first diode
N_2	Diode ideality factor of the second diode
p	number of cells that are in a basic module
P	Sunray that is reflected from the concentrator
$P_{CPV,in}$	Solar power input received by CPV assembly [W]
q	Electron charge
R_{d}	Turn-on resistance of diode [Ω]
R_{P}	Parallel resistance [Ω]
R_{S}	Series resistance [Ω]
R_{th}	Thermal resistance, Km^2W^{-1}
$R_{t\text{ot}}$	Total thermal resistance from cooling block to CPV cell
S	Number of reflective points
$S_{x,\,y}$	Location of each CPV cell in and array with x rows and y columns of solar cells
T	Operating Temperature [K]
T_{CB}	Temperature of cooling block [K]

T_{CPV}	Concentrator solar cell temperature [K]
V	Voltage across the solar cell [V]
V_{d}	Forward voltage of diode [V]
V_{mp}	Voltage of maximum power point [V]
V_{OC}	Open-circuit voltage [V]
$V_{\mathrm{OC,T}}$	Open-circuit voltage at temperature T [V]
$V_{\mathrm{OC\text{-}STC}}$	Open-circuit voltage when operating at STC [V]
V_{t}	Thermal voltage [V]
W	Side dimension of the facet mirror [cm]
γ	Axis that is parallel with the *x*-axis
σ	Axis that is perpendicular to the *x*-axis
θ	Incident angle of the principal solar ray [deg]
η_{CPV}	Conversion efficiency of the dense-array assembly [%]

CHAPTER 1

INTRODUCTION

1.1 Research Background

Solar power generation commonly incur a substantial amount of upfront investment cost. Therefore, extensive research activities are currently focused on developing more efficient solar power applications by introducing the utilization of solar energy together with new technologies. With the aim of offsetting the expensive cost of semiconductor material and encourage more CPV installations, solar concentrator systems employ comparatively inexpensive optical elements like mirrors or Fresnel lenses that will form the main part of a solar concentrator system to be incorporated with high-efficiency multi-junction solar cells. Solar concentrator technologies have made considerable progress in the past decade and can be applied to generate cost-effective electricity, and at the same time provide supplementary thermal energy in other application needs. For further reduction in the electricity generation cost from solar concentrator systems, optimal system design is key so that the CPV cells are able to harness maximum solar energy (Nishioka *et al.*, 2006; Luque *et al.*, 2006].

Nevertheless, the delivered electrical power in field conditions is often lesser than the offered output power on the array ratings, mainly due to mismatch losses. Some of the factors that cause mismatch losses are soiling, non-uniform irradiance, shading, temperature variations, cell quality, as well as cell aging. All of these factors will affect current-voltage (*I-V*) curve as well as power-voltage (*P-V*) curve of the CPV array, subsequently leading to serious reduction of output power during site measurements (Nishioka and Rai, 2007; Picault *et al.*, 2007).

Non-uniformity of concentrated solar irradiation is one of the most challenging problems faced by solar concentrator systems. Non-uniform solar irradiation is more evident around the receiver edges, and is commonly caused by optical design limitations, structure alignment imperfections, and low tracking accuracy. Over the last decades, many studies have been carried out to seek improvement on the solar concentrator optical design in order to produce more uniform solar flux distribution at high concentrations (Mills and Morrison, 2000; Chen *et al.*, 2001; Chen *et al.*, 2003; Chong *et al.*, 2009; Chong *et al.*, 2010; Picault *et al.*, 2010; Chong *et al.*, 2011). This is because the output current of a typical CPV dense-array is highly influenced by the uniformity of solar flux distribution. With factors like circumsolar effect, aberration, imperfection of mirrors etc., it is evident that perfectly uniform illumination is impossible to be produced. Under conventional design approach of simple series-connected array, there will be significant power losses due to low conversion system efficiency (Faiman *et al.*, 2002; Andreev *et al.*, 2003; Sherif et al., 2003; Coventry, 2005; Nishioka *et al.*, 2006).

Despite the employment of flat mirrors in the non-imaging planar concentrator (NIPC), the solar flux distribution results from simple super-positioning of mirror images onto the target receiver is unavoidably non-uniform at the peripheral region. Therefore a specially designed algorithm is required for analysing the current-voltage (*I-V*) curve of dense-array CPV cell arrangements for optimizing system efficiency and increasing generated output power. In our study, solar flux distribution of an NIPC prototype is measured so that the actual solar concentration ratio that is directed to every CPV cell's location at the receiver is identified. The measured solar flux distribution shows deviation from a perfect uniform distribution owing to various aforementioned practical installation imperfections, such as mechanical structure and mirror alignment.

Differing to considerable studies in partially shaded photovoltaic (PV) array for minimizing mismatch losses through the use of changing interconnection arrangement, this paper aims to develop a new approach using Simulink computational method to accurately simulate CPV dense array *I-V* and *P-V* curves. In the study, possible configurations are simulated and analysed based on real data of NIPC solar flux distribution to obtain the best array layout configuration. For verification purpose, the optimised configuration of CPV array is constructed and tested on the NIPC prototype. In following chapters, the methodology and process of CPV dense-array performance optimization are described in detail.

1.2 Objectives

In attempt to address the above identified non-uniformity problem in solar concentrator systems, a systematic and comprehensive study on dense-array design for the application in NIPC concentrator has been developed and explored. The main objectives are as follows:

- To design and construct a non-imaging planar concentrator (NIPC) for the application with dense array concentrator photovoltaic (CPV)
- Development of a systematic method of dense-array CPV interconnection design to enable system designers in identifying all possible interconnection options
- Development of a comprehensive electrical modeling method for dense-array CPV system that considers parameters from the two-diode model with verification from practical experimental data.
- Optimization of the electrical performance of NIPC system through identifying the most cost effective and highest output power combination of CPV dense-array.

1.3 Outline of the Thesis

The organization of the thesis is as follows: In Chapter 1 of this thesis an introduction to the background of CPV systems is presented. This section discusses the background of CPV cells, and then highlights factors of mismatch losses that limit the potential of solar concentrator systems. The findings have motivated this study to enhance the performance of dense-array solar concentrator, through optimization of the system using strategic solutions. In Chapter 2, critical literature review is carried out to study mismatch issues that are faced by different solar concentrator systems. Besides that, critical and detailed evaluation is conducted on scholarly articles, books and other sources that have proposed solutions with the aim to address current mismatch problem.

Next, the methodology of theoretical study and experimental procedure is discussed in Chapter 3 which includes optical analysis, temperature analysis, CPV dense-array analysis with FPM simulation method, as well as using comprehensive Simulink simulations. A major part of this research is focused on the design and development methodology. Modeling work that was performed in optical analysis and circuit-analysis for the development and optimization phase is presented in this section. The detailed setup of prototype NIPC and assembly process of dense-array are also included.

Results from theoretical study and field measurements are collected and analysed in Chapter 4. This chapter discusses the experimental studies performed to collect data and verify simulated prediction methods. By comparing all the different options produced in this study, an optimised CPV system is achieved. The last chapter is Chapter 5 which is the ending of this thesis summarizes the experimental studies of the developed methodology and optimised dense-array for the application to the NIPC system. The thesis concludes with the outcomes of the overall research achievements, discussion on advantages of the developed system.

1.4 Publications

Based on the findings from this research, several papers have been published in peer-reviewed international journals and conference proceedings. A full list of publications is presented in Table 1.1.

Table 1.1: Papers that are published in international journals and conferences

Appendix	Paper Title	Year	Journal /Conference	Impact Factor
A	"Design and construction of non-imaging planar concentrator for concentrator PV system" http://dx.doi.org/10.1016/j.renene.2008.09.001 **(Published)**	2009	Renewable Energy	2.989
B	"Integration of an on-axis general sun-tracking formula in the algorithm of an open-loop sun-tracking system" http://dx.doi.org/10.3390/s91007849 **(Published)**	2009	Sensors	1.953
C	"On-axis general sun-tracking formula and its application in improving sun-tracking accuracy of a 25kWth non-imaging planar concentrator prototype" http://dx.doi.org/10.4229/24thEUPVSEC2009-1DV.5.23 **(Published)**	2009	24^{th} European Photovoltaic Solar Energy Conference, Hamburg, Germany	N/A
D	"Optical characterization of nonimaging planar concentrator for the application in concentrator PV system"	2010	Journal of Solar Energy Engineering	0.94

	http://dx.doi.org/10.1115/1.4000355 **(Published)**			
E	"Solar flux distribution analysis of non-imaging planar concentrator for the application in the concentrator PV system" http://dx.doi.org/10.1109/PVSC.2010.5614112 **(Published)**	2010	35th IEEE Photovoltaic Specialists Conference (PVSC)	N/A
F	"Temperature effects on the performance of dense array concentrator PV system" http://dx.doi.org/10.1109/STUDENT.2012.6408385 **(Presented and Published)**	2012	IEEE Sustainable Utilization and Development in Engineering and Technology (STUDENT) Conference	N/A
G	"Electrical characterization of dense-array concentrator PV system" http://dx.doi.org/10.4229/27thEUPVSEC2012-1AV.3.18 **(Published)**	2012	27th European Photovoltaic Solar Energy Conference and Exhibition, Frankfurt, Germany	N/A
H	"An interconnection reconfiguration method for concentrator PV array" http://www.ieee-pvsc.org/ePVSC39/core_routines/view_abstract_no.php?show_close_window=yes&abstractno=664 **(Published)**	2013	39th IEEE Photovoltaic Specialists Conference, Florida. USA	N/A
I	"A dense-array layout reconfiguration method to minimize current mismatch losses for non-imaging planar concentrator" http://dx.doi.org/10.4229/28thEUPVSEC2013-1CV.6.34 **(Presented and Published)**	2013	28th European Photovoltaic Solar Energy Conference and Exhibition, Paris, France	N/A
J	"A systematic method of interconnection optimization for dense-array concentrator PV system" http://dx.doi.org/10.1155/2013/275169 **(Published)**	2013	The Scientific World Journal	1.730
K	"A comprehensive study of dense-array concentrator PV system using non-imaging planar concentrator" http://dx.doi.org/10.1016/j.renene.2013.08.014 **(Published)**	2014	Renewable Energy	2.989

CHAPTER 2

LITERATURE REVIEW

2.1 Introduction

High concentration CPV system developers have recently emerged over the recent years and they promise higher system efficiency as well as cost advantage over flat-plate PV systems. In CPV systems, direct sunlight is concentrated hundreds of times using mirrors and lenses and is focused onto high efficiency CPV cells. According to Zubi *et al.* (2009), concentrator systems are typically designed to operate at around 400 to 700 suns, although a few system developers have promoted systems that can go up above 1000 suns. The motivation behind developing very high concentration system is to offset the expensive CPV cell materials by achieving cost reduction via savings in semiconductor utilization. Nevertheless, most recognise that this is not an easy task especially with aggressive price decrease of crystalline silicone and thin-film solar modules. The higher costs of these state-of-the-art CPV cells as compared to silicon or thin-film solar modules are prohibiting their application in large scale installations.

Despite the temporary cost-advantage of the PV systems as compared to CPV systems, multi-junction solar cells have the potential of achieving the highest efficiency of any photovoltaic device by having two or more cells stacked together, optimally designed for a particular wavelength range within the solar spectrum. Combining III-V elements, cells of different band gaps can be combined in a tandem design to cover almost the full solar spectrum, whereby each cell convert an interval of the solar spectrum into electricity. The multi-junction cells are well suited for solar concentrator systems, and when properly designed the advantage of high efficiency CPV cells while mitigating the cell cost can be realised (Wang *et al.*, 2013).

One major factor that hinders concentrator photovoltaic (CPV) system to perform to its full potential is non-uniform flux distribution, which is common in all solar concentrator systems (Faiman *et al.*, 2002; Luque and Andreev, 2007; Chong *et al.*, 2010). When CPV cells are subjected to non-uniform illumination, the system performance will be negatively affected. This is because of current mismatch that occur among solar cells that are connected in series, leading to degradation of output power, and may even cause damage to solar cells due to reverse-bias operation and overheating (Kovach and Schmid, 1996; Nguyen and Lehman, 2008).

2.2 Concentrator Solar Cells

There are two broad categories of CPV systems, whereby the first group consists of point-focus systems utilizing Fresnel lenses, parabolic dishes and central receivers, while the second group consists of line-focus systems with linear Fresnel lenses and parabolic troughs. According to Luque and

Andreev (2007) line-focus concentrator systems are operated at concentration ratio of about ten times smaller than point-focus systems. Typically, the concentration level is 100 - 500 suns for point-focus concentrators and is lower at the range of 10 - 50 suns for line-focus concentrators. Generally, solar concentrators that operate at higher concentration ratio also require higher accuracy in sun tracking and smaller manufacturing and assembly tolerances.

2.2.1 Silicon Cells

High efficiency silicon solar cells that are used in solar concentrator systems are fabricated with requirements such as material quality with long minority carrier lifetimes, design of diffusion to minimize resistance and recombination losses, surface passivation, passivation of cell edges, reflection control, as well as design of metallization with minimal optical and resistance losses. Concentrator silicon solar cells of the traditional design have achieved efficiencies above 24%, and it can be further enhanced with better design specifications (Luque and Andreev, 2007).

Nevertheless, the growth of silicon solar cell efficiency has been slow in the recent years, mainly due to limitation of surface recombination. With price competition from triple-junction III-V CPV cells that can reach efficiency of above 40% (Castro *et al.*, 2008), demand for silicon solar cells is small and there is no large-scale manufacturing of high performing (above 24% efficiency) silicon solar cells for solar concentrator systems. This leads to higher cost of these silicon solar cells, which further deters their market growth.

2.2.2 Multi-junction Cells

Tandem solar cells based on III-V materials are the only available solar cells reaching efficiencies above 40% and their performance is superior to any other photovoltaic device through the use of several materials with different energy gaps across the solar spectrum. As an example, the top cell of a triple-junction CPV cell converts violet-blue radiation, while the middle cell converts green-yellow radiation, and the bottom cell converts red-infrared radiation. Due to the higher cost of multi-junction solar cells as compared to silicon or thin-firm solar cells, these cells are not currently applied to flat-plate modules. To offset the expensive cost of III-V solar cells in solar concentrator systems, expensive solar cell materials are replaced by cheaper optics which enables the system to operate at high solar concentration levels. Solar concentrators that can operate at higher efficiency require lesser solar cell material and hence able to achieve lower overall system costs.

Today, the demand for III-V cells for the terrestrial market have increased and concentrator system developers that were previously using silicon cells are shifting to more efficient III-V triple-junction CPV cells. Solar concentrator systems above 400 suns commonly utilize triple-junction solar cells produced from elements such as gallium, indium, phosphorus, arsenic, etc. which are from the 3rd and 5th group of the Periodic Table (Zubi *et al.*, 2009; Luque and Andreev, 2007). As an example, Amonix being one of the first companies to develop high concentration solar concentrator systems used to adopt silicon CPV cells but is now demonstrating application of triple-junction solar concentrator cells in their systems.

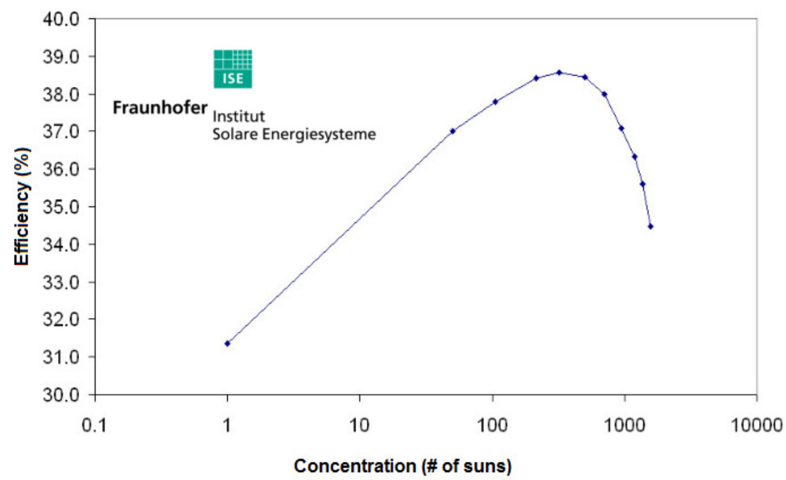

Figure 2.1: This figure show the relationship between efficiency and solar concentration for triple-junction CTJ cell (EMCORE, 2008), with highest performance efficiency of about 38% at around 500 suns.

In Figure 2.1, the relationship between efficiency and solar concentration for EMCORE's CTJ cell operating at 25^{o}C. From the figure, it is clear that the efficiency of InGaP/InGaA/Ge triple-junction solar cell is not always at a continuously increasing trend with increasing solar concentration ratio. In fact, there is an optimum operating point for the concentrator cell, which is at around 500 suns for this EMCORE cell. According to Zubi *et al.* (2009) higher concentration above 1000 suns could still be economically viable, even with the gradual reduction in efficiency. Nevertheless, the implication of operating the cells under these conditions should be carefully considered as there might be a negative effect to the life expectancy of the solar cell.

2.3 Causes of non-uniformity Issue

High concentration system requires complex engineering and management of high fluxes of light, heat and electricity to achieve maximum power output. Solar concentrators are conventionally designed in such a way that the concentrated solar flux distribution falls well inside the receiver area to avoid light spillage, because most solar concentrators have inherently inhomogeneous illumination (Luque *et al.*, 1998). Non-uniform illumination produces significant local heating in concentrator solar cells. In this aspect, the photocurrent increases with temperature, and therefore enhances the influence of the irradiance non-uniformity on the current-voltage curve (Andreev *et al.*, 2003), and leads to higher ohmic drops because the cell operates locally at higher solar irradiance levels.

There are several underlying causes of non-uniform concentrated solar flux distribution (Baig *et al.*, 2012; Chong *et. al*, 2013). Non-uniform illumination is contributed by limitation in concentrator optics design, slope error in concentrator profile, tracking error, misalignment of concentrator, as well as the condition of refractive lenses and reflective mirrors. Among the causes, the concentrator geometry and optics is one of the key factors that determine the severity of non-uniformity. If the optical design of a solar concentrator is not proper, serious performance degradation and reduction in efficiency will happen. There are many kinds of optical elements in a concentrator system, and each system exhibits unique non-uniformity issues. As an example, the Fresnel lens system experiences inherent difficulty to maintain the focus of concentrated light on the solar cells.

The effect of non-uniformity cannot be completely eliminated in any solar concentrator. This is because it is difficult to manufacture and control the geometry of solar concentrator to be exactly the same as theoretical design. Hence, testing of the surface profile for errors is a very important step. Shape errors on the concentrator would have significant effect on solar flux distribution. Solar reflectors like mirrors are likely to have shape errors during manufacturing and become the cause of non-uniformity. Baig *et al.* (2012) reported in their paper that common defects in solar concentrators include discoloration of concentrator optics, mechanical fatigue, bucking, and warping.

In addition to that, tracking error is also a concern to the performance of CPV systems. When a concentrator is off-focus due to tracking inaccuracy, some solar cells will not receive concentrated light, and become shaded. When solar cells are shaded, the photo-generated current is reduced or eliminated. If this cell is connected in series to other string cells in a module and producing less current, it becomes reverse bias by the voltage generating capabilities of the other string cells (Quaschning and Hanitsch, 1996). Shaded cells are often driven in the negative voltage range, and when a cells become reverse biased it acts as loads and dissipates heat (Meyer *et al.*, 2005; Alonso-Garcia *et al.*, 2006). If the reverse bias exceeds the breakdown voltage of the shaded solar cell, the cell will be damaged. Consequent effects that could be observed are cracking or the formation of hot spots. If the shaded module is connected to other modules in series, an open-circuit from the hot spot will disconnect the shaded PV module from the other modules in an array. The characteristic parameters of a CPV module present substantial variations in case of shading resulting in important reduction of the power output. Shading of solar cells reduces the maximum power, changes the open-circuit voltage, short-circuit current, fill factor, and the efficiency (Silvestre *et al.*, 2007).

While some of the causes of non-uniformity such as concentrator optics design and improper tracking could be addressed and minimized via implementation of new optical design and using refined tracking methods, other causes like the condition of refractive lenses and reflective mirrors are inevitable defects from the process of manufacturing, installation or aging and require more strategic solution.

2.4 Optical Design of Solar Concentrators

Solar concentrators such as the parabolic trough, linear Fresnel reflector, Fresnel lens, power tower and parabolic dish are capable of generating electrical power through the use of CPV cells. Recently, many studies can be found discussing on more advanced concentrator optical design such as new classes of high-flux, ultra compact, practical optics to improve solar illumination uniformity at high concentrations, in order to provide a cost-effective and practical CPV system. The most advanced CPV cells actually performs better with high conversion efficiency when focused under high solar concentration as compared to operating under one sun. According to Chong et al., 2013, the latest state-of-the-art triple-junction cells are achieving around 40% conversion efficiency at 100× to 900× concentration ratios, while the world record was at 41.1% at 454× concentration. Therefore, new optical design has to tackle non-uniformity issue, while still achieving high solar concentration to enable the highest possible conversion efficiency.

2.4.1 Modular Fresnel Lenses

A new Fresnel concentrator was introduced by Ryu *et al.* (2006) with the aim to produce a uniform distribution of solar irradiance with moderately high concentration ratio and increase PV generation efficiency. In conventional Fresnel lenses that have circular shaped facers to focus a collimated beam to a point, CPV solar cells are unable to extract maximum power due to irregular resulting illumination. As shown in Figure 2.2, an array of modular Fresnel lenses is based on superposition concept, whereby each modular Fresnel lens bends the normal incident solar flux onto the targeted CPV cell area. According to Ryu *et al.* (2006), the recommended design uses prism rings for the facets so that the segments can be kept larger in size. Since no sunlight should bend at the central region, no facets are present at the central lens block.

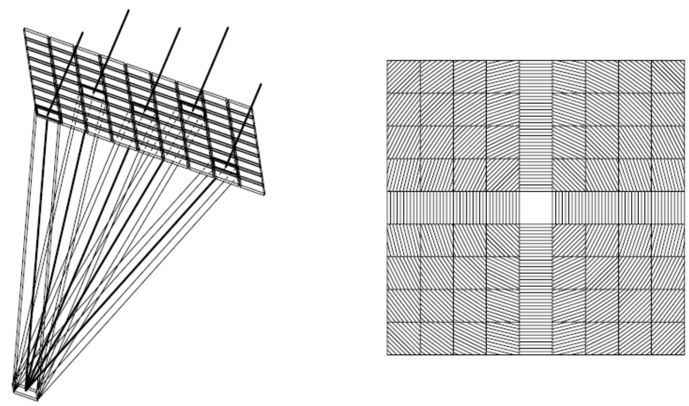

(a) (b)

Figure 2.2: Schematics that explains the concept of modular Fresnel lenses for concentrator solar PV system that are presented in (a) 3-D view of the optical structure, and (b) facet directions of modularly faceted Fresnel lenses (Ryu *et al.*, 2006).

The devised optical system for such solar concentrators promises effective conversion of optical energy into electrical power with reasonable cost and minimal resources. The flux distribution at the cell plane is estimated to be about 20% uniform with transmission efficiency of above 65% for Fresnel lens arrays of 3×3, 5×5 and 7×7 (Chong *et. al.*, 2013). The transmission efficiency is rather low, which is less than 80% owing to reflection at the lens surface and absorption by the material of the lens (Kemmoku *et al.,* 2003; *Araki et al.*, 2006; Ryu et al., 2006). Another limitation of the modular Fresnel lens method is that the application of the selected acrylic resin to be used as lens material is not yet feasible for high concentration ratios. Unless typical lens material like polymethyl-methacrylate (PMMA) can be substituted by other materials with similarly characteristics such as high transmission and low optical dispersion throughout the solar spectrum, the current lenses will be limited by its material to only operate at low and moderate level concentration ratios.

2.4.2 Parabolic Dish

Parabolic dish concentrators consist of solar reflectors like mirrors that are arranged in the parabola shape to concentrate incident sunlight onto a focal point (Reddy and Veershetty, 2013), and can offer the highest thermal and optical efficiencies among all the concentrator options (Lovegrove *et al.*, 2011). At the focal point, a CPV receiver will convert concentrated solar irradiation into electrical energy.

The design of a parabolic dish concentrator requires rigorous system-design principles, and detailed consideration of the interactions between key subsystems of mechanical structure, mirrors, receiver, foundation as well as actuation or tracking system. At the same time, the optical performance of the concentrator is also of great importance to be studied. It is common knowledge that a parabolic dish will produce a Gaussian image at the receiver target. Figure 2.3 shows on-sun measurements using a representative mirror panel. Besides optical uniformity assessment, this distribution suggests that there is an average surface slope error of 1.3mrad (Lovegrove *et al.*, 2011).

The large paraboloidal dish by Australian National University (ANU) that was presented by Lovegrove *et al.* (2011) was able to achieve the highest conversion efficiency and at the same time justify the higher capital cost per unit area. The prototype has proven that the novel design features can achieve lower construction material via the use of mirror panels to act as part of the structure itself. Moreover, trough optical analysis has shown that receivers with geometric concentration ratios of at least 2000 times are deemed possible. Nevertheless, the image of focused sunlight at the target is inherently non-uniform. While there is good potential of harnessing thermal energy at high solar concentration ratio, the reliable use of CPV cells at solar concentrations in the range of 1000 - 2000 suns is not yet established, and requires further studies. In addition to that, the design concept of this system has not yet incorporated solar flux uniformity concerns, for application with CPV cells.

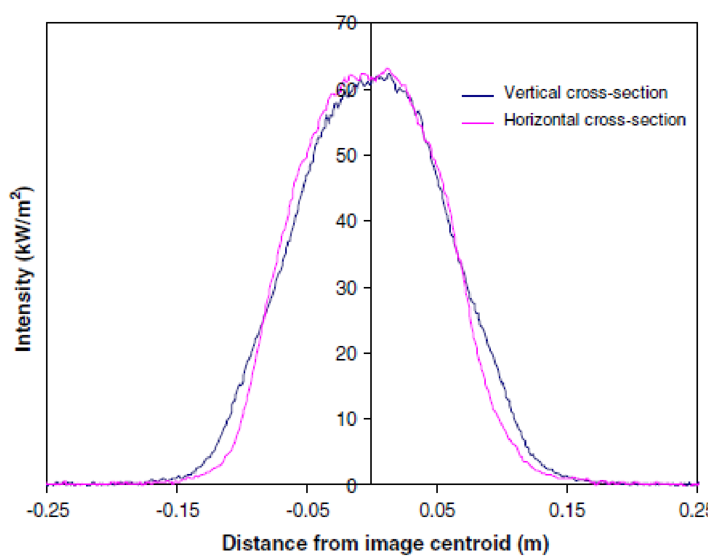

Figure 2.3: Flux mapping results for a 500m^2 paraboloidal dish solar concentrator using one mirror panel (Lovegrove *et al.*, 2011).

2.4.3 Homogenizer Technology

In CPV systems with single optic/single cell configuration, sunlight is focused onto each cell individually. In these point-focus systems, current mismatch problem is less critical because the optical units are all reasonably well aligned to ensure that same incident power is received at all solar modules. For systems that have a number of CPV receivers, usually Fresnel lens system, flux homogenizer is added to act as additional secondary optical element (SOE) to improve the flux distribution and produce more uniform illumination, as presented in Figure 2.4 (Araki *et al.*, 2006; Chong *et al.*, 2013). The homogenizer that may act as secondary optics is also used for guiding concentrated sunlight from the primary optics to the solar module.

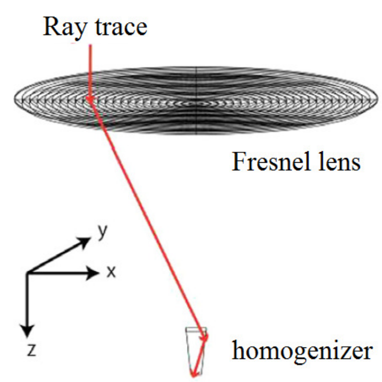

Figure 2.4: Schematic illustration of a Fresnel lens system's optics model with a homogenizer (Ota and Nishioka, 2012)

Flux homogenizers are able to improve optical performances by producing uniform flux distribution over solar cells and hence minimize conversion losses caused by chromatic aberration as well as surface voltage variation (Figure 2.5). Nonetheless, due to the requirement of precise engineering, additional SOE increases manufacturing cost, needs active cooling at very high solar intensities and adds complexity to a solar concentrator system, (Victoria *et al.*, 2009; Benitez *et al.*, 2010). In addition to that, the introduction of a typical flux homogenizer will inflict optical losses that can reach 10% or more (Kreske, 2002)

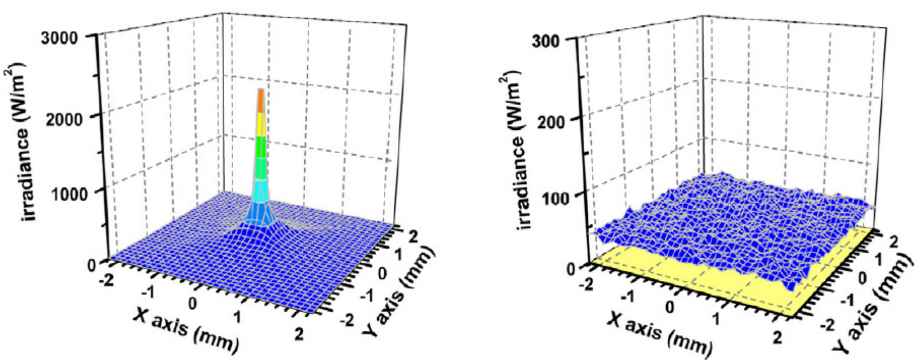

(a) (b)

Figure 2.5: A comparison of simulated irradiance distribution using (a) Fresnel lens only, and (b) Fresnel lens and a homogenizer (Ota and Nishioka, 2012)

2.5 Non-conventional CPV Cells

Another alternative method of overcoming non-uniform irradiation to improving system performance is by refining optical mismatch via exchanging standard-sized CPV cells with non-conventional geometry cells, which typically incur extra cost. These CPV cells are specially designed according to a specific concentrated solar flux profile and are only suitable for a specific type of solar concentrator.

2.5.1 Radial Solar Cells

In conventional dense-array receivers made of square or rectangle cells that are connected in series, significant current mismatch is observed because the irradiance at the focus is usually not uniform. Vivar *et al.* (2009) presented a radial large area Si-cell receiver that uses custom-shaped solar cells that can divide the incident flux evenly between the cells. Radial solar cells are designed and manufactured from EUCLIDES III solar cells, by incorporating additional laser cutting process to obtain trapezoidal cells to be arranged into circular sectors that matches the spot produced by parabolic dishes. As the concentrated sunlight of a parabolic dish is usually radially symmetry, the suggested radial CPV cell may be the best in geometry to reduce current mismatch. These custom-made cells can decrease the losses from non-uniformity and misalignment by nearly 6 times lesser, as compared to connecting CPV cells in a full series configuration (Vivar *et al.*, 2010).

Although the performance is improved, the radial cell parquets receiver is still susceptible to current mismatch when the spot of concentrated sunlight is not centred, due to tracking errors or optical misalignment. Referring to Figure 2.6, as the spot of concentrated sunlight moves across the target receiver, the distribution and intensity of solar irradiation on certain solar cells will be reduced while the intensity on some cells is increased and on others will remain the same. This limitation can be curtailed by an additional process of parallel interconnecting opposite circular sectors, in order to allow current compensation when tracking error occurs and the concentrated solar flux is off focus to the centre.

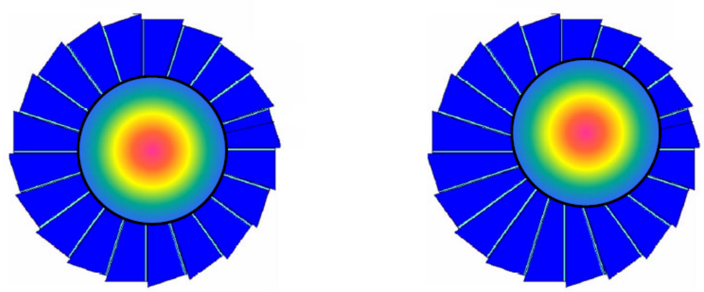

(a) (b)

Figure 2.6: A scenario analysis to compare when (a) concentrated solar flux is correctly aligned with an array of radial parquet of solar cells (b) concentrated solar flux is out of focus to the same array of radial parquet of solar cells (Vivar *et al*, 2009)

While the idea of parallel interconnection of opposing circular sectors seems logical, wiring complexity and resistance losses from the multiple parallel-connected cells should be taken into account in producing a practical receiver. Furthermore, the concentrated solar flux distribution does not fully cover the whole receiver area, and therefore this design will utilise more CPV cells as compared to other dense-array design.

2.5.2 Solar Cells with Different Widths

With similar approach, Azur Space Solar Power GmbH (2010) has developed custom-made CPV dense-array modules for the application in parabolic solar concentrator systems without homogenizers. For a parabolic concentrator, the outer segments of the concentrated solar flux distribution receive lesser intensity of sunlight, as compared to middle segment. Hence the usable power per segment will be limited by the low power of the outer segments, due to current mismatch. To solve this problem, the lower light intensity at the edges of the concentrated sunlight is compensated with wider solar modules, while the higher light intensity at the middle region is exposed to narrow-sized solar modules, thus achieving good current matching.

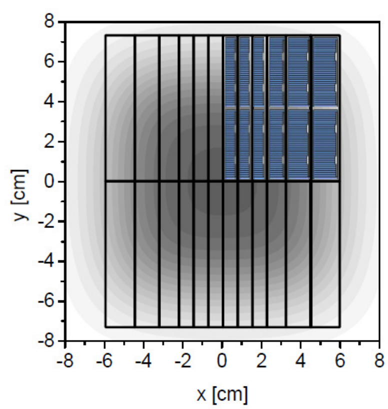

Figure 2.7: Dense-array module is designed with four different widths according to the inhomogeneous illumination of a parabolic solar concentrator. The solar cells are presented only in one quarter of the array as an example (Lockenhoff *et al.*, 2010)

For this project, the custom-made module consists of four different geometries of CPV solar cells that are arranged in a specific manner that compensates inhomogeneous solar irradiation (Figure 2.7). The outer section of the array receives lesser light, and hence is compensated by using wider segments of CPV modules while the inner section of the array that receives more concentrated light is filled with smaller segments of modules. Nevertheless, each type of solar cell width required its own tooling for production and hence resulted in high investment and logistic costs. To avoid high investment cost due to having too many uniquely- sized cells, the modules are optimised and reduced from four different types to two different types, as shown in Figure 2.8 (Lockenhoff *et al.*, 2010). Needless to say, streamlining different solar cell widths would compromise optical matching of the modules.

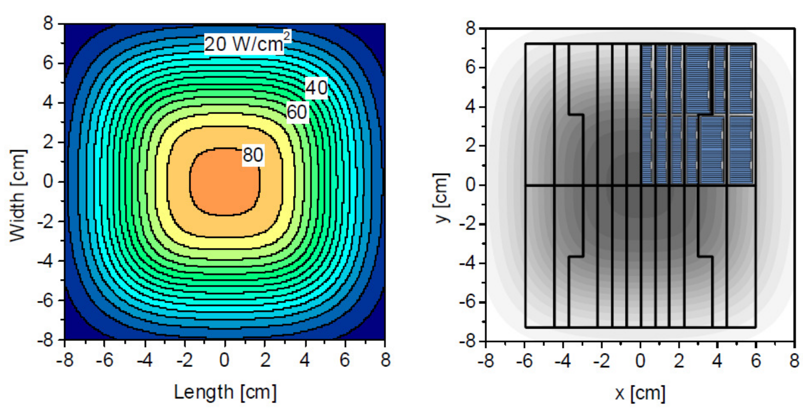

Figure 2.8: Azur Space has developed a dense array receiver target by combining two types of custom-made solar cells in different combination for the application with a parabolic dish (Lockenhoff *et al.*, 2010)

2.5.3 High-voltage CPV Cells

Silicon Vertical Multi-Junction (VMJ) solar cell is an alternative type of CPV cell that is produced in a process of stacking multiple wafers, and then going through orthogonal cutting (Sater and Sater, 2002). The number of stacked wafers, which is same as the number of junctions connected in series, will determine the final solar cell voltage (Figure 2.9). Unlike conventional CPV cells, the VMJ solar cells that exhibit high cell voltage and low corresponding cell current can operate without severe degradation due to series resistance under high concentration. Recently, Segev and Kribus (2013) have introduced high-voltage Silicon VMJ solar cells for parallel connection in a CPV dense-array. These CPV cells can accept high solar concentration with reported peak efficiency reaching close to 30%.

In a parallel connected array, voltage matching instead of series matching is attempted to minimize non-uniform illumination mismatch losses. Since voltage is less sensitive to solar concentration variations, the new VMJ modules have greater tolerance to non-uniform illumination and tracking error. As a comparison, dense-arrays that are designed with series-connected conventional cells show high sensitivity to non-uniformity and thus require longer homogenizer to reduce mismatch losses. On the other hand, dense-array using VMJ cells may only need to use shorter homogenizers or possibly no usage of homogenizer altogether while only experiencing a minor reduction in efficiency. Furthermore, the use of bypass diodes in VMJ arrays is avoided since there is very little current mismatch.

Nonetheless, a dense-array with solar cells that are interconnected in parallel rather than in series will have very high array current because individual current from every CPV module is added up. The effect of high array current to resistive losses should be examined in detail to ensure that the overall conversion efficiency is not jeopardized. In addition to that, it should be noted that although bypass diodes can be avoided in an all-parallel connection, current bypassing may still be useful when there is malfunction of a single vertical junction within a VMJ solar cell. It should also be noted that Segev and Kribus (2013) highlighted that the fabrication process using very densely placed narrow junctions of 40 μm width is quite challenging.

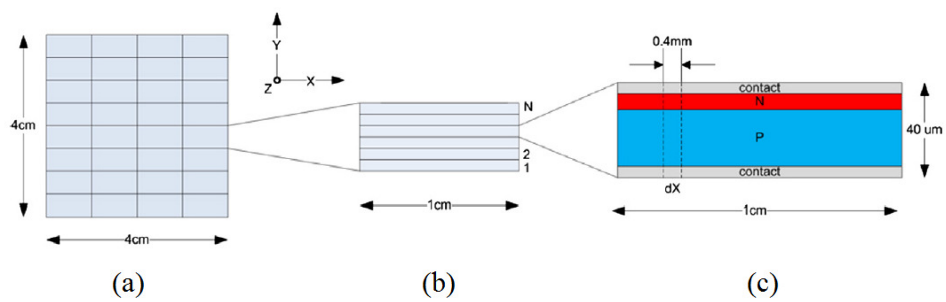

Figure 2.9: A schematic presenting the architecture of (a) a CPV module; (b) a VMJ solar cell made from several vertical junctions that are connected in series internally; (c) a vertical junction and its segment of length *dx* (Segev and Kribus 2013)

2.6 Bin-packing Interconnection Reconfiguration

Conventionally, bin-packing models are used in areas such as computer network storage allocation, assigning commercial breaks on television and packing boxes into shipping containers. The one-dimensional bin-packing problem (BPP) is essentially finding packing solutions for objects via minimum number of bins with pre-sized capacity with a given list of objects and their separate sizes. According to Coffman *et al.* (1999) and Applegate *et al.* (2003), BPP is an NP-hard problem which is tedious and time-consuming to solve, and various heuristics can solve these classical bin-packing problem (Appendix H).

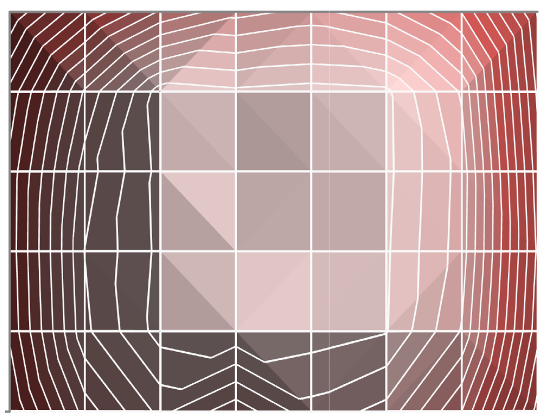

Figure 2.10: A contour plot of concentrated solar flux distribution was acquired with an optical scanner (Siaw and Chong, 2013)

Recently, Siaw and Chong (2013) have investigated Best Fit (BF) and Best Fit Decreasing (BDF) heuristics for application in one-dimensional bin-packing problem to solve current mismatch losses in solar concentrator systems. In the simulations, bin capacity is defined as 2A, also known as the starting point, and the value is slowly increased until 20A. From the presented results, the best solution having minimal mismatch losses is BFD 9.4A, which is an array with five series-connected strings. In Figure 2.10 and Figure 2.11, each series string is represented with a different colour and CPV cells that are grouped within similar string have the same colour.

In the paper by Siaw and Chong (2013), by using measured flux profile to derive current values of each CPV cell at the receiver target, the current values are used as objects for packing. Using this method, current mismatch can be almost eliminated from 1.03 A to as low as 0.07 A when the array is operating at DNI of 604.19 W/m^2. Using this improved method boosts output power to 112.91 W, which is 26.83 W more than the conventional 22 × 2 TCT array that only produced 86.08 W.

Although this approach enables automatic reconfiguration of new array topologies, as compared to the conventional series-parallel (SP), bridge-link (BL) and total-cross-tied (TCT), the proposed interconnection is very complicated and not practical for implementation. Referring to Figure 2.11 and Figure 2.12, we can observe that it is very tedious to link any one of the series string. For example, lime green solar cells which belong to the fifth string are distributed among all four quarters of the CPV array, hence complicating electrical circuit interconnection. Unless a new substrate or technology is developed for this purpose, the dense array design is too complex for practical implementation.

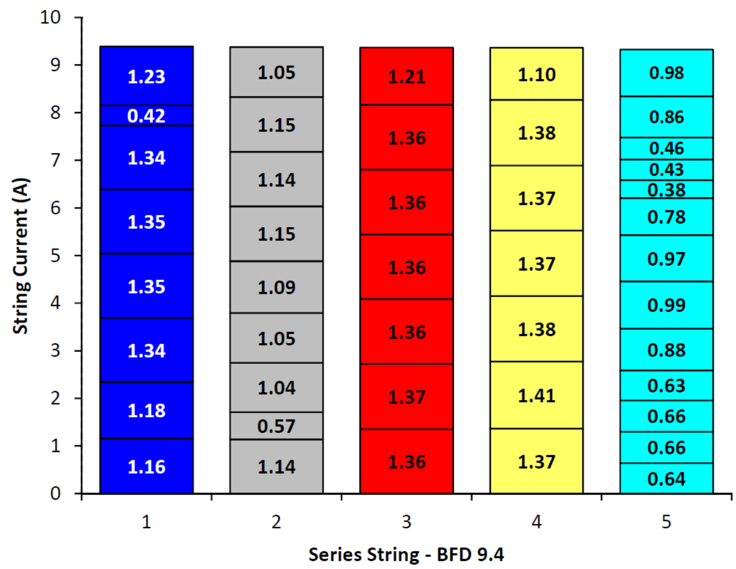

Figure 2.11: This bar chart shows packing configuration of an array with five series-connected strings at 0.07A current mismatch. (Siaw and Chong, 2013)

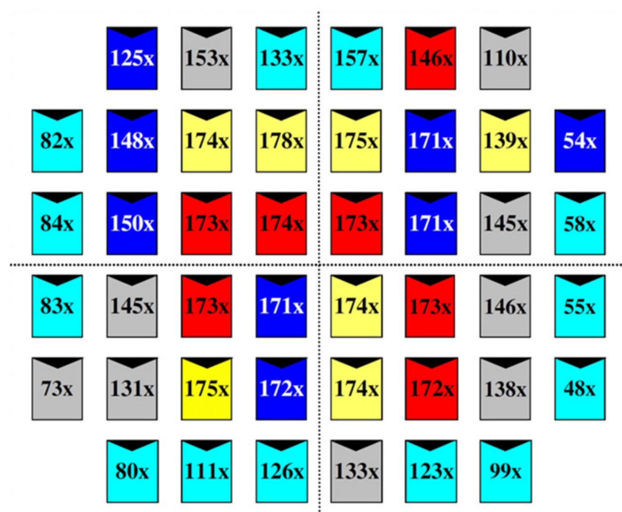

Figure 2.12: A diagram showing the complicated distribution of CPV cells from different strings across a dense-array. Solar cells that are from the same series string are presented with the same color for easy reference (Siaw and Chong, 2013)

CHAPTER 3

MATERIAL AND METHODS

3.1 Theoretical Development of NIPC

To achieve both good uniformity as well as reasonable high concentration ration of solar irradiation on the target, an NIPC that is based on non-imaging optics to concentrate sunlight is proposed. The idea of concentrating solar irradiation in the planar concentrator is similar to that of a non-imaging focusing heliostat, whereby uniform intensity on the target is achieved by super positioning flat mirror images at one point. In this concept, the incident rays are reflected by an array of identical flat mirrors to the target, and that mirror size and shape are nearly the same as that of the target.

Referring to Figure 3.1, the NIPC is formed by arranging numerous square flat mirrors to act as the optical aperture for collecting incident light and focussing the incident sunlight at any focal distance along its optical axis onto a target receiver. The difference of this design as compared to other optical concept of solar concentrators such as parabolic reflectors is that the geometry of an NIPC cannot be explicitly defined with any analytical surface formula (Chong *et al*., 2009; Chong *et. al*., 2010). Therefore, numerical simulation becomes necessary in the optical analysis of the NIPC. For optical modeling of NIPC, the techniques employed to express the reflection of sunlight by the concentrator as well as to generate solar flux distribution on the receiver target is by coordinate transformations and ray-tracing. In an attempt to reduce computing time with negligible effect to the results, two good assumptions are used. In the first assumption, to account for the spreading of solar irradiation from solar disk effect upon reflection from mirror surface, each sunray that is reflected from the concentrator is spread into sub-rays, *P,* and each sub-ray carries 1/ *P*-th of energy from the incident sun ray. These rays uniformly spread as a form of light cone that subtends to the solar disk half angle of 4.65 mrad. The second assumption is that each facet mirror consists of a finite number of smaller elements, called reflective points. The assumptions are presented in Figure 3.1, to show the application of concept in the optical modeling of the concentrator (Appendix D).

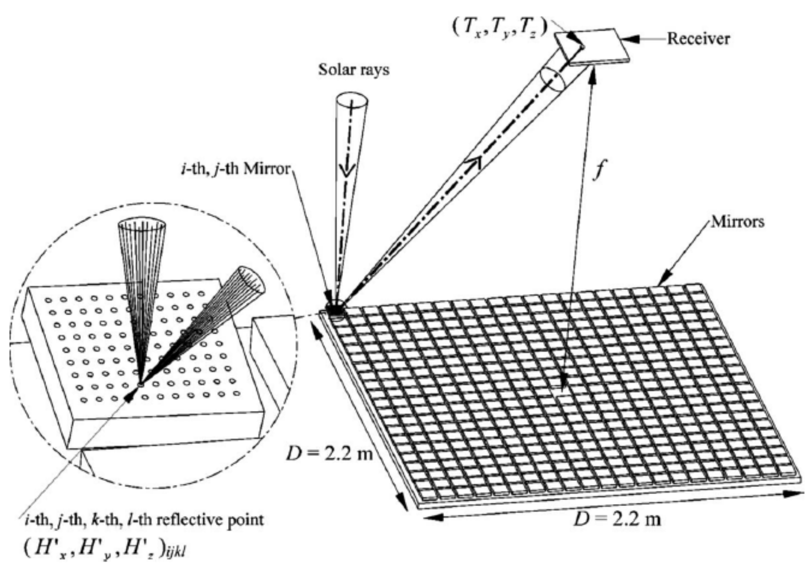

Figure 3.1: A non-imaging planar is formed using flat mirrors, whereby every mirror comprises a finite number of reflective points, and each reflective point is illuminated by a discrete number of sub-rays

For geometrical representation, Cartesian coordinate system (x, y, z) acts as the main coordinate system, and it is defined in the plane of the NIPC. The origin of the coordinate system lies at the centre of the planar concentrator. On the other hand, the sub-coordinate system (x', y', z') is defined at the local facet mirror. The x-axis of the planar concentrator is along the central column of mirrors, the y-axis is along the central column of mirrors, and the z-axis points towards the receiver (Chong *et al.*, 2010).

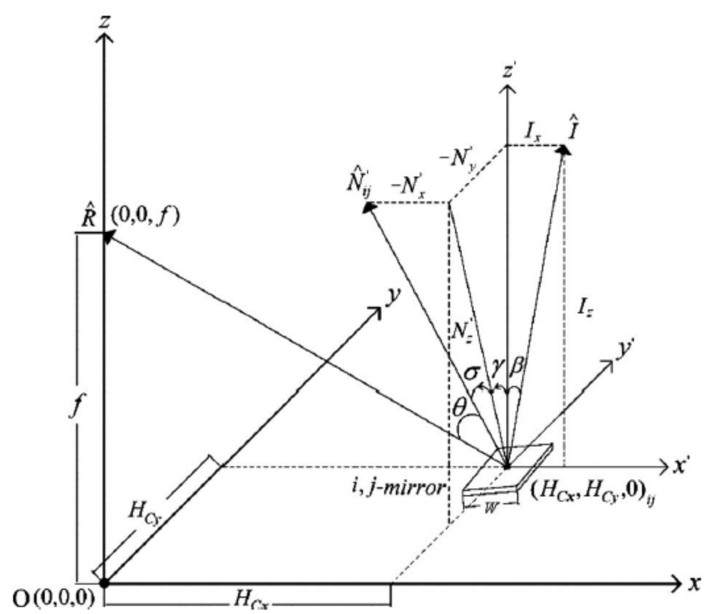

Figure 3.2: The main coordinate system is (x, y, z), and is defined in the planer of the NIPC with its origin at the center of the concentrator. On the other hand, sub-coordinate system (x', y', z') is defined at the local facet mirror

The coordinates for the central point of an *i*, *j*-mirror are designated as (H_{Cx}, H_{Cy}, 0)$_{ij}$, and *i* as well as *j* denote the location of flat mirrors at the *i*th row and *j*-th column of the concentrator, respectively. The coordinates of the focal point of the NIPC is denoted by (0, 0, *f*). To reflect sunray towards the receiver, the tilting angle of the *i* ,*j*-mirror about the axis that is in parallel with the *x*-axis is represented by γ, and the tilting angle about the axis that is perpendicular to the *x*-axis is represented by σ. These two tilting angles can be expressed as follows:

$$\gamma = \arctan\left[\frac{H_{Cy}}{f + \sqrt{H_{Cx}^2 + H_{cy}^2 + f^2}}\right] \tag{3.1}$$

$$\sigma = \arctan\left[\frac{H_{Cx}}{\left(H_{Cx}^2 + 2H_{Cy}^2 + 2f^2 + 2f\sqrt{H_{Cx}^2 + H_{Cy}^2 + f^2}\right)^{1/2}}\right] \tag{3.2}$$

The incident angle of the sunray is denoted by θ, and is relative to the *i* ,*j*- mirror, as presented in equation (3.3). For the initial coordinates of the reflective point for facet mirror, they are arranged into the *i*-th row and *j*-th column and designated as (H_x, H_y, H_z)$_{ijkl}$. The subscripts *k* and *l* denotes the reflective point's position at the *k*-th row and *l*-th column in the facet mirror. Referring to Figure 3.1, each mirror is tilted with its corresponding tilting angles σ and γ to move the reflective point at new coordinates $\left(H_x^{'}, H_y^{'}, H_z^{'}\right)_{ijkl}$ to superposition all of the mirror images to the target receiver.

In order to ease mathematical representation of coordinate transformation, the translation is prepared as a linear transformation by increasing the dimensionality of the space (Chong *et al.*, 2010). Therefore, the coordinates $(H_x, H_y, H_z)_{ijkl}$ can also be represented as $(H_x, H_y, H_{z,\ 1})_{ijkl}$, and is treated as a vector in matrix form in equation (3.4). The final position of the reflective point is presented as a matrix form in equation (3.5).

$$\theta = \frac{1}{2}\arctan\left[\frac{\sqrt{H_{Cx}^2 + H_{Cy}^2}}{f}\right] \tag{3.3}$$

$$[H]_{ijkl} = \begin{bmatrix} H_x \\ H_y \\ H_z \\ 1 \end{bmatrix}_{ijkl} \tag{3.4}$$

$$[H^i]_{ijkl} = \begin{bmatrix} H_x^{'} \\ H_y^{'} \\ H_z^{'} \\ 1 \end{bmatrix}_{ijkl} \tag{3.5}$$

After transformation process, as detailed out in our previous publication (Chong *et al.* 2010), it is possible to plot the resultant solar flux distribution pattern on the receiver target. To attain smooth simulation results of illumination distribution, a fairly high resolution is necessary in the optical modeling of the reflective point, solar disk effect, as well as the receiver plane. In our work, numerical simulation uses facet mirrors of the dimension $W \times W$ and is subdivided into $S \times S$ reflective points. Similarly, the sub-rays within a light cone have a reasonable resolution of 65 rays per aperture diameter. In addition to that, the receiver area 20 × 20 cm^2 is represented by a matrix of pixels with 201 rows and 21 columns. The solar concentration ratio C, also known as number of suns, of each pixel is a measure of the level of solar irradiation that that pixel receives compared with direct normal solar irradiation, and it is calculated as follows:

$$C = \sum_{n=1}^{N_C} \frac{A_{reflective}}{A_{pixel}} \times \frac{\cos\theta}{P} \tag{3.6}$$

Where the $A_{reflective}$ is the area of reflective point (W/S)^2 in cm^2, while A_{pixel} is the area of receiver pixel = (20/201)^2 cm/pixel in cm^2, N_C is the total counts of sub-rays that hits on the resultant pixel on the receiver plane, P is the total sub-rays within a light cone, and θ is the incident angle of the principal solar ray relative to the normal vector of the corresponding i ,j-th mirror (Appendix E).

3.2 CPV Array Parameters

Triple-junction solar cells can be represented by using the comprehensive equivalent circuit model of three current sources connected in series (Vorster *et al.*; 2002). However, not all of the required parameters can be readily obtained via field data measurements or from a standard manufacturer's datasheet. For that reason, the two-diode model which is a model that is capable of representing solar PV as well as CPV cells is selected for dense-array CPV study (refer to Figure 3.3). The temperature of 55° C that was measured by a k-type thermocouple is used in circuit simulation for better modeling accuracy.

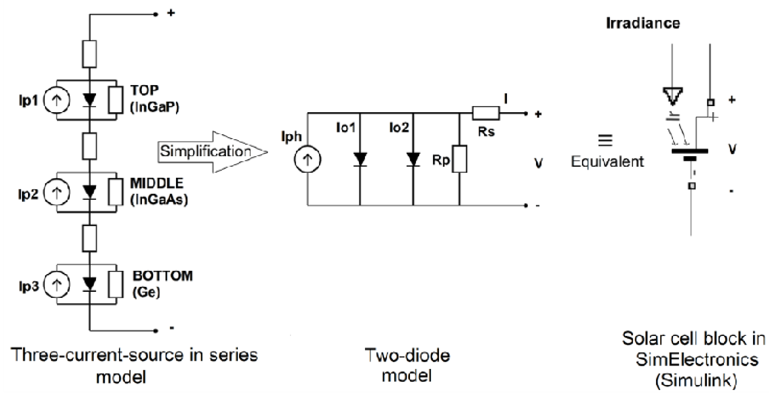

Figure 3.3: A representation of triple-junction solar cell that is simplified from three-current source in series model into a two-diode model. In this study, an equivalent of the two-diode model, which is a solar cell block in SimElectronics, Simulink is adopted as the basic block of our dense-array.

The solar cell block in SimElectronics, Simulink is represented by a single solar cell as current source with two exponential diodes, a parallel resistance (R_P), and a series resistance (R_S). Solar cell blocks are arranged into subsystems in Simulink to form the required CPV dense-array. The output current, I, can be represented by equation (3.7), where I_{ph} is the solar-induced current, I_{o1} is the saturation current of the first diode, I_{o2} is the saturation current of the second diode, V_t is the thermal voltage, N_1 is the diode ideality factor of the first diode, N_2 is the diode ideality factor of the second diode, and V is the voltage across the solar cell.

$$I = I_{ph} - I_{o1} \times \left(e^{(V+IR_S)/(N_1 V_t)} - 1\right) - I_{o2} \times \left(e^{(V+IR_S)/(N_2 V_t)} - 1\right) - (V + IR_S)/R_P \quad (3.7)$$

In Simulink environment, we may choose between an eight-parameter model where the preceding equation describes the output current, I as in equation (3.7), or a five-parameter. Unlike the eight-parameter model, two simplifying assumption are made, where the first assumption is that saturation current of the second diode to have zero in value, and the second assumption is that the parallel resistor to have infinite impedance value. Since the five-parameter model is sufficiently good to perform a good analysis with reasonable accuracy that is successfully verified in the field test that will be presented in the later sections, it is chosen for the simulations of this study (Appendix G).

The five-parameter model is adopted in solar cell blocks from SimeElectronics, and hence the models of solar cells are parameterized in terms of short-circuit current (I_{SC}) and open-circuit voltage (V_{OC}). Short-circuit current and open-circuit voltages are both common parameters that are easily available from manufacturers' datasheet or measured from field operations. In completing the modeling of the whole dense-array, each CPV cell's short-circuit current (I_{SC}), open-circuit voltage (V_{OC}), diode ideality factor (N), series resistance (R_S) and irradiance level are keyed-in to Simulink program.

3.2.1 Electrical Characteristics of CPV cells

To extract main electrical parameters of EMCORE high efficiency Concentrating Triple Junction (CTJ) CPV cells datasheet, graph digitizing method is used to extract data points from the *I-V* curves from 50× to 1182× (Siaw and Chong, 2012). In our work, graph digitizing is done through a web-based WebPlotDigitizer v2.5 that is able to automatically follow and acquire data points from a given high resolution image of *I-V* curve, in order to extract digitized current, voltage and solar concentration information (refer to Figure 3.4). Before acquiring *I-V* curve data, the two axis limits are set. Then, data points were selectively picked for checking to confirm its accuracy to experimental observation during operation conditions. From there, data are transferred into excel spreadsheets, to form correlation equations of I_{SC}, V_{OC} and solar concentration ratio (C), at R^2 value of 0.99 (Figure 3.5).

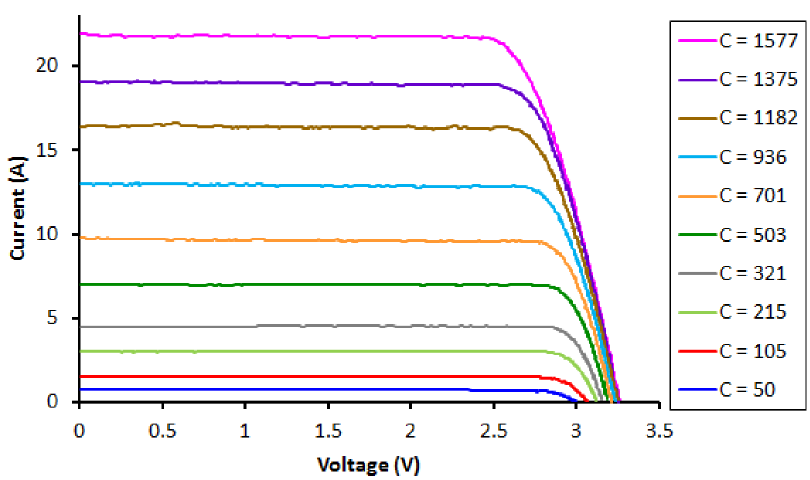

Figure 3.4: Current-voltage (*I-V*) curve of triple-junction InGaP/InGaAs/Ge CPV cells from EMCORE 2008 datasheets, plotted at various solar concentration levels and temperature 25 °C.

From Figure 3.5, a linear relationship is observed for short-circuit current short-circuit current with solar concentration ratio from 50× to 1182×, whereas open-circuit voltage increases logarithmically with solar concentration ratio. The other electrical parameters like series resistance (R_S), and diode ideality factor (*N*) are derived from calculation from measured *I-V* curves (Appendix M).

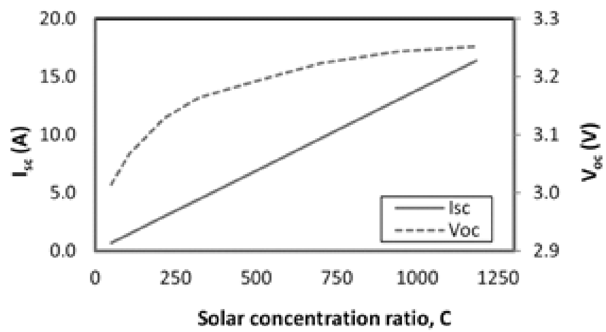

Figure 3.5: From current-voltage measurement data, the relationship of short-circuit current (I_{SC}) and open-circuit voltage (V_{OC}) versus solar concentration ratio *C* from 50× to 1182× of EMCORE CTJ solar cells can be derived

In Figure 3.4, the graph of V_{OC} versus *C* is presented in logarithmic scale, and we can observe that V_{OC} is gradually increasing as ln C rises. We can express the curve with equation (3.8) to find the value of open-circuit voltage of a CPV cell, at any solar concentration ratio.

$$V_{OC} \cong V_{OC}^{1} + N(kT/q)\ln C \tag{3.8}$$

In equation (3.8), N is the effective diode ideality factor, T is the operating temperature in Kelvin, V_{OC}^{1} is the open-circuit voltage when CPV cell is operating under one sun, k is Boltzmann constant and q is the electron charge. As the I-V curve data are extracted at the temperature of 25 ^{o}C, equation (3.9) and (4.0) can be used to calculate current and voltage values when CPV cells are operating at higher temperatures (Chong and Siaw, 2012). For equation (3.9), $I_{SC,T}$ is the operating short-circuit current, I_{SC-STC} is short-circuit current when operating at Standard Test Conditions (STC), K_i is a short-circuit current coefficient provided from the manufacturer datasheet in A/^{o}C, and finally $\Delta T = T - T_{STC}$ (^{o}C). As for equation (3.10), $V_{OC,T}$ is the open-circuit voltage, V_{OC-STC} is the open-circuit voltage when CPV cells are operating at STC, and K_v is the open-circuit voltage coefficient from the manufacturer (V/ ^{o}C).

$$I_{SC,T} = I_{SC-STC} + K_i \Delta T \tag{3.9}$$

$$V_{OC,T} = V_{OC-STC} + K_v \Delta T \tag{3.10}$$

With regards to the parameter of diode ideality factor (N), it can be derived from curve fitting method, using the plots of the CTJ solar cells at medium to high concentration ratio in Figure 3.6 and equation (3.8). This approach is in agreement with the work presented by King *et al.* (2010) and Vossier *et al.* (2012), which pointed out that diode ideality factor of triple-junction CPV cells is close to N = 3. This can be derived from V_{OC} versus solar concentration graphs for medium to high concentration ratios. Moreover, Kinsey et al. (2008) have also highlighted that the diode ideality factor is not affected by moderate temperature fluctuations. Hence, diode ideality factor of N = 3.01 can still be applied in our modeling when CPV dense-array is operating at the temperature of 55°C

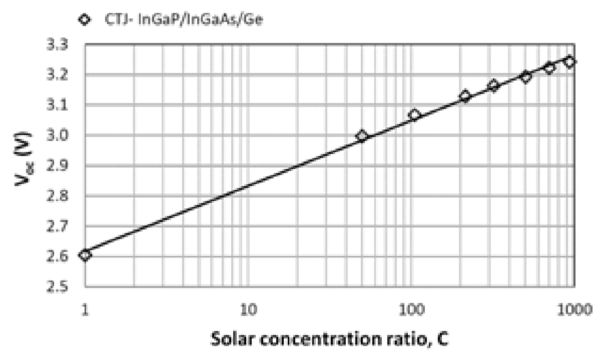

Figure 3.6: This graph shows that V_{OC} changes linearly with the logarithm of solar concentration ratio (ln C)

3.2.2 Series Resistance

It is generally known that there are two approaches that can extract series resistance (R_S) from solar cells effectively. The first possibility of estimating series resistance is from illuminated *I-V* data, and the second possibility is by calculation from dark-condition *I-V* data. In the first case of illuminated condition, electrons are being generated homogenously over the entire solar cell and also being diffused rather homogenously over to its emitters. Hence, in the illuminated state, there will be larger lateral electron flow in the emitter, which results to a more accurate value of series-resistance when compared to the series resistance value that is obtained from dark condition *I*-*V* data (Pysch *et al.*, 2007). For better accuracy, the method of series resistance estimation under illuminated condition is used, by analyzing the slopes of *I*-*V* curves around the point of open-circuit voltage (V_{OC}). In our study, the series resistance calculation is conducted according to *I*-*V* curves at varying solar concentration levels, as provided by the manufacturer's datasheet to better characterize the solar cells in our dense-array modeling.

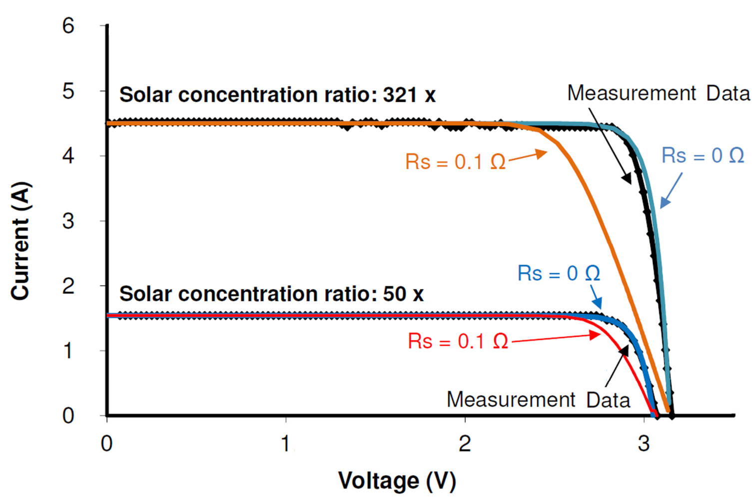

Figure 3.7: This figure shows a comparison of *I*-*V* curves between different series resistance at solar concentration 50× and 321× for InGaP/InGaAs/Ge concentrator solar cells (EMCORE, 2008)

Referring to Figure 3.7, it is shown that an increase in series resistance will lower the electrical performance of CPV cell. When series resistance R_S = 0.1 Ω is applied to both 50× and 321× solar concentration ratio, the electrical performance of 321× is more badly affected as compared to the *I-V* curve of 50×. Besides that, an increase in series resistance would change the shape of *I-V* curve around the “knee”, hence shifting the maximum power point. It can be concluded that series resistance’s effect to *I-V* curve is dependent on solar concentration ratio.

3.2.3 Bypass Diode

Bypass diodes are important for protecting CPV cells from going into reverse-bias breakdown that may lead to permanent damage. If a solar cell is shaded or receives lower solar irradiance, as compared to other solar cells in the same array, the bypass diode that is connected in parallel to its corresponding solar cell in the opposite polarity, will become forward bias. This will allow array current to pass safely through the CPV cell-bypass diode set. For an array that is exposed to non-uniform solar irradiance, bypass diode becomes very vital in avoiding CPV cells that are receiving low irradiation to become load to the rest of the CPV cells that are receiving high solar irradiation. The addition of bypass diode creates an alternate route for the array current to flow so as the underperforming CPV cell can be protected. As current is flowing through a bypass diode, the diodes turns on and holds its corresponding solar cell or group of solar cells to a small negative voltage. This is desirable because it aids in limiting any further drop in the reverse bias voltage of the dense-array (Karatepe *et al.*, 2007).

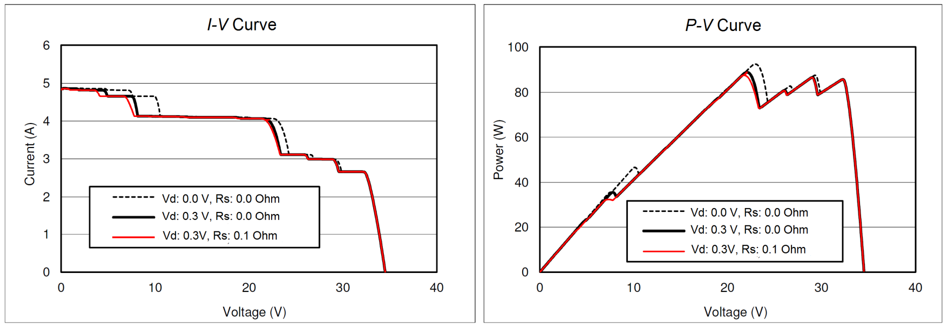

Figure 3.8: Figures of *I-V* and *P-V* curves aim to show the variation of maximum power point, to highlight the importance of selecting bypass diode parameters for accurate CPV dense-array modeling

In Figure 3.8, different *I-V* and *P-V* curves are presented for three bypass diode parameters. As observed, simulated maximum output power of the array can deviate from the real value if parameters of the bypass diode i.e. forward voltage (V_d) as well as turn-on resistance (R_d) are not properly predicted. In this study, *I-V* and *P-V* curves for an array of 12×4 CPV cells in Total Cross Tied (TCT) configuration is presented in Figure 3.7, using three sets of V_d and R_d values. In our dense-array, the bypass diode selected for application is MBRB4030 Schottky diode from On Semiconductor, with parameters having values of $V_d = 0.3$ V and $R_d = 0.1\ \Omega$ at temperature 55 °C.

3.3 Temperature Simulation and Measurements

To ensure that the operating temperature of CPV dense array is operating within the allowable range, a copper block is prepared in the size of 0.146 m width × 0.180 m length × 0.200 m height and subsequently machined with multiple water channels. The water channels are designed to facilitate water circulation to maintain the solar cells' temperature (refer to Figure 3.9). Before machining of the water channels, temperature simulations are carried out to verify our copper block design. In the simulation, concentrated solar flux distribution is applied into an area of 0.1 m × 0.1 m located at the centre region of the cooling block. Theoretical modelling is then conducted with defined parameters such as solar heat flux input, water mass flow rate, and water inlet temperature (Appendix F).

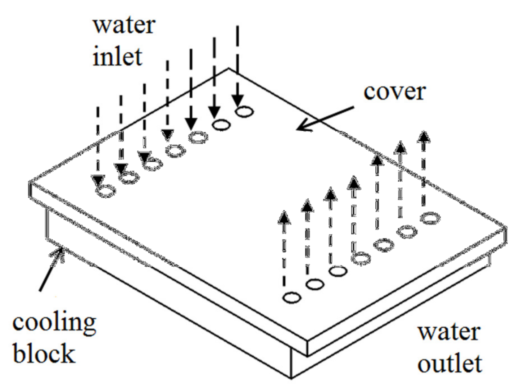

Figure 3.9: Designed cooling block assembly with water inlet and water outlet locations at the opposite ends of the assembly. Dense-array is attached to the cooling block surface using thermal adhesive

After that, Computational Fluid Dynamic (CFD) program via NX6 is used to perform flow and heat transfer analysis on the cooling block. For water flow rate of 0.400 kg/s and water inlet temperature fixed at 30 ^{o}C, a simulated temperature distribution on the cooling block can be generated (Siaw and Chong, 2012). The temperature distribution results generated from CFD is presented in Figure 3.10.

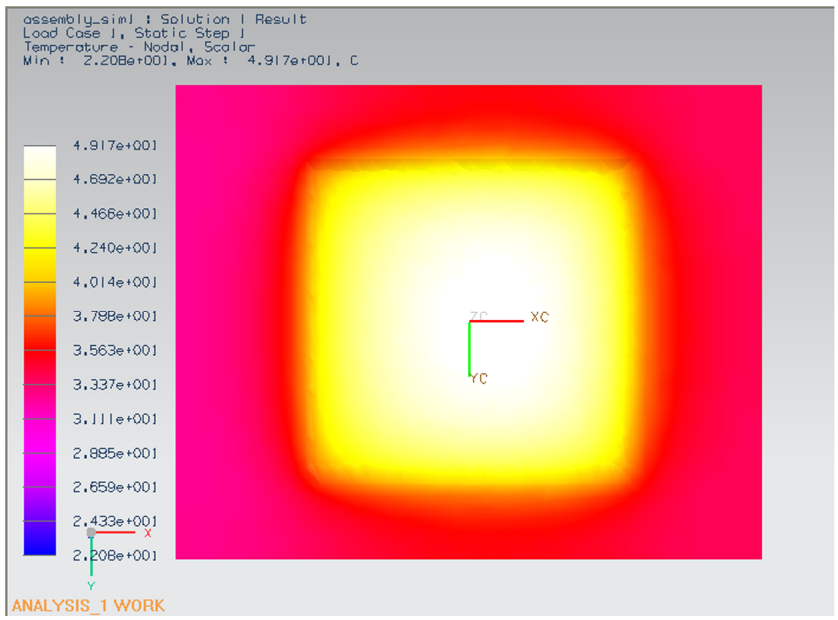

Figure 3.10: This screen shot is a CFD temperature distribution results on CPV dense array at water flow rate of 0.400 kg/s and inlet temperature 30 ^{o}C. It is observed that the maximum temperature on surface is 49.17 ^{o}C, at the cooling block centre region

For a large CPV dense-array, each cell is located at different positions on the cooling block, and therefore each solar cell is operating at a slightly different localized temperature. In order to obtain the individual solar cell's

CFD simulated temperature, every CPV cell's centre point coordinate is determined and its corresponding temperature value is recorded. In addition to that, the thermal resistance from cooling block to CPV cell is also important and has to be considered. The total thermal resistance in this study consists of materials like Arctic Silver thermal adhesive, copper layer in DBC substrate, alumina layer in DBC substrate, solder, and CPV cell. A schematic drawing of the entire material stack is showed in Figure 3.11.

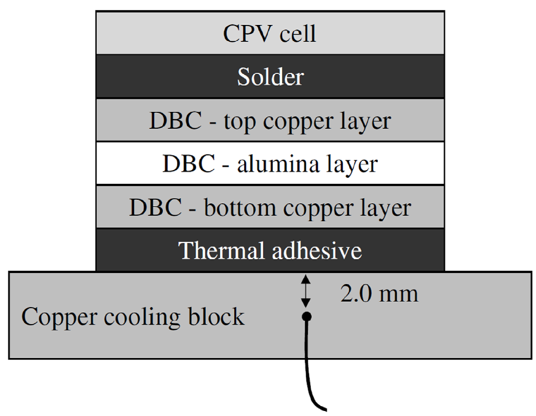

Figure 3.11: This figure shows the cross-sectional drawing of materials stack for the calculation of CPV cell temperature: solar cell's surface temperature can be derived from the measured temperature using k-type thermocouple which is located at 2.0 mm from the front surface of cooling block

To derive solar cell temperature (T_{CPV}), a calculation is performed by getting the measured temperature from k-type thermocouple that is located 2.0 mm from the cooling block's upper surface. The thermal conductivity of all the materials is listed in Table 3.4. From the table, the total thermal resistance of the stack from CPV cell to the measurement point is 4.22×10^{-5} Km^2W^{-1}.

Table 3.1: All of the materials' thickness, thermal conductivity and thermal resistance values used for CPV cell temperature calculation are listed below

Material	Material Thickness, l (mm)	Thermal conductivity, k_c ($Wm^{-1}K^{-1}$)	Thermal resistance, R_{th} (Km^2W^{-1})
CPV Cell	0.20	55	3.64×10^{-6}
Solder	0.15	50	3.00×10^{-6}
DBC, top copper layer	0.30	400	7.50×10^{-7}
DBC, alumina layer	0.38	24	1.58×10^{-5}
DBC, bottom copper layer	0.30	400	7.50×10^{-7}
Thermal adhesive	0.10	7.5	1.33×10^{-5}
Copper layer from thermocouple location to cooling block surface	2.00	400	5.00×10^{-6}
R_{tot}			4.22×10^{-5}

To calculate CPV cell temperature, the following equations are applied (Peharz et al., 2011). In equation (3.15) and equation (3.16), $P_{CPV,in}$ represents the solar power input received by CPV assembly, η_{CPV} is the electrical conversion efficiency of the dense-array assembly, A_r represents the total mirror area which reflects solar flux to the target of NIPC, A_{CPV} is the total active area of dense-array assembly, A_{image} is the total image area of concentrated sunlight on the cooling block, T_{CB} is the temperature of cooling block, and R_{tot} is the total thermal resistance from cooling block to CPV cell.

$$P_{CPV,in} = \eta_{CPV} \times DNI \times A_r \times \left(A_{CPV} / A_{image}\right) \tag{3.15}$$

$$T_{CPV} = P_{CPV,in} \times R_{tot} \times \left(1 / A_{CPV}\right) \times \left(1 - \eta_{CPV}\right) + T_{CB} \tag{3.16}$$

The total thermal resistance from cooling block to CPV cell (R_{tot}) consists of the these materials: copper (cooling block), Arctic Silver thermal adhesive, bottom copper layer of DBC substrate, alumina layer of DBC substrate, top copper layer of DBC substrate, solder, and CPV cell that can be computed with equation (3.17).

$$R_{\text{tot}} = R_{\text{CPV}} + R_{\text{solder}} + R_{\text{DBC-copper}} + R_{\text{DBC-alumina}} + R_{\text{DBC-copper}} + R_{\text{arctic silver}} + R_{\text{copper}} \tag{3.17}$$

on condition that,

$$R_{\text{CPV}} = l_{\text{CPV}} / k_{\text{CPV}} \tag{3.18}$$

$$R_{\text{solder}} = l_{\text{solder}} / k_{\text{solder}} \tag{3.19}$$

$$R_{\text{DBC-copper}} = l_{\text{DBC-copper}} / k_{\text{DBC-copper}} \tag{3.20}$$

$$R_{\text{DBC-alumina}} = l_{\text{DBC-alumina}} / k_{\text{DBC-alumina}} \tag{3.21}$$

$$R_{\text{arctic silver}} = l_{\text{arctic silver}} / k_{\text{arctic silver}} \tag{3.22}$$

$$R_{\text{copper}} = l_{\text{copper}} / k_{\text{copper}} \tag{3.23}$$

whereby l_{CPV}, l_{solder}, $l_{DBC\text{-}copper}$, $l_{DBC\text{-}alumina}$, $l_{arctic\ silver}$, and l_{copper} are the thicknesses of the individual materials at 0.2 mm, 0.15 mm, 0.3 mm, 0.38 mm, 0.1 mm and 2.0 mm respectively; k_{CPV}, k_{solder}, $k_{DBC\text{-}copper}$, $k_{DBC\text{-}alumina}$, $k_{arctic\ silver}$, and k_{copper} are referred as the thermal conductivity of the individual materials with the values of 55 $Wm^{-1}K^{-1}$, 50 $Wm^{-1}K^{-1}$, 400 $Wm^{-1}K^{-1}$, 24 $Wm^{-1}K^{-1}$, 7.5 $Wm^{-1}K^{-1}$, 400 $Wm^{-1}K^{-1}$ respectively, as presented by Luque and Andreev (2007). By substituting all the values into equation (3.16), it is possible to calculate the temperature at the surface of CPV dense-array. This temperature value is applied into our FPM modeling as well as detailed Matlab modeling to achieve more precise simulation results.

3.4 Dense-array Modeling

There are several stages of dense-array modeling, and the first stage is a simple combination of CPV cell and bypass diode. In our modeling of dense-array, this combination set is the lowest layer of sub-system (Figure 3.12). In the second stage, full connection of forty-eight sub-systems is simulated, where each one is labelled from C1 until C48. The array of subsystems are connected together according to interconnection design to form a circuit that represents a CPV dense-array (refer to Figure 3.13).

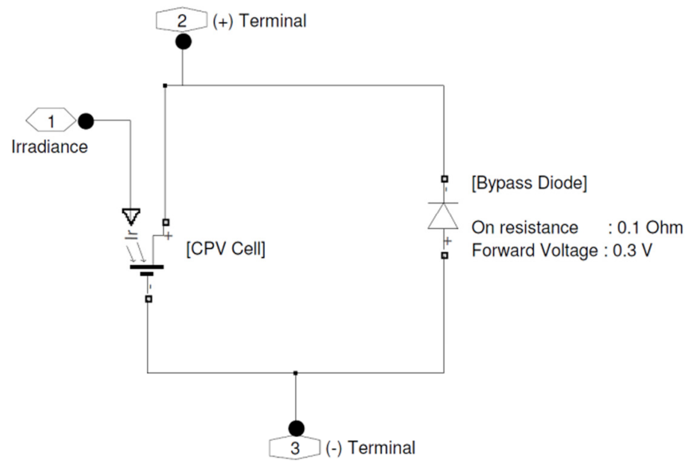

Figure 3.12: The first stage modeling is also the lowest layer of sub-system modeling, and it consists of a CPV cell and bypass diode each. As an example, an array consisting 24 × 4 cells would have twenty eight sub-systems

In the last stage of dense-array modeling is presented in Figure 3.14, where the manner of computing *I-V* and *P-V* data is summarized in block diagrams. All lower stages of array modeling, i.e. first stage and second stage, are masked as a representative sub-system of 'CPV array' block. Now that the three stages are completed, our model is ready for computer simulation with a designated simulation time that typically affects *I-V* curve resolution. Generated results, such as array current, voltage and output power are stored in a workspace in Matlab which can be later exported to excel for more thorough analysis. Figure 3.15 depicts a flow chart to explain on the step-by-step procedure of modeling and simulation approach in Simulink. Upon completion of simulation, the severity of each simulation's mismatch conditions and the degradation to output power is investigated via *I-V* characteristics evaluation.

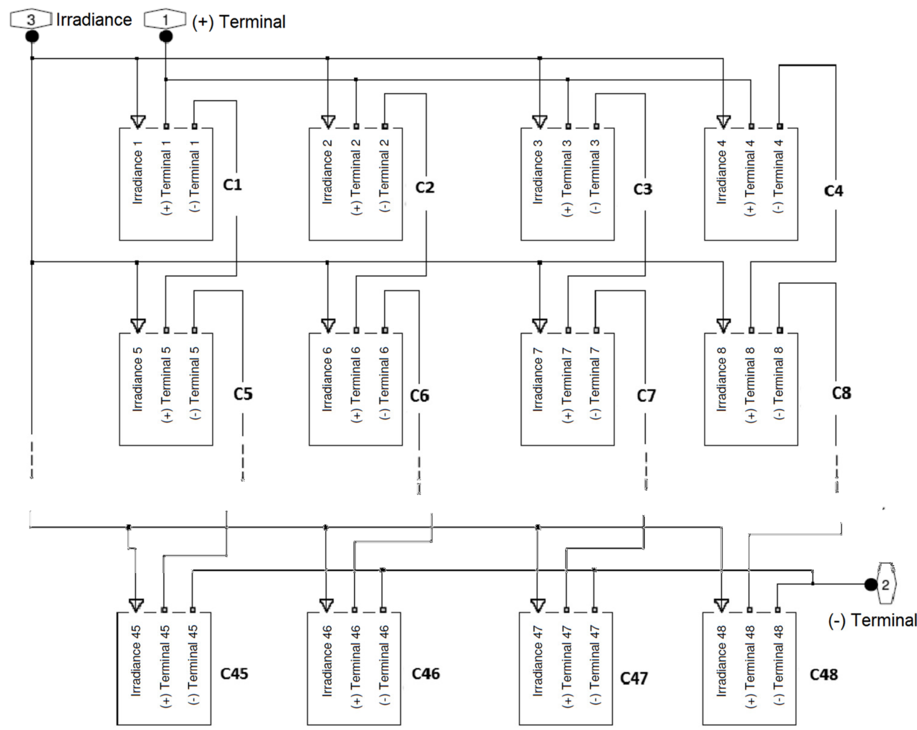

Figure 3.13: In the second stage of dense-array modeling, 12 × 4 Simulink sub-systems blocks are connected according to the desired interconnection design to form a complete array

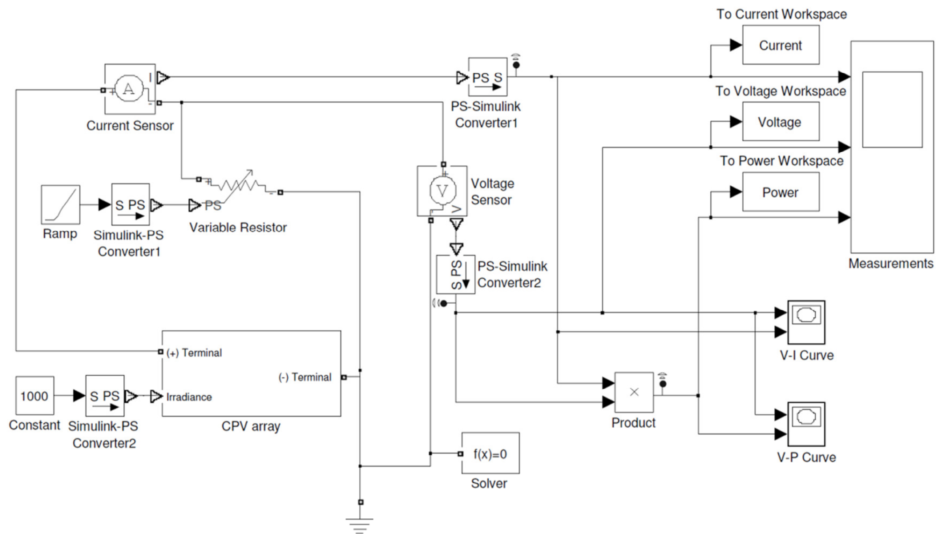

Figure 3.14: In the final stage of Simulink implementation, all lower stages of array modeling, i.e. first stage and second stage, are masked as a representative sub-system of 'CPV array'

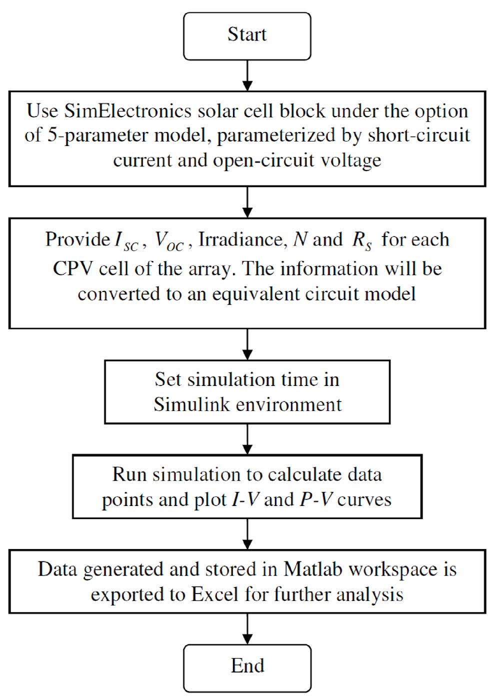

Figure 3.15: A flow chart that explains the flow of dense-array modeling and simulation approach using Simulink, Matlab

3.4.1 Optimizing Dense-array Performance

The process of optimizing a CPV dense-array design is fairly complex and requires a strategic approach in order not to rely on the conventional trial-and-error practice. Usually, a dense-array design is rather dependent on a designer's experience to come up with the initial design. After the first design estimation, comprehensive and detailed design must be carried out to examine preliminary results. According to Arora (2004), if the preliminary results are unsatisfactory, the first design is rejected and further trial designs are started from the initial design stage again. Finally, all the trial designs are analyzed to find the best design with the highest output power. The best design is later checked and verified through experimental results. The conventional approach is exhaustive and time-consuming in finding a good dense-array design that suits a solar concentrator system.

In this study, a novel fast-prediction method (FPM) that is both systematic and reasonably accurate is proposed to replace the conventional method of trial-and-error that typically depends on system designer's familiarity, intuition, and mathematical analysis capability. In Figure 3.16, a flow chart demonstrates the complete design process from start until a satisfactory and optimized CPV dense-array design is achieved. In addition to that, four stages of the newly proposed FPM approach for optimizing dense-array interconnection design to achieve the best performance are presented in Figure 3.17.

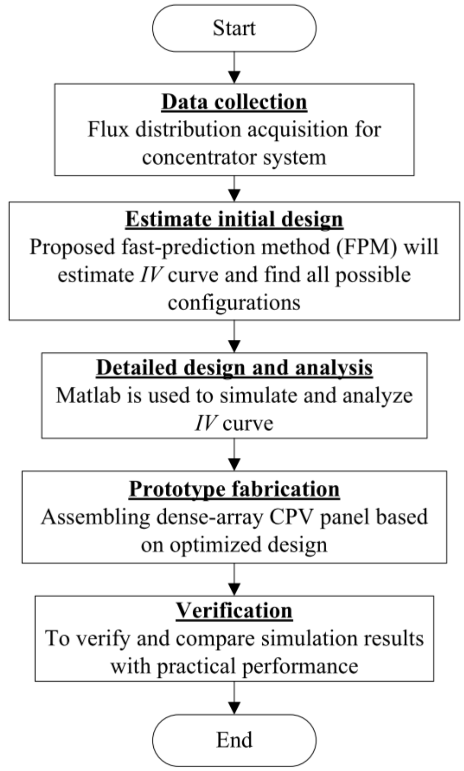

Figure 3.16: This flowchart shows a systematic and complete fast prediction method (FPM) as a novel approach to replace the conventional method in CPV dense-array design

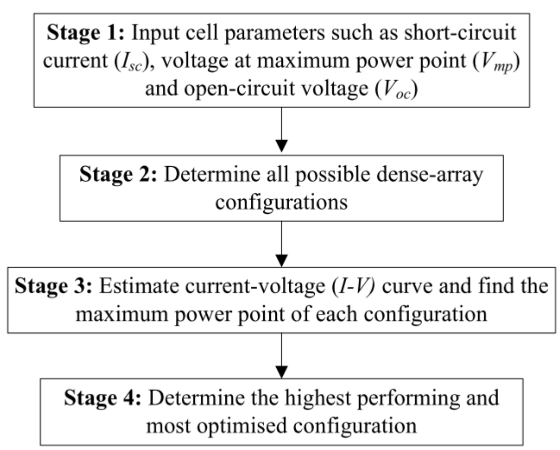

Figure 3.17: A detailed stage-by-stage description that explains the methodology of the proposed four stages of novel FPM

3.5 Prototype of Non-imaging Planar Concentrator

As presented in Figure 3.20, a dense-array design begins with solar flux distribution measurement of a solar concentrator to understand its optical characteristics. For this study, an NIPC prototype that was constructed within the compounds of Universiti Tunku Abdul Rahman (UTAR) at 3.22° North, 101.73° East is selected (Chong and Tan, 2012). This concentrator utilizes azimuth-elevation sun-tracking method, and its orientation is driven by some stepper motors connected to worm gear reducer to keep and maintain the position of the concentrator throughout the day (Chong *et al.*, 2009; Chong and Wong, 2011).

Aluminium is selected as the material of structural frame to ensure that the whole solar concentrator is light which can later allow low power stepper motors to be used for installation on the NIPC prototype. A Windows-based program that is implemented in Microsoft Visual Basic.net environment was developed for sun-tracking purposes (Appendix A). This computer program can automatically control sun-tracking mechanism according to the day number, local time, time zone, and coordinate of the site installation (latitude and longitude). By applying the aforementioned parameters, the computer program is able to calculate both azimuth and elevation angles of the sun and hence can trigger stepper motors to drive the NIPC concentrator frame to the correct orientation (Chong and Wong, 2011). Since the apparent sun position varies with time throughout the day, a computer continuously sends signals through parallel port to a driver to manoeuvre the orientation of solar concentrator frame about the azimuth and elevation axes to maintain accurate tracking position (Appendix B and C).

The concentrator frame is installed with 192 mirror sets that are pre-aligned individually to focus sunlight to the receiver target for producing reasonably high solar concentration levels. Referring to Figure 3.18, three outer rings of mirror and some mirror sets at the centre region of the NIPC were taken out from this study due to serious blocking issues between mirrors and shading caused by the receiver target setup. Last but not least, a copper cooling block is installed at the target receiver for the purpose of optical alignment as well as solar flux distribution investigation.

Figure 3.18: A prototype of non-imaging planar concentrator that was installed within the Setapak campus of University Tunku Abdul Rahman (UTAR)

3.6 Measurement of Solar Flux Distribution

It is necessary to carry out solar flux distribution measurement at the concentrator receiver target, after the completion of optical alignment of mirror sets at any solar concentrator. Hence, a specially designed optical scanner is installed on the concentrator receiver target for retrieving 2-D solar flux distribution by scanning along the column direction during operation. The optical scanner consists of a row of triple-junction cells (InGaP/InGaAs/Ge) that is 1.0 cm × 1.0 cm in dimension each, which is of similar size with the CPV cells of the dense-array.

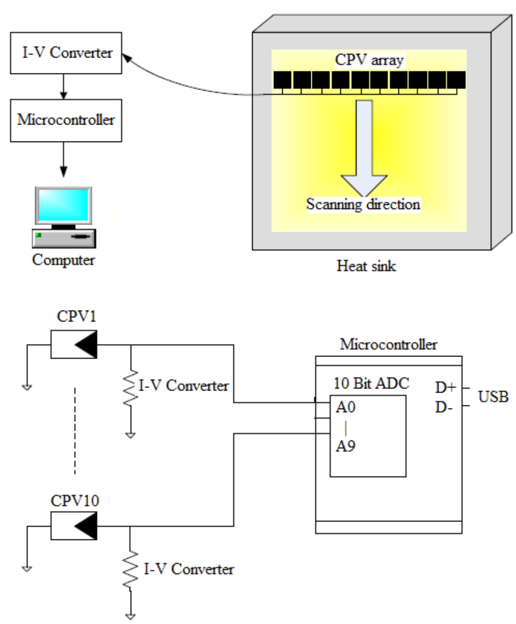

Figure 3.19: Schematic diagram to show the configuration of the optical scanner together with its circuit diagram

Full device setup information of the optical scanner have been discussed by previous publications in Chong *et al.* (2011) as well as Chong and Yew (2011), with the exception that the sensors used earlier were photodiodes with lower limit of irradiance level that is not suitable for applications in solar concentrators (refer to Figure 3.19). During sun-tracking, measurements of solar flux-distribution were acquired as the image is well focused at the target receiver, as well as during off-tracking condition of as much as 2.94 mrad which is 5.0 mm for this system. The high speed scanning device operates at about 5 seconds across the target receiver, to acquire concentrated solar flux distribution with a full coverage area of 95 cm × 98 cm. The measurements data are then exported into excel to be correlated to absolute solar irradiation levels (Figure 3.20).

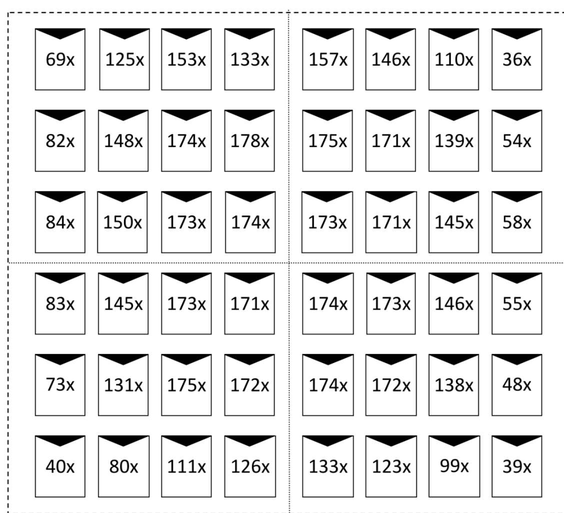

(a) Array arrangement A, with solar flux distribution A

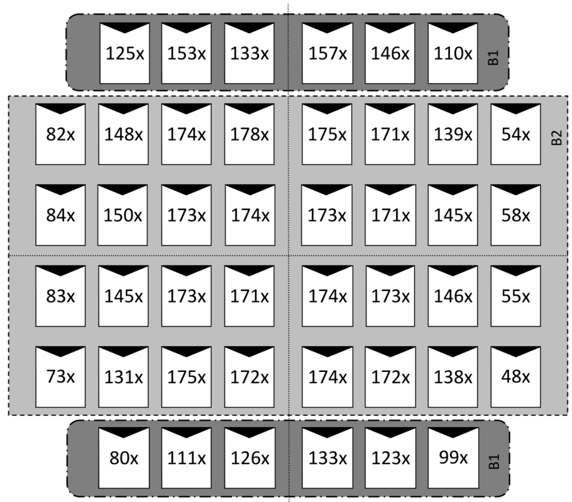

(b) Array arrangement B, with solar flux distribution B

Figure 3.20: The solar concentration ratio at each CPV cell location can be determined by referring to measured solar flux distribution information that was measured at the receiver target. Two types of flux distributions are considered for this study, namely (a) Array arrangement A, with solar flux distribution A, and (b) Array arrangement B, with solar flux distribution B

In Figure 3.20 (a), the corner cells are subjected to very low solar concentration ratio mainly due to solar disc effect. As array current will follow the lowest performing CPV cell's current in a series-connected assembly, the cells at the corner contribute to greater current mismatch that causes power losses. Therefore, by omitting the corner cells, better overall dense-array performance may be achieved due to current mismatch reduction. To analyze and compare the performance of dense-array with full array of CPV cells and without corner CPV cells, two different CPV array layout are considered in, namely (a) Array arrangement A, with solar flux distribution A, and (b) Array arrangement B, with solar flux distribution B (Figure 3.20).

3.7 Development of FPM

Once solar flux distribution measurement is completed, we continue to the second process which is estimating initial dense array design. In this process, a novel approach is introduced to formulate initial design through the implementation of three point method (TPM) *I-V* curve (Appendix I). The TPM approach is simplistic, fast, and useful for the application in any solar concentrator system. Fundamentally, the TPM *I-V* curve aims to predict and approximate the nonlinear *I-V* curve of a CPV cell by means of three critical points (refer to Figure 3.21). For stage 1 of the newly proposed TPM prediction process, *I-V* curve of every solar cell is represented by three points which are $(0, I_{sc})$, (V_{mp}, I_{sc}) and $(V_{oc}, 0)$. These three points consists of parameters of the short-circuit current, open-circuit voltage, and the voltage at maximum power point. Referring to Figure 3.21, the difference in current ΔI is very small because the current of maximum power point (I_{mp}) is very close (97% to 98%) to short-circuit current (I_{sc}). Therefore, we approximate the maximum power point at (V_{mp}, I_{sc}) in preference to (V_{mp}, I_{mp}). The motivation of this approach is to produce a fairly precise approximation model with reduced electrical parameters to reduce computing time. For large dense-array that has x rows and y columns of solar cells, the location of each CPV cell is denoted by $S_{x,\,y}$ in a TCT connection, as presented in Figure 3.22. For accurate prediction of dense-array I-V curve, solar concentration ratio (C), of all CPV cells in the array are prerequisite to retrieve corresponding parameters like I_{sc}, V_{oc}, and V_{mp}. The retrieved parameters are saved in three different matrix files in Matlab for sorting.

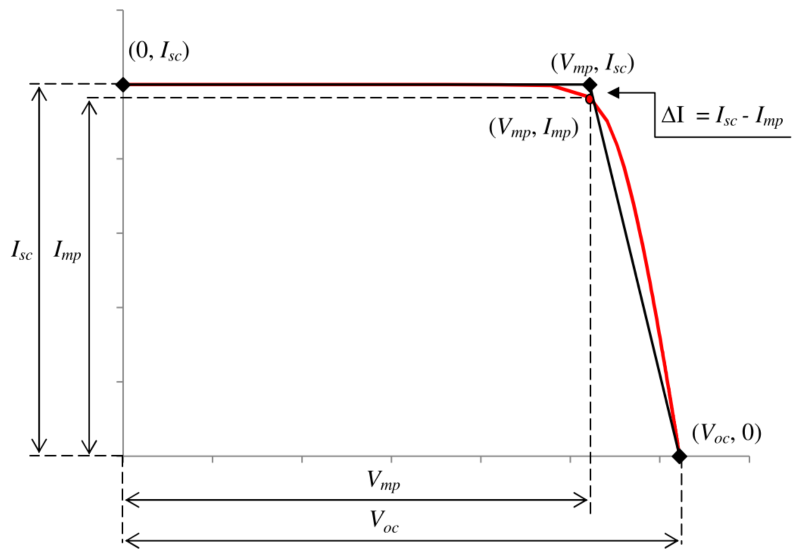

Figure 3.21: This graph demonstrates the basic principle of a TPM prediction model (black line) that aims to represent a nonlinear I-V curve (red line) with three critical points, namely (0, I_{sc}), (V_{mp}, I_{sc}) and (V_{oc}, 0)

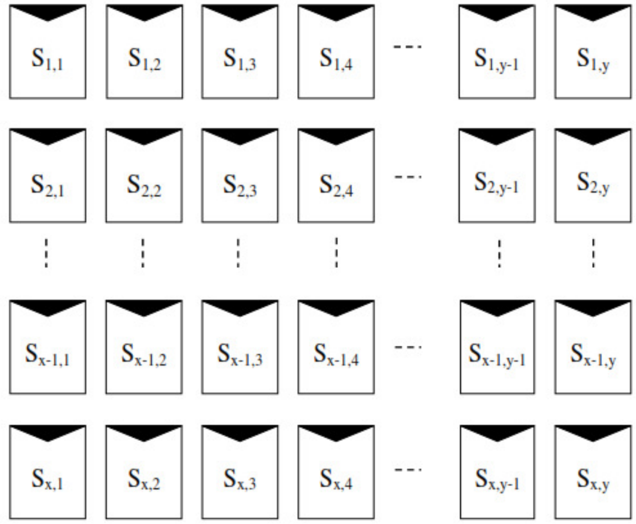

Figure 3.22: A general CPV dense-array layout in an assembly of x rows and y columns of solar cells

3.7.1 Determining All Configurations

In FPM modeling, all solar cells that are within a basic module are considered to be parallel-connected; while the connection between basic modules to basic modules is considered to be series-connected. To determine all possibilities of dense-array configurations, the process is initiated through checking the quantity of solar cells that are present at the corresponding row. The number of cells that are in a basic module (p) can be determined using the equation below (Appendix J):

$$p = N_{cell} / d \tag{3.11}$$

In equation (3.11), d represents the number of basic modules in each row (using integer number: 1, 2, 3, etc.), while N_{cell} represents the total quantity of solar cells per row. In our analysis, only integer whole numbers of cells are accepted to be used in a basic module. The smallest allowable value of p is 1 in a basic module with only one CPV cell. The condition of $p = 1$ is the smallest basic module size.

Referring to Figure 3.20 (a), the array consists of six equal rows with eight solar cells per row. By applying equation (3.11), every possible basic module size for different array configurations can be computed. In Table 3.2, all values of p are listed to illustrate the different possibilities of basic modules. From the subsequent table, it can be observed that the solar cells in region B1 can be connected in four different parallel configurations of basic module which are, six solar cells in parallel ($p_{B1} = 6$), three solar cells in parallel ($p_{B1} = 3$), two solar cells in parallel ($p_{B1} = 2$) and just one solar cell in a basic module ($p_{B1} = 1$). On the other hand, array arrangement A has equal number of cells in all six rows throughout the array and hence, the values of p are the same.

As flux distribution A shows equal quantity of solar cells in each row, series connection for this distribution is straightforward which are 48 × 1 cells ($p = 1$), 24 × 2 cells ($p = 2$), 12 × 4 cells ($p = 4$), and 6 × 8 cells ($p = 8$). With these configurations, we can proceed to *I-V* curve prediction. Nevertheless, flux distribution B consists of region B1 and region B2 with different number of cells in both regions (Figure 3.20 (b)). Therefore, we recommend breaking the array of flux distribution B into two groups for further processing. In the first group in region 1, which is the top and bottom row, there are six solar cells per row. In the second group, which consists of rows that are located at the center of the array, each row consists of eight cells. By applying the nodes method (presented in Figure 3.23), it is found that there are as much as sixteen possibilities of configurations for the array in flux distribution B.

Table 3.2: The quantities of solar cells in a basic module (p) for two regions in flux distribution B are listed down in this table

Integer (d)	$p_{B1} = N_{cell} / d$ (In region B1, $N_{cell} = 6$)	$p_{B2} = N_{cell} / d$ (In region B2, $N_{cell} = 8$)
1	6	9
2	3	4
3	2	-
4	-	2
5	-	-
6	1	1
7	-	-
8	-	1

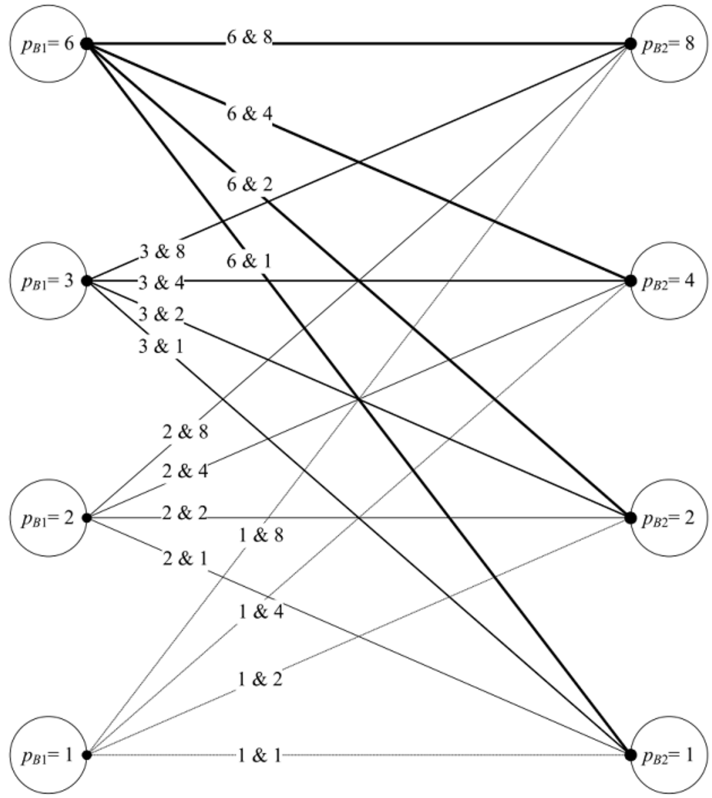

Figure 3.23: By applying the nodes method to the array of flux distribution B, as much as sixteen possible configurations are found

3.7.2 Predicting *I-V* Characteristics

In this section, the flow of dense-array *I-V* curve prediction will be explained. As presented in the flow chart of Figure 3.24, the process starts with initialization of counting parameters that will be used for the entire algorithm. Based on the computed *p*, new parameter values like short-circuit current $I_{sc\text{-}module}$), module open-circuit voltage ($V_{oc\text{-}module}$) and module voltage at maximum power point ($V_{mp\text{-}module}$) can be calculated in the sequence of row-by-row until the whole array is covered (Figure 3.23). The equations that are used to calculate the module parameters are presented in the flowchart below, whereby (x, y) represents the position of CPV cell at the x-th row and y-th column (see Figure 3.21), N_{row} represents the total number of rows and N_{column} represents the total number of columns in the array.

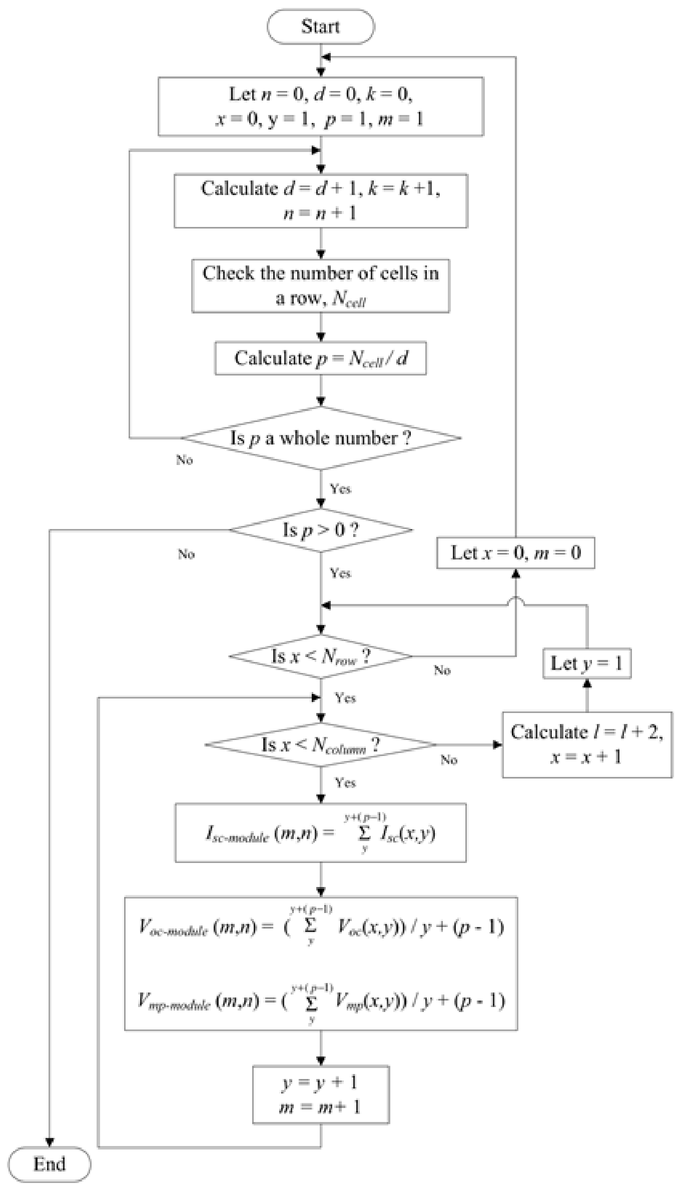

Figure 3.24: This flowchart depicts a method of grouping short-circuit current ($I_{sc,}$), open-circuit voltage (V_{oc}), and voltage at maximum power point (V_{mp})

In the next process, sorting will be conducted for the modules parameters like $I_{sc\text{-}module}$ and $V_{oc\text{-}module}$ of the whole dense-array, based on decreasing order of $I_{sc\text{-}module}$. Upon sorting, the module with the highest value of $I_{sc\text{-}module}$ is reassigned to $I_{sc\text{-}module,n}$. At the same time module open-circuit voltage and module voltage at maximum power point are reassigned to $V_{oc\text{-}module,n}$ and $V_{mp\text{-}module,n}$ respectively. In the new designation, n symbolizes the total quantity of basic modules in the array. In addition to that, it is also assumed that each basic module is well protected with a bypass diode that is connected in parallel to the said module in the opposite polarity. By having this configuration, if a basic module is experiencing lower solar flux distribution, a bypass diode will become forward biased to allow array current to safely pass through the circuit. As the array current flows through the bypass diode, it will turn on while holding its corresponding solar cell or group of solar cells to a small negative voltage that will prevent further reverse bias in the array voltage. In equation (3.12), the method of calculating bypass diode forward voltage ($V_{d,n}$) is shown.

$$V_{d,n} = (n - 1) \times V_d \tag{3.12}$$

In the equation above, n also denotes the total number of series-connected basic module in a CPV array. It should be noted that $I_{sc\text{-}module,1}$ is the lowest in the series string in the case when $n = 1$ and $V_{d,1} = 0$. Last but not least, the array open-circuit voltage as well as the array short-circuit current are calculated. In the short-circuit condition, array current has the highest current value when array voltage is zero (0, $I_{sc\text{-}array}$); while in the open-circuit condition, array current has the lowest current value of zero when array voltage is ($V_{oc\text{-}array}$, 0), as displayed in equation (3.13).

$$V_{oc\text{-}array} = \sum_{i=1}^{n} V_{oc\text{-}module,i} \tag{3.13}$$

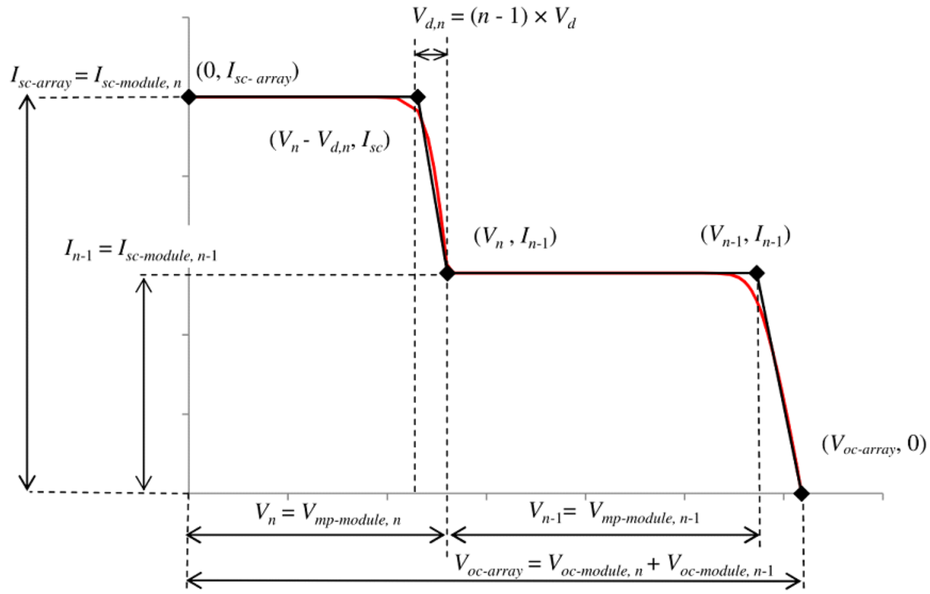

Figure 3.25: An example of *I-V* curve prediction of two series-connected strings in an array (n = 2), with the critical points (in black dots) of the new approximation methodology (black line)

In the figure above, an example of *I-V* curve of a full CPV array with two modules is presented (refer to Figure 3.25). To get the maximum power, the resultant output power at each critical point in the array is calculated simply by multiplying the voltage to its current value. Nevertheless, it is observed that location of maximum power point (P_{mp}) of a well-designed dense-array with negligible current mismatch typically appears around the 'knee' point (V_1, I_1). To illustrate a bigger dense-array that has more series-connected modules, another *I-V* prediction curve showing critical points is depicted in Figure 3.26. In a very large dense-array with even more series-connected modules, some critical points may lie in the negative voltage region. In these cases, *y*-axis will be readjusted while $I_{sc\text{-}array}$ is reviewed to the array current value that crosses the *y*-axis instead of using highest current value (see Figure 3.27).

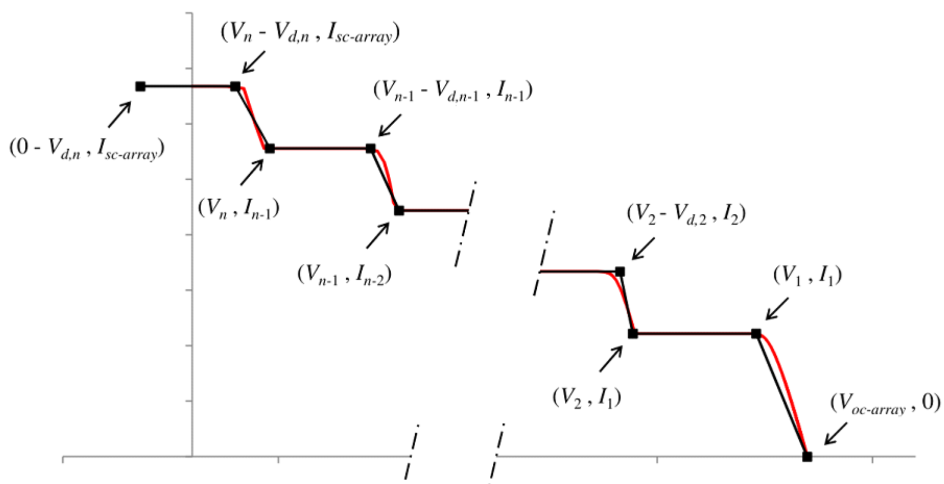

Figure 3.26: This *I-V* prediction curve of a string of modules shows several critical points of *n* series-connected basic modules in a dense-array

In the fourth stage of FPM (see Figure 3.17) the best configuration that produces the highest performance is determined. Here, detailed analysis is conducted to discover the best dense-array design option. One important evaluation criterion when deciding the dense-array initial design is power density (equation 3.14).

$$\text{Power density} = P_{mp} \,/\, [\text{total cells in dense-array}] \tag{3.14}$$

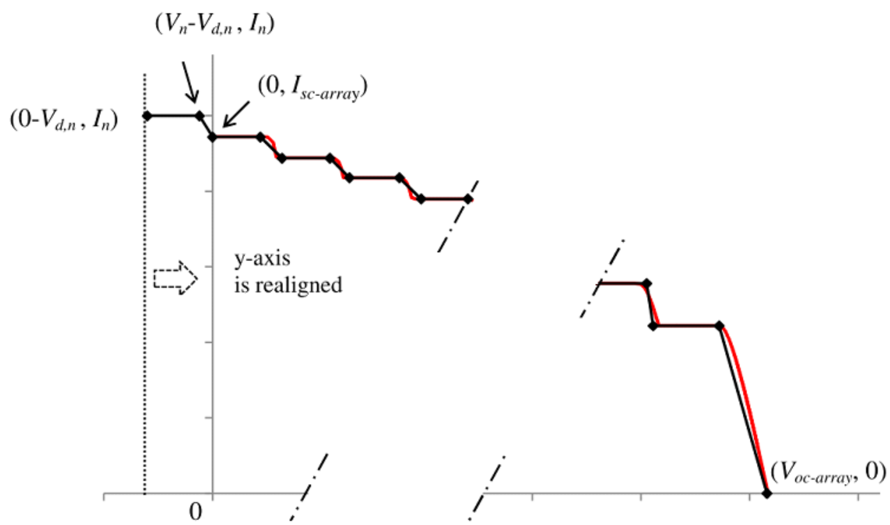

Figure 3.27: In the event that some critical points appear in the negative voltage region, realignment of y-axis is performed, and at the same time $I_{sc\text{-}array}$ is revised to the current value that crosses the axis

3.8 Assembly Process of Dense-Array

The assembly process of dense-array that includes fitting CTJ solar cells into basic modules, and then completing the whole set of array by putting together all basic modules is a very critical and delicate process that needs careful planning. The interconnect design not only have to take into consideration of CPV cell dimensions, machinery tolerances and limitations also has to be taken into account while not jeopardizing overall electrical performance. As CPV cells are much thinner in thickness than flat-plat photovoltaic (PV) cells, they are very delicate and hence require low-impact handling and stringent heat dissipation requirements.

Before starting the assembly process, solar cell testing and classification must be considered so that sorting and grouping of good cells from not-up-to-par CPV cells can be conducted. Essentially, an underperforming solar cell within a series connected array will limit the output current and bring down the power generation capability of the whole array. Nevertheless, this limitation can be curbed by preselecting good solar cells with similar electrical characteristics so that module mismatch is minimized. In our study, bare CPV cells were sorted based on *I-V* curves monitoring when exposed under illumination as well as under dark condition using the established Keithley 4200-SCS semiconductor characterization system.

Next, pre-selected CPV cells are attached onto small DBC substrates to form individual module through solder reflow process. The solder reflow process that is chosen for dense-array offers low-void-content bonding in addition to excellent thermal conductivity between the solar cells and the substrates. This project uses Curamik DBC substrates that consist of a ceramic isolator (material Al_2O_3) that is sandwiched in the middle of two copper sheets. The mentioned DBC substrates are suitable for high concentration CPV application due to many factors such as its high thermal conductivity at 24 $Wm^{-1}K^{-1}$, high voltage isolation, and adjusted coefficient of thermal expansion. To prevent CPV modules from suffering hot-spot issues, X-ray scanning is scheduled and conducted on every CPV module. The modules with minimal voids are chosen for further assembly work to group them into a large dense-array (Figure 3.28)

Then, Arctic Silver thermal adhesive is selected and applied thinly with thickness 0.1 mm, to attach a basic module (that consists of two solar cells in parallel) onto a copper cooling block. To cure the thermal adhesive, a small pressure is pressed onto the basic module for approximately 5 minutes. This method is preferred as compared to heat curing because of its simplicity and ease of rework if there is a need to do module rearrangement or replacement of non-performing modules. Upon completion of the thermal adhesive process, ribbon-bonding process begins. On the front-side of the triple-junction solar cell, bus bar contact is connected using 1 mil × 10 mil aluminium ribbons to the next basic module's DBC copper layer. The mentioned DBC copper layer is electrically isolated to the preceding module to form a series connection. Last but not least, bypass diodes and electrical cables are affixed to the assemble using electrically conductive epoxy that cures under room temperature.

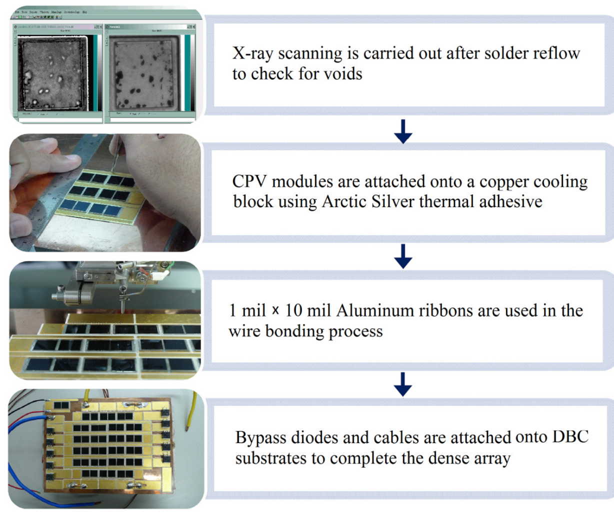

Figure 3.28: The assembly processes of fabricating a CPV dense-array

CHAPTER 4

RESULTS AND DISCUSSION

4.1 Theoretical and Experimental Results

The theoretical and experimental results can be divided into four parts which is the optical analysis, temperature analysis, analysis of CPV dense-array using the FPM simulation method as well as using comprehensive Simulink simulations. With the outcome from theoretical study, the most optimal dense-array design is selected for implementation in NIPC concentrator system.

4.2 Optical Analysis

To evaluate the planar concentrator's performance, two major considerations that require detailed study are solar concentration ratio and the uniformity of solar flux distribution on the concentrator's receiver target. In this study, solar flux distribution at the receiver of the NIPC is simulated via varying the f/D ratio, whereby f is defined as the focal distance and D is defined as the reflector width of the solar concentrator. Simulation results presented in this research are based on f/D ratio because this approach enables generalization of the results to any concentrator size for ease of reference.

In the following sections, optical analysis of planar concentrator has comprising cases such as 17×17, 19×19, 21×21, 23×23, and 25×25 arrays of mirrors are presented in Table 4.1. In the aforementioned table, the facet mirror's dimension as well as the total reflective points per facet mirror are selected based on the total reflective area of the solar concentrator and the area of reflective element (point) remained almost identical for the different cases. With the exception of the mirror that is located at the center of the solar concentrator, the total number of mirrors for the cases 17×17, 19×19, 21×21, 23×23, and 25×25 arrays of mirrors are 288, 360, 440, 528, and 624 pieces respectively, while total reflective area is fixed at approximately 4.4 m^2.

Table 4.1: Optical simulation of the planar concentrator is considered for the cases of 17×17, 19×19, 21×21, 23×23, and 25×25 arrays of mirrors

Array of mirrors	Dimension of facet mirror ($W \times W$), in cm^2	Total reflective points per facet mirror ($S \times S$)
17 × 17	12.0 × 12.3	79 × 79
19 × 19	11.0 × 11.0	71 × 71
21 × 21	10.0 ×10.0	65 × 65
23 × 23	9.1 × 9.1	59 ×59
25 × 25	8.4 × 8.4	55 × 55

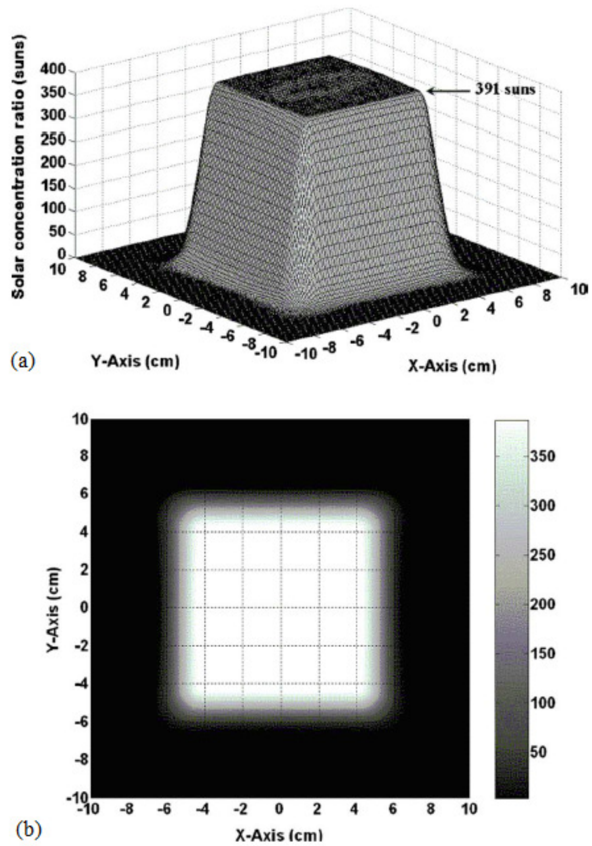

Figure 4.1: Simulation results are presented for the case of 21 × 21 mirror array with focal distance at 170 cm, displayed in two means, namely in (a) 3-D plot of solar flux distribution, and (b) 2-D plot of solar flux distribution

From the solar flux distribution results plotted in Figures 4.1(a) and 4.1(b), 3-D and 2-D plots can be observed for the case of 21×21 mirror array with focal distance at 170 cm. In our study, the same methodology has been repeated for each case, i.e. 17×17, 19×19, 21×21, 23×23, and 25×25 arrays of mirrors, in order to compile simulated flux distribution results for different focal lengths (f) which is from the range of f = 100 cm to f = 300 cm which corresponds to a change in f / D ratio from 0.4545 to 0.3636 with a small step of increment each time. For referencing purpose, every 10 cm increment is equivalent to an increment of 0.04545. It was observed that all of the results in each case showed similar characteristics as can be observed from Figure 4.1, whereby the figure's top area at the central region of the flux distribution is consistently flat. In our research the central region where solar concentration ratio is found to be rather constant is referred to as uniform illumination area (Chong *et al.*, 2010).

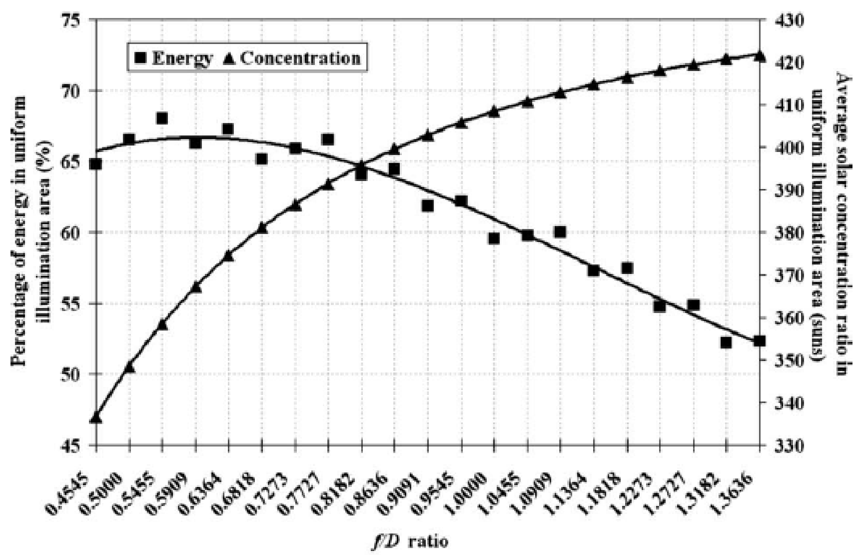

Figure 4.2: The relationship between average solar concentration ratio in the region of uniform illumination area and the percentage of total energy in the uniform area against *f /D* ratio is presented for the case of 21 × 21 array of facet mirrors

As observed from Figure 4.2, increasing focal distance can increase the average solar concentration ratio in the uniform illumination area of the solar flux distribution, but the percentage of energy in uniform area will often be sacrificed. For that reason, a trade-off between the average solar concentration ratio within the uniform illumination area and the total energy harnessed in the uniform illumination area has to be pursued, so as to obtain the best concentrator performance.

For more detailed investigation, receiver size is fixed and two parameters of the solar flux distribution are simulated, namely spillage loss and lowest solar concentration ratio at the receiver edge. This is an important part of our study, especially for optimizing the receiver size via considerations of both spillage loss and the variation of solar flux distribution. Spillage loss is simply defined as the percentage of solar irradiation that falls beyond the boundary of the receiver target. The lowest solar concentration ratio at the receiver edge is consistently equivalent to the lowest solar concentration ratio within the receiver boundary. Hence, the variation of solar flux distribution is the difference between the maximum and the minimum level of solar concentration ratio that falls within the receiver target boundary, which can be calculated in percentage.

The spillage loss (black solid line), and its corresponding lowest solar concentration ratio at the receiver edge (black dotted line) versus square receiver size is plotted from the size of 6 cm to 13 cm and the results for cases of 17×17, 19×19, 21×21, 23×23, and 25×25 arrays of facet mirrors are presented in Figure 4.3. The focal distances that have been considered are 120 cm, 170 cm, and 230 cm. From analysis it was observed from plotted graphs that the spillage loss curves for the three different focal distances do not differ much from each other (Chong *et al.*, 2010). This is especially true for the curves of focal distances 120 cm and 170 cm, as the results are very similar with minimal deviation.

The largest receiver size that is able to reasonably collect uniform solar flux distribution with less than 5% of deviation in flux distribution, with its corresponding spillage loss for different arrays of facet mirrors and focal distances 120 cm, 170 cm and 230 cm are as follows: For the case of mirror array configuration in 17×17, the optimised receiver sizes (spillage losses) are 11.25 cm (30.1%), 11.00 cm (27.9%), and 10.50 cm (33.1%). Next, for the case of mirror array configuration in 19×19 arrangement, the optimised receiver sizes (spillage losses) are 10.00 cm (30.4%), 9.75 cm (31.40%), and 9.25 cm (34.70%) for the focal distance of 120 cm, 170 cm and 230 cm, respectively. As for the case of 21×21 mirror array configuration, the optimised receiver sizes (spillage losses) are 9.00 cm (32.0%), 8.75 cm (33.5%) as well as 8.25 cm (37.2%) for the focal distance of 120 cm, 170 cm and 230 cm, respectively (Figure 4.3). In the case of mirror array configuration in 23×23, the optimised receiver sizes (spillage losses) are 8.00 cm (35.2%), 7.75 cm (37.3%), and 7.25 cm (41.6%) for the focal distances of 120 cm, 170 cm, and 230 cm respectively. Last but not least, in the case of mirror configuration of 25×25, the optimised receiver sizes (spillage losses) are 7.25 cm (38.4%), 7.00 cm (37.7%) and 6.75 cm (42.4%) for the focal distance of 120 cm, 170 cm and 230 cm, respectively.

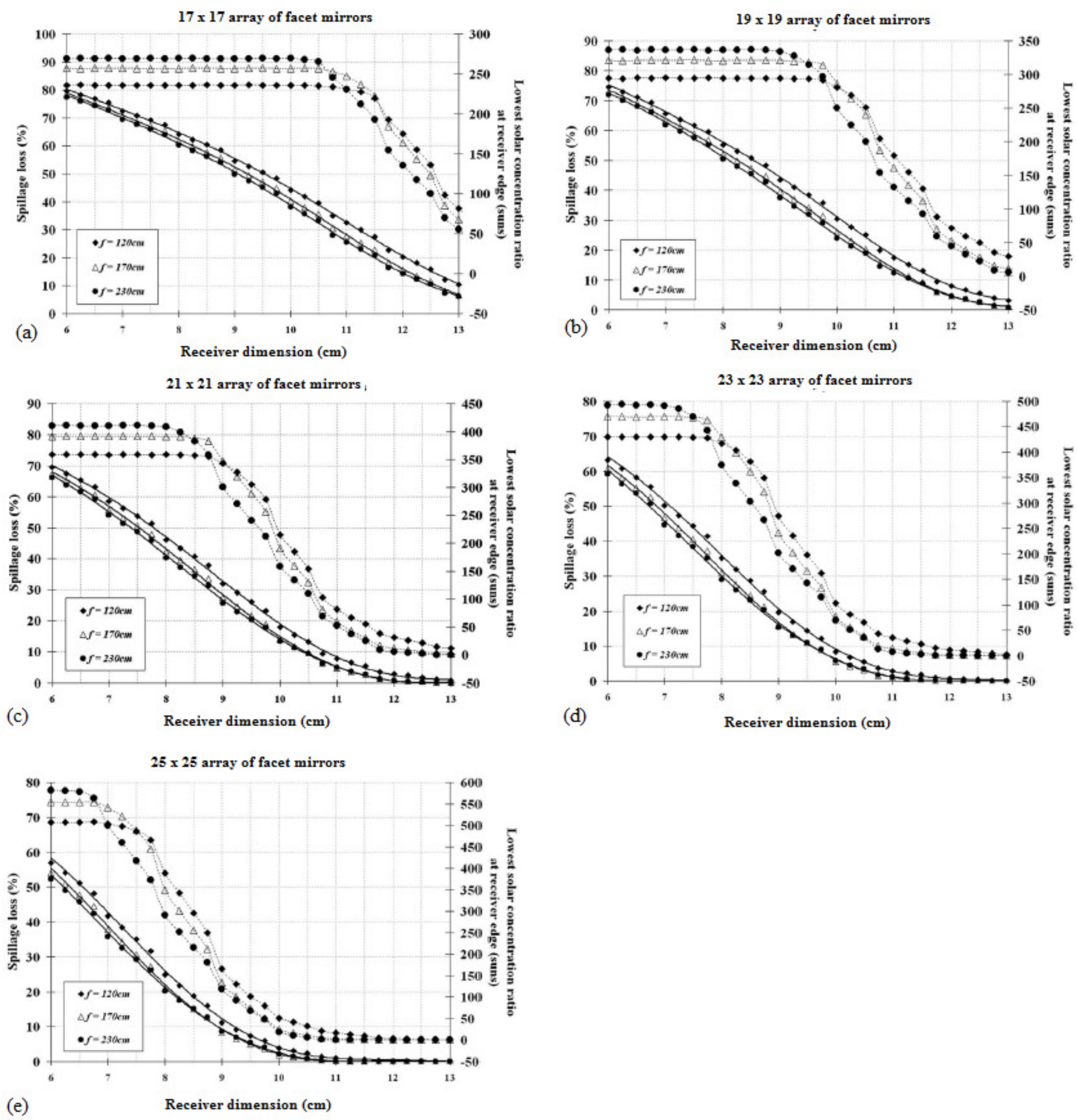

Figure 4.3: Line graphs for (a) 17×17 array of facet mirrors, (b) 19×19 array of facet mirrors, (c) 21×21 array of facet mirrors, (d) 23×23 array of facet mirrors and (e) 25×25 array of facet mirrors to represent the relationship between spillage loss (black solid line) and the corresponding lowest solar concentration ratio value detected at the receiver edge (black dotted line), versus square receiver size for focal distances namely at 120 cm, 170 cm and 230 cm

The analysis mentioned above can also help in the optimization of receiver size and total energy collected, provided that higher tolerance of uniformity in the solar flux distribution is permitted. From our analysis, the average uniform solar radiation of the three focal distances for 17×17 array of facet mirrors is approximately 275 suns; the uniform solar concentration for 19×19 array of facet mirrors is approximately 325 suns; the uniform solar concentration for 21×21 array of facet mirrors is approximately 400 suns; the uniform solar concentration for 23×23 array of facet mirrors is approximately 475 suns; and the uniform solar concentration for 25×25 array of facet mirrors is approximately 550 suns.

One key parameter that influenced the selection of array of facet mirrors is the characteristics of the CPV cell. As presented in Figure 2.1, it is possible to observe the relationship between efficiency and solar concentration for EMCORE triple-junction CTJ cell. From the Figure, efficiency of the CPV cell increases from 1 sun and slowly peaks from 350 suns – 500 suns, until it finally reaches the highest efficiency of 38% at 500 suns. After that point, the efficiency of the mentioned CPV cell drops considerably. Considering this factor, the array of facet mirrors that are able to operate within the reasonably high efficiency range are 21×21 array and 23×23 array. Nevertheless, if we consider the factor of spillage loss and to limit it to be within 35%, the optimal receiver size (spillage losses) would be in the case of 21×21 array the 9 cm (32.0%), and 8.75 cm (33.5%) for the focal distance of 120 cm and 170 cm respectively. The final selection of receiver size would typically be influenced by CPV array design. In the case of 23×23 array, the spillage losses for the different focal distances are all above 35% and hence not further considered.

Furthermore if we analyse from Figure 4.3 (c) which presented the case of 21×21 array with a focal distance of 170 cm, it can be observed that 8.75 cm is the largest receiver size to contain a reasonably uniform solar irradiation with 2.5% of variation in flux distribution (solar concentration ratio changes from 383 suns to 393 suns) and spillage loss of 33.5%. In the case when the size of receiver is increased to 9.5 cm, the lowest solar concentration ratio will be lower at 289 suns while spillage loss is reduced to 21.6%. This demonstrates that even though the variation of flux distribution has increased to 26.5% (solar concentration ratio changes from 289 suns to 393 suns), the collectable energy is enhanced to 78.4%. As a comparison, if the size of receiver is further increased to 10.25cm, variation in solar flux distribution will be greater at 59.3% and solar concentration ratio at the receiver edge at 160 suns. Nevertheless, the spillage loss is further minimized to become 11.7%. Hence, tolerance in the variation of flux distribution also influences spillage loss of the concentrator system.

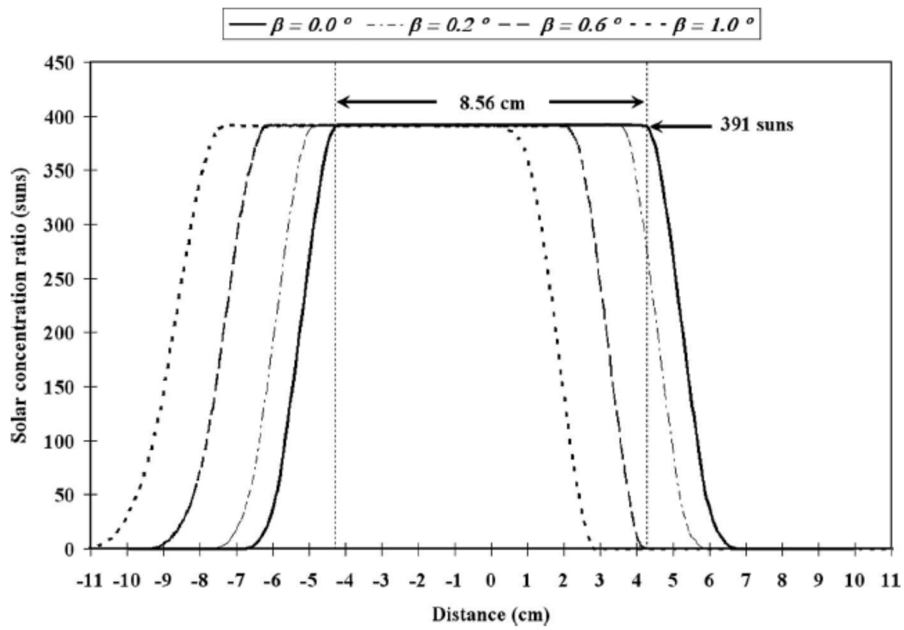

Figure 4.4: A figure showing the relationship between solar concentration ratio and the different distance of off-axis angles i.e. 0 deg, 0.2 deg, 0.6 deg, and 1.0 deg for f = 170 cm in the 21 × 21 mirror array configuration

4.2.1 Off-axis Aberration Effects

In this section, off-axis aberration effects to the solar flux distribution due to sun-tracking error is analysed by changing the simulation off-axis angles β from the range of 0 deg - 1 deg (Figure 4.4). The relationship between the variation of solar flux distribution from the centre of receiver and focal distances at 100 cm to 300 cm is presented for β = 0.6 deg as well as β = 1.0 deg (Figure 4.5). The graph in Figure 4.5 indicates that the variation from the centre of target receiver is rather linearly proportional to the focal distance, while the slope is reliant on the off-axis angle.

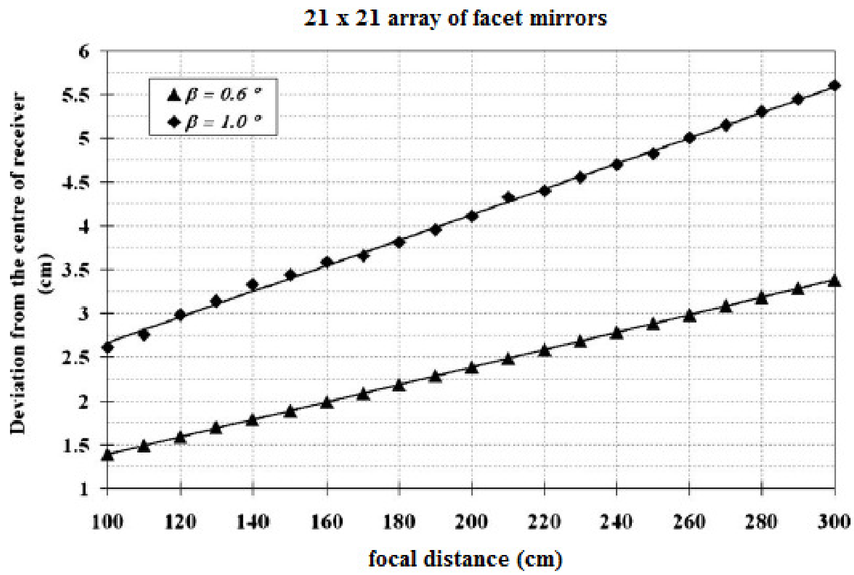

Figure 4.5: A graph showing deviation from the centre of receiver against focal distance for the off-axis angles of 0.6 deg as well as 1.0 deg

The three characteristics of solar flux distribution due to sun-tracking error are reviewed, in terms of spillage loss, non-uniformity, and total acceptance angle, to ensure that the level of damage inflicted by sun-tracking error is within acceptable levels. Referring to Figure 4.6, the changes in spillage loss according to receiver size with off-axis angles at 0.0 deg, 0.2 deg, 0.4 deg, 0.6 deg, 0.8 deg, and 1.0 deg is presented. Taking 9.5 cm as the receiver size, spillage loss has increased substantially from 21.6% when β = 0.0 deg to 23.5% when β = 0.2 deg, to 28.2% when β = 0.4 deg, to 34.1% β = 0.6 deg, to 40.0% when β = 0.8 deg, and lastly to as much as 45.9% when β = 1.0 deg (Chong *et al.*, 2010). From the upwards trend in spillage loss that is listed above, sun-tracking accuracy is a very critical parameter to manage so that the resultant spillage loss is within a minimal range, to enable good performance of a solar concentrator as the system tracks the sun position throughout the day.

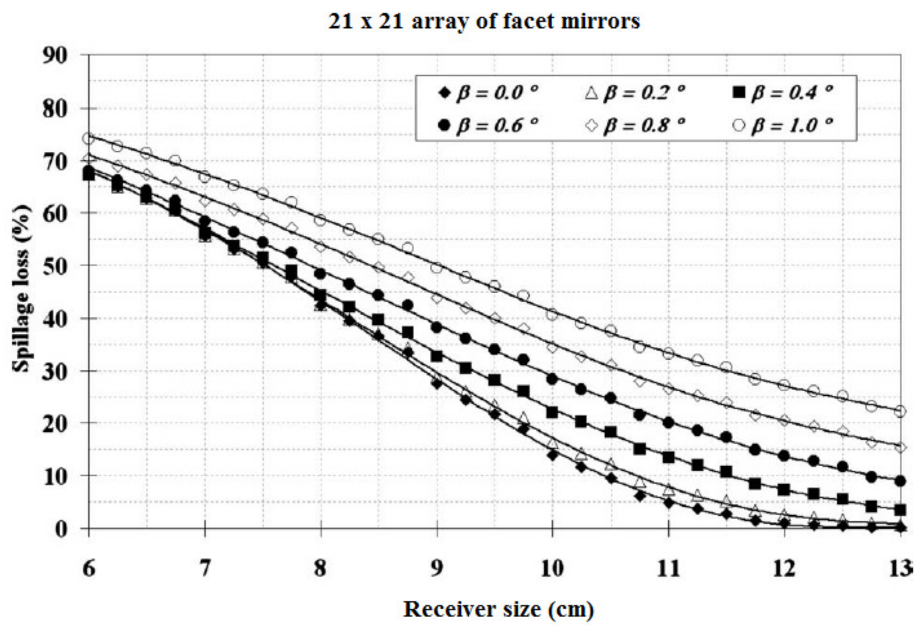

Figure 4.6: A graph to present spillage loss versus receiver size for a variation of different off-axis angles such as β = 0.0 deg, 0.2 deg, 0.4 deg, 0.6 deg, 0.8 deg, and 1.0 deg when focal distance f = 170 cm

To further analyse the effects of sun-tracking error to non-uniformity of solar flux distribution, an imaginary boundary with the size of 8.56 × 8.56 cm^2 is defined to contain the maximum size of uniform illumination area at zero tracking error. For the off-axis angle of 0.0 deg to 1.0 deg, the flux distribution from zero tracking error will shift away from the centre of the aforementioned defined boundary and the solar concentration ratio at the edge of the boundary will decrease. According to the graph presented in Figure 4.7, the seriousness of non-uniformity can be checked and quantified, by referring to solar flux distribution variation across off-axis angle of 0.0 deg to 1.0 deg for 21 × 21 array of facet mirrors and focal distance f = 170 cm.

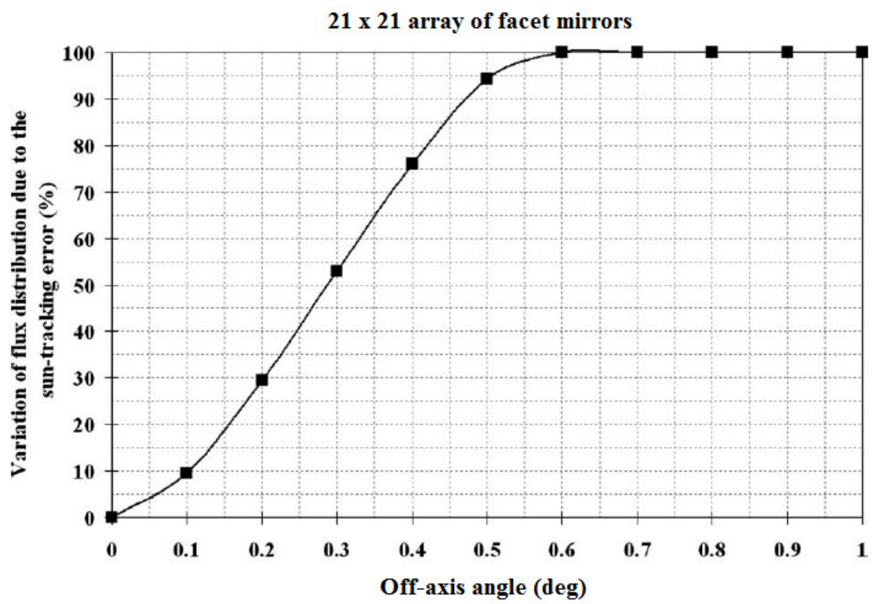

Figure 4.7: A graph showing the variation of flux distribution due to sun-tracking error, that is within a defined boundary area of 8.56 × 8.56 cm^2, with regards to different off-axis angles ranging from 0.0 deg to 1.0 deg simulated at 0.1 deg increment, and focal distance f =170 cm

Next, it is of interest to find the maximum allowable angular error, while still maintaining the collected energy almost constant. Here, the acceptance angle of the NIPC is defined as a range of allowable angles with the condition that less than 5% of energy loss can be caused by sun tracking error as compared to zero tracking error. A figure representation to show the percentage of energy that is within the defined area of 10.54 x 10.54 cm^2 as compared to ideal tracking with no error across off-axis angle from -1.0 deg to 1.0 deg is plotted for easy reference (Figure 4.8).

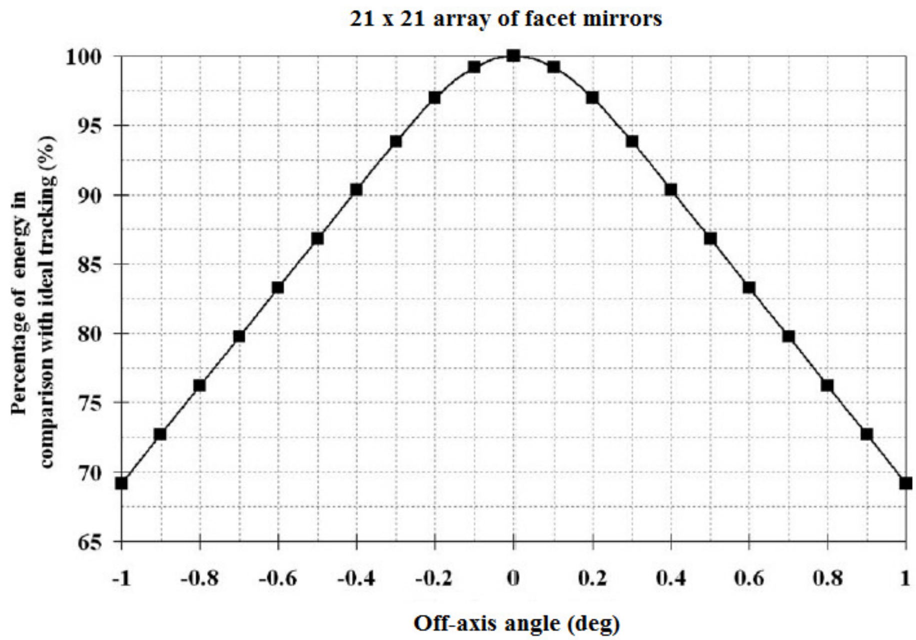

Figure 4.8: This figure shows a comparison of ideal tracking (no error) versus off-axis tracking for -1.0 deg to 1.0 deg, and its effect to the percentage of energy that falls in the defined area 10.54 x 10. 54 cm^2, at f = 170 cm

In this study, the defined area of 10.54 × 10.54 cm^2 is determined based on common practise in optics known as full width at half maximum (FWHM), which means that solar concentration ratio at the edge of the defined area is half of the maximum solar concentration ration. Based on results in Figure 3.10, the energy that lies within the receiver at the off-axis angles of ± 0.1 deg, ± 0.2 deg, ± 0.3 deg, ± 0.4 deg, ±0.5 deg, and ± 0.6 deg are found to be 99.21%, 96.98%, 93.81%, 90.33%, 86.81% and 83.29 %, correspondingly. As a benchmark, the acceptance angle of the NIPC that allows at least 95% of energy is 0.48 deg (Figure 4.8).

4.3 FPM Simulation Analysis

In Table 4.2, a list of simulated *I-V* curve results from FPM approach is showed for both A and B flux distributions. From column of P_{mp} (refer to Table 4.2) a comparison among all simulations have revealed that the maximum output power from simulation 4 and simulation 6 are the highest among all other configurations. Seeing that both of simulation 4 and 6 yields the same output power, further analysis is necessary to determine the best configuration. It is worthy to highlight that although fill factor (FF) is typically used for performance evaluation of single solar cell, it does not apply for dense-array solar cells that has *I-V* curve with several current mismatch steps. Even though FF generally depends on the series and shunt resistance of the solar cells in a module to relatively reflect the quality of module performance, the FF does not consider the existence of reverse-bias steps and therefore this parameter is not useful for evaluating the quality of array *I-V* curve that comprises current mismatched cells (Vorster *et al.*, 2002; Vorster and Dyk, 2005). Moreover, array-current isn't precisely determined from the FPM process when there is serious current mismatch in the circuit.

In power density column of Table 4.2 (far right column), the power density from simulation 6 is 2.58 W/cell and is higher than the power density calculated for simulation 4 which is just 2.37 W/cell. The results divulge that in average, every solar cell in simulation 6 produces more electrical power as compared to simulation 4. In fact, Simulation 6 has lesser number of solar cells (forty-four CPV cells) than simulation 4 (forty-eight CPV cells). Overall, simulation 6 is found to be superior in power density while still achieving the highest output power among all other configurations, and its configuration is ultimately selected for practical implementation (Appendix L).

Table 4.2: A list of simulation results for all possible dense-array configurations at DNI : 641 W/m^2

Simulation No.	**Array configuration**	**Flux distribution**	$\boldsymbol{P_{mp}}$ **(W)**	**Fill factor (FF) (%)**	$\boldsymbol{V_{mp}}$ **(V)**	$\boldsymbol{I_{mp}}$ **(A)**	$\boldsymbol{V_{oc}}$ **(V)**	$\boldsymbol{I_{sc}}$ **(A)**	**Power density** P_{mp} / # cells **(W/cell)**
1	48 × 1	A	79.36	39.74	77.77	1.02	137.71	1.45	1.65
2	24 × 2	A	82.09	41.82	52.98	1.55	68.88	2.85	1.71
3	12 × 4	A	91.24	54.96	30.72	2.97	34.44	4.82	1.90
4	6 × 8	A	113.62	68.95	15.36	7.4	17.22	9.57	2.37
5	2 × 6 (B1) and 4 × 8 (B2)	B	86.01	53.15	15.4	5.58	17.27	9.37	1.95
6	2 × 6 (B1) and 8 × 4 (B2)	B	113.64	57.71	25.68	4.43	28.79	6.84	2.58
7	2 × 6 (B1) and 16 × 2 (B2)	B	71.63	20.2	46.22	1.55	51.83	6.84	1.63
8	2 × 6 (B1) and 32 × 1 (B2)	B	71.09	10.62	61.86	1.42	97.9	6.84	1.62
9	4 × 3 (B1) and 4 × 8 (B2)	B	81.69	38.14	9.07	9	23.03	9.3	1.86

10	4 × 3 (B1) and 8 × 4 (B2)	B	85.63	51.33	19.35	4.43	34.54	4.83	1.95
11	4 × 3 (B1) and 16 × 2 (B2)	B	79.58	40.29	51.36	1.55	57.58	3.43	1.81
12	4 × 3 (B1) and 32 × 1 (B2)	B	76.99	21.66	66.99	1.15	103.65	3.43	1.75
13	6 × 2 (B1) and 4 × 8 (B2)	B	76.29	28.29	8.47	9	28.78	9.37	1.73
14	6 × 2 (B1) and 8 × 4 (B2)	B	82.97	42.64	18.75	4.43	40.29	4.83	1.89
15	6 × 2 (B1) and 16 × 2 (B2)	B	87.53	47.17	56.49	1.55	63.33	2.93	1.99
16	6 × 2 (B1) and 32 × 1 (B2)	B	82.88	31.44	72.12	1.15	109.4	2.41	1.88
17	12 × 1 (B1) and 4 × 8 (B2)	B	60.09	13.93	6.67	9	46.03	9.37	1.37
18	12 × 1 (B1) and 8 × 4 (B2)	B	75.01	26.99	16.95	4.43	57.55	4.83	1.70
19	12 × 1 (B1) and 16 × 2 (B2)	B	61.7	26.13	60.47	1.02	80.58	2.93	1.40
20	12 × 1 (B1) and 32 × 1 (B2)	B	80.58	42.99	78.97	1.02	126.66	1.48	1.83

4.4 Comprehensive Matlab Simulation

Upon completion of the initial design process, more comprehensive computer simulation in Matlab is conducted. In the detailed simulation work, effects of non-uniform concentrated solar flux distribution and temperature are taken into account so as to achieve more accurate *I-V* and *P-V* curve results. Using the specially developed modelling method in Simulink from our previous publication, the dense-array interconnection for simulation 6 (see Table 3.3) is built (Siaw and Chong, 2012; Chong and Siaw, 2012; Siaw and Chong, 2014). The simulations were based on direct normal irradiance (DNI) 641 W/m^2 in addition to operating temperature 55 ^oC, and the resultant *I*-*V* and *P*-*V* plots are presented in Figure 4.9 and Figure 4.10. From the simulation results, comparisons showed that the estimation of P_{mp} that is computed from FPM is 113.64 W which is very similar to Simulink simulation results which yielded 111.54 W, with only 1.88% in error.

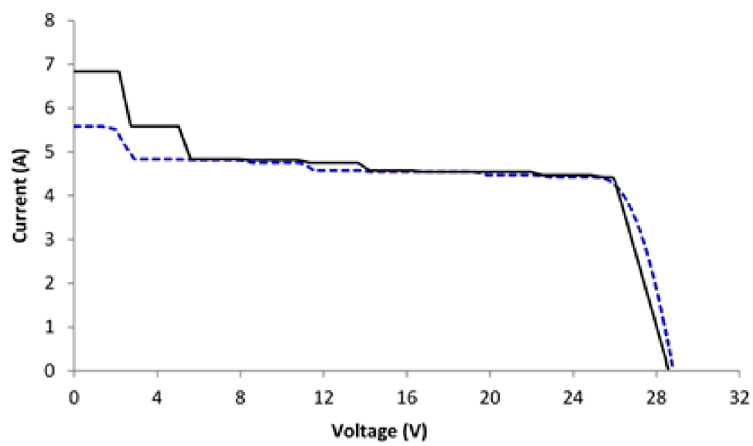

Figure 4.9: An FPM simulated *I*-*V* curve (black solid line), is compared with a Matlab simulated *I*-*V* curve (blue dashed line) for comparison purposes

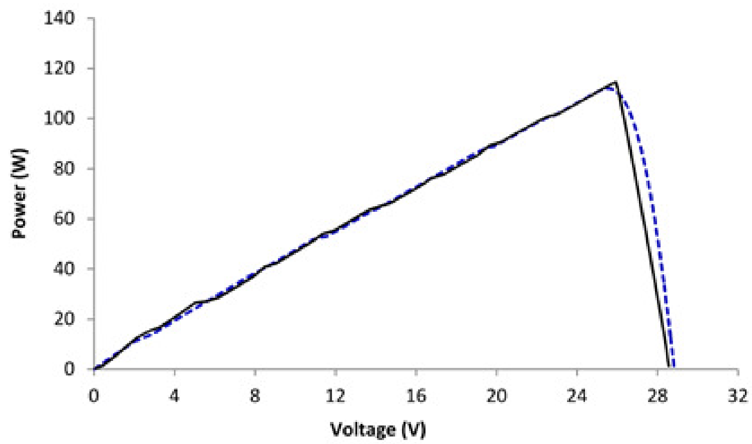

Figure 4.10: An FPM simulated *P-V* curve (black solid line) is superimposed on a *P-V* curve from Matlab simulation (blue dashed line)

4.5 Experimental Results

Referring to the confirmed dense-array configuration that is optimised from simulation 6 of Table 3.3, a CPV dense-array is designed, assembled, and tested in the field to validate the proposed FPM computational modelling approach. Firstly, the dense-array assembly, consisting of many basic modules is attached onto a copper cooling block so that the temperature of CPV array is able to be regulated during operation at 55 ^{o}C (Figure 4.11 and figure 4.12). Once the dense-array assembly set is completed, it is installed onto a prototype of planar concentrator for data collection (Appendix K).

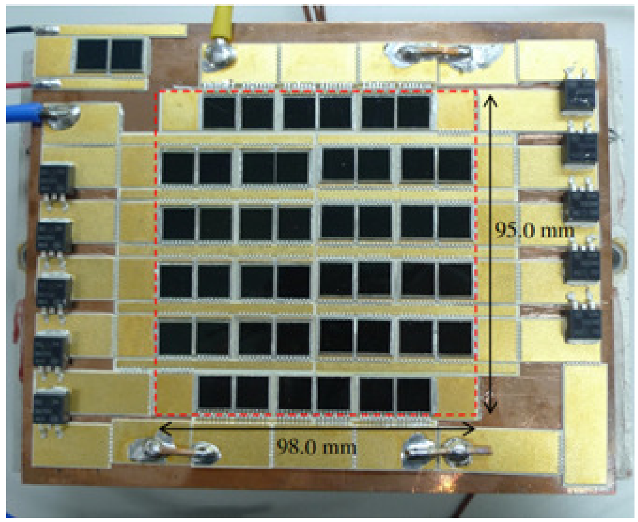

Figure 4.11: A completed CPV dense-array assembled using triple junction solar cells (Emcore, 2008) that is arranged according to the optimized configuration from simulation 6 (refer to Table 3.4)

For real-time *I-V* curve data collection, an N3300A configurable DC electronic load mainframe that is installed together with two units of N3305A electronic load modules (500 Watts) are used. During the process of data acquisition, other auxiliary data such as CPV dense-array operating temperature, direct normal irradiation (DNI), as well as global irradiation were measured. Therefore, the simulations of this study were based on operating conditions with real-time measured parameters like DNI, operating temperature and taking into consideration 15% of optical losses. To show the effectiveness of the FPM simulated *I-V* curve, a comparison of measured data which is superimposed onto simulated *I-V* curve is presented in this section. According to the comparison made in Figure 4.13 and Figure 4.14, it can be observed that a very close match between measured data and computer simulation data is achieved, which is about 1.34% of error for P_{mp} (Table 4.3).

Figure 4.12: Completed CPV dense-array with the optimised layout is exposed to concentrated solar flux distribution at NIPC's receiver plane for field measurements

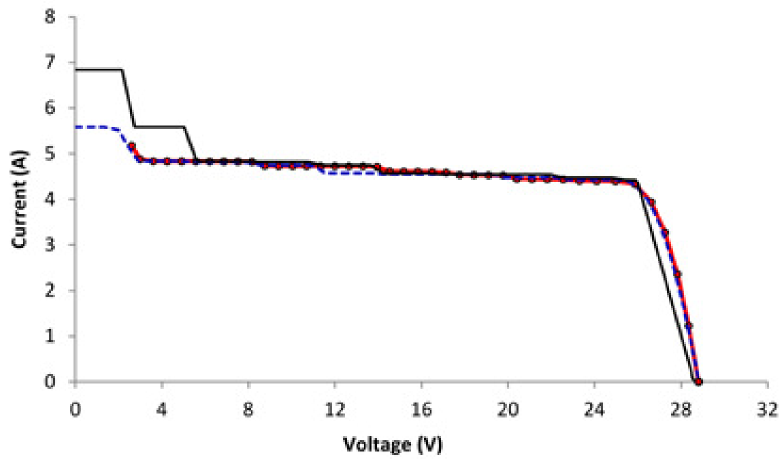

Figure 4.13: A comparison between *I-V* curve from field measurement data (red line with dots) with FPM simulation curve (black solid line) and comprehensive Matlab simulation *I-V* curve (blue dashed line)

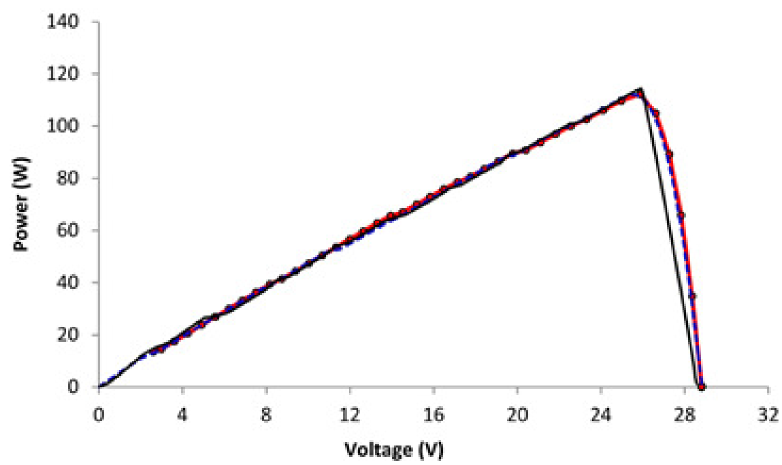

Figure 4.14: This graph compares *P-V* curve from the optimised array's filed measurement data (red line with dots) with FPM simulation curve (black solid line) and comprehensive Matlab simulation *P-V* curve (blue dashed line)

According to the graphs presented in Figure 4.9 Figure 4.13, The *I-V* curve derived from optimized array's field measurement data matches rather well with the newly proposed FPM prediction *I-V* curve. The only evident variance appears around the region from 0 V to 5.6 V. In the prediction curve, the presence of steps implies that there current mismatch occurs around the mentioned voltage region. These mismatch steps aren't that obvious in the measured *I-V* curve as compared to the FPM prediction curve as the combined array current has reduced when some CPV cells were functioning at reverse biased condition (Solanki, 2011).

The calculation methodology of the proposed FPM approach is a fairly straight-forward adding of current values from parallel-connected solar cells. Therefore clear signs of current mismatch can be observed in the *I-V* results. The distinct indication of mismatch steps in our *I-V* prediction curve can be very useful to concentrator system designers for evaluating mismatch issues in CPV dense-array design. In addition to that, current mismatch that occurred at the region of 0 V to 5.6 V has negligible impact to the output power and has minimal effect to the *P-V* curve (refer to Figure 4.10 and 4.14). Hence, it can be summarized that phenomena will not affect P_{mp} calculation of a well-designed CPV array, as the maximum power point is typically found close to the V_{oc} region of a dense-array *P-V* curve.

Table 4.3: This table aims to show a comparison between simulated (FPM) and measured results from dense-array operation for the NIPC prototype, in the following parameters: maximum output power P_{mp}, voltage at maximum output power V_{mp}, current at maximum output power I_{mp}, dense-array efficiency, and percentage error of maximum output power P_{mp}

	DNI: 641 W/m^2		
	P_{mp} (W)	V_{mp} (V)	I_{mp} (A)
Field Measured results	112.14	25.87	4.33
FPM simulated results	113.64	25.68	4.43
Efficiency: measured (%)		34.19	
Efficiency: simulated (%)		34.64	
Error, P_{mp} (%)		-1.34	

4.6 Off-axis Scenario

Off-axis condition occurs mainly resulted from tracking errors that causes angular offset between incident sunrays and optical axis of solar concentrator. Since solar concentrator is normally designed to concentrate sunrays that are parallel to the optical axis falling precisely on the receiver area, off-axis conditions will cause CPV array transient mismatch. Figures 4.15(a) and (b) illustrate two cases of misalignment between solar flux distribution and CPV dense-array. Figure 4.15 (a) shows the off-axis solar flux distribution pattern for the case of angular flux displacement 2.94 mrad to the right or equivalent to 5 mm of relative distance offset between solar flux distribution and CPV array. On the other hand, 4.15 (b) shows an off-axis solar flux distribution pattern for the case of angular flux displacement 2.94 mrad to the right and angular flux displacement 2.94 mrad to the bottom.

This scenario causes the current values of cells across the array to vary and it is especially significant between optimally illuminated and minimally illuminated cells. Figures 4.16 to 4.19 show *I-V* and *P-V* curves with mismatch steps for both cases. These are basically bypass-diode-induced mismatch steps between strings as a result of local variations in the solar flux distribution upon each concentrator cell during off-axis condition. Nevertheless, it could be observed that the mismatch steps that are observed are minimal, and the effect to performance efficiency is a reduction of 4.40% for off-axis flux distribution I, and a reduction of 2.33 % for off-axis flux distribution II (Figure 4.15).

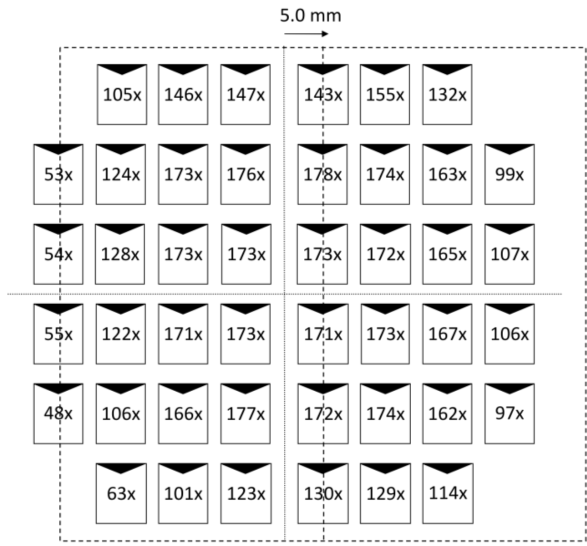

(a) Off-axis flux distribution I

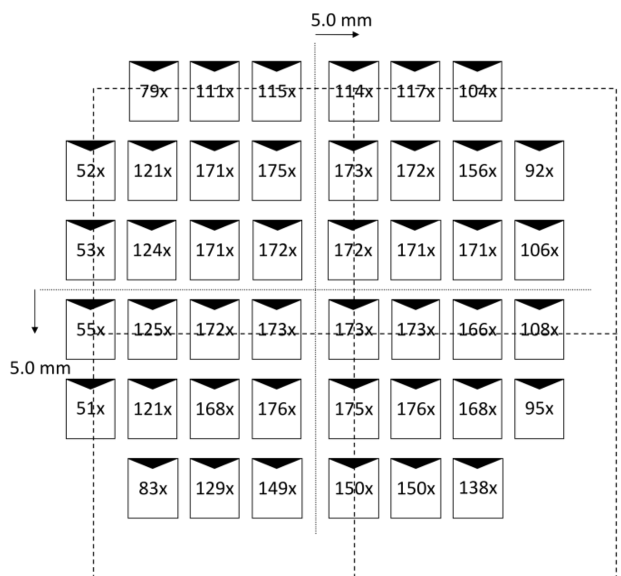

(b) Off-axis flux distribution II

Figure 4.15: Measured flux distribution data during off-axis scenario is acquired from an optical scanner. The two off-axis scenarios are: (a) Off-axis flux distribution I: 5.0 mm off tracking to the right, and (b) Off-axis flux distribution II: 5.0 mm off-tracking to the right and 5.0 mm to the bottom

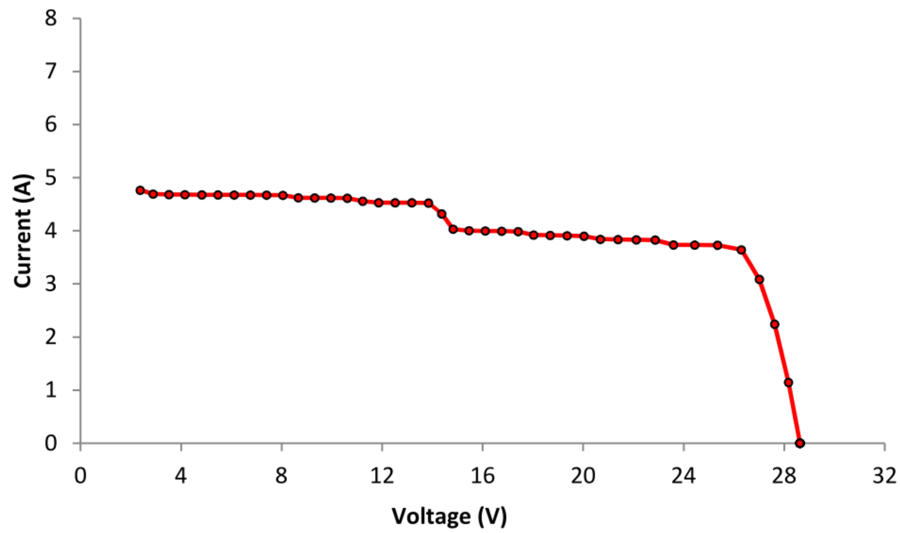

Figure 4.16: Measured *I-V* curve (red line with dots) at DNI = 616.52 W/m^2 with 5.0 mm off tracking to the right (Off-axis flux distribution I)

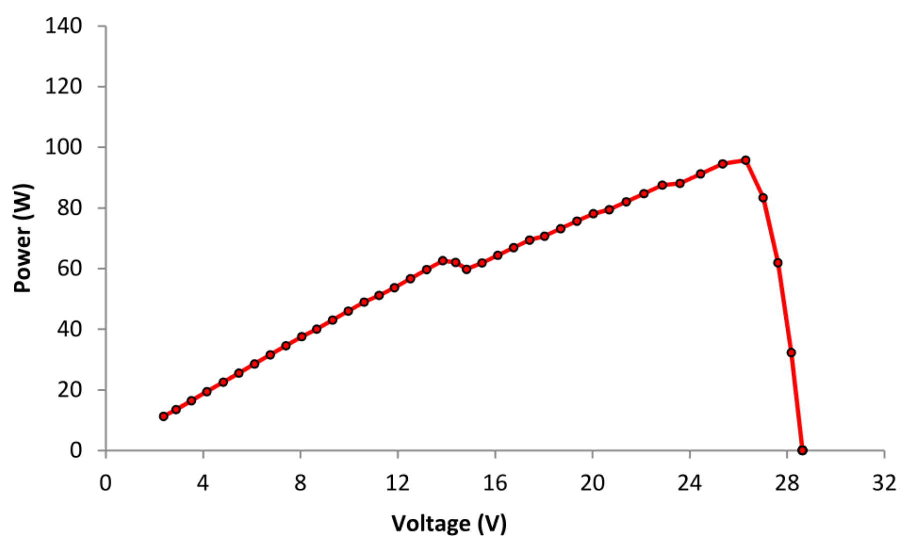

Figure 4.17: Measured *P-V* curve (red line with dots) at DNI = 616.52 W/m^2 is superimposed on Matlab simulation curve (blue dashed line) with 5.0 mm off tracking to the right (Off-axis flux distribution I)

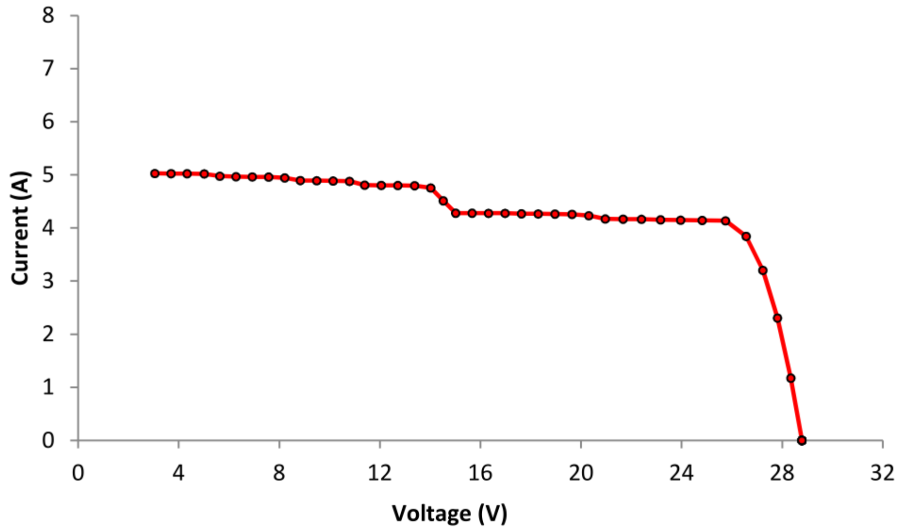

Figure 4.18: Measured *I-V* curve (red line with dots) at DNI = 641.18 W/ with 5.0 mm off tracking to the right + 5.0 mm to the bottom (Off-axis flux distribution II)

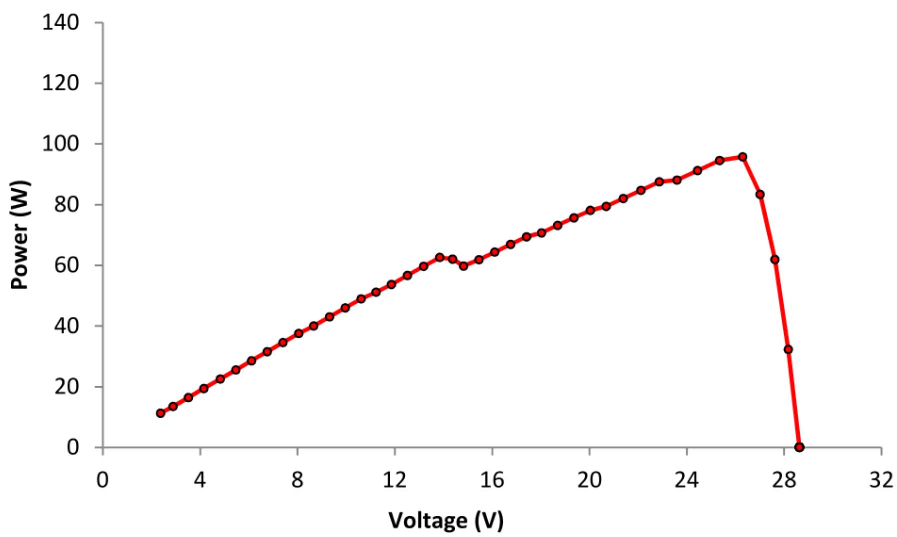

Figure 4.19: Measured *P-V* curve (red line with dots) at DNI = 641.18 W/m^2 with 5.0 mm off tracking to the right + 5.0 mm to the bottom (Off-axis flux distribution II)

Table 4.4: The performance of dense-array assembly under off-axis scenariois presented in terms of maximum output power P_{mp}, maximum voltage V_{mp}, maximum current I_{mp}, array efficiency, and error of maximum output power P_{mp}

	Off-axis flux distribution I (DNI: 616.52 W/m^2)		
	P_{mp} (W)	V_{mp} (V)	I_{mp} (A)
Measured results	95.76	26.05	3.73
Efficiency - measured (%)		29.79	

	Off-axis flux distribution II DNI: 641.18 W/m^2		
	P_{mp} (W)	V_{mp} (V)	I_{mp} (A)
Measured results	106.49	25.75	4.14
Efficiency - measured (%)		31.86	

CHAPTER 5

CONCLUSION

5.1 Concluding Remarks

The overall aims of this research is to study the non-uniformity issue of solar concentrators that have deterred CPV systems from achieving its full electrical generation potential and to develop a novel NIPC prototype and dense-array design methodology to in order to improve the performance of CPV systems. The research objectives of theoretical and experimental study in optimizing the performance of CPV dense-array NIPC system, as specified in Chapter 1, has been achieved. The major outcomes of this research are the development of an NIPC prototype, a new systematic FPM dense-array design method, and the demonstration of its enhanced performance via comprehensive dense-array simulation at on-axis and off-axis scenarios.

5.2 NIPC System

Comprehensive analyses of solar flux distribution from numerical simulation are carried out to examine the optical characteristics of the proposed non-imaging planar concentrator. The planar concentrator recommended consists of 21 × 21 arrays of facet mirrors which contribute to a total reflective area of approximately 4.4 cm^2, and focal distance of 170 cm. In the initial part of the optical study, the average solar concentration ratio as well as percentage of energy that lies in within the uniform solar flux distribution area is plotted for different cases. Depending on the mirror array configuration (from 17×17 to 25×25), the average solar concentration ration that is observed at the region of uniform illumination area is between 222 suns to 598 suns, while the percentage of energy in the uniform area of solar flux distribution is 43% to 70%.

Next, the second part of the study deals with the relationship between spillage loss and variation of solar flux distribution. If solar flux distribution variation is permitted to go as much as 20-30%, the total energy that will be collected at the receiver is almost 80%. Alternatively, depending on a system designer's requirements, a secondary concentrator can be added to the concentrator system to enhance the total energy output that can be collected without affecting the variation of flux distribution.

Last but not least, off-axis angle study and for sun-tracking error of up to 1.0 deg and the effects to solar flux distribution is investigated. Here, three analyses are carried out on the characteristics of solar flux distribution which are spillage loss, non-uniformity, and total acceptance angle where the inflicted damage from sun-tracking error is still within an acceptable range. With the target to collect at least 95% of energy (as compared to no-tracking error), the total acceptance angle is determined to be 0.48 deg. Overall, the simulated results have shown reasonably good uniformity in solar flux distribution with reasonably high concentration ratio for the application with high concentration solar cells. From all of the optical simulation analyses, the NIPC is found to be suitable as a concentrator for a dense-array CPV system.

5.3 FPM Dense-array Design

Conventionally, it is very exhaustive to design a CPV dense-array because it is typically an iterative process to achieve a target output power requirement. In the conventional process, a designed would first estimate a trial design and checks if it is acceptable. This attempt is repeated for a couple of times according to the system designer's past experience to find other possible trial attempts. Finally, all trial designs will be analysed to determine the best option that satisfies a system output requirement. However, a target-based design approach is not comprehensive enough because system designers do not search for all possibilities of dense-array configurations.

In this study, a new approach that is both systematic and complete is introduced in achieving the most optimal dense-array design using the novel FPM as the initial design phase. The FPM approach encompasses four stages, and is developed to optimize CPV dense-array configurations through a systematic way to replace the conventional trial and error practice that is time-consuming and not comprehensive. The first stage of FPM is when parameters like I_{sc}, V_{mp} and V_{oc} are calculated from measured solar flux distribution data of the solar concentrator system. After that, all possibilities of dense-array configuration are generated at the second stage of FPM process. In the third stage, *I-V* and *P-V* prediction curves using critical points of CPV cells and bypass diodes that are connected across each basic module are produced. Finally, all *I-V* and *P-V* prediction curves are analyzed by comparing the respective maximum output power. This four-stage approach that is presented is more systematic, fast and is able to explore all possibilities of dense-array designs, while maintaining reasonably accuracy.

From this method, an optimized configuration which is simulation 6 from Table 4.2 is revealed to achieve the highest electrical output, together with simulation 4. After careful evaluation, simulation 6 was chosen as the optimum design because its power density is superior (2.58 W/cell) to the power density achievable by simulation 4 (2.37 W/cell). Through this study, it was found that simulation 6 with merely 44 CPV cells is able to achieve the exact same output power to simulation 4 that consists of 48 CPV cells. When lesser solar cells are needed in a design, the system designed will be able to reduce project installation cost while increasing the competitiveness of concentrator solar technology.

This study highlights a new critical factor that affects power density which is array interconnection layout configuration, in addition to the influence of high solar concentration ratio. In addition to that, the study further reveals that FF is not a conclusive benchmark when assessing CPV dense-array *I-V* curve. Although FF is typically used for the evaluation of single solar cell's quality and performance, FF can only be a guideline and not a deciding factor when finalizing dense-array design. This was confirmed when comparing the FF outcome from simulation 6 and simulation 4. Although the FF value from simulation 4 is higher at 68.95% as compared to simulation 6 which is just 57.71%, it was found that simulation 4 requires more CPV cells in order to be on par with simulation 6 in terms of output power generation.

5.4 Comprehensive Dense-array Simulation

After the initial design of dense-array has been completed, detailed simulations are performed to check the FPM prediction results. Comprehensive simulation using Matlab has verified that the proposed FPM approach as presented in Chapter 4 with P_{mp} error of only 1.88%.

Last but not least, an actual dense-array assembly was constructed and implemented together with an NIPC prototype to verify simulation results. The modeling methods have been successfully confirmed with the NIPC system to achieve filed conversion efficiency of 34.19% with *I-V* curve characteristics that are alike. Comparing the results from measurements during operation with FPM & Matlab comprehensive simulation results, a very close match is achieved. The maximum output power (P_{mp}) estimation from computational modeling is just 1.34% in error.

5.5 Field Measurements during Off-axis Condition

Off-axis condition of as much as 2.94 mrad which is equivalent to 5 mm displacement is also studied for this system. This scenario generally causes the current values of CPV cells across the array to vary especially between optimally illuminated and minimally illuminated solar cells. Nevertheless, the mismatch steps that are observed in the optimized dense-array is minimal, and the effect to electrical efficiency is a small reduction of 4.40% for off-axis flux distribution I, and a reduction of 2.33 % for off-axis flux distribution II.

5.6 Outlook and Future Work

CPV systems are currently facing slower installed capacity growth in the market as compared to PV systems, while facing concerns such as cost effectiveness and reliability of performance. In CPV applications, improved module or array performance can directly counterbalance the cost of expensive solar cell materials, which in turn has the potential of reviving the market demand for concentrator system installations. By reducing overall installation cost of a solar system, photovoltaic energy can become one of the main renewable energy sources in the future.

In conclusion, this research has successfully met the objectives of addressing non-uniformity of concentrated solar flux distribution in solar concentrators via improvements in the optical design with the novel NIPC design, optimised CPV dense-array electrical interconnection design, as well as the development FPM which can systematically optimize dense-array interconnection design in order to improve the overall system efficiency.

To extend this research work towards the commercialization stage, it is desirable to apply similar research approach on a bigger size of NIPC concentrator in order to find the most optimised size of NIPC system by considering factors like output power, level of solar concentration ratio and manufacturing approach. At the same time, cooling system design for high concentration (above 500 suns) can be further improved to achieve lower or at least the same operating temperature at $55^{o}C$, while studying the relationship between temperature, solar concentration and generated power.

In addition to that, future work could incorporate a thorough study using the novel methodology developed for interconnection design, as well as adopting similar optical and electrical analysis on different kinds of CPV concentrator systems to compare the optimization potential of solar concentrators. It is envisioned that the said methodology would be able to improve output power generation for other types of concentrator systems that face solar concentration non-uniformity issue as well.

APPENDIX A

Renewable Energy 34 (2009) 1364–1370

Contents lists available at ScienceDirect

Renewable Energy

journal homepage: www.elsevier.com/locate/renene

Design and construction of non-imaging planar concentrator for concentrator photovoltaic system

K.K. Chong*, F.L. Siaw, C.W. Wong, G.S. Wong

Faculty of Engineering and Science, Universiti Tunku Abdul Rahman, Off Jalan Genting Kelang, Setapak, 53300 Kuala Lumpur, Wilayah Persekutuan, Malaysia

ARTICLE INFO

Article history:
Received 28 March 2008
Accepted 6 September 2008
Available online 5 November 2008

Keywords:
Non-imaging planar concentrator
Concentrator photovoltaic
Sun tracking
Uniform concentration
Illumination distribution
Ray tracing

ABSTRACT

A novel configuration of solar concentrator, which is the non-imaging planar concentrator, capable of producing much more uniform sunlight and reasonably high concentration ratio, is designed and constructed. This design is envisioned to be incorporated in concentrator photovoltaic (CPV) systems. The work presented here reports on the design, optical alignment and application of the prototype, which is installed at Universiti Tunku Abdul Rahman (UTAR), Malaysia. In the architecture of the prototype, 360 flat mirrors, each with a dimension of 4.0 cm × 4.0 cm, are arranged into 24 rows and 15 columns with a total reflection area of about 5760 cm^2. In addition to that, illumination distribution for the prototype is simulated and its results are then compared with the experiment result.

1. Introduction

At present, there is an increasing interest in concentrator photovoltaic (CPV) power generation systems as an alternative to replace or complement the existing power generation systems that consume fossil and nuclear fuels [1–3]. The idea of concentrating solar energy to generate electricity has ingeniously made use of the concept in concentrator optics especially for designing a specific geometry of reflectors or lenses to focus sunlight onto a small receiving solar cell [4]. Lenses or mirrors in the concentrator photovoltaic system will replace most of the solar cell material and the price of both is taken into account for determining the optimum configuration. The price of solar concentrator is commonly lower than that of solar cells and hence efforts have been put into finding ways for lowering the manufacturing cost using various types of solar concentrators to develop a concentrator photovoltaic system [5].

This paper explores a different approach that came from a realization that the available concentrating systems require complex engineering efforts to build and the need for uniform distribution of solar flux, to have higher efficiency in CPV power generation. Franklin and Coventry [6] as well as Luque and Andreev [7] have discussed that many of the existing concentrator systems produce non-uniform focused illumination. The CPV cells that receive non-uniform illumination will experience a drop in efficiency, as opposed to CPV cells under uniform illumination [8,9]. With this reason, Mills and Morrison advocated the use of an advanced form of linear Fresnel reflector that can produce a better uniformity of solar irradiation compared to parabolic trough or parabolic dish systems [10]. However, the solar concentration ratio for linear Fresnel reflector is normally lower than 100 suns. To achieve moderate solar concentration ratio (several hundreds of suns), modular Fresnel concentrator has been introduced for the application in CPV system and the results show that the modularly faceted Fresnel lenses can provide a better uniformity of solar irradiance but the transmission efficiency is relatively low, which is less than 80% due to the reflections at the lens surfaces and absorption by the lens material [11].

Chen et al. [12–16] proposed a non-imaging focusing heliostat in which high solar concentration ratio can be achieved through the superposition of all the mirror images into one at the fixed target. According to them, since the sunlight is not coherent, the resulted solar concentration is the algebra sum of the solar rays without creating a specific optical image. Inspired by the combined idea from both non-imaging focusing heliostat and the modular Fresnel lenses' technology, a non-imaging planar concentrator has been designed and constructed. It will be a cost-effective alternative with a simple mechanical structural design, to keep the fabrication cost relatively low and more importantly, to achieve much better

* Corresponding author. Tel.: +60 3 41079802/12 2829862; fax: +60 3 41079803.
E-mail addresses: chongkk@mail.utar.edu.my, kokkeong_c@yahoo.com (K.K. Chong).

0960-1481/$ – see front matter © 2008 Elsevier Ltd. All rights reserved.
doi:10.1016/j.renene.2008.09.001

uniform intensity at the target area with a reasonably high concentration ratio. We have adopted the concept into our research and designed a prototype of non-imaging planar concentrator consisting of flat mirrors. The fundamental scheme of this design is for the image to have a square shape at the target, which can correspond to the sensitive area of the CPV array for future application. It is also important to pay attention to the uniformity of the beam intensity over the whole sensitive area for maximum exploitation of the photovoltaic cells. Finally, the prototype's performance has been evaluated based on the experiment and simulation results of the illumination distribution.

2. Principle and concept of non-imaging planar concentrator

To achieve a good uniformity of the solar irradiation with a reasonably high concentration ratio on the target, a non-imaging planar concentrator has been proposed to apply the concept of non-imaging optics to concentrate the sunlight. This non-imaging planar concentrator is formed by numerous square flat mirrors acting as an optical aperture to collect and to focus the incident light into a target. The conceptual layout design of non-imaging planar concentrator is illustrated in Fig. 1(a) and (b). The idea of concentrating the sunlight in the planar concentrator is similar to that of non-imaging focusing heliostat, where the uniform intensity on the target can be acquired

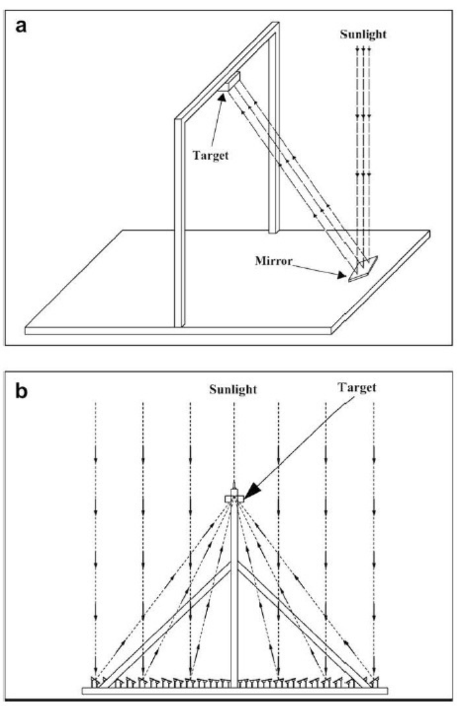

Fig. 1. Conceptual layout design of the non-imaging planar concentrator. (a) 3D view of the concentration optics with only one mirror. (b) Cross-sectional view of the planar concentrator to show how the individual mirror directs the solar rays to the target.

from the superposition of the flat mirror images into one as shown in Fig. 1(b). In this design, the incident sunrays are reflected by an array of identical flat mirrors to the target, in which their size and shape are nearly same as that of the receiver.

Let us consider the non-imaging planar concentrator consisting of $m \times n$ array of mirrors. For a geometrical representation, a general Cartesian coordinate system is defined in the plane of the planar concentrator, with its origin located at the centre of concentrator, x-axis lying along the row of mirrors, y-axis lying along the column of mirrors and z-axis pointing towards the target. The position for each mirror in the planar concentrator can be indexed as (i, j), where i and j express the mirror located at ith row and jth column of the concentrator. The coordinate of the central point for the corresponding i,j-mirror, $H_{i,j}$, can be written as

$$H_{i,j} = \begin{bmatrix} H_x \\ H_y \\ H_z \end{bmatrix}_{i,j} = \begin{bmatrix} (w+g)\left(i - \frac{m+1}{2}\right) \\ (w+g)\left(j - \frac{n+1}{2}\right) \\ 0 \end{bmatrix}_{i,j} \tag{1}$$

where w is the width of the square flat mirror and g is the gap spacing in between two adjacent mirrors. On the other hand, the coordinate of the target is defined as

$$T = \begin{bmatrix} T_x \\ T_y \\ T_z \end{bmatrix} = \begin{bmatrix} 0 \\ 0 \\ F \end{bmatrix}$$

where F is the focal length of the non-imaging planar concentrator or the perpendicular distance between the central point of the concentrator frame and the target. Then, the total reflective area, A, for the $m \times n$ mirror array of non-imaging planar concentrator is given as

$$A = \left(w^2\right)(m \times n)$$

Referring to Fig. 2, the incident angle of the solar ray can be formulated as

$$\theta_{i,j} = \frac{1}{2}\arctan\left(\frac{\sqrt{H_x^2 + H_y^2}}{F}\right) \tag{2}$$

In order to direct the solar ray from the mirror towards the target, the unit vector normal of each mirror has to bisect the angle between incident ray and reflected ray. Thus, from Fig. 2, the unit vector normal for the i,j-mirror, $\vec{N}_{i,j}$, can be derived from the Snell–Descartes law of reflection as

$$\vec{N}_{i,j} = \begin{bmatrix} N_x \\ N_y \\ N_z \end{bmatrix}_{i,j} = \frac{\vec{I} + \vec{R}_{i,j}}{2\cos\theta_{i,j}} = \begin{bmatrix} N_x = \frac{-H_x}{2\cos\theta_{i,j}\sqrt{H_x^2+H_y^2+F^2}} \\ N_y = \frac{-H_y}{2\cos\theta_{i,j}\sqrt{H_x^2+H_y^2+F^2}} \\ N_z = \frac{F+\sqrt{H_x^2+H_y^2+F^2}}{2\cos\theta_{i,j}\sqrt{H_x^2+H_y^2+F^2}} \end{bmatrix}_{i,j} \tag{3}$$

provided that $\vec{I}$ is the unit vector of incident ray that is given by (0, 0, 1), $\vec{R}_{i,j}$ is the unit vector of reflected solar ray, $\theta_{i,j}$ is the incident angle of the solar ray and F is the focal length of the concentrator. The tilting angles of the i,j-mirror about the row direction of α and about column direction of β are expressed as follows:

$$\alpha = \arcsin(-N_x) \tag{4}$$

$$\beta = \arctan\left(\frac{-N_y}{N_z}\right) \tag{5}$$

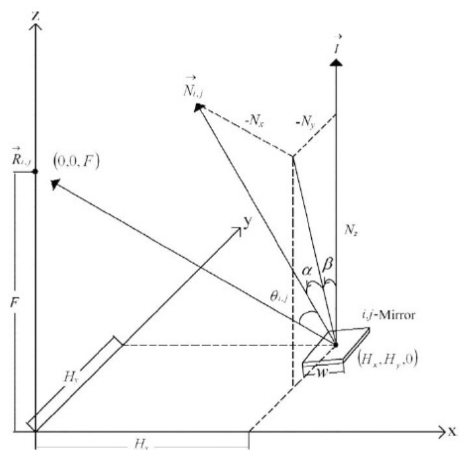

Fig. 2. Geometrical representation of the concentrator: a general Cartesian coordinate system is defined in the plane of the planar concentrator, with its origin located at the centre of concentrator, *x*-axis lying along the row of mirrors, *y*-axis lying along the column of mirrors and *z*-axis pointing towards the target. $\vec{I}$ is the unit vector of incident ray that is given by (0, 0, 1), $\vec{R}_{i,j}$ is the unit vector of reflected solar ray, $\theta_{i,j}$ is the incident angle of the solar ray and F is the focal length of the concentrator. The titling angles of *i,j*-mirror about the row direction is α and about the column direction is β.

3. Design and construction of prototype

A non-imaging planar concentrator is an on-axis focusing device, with the target placed at the focal point. In the design of the concentrator, 360 pieces of flat glass mirrors are prepared and arranged to form a total reflective area of about 5760 cm^2. There is a gap spacing of 0.5 cm in between the mirrors. This gap will avoid any possible blocking when the mirrors are tilted and can also reduce the wind pressure on the concentrator frame.

The concentrator operates on a two-axis sun-tracking system. We adopted elevation–azimuth sun-tracking formulas into the control design to predict the sun's movement [17]. A computing program is then created to calculate the position of the sun as well as to ensure correct orientation of the concentrator. The planar concentrator that consists of the hardware and software section is schematically represented in Fig. 3. On the hardware part, a mechanical platform is located outdoors where the concentrator frame and its drive mechanism are placed. A Windows-based control program is developed to move the concentrator along the azimuth (AA') and elevation (BB') axes for the software section. The movement of the whole system is directed by off-the-shelf components such as stepper motors, bearings and their associated gears. Two optical encoders are used to send feedback signals to eliminate tracking errors resulted from mechanical backslash, wind effect or any other external disturbances exerted at the concentrator frame.

3.1. Hardware design

The structure of the non-imaging planar concentrator can be divided into four main components: concentrator frame, concentrator arm, pedestal and flat mirror array. The architectural design of the planar concentrator prototype is depicted in Fig. 3. Since this system is assembled using components that are readily available (off-the-shelf) and reasonably priced, immediate and easy implementation is possible.

The main material that is selected for constructing the concentrator frame is aluminium, which is weather resistant. The core reason for choosing this material is due to its light weight characteristic. Because of that, the concentrator frame will not

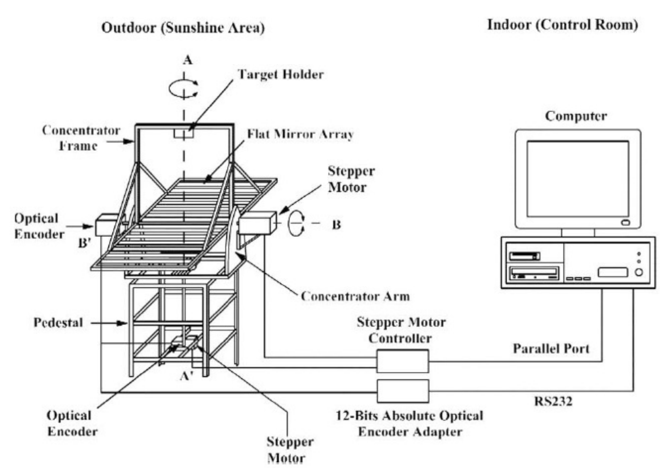

Fig. 3. Hardware and software design for the non-imaging planar concentrator. The concentrator operates on a two-axis sun-tracking system. We adopted some mathematical formulas into the control design to predict the sun's movement. A computing program is then created to calculate the position of the sun as well as to ensure correct orientation of the concentrator.

apply much load on the turning mechanism, and subsequently eases the process of structure development. Fig. 3 also shows the frame structure of the non-imaging planar concentrator.

Aluminium square tubes are used to form the base frame with a dimension of 115.7 cm × 73.0 cm. Next, twenty-four pieces of flat aluminium bars are laid across the base frame. Fifteen units of mirror sets will be mounted on each of the flat aluminium bars. Another structure, which is the target supporter, is built using square tubes and is fixed onto the centre of the base frame. For a CPV system application, solar cells can be placed at this target supporter frame of 78.0 cm in height.

The concentrator arm is a steel structure that supports the concentrator frame. The major function of the concentrator arm is to turn the concentrator frame about the elevation axis and it is connected to a rotation shaft so that the frame can turn about the azimuth axis. The pedestal is made from steel bars and functions as a support to the concentrator frame and the concentrator arm structure. To provide a strong and firm base as foundation to the whole system, the footings of the pedestal are constructed with concrete.

Flat mirrors with the dimension of 4.0 cm × 4.0 cm and a thickness of 0.2 cm are selected as the reflective material for the present project. There is a total of 360 pieces of flat mirrors, and they are arranged into twenty-four rows and fifteen columns on the concentrator frame. Besides that, the concentrator mirror sets consist of several other components, namely, the compression springs, machine screws, silicone paste and nuts (Fig. 4). The idea of this design is for the presetting of each mirror along the row and column directions. There are in total three contact points in each of these screw–spring assemblies from which one of them acts as the pivot point, and the remaining two are adjustable points. Each mirror can thus be freely tilted to focus sunlight onto the target by turning the nuts of the adjustable screw–spring sets manually.

3.2. Software control system

A Windows-based program is implemented using Microsoft VisualBasic.net to control the sun-tracking mechanism according to the day number of the year, the local time, time zone, latitude and longitude of the concentrator installation. The program uses these data to calculate the azimuth and elevation angles of the sun. As the sun moves along its trajectory throughout the day, the computer sends signals via the parallel port and hence the driver will turn the concentrator frame appropriately about the azimuth and elevation axes corresponding to the calculated angles. The tracker is commanded to follow the sun at all times because the program is run in repeated loops, which will cause continuous movement of the driver motors.

Two stepper motors, with the specification of 0.9° in the half step mode, are used to rotate the concentrator around the azimuth and elevation axes. One of them is coupled to the azimuth shaft and the other is coupled to the elevation shaft. Each stepper motor is coupled to its respective shaft via a gearbox at a gear ratio of 100:1, yielding an overall resolution of 0.009°/step. The tracking is designed to have a closed-loop feedback by using two 12-bit absolute encoders with the resolution of 2048 counts/revolution to confirm that the concentrator is tracking the sun correctly. The encoders detect the rotation angles of the shaft, and send feedback signals to a remote computer through an RS-232 interface. The calculated values are then compared with the current positions of the concentrator frame recorded in the computer to obtain a differential value in position. If the positional difference in angular degree is greater than the resolution of the optical encoder, i.e. 0.176°, the computer will command the relevant stepper motor to move the frame to the calculated position.

4. Optical alignment

The prototype of non-imaging planar concentrator has been installed in the south–north orientation at latitude of 3.2° and longitude of 101.7°, in Kuala Lumpur, Malaysia. Over the past few months, the prototype has proved to be robust, reliable, and capable of operating for long periods in the field. Fig. 5 shows the layout of the prototype that has been constructed using the two-dimensional array of flat mirrors.

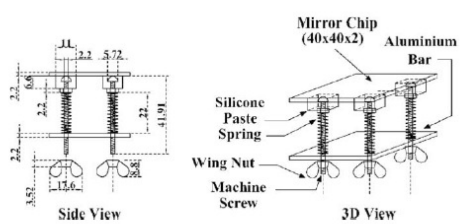

Fig. 4. Structure of the concentrator mirror set. The concentrator mirror sets consist of several components, namely, the mirror, compression springs, machine screws, silicone paste and nuts. The idea of this design is for the presetting of each mirror along the row and column directions. There are in total three contact points in each of these screw–spring assemblies from which one of them acts as the pivot point, and the remaining two are adjustable points.

Fig. 5. The prototype of the non-imaging planar concentrator has successfully focused 360 mirror images onto a target area. The prototype has been installed in the south–north orientation at latitude of 3.2° and longitude of 101.7°, in Kuala Lumpur, Malaysia.

There are two stages in the optical alignment process. The first stage is to fine tune the input parameters for the planar concentrator so that the system can track the sun accurately. The parameters that will affect the tracking accuracy are latitude, longitude and the local clock time. At this stage, nine mirrors which are at the centre of the concentrator frame are selected to concentrate sunlight onto the target area during tracking for optical alignment purposes, whereas the remaining mirrors are covered. When the exposed mirrors achieve the smallest tracking error, a small offset value from the solar image to the expected target area, the second stage of optical alignment can be started. The second stage is to tilt the remaining mirrors to focus sunlight towards the target. This mirror alignment work must be carried out while the concentrator mirrors are in operation and tracking the sun. Fig. 5 shows the prototype with mirrors that are aligned to the target.

5. Solar illumination distribution study

5.1. Theoretical analysis

A theoretical study of the illumination distribution on the receiver has been carried out with the aid of computer simulation. In the simulation program, ray tracing technique was used to model the reflection of sunlight by the non-imaging planar concentrator and to plot the distribution of solar flux at the target plane. All the parameters used in the simulation follow the practical design parameters of the prototype and the solar disc effect is also included in which the sunlight that strikes on the mirror surface is treated as cone rays. In order to achieve a smooth simulation result of illumination distribution at the target, a reasonably high resolution is required in the optical modelling for the mirrors, cone rays and the target plane. In this context, each mirror with a dimension of 4.0 cm × 4.0 cm is represented by 35 × 35 equally spaced reflective points. To emulate the solar disc effect to the final image size, the sunlight reflected from each reflective point will be then represented by a group of equally distributed solar rays within a cone with half aperture angle of 0.2666° and the resolution of 69 rays per aperture diameter. The target plane of dimension 8.0 cm × 8.0 cm is represented by a grid of 100 × 100 equally spaced points in the simulation and therefore each pixel of illumination distribution plot has an area of 0.08 cm × 0.08 cm. The solar concentration of each pixel is essentially a measure of how much solar irradiation a pixel receives compared to the situation with direct normal solar irradiation. Consequently, the calculation of solar concentration (number of suns) on each pixel can be shown as

$$C = N \times \frac{\text{Area of Reflective Point (cm}^2)}{\text{Area of Target Plane Pixel (cm}^2)} \times \frac{\cos\theta_{i,j}}{P} \qquad (6)$$

where N is the number of solar rays that strike on the corresponding pixel at the target plane and P is the total number of solar rays within the cone. In the algorithm for optical simulation of the solar concentrating system, sunlight that is reflected by each of the reflective points on the flat mirror will be modelled to be comprised of P rays per cone and each ray within the cone will be traced from the reflective point to the target plane. The target plane consisting of 100 × 100 equally spaced pixels will have a particular pixel to increase its count by 1 unit if there is any solar ray impinging on that particular pixel. The algorithm is repeated for all the reflective points at the mirror surface and for all the mirrors at the planar concentrator. If the total count of a particular pixel at the target plane is N unit, the solar concentration for that pixel can be determined from Eq. (6) and the illumination distribution will be generated by computing the solar concentration for each pixel on the target plane.

To study the characteristics of maximum solar concentration and uniform illumination area, the solar illumination distribution of the non-imaging planar concentrator with different focusing distance has been simulated. Fig. 6(a)–(c) shows the pattern of the illumination distribution when the focusing distance (F) is set at 78 cm. From Fig. 6(b) and (c), the maximum solar concentration and the uniform illumination area are identified as 298 suns and 3.36 cm × 3.39 cm (11.4 cm^2), respectively. Following this result, the illumination distribution is also simulated for other focusing distances, F, such as at 30 cm, 40 cm, 50 cm, 60 cm, 70 cm, 80 cm, 90 cm, 100 cm, 110 cm, 120 cm, 130 cm and 140 cm. Fig. 7 reveals the graph of maximum solar concentration and total uniform illumination area versus focusing distance. Increasing focusing distance can in fact improve the maximum solar concentration but the total uniform illumination area will be sacrificed. The increase of the solar concentration with focusing distance has shown a tendency towards saturation after $F = 80$ cm, while the reduction in the uniform illumination area with focusing distance follows a linear graph. By increasing focusing distance from 80 cm to 140 cm, the maximum achievable solar concentration only improves 7% (from 301 suns to 320 suns), but the uniform illumination area has been reduced 30% (from 11.29 cm^2 to 7.83 cm^2). There are a few factors affecting the solar concentration and uniform illumination area when the focusing distance is varied, which include cosine effect (effective collection area of solar radiation inversely proportional to $\theta_{i,j}$ and hence proportional to F), image projection effect (projection of mirror image onto the target plane proportional to $\theta_{i,j}$ and hence inversely proportional to F) and solar disc effect (the image size of the solar disc inversely proportional to F), etc. Among all these factors, only cosine effect and image projection effect will cause the solar concentration to increase with the focusing distance, while solar disc effect is otherwise. Therefore, we can conclude that the cosine effect and the image projection effect are two dominant factors affecting the performance of the non-imaging planar concentrator.

5.2. Experimental data

To optimise the performance of the concentrator, the focusing distance of the prototype is finally set at 78 cm and experiment data have been collected to validate the simulation result. The simulation result shows a uniform illumination profile with a concentration of 298 suns. Thus, to verify these two important information, the sand-paper carbonizing experiment is carried out to check the shape of the image while the material-melting experiment is used to confirm the magnitude of achievable concentration. Comparing the simulation result in Fig. 6(a) with the experiment result as shown in Fig. 8, both of them have shown similar characteristics, especially the total area of uniform illumination and the profile of solar flux distribution. As for the distribution pattern of the solar flux study, we have exposed a piece of sand paper at the target area for a few seconds and the concentrated sunlight has generated different grades of burnt mark on the sand paper. Fig. 8 shows the result of the above experiment and the sand paper has shown a reasonably uniform carbonised burnt mark especially at the area of 3.3 cm × 3.4 cm.

In addition, another experiment has also been conducted to confirm the maximum solar concentration ratio of 298 suns as predicted in the simulation result. According to the black body radiation theory, the solar concentration ratio of 298 suns can be indirectly verified through confirming the maximum achievable temperature of 1159 °C under the solar insolation of 800 W/m^2 [18]. From the above hypothesis, we proceeded with further experiments to determine the maximum achievable temperature using material-melting method. This experiment was conducted from 4th November 2007 to 5th November 2007. Metal sheets are cut

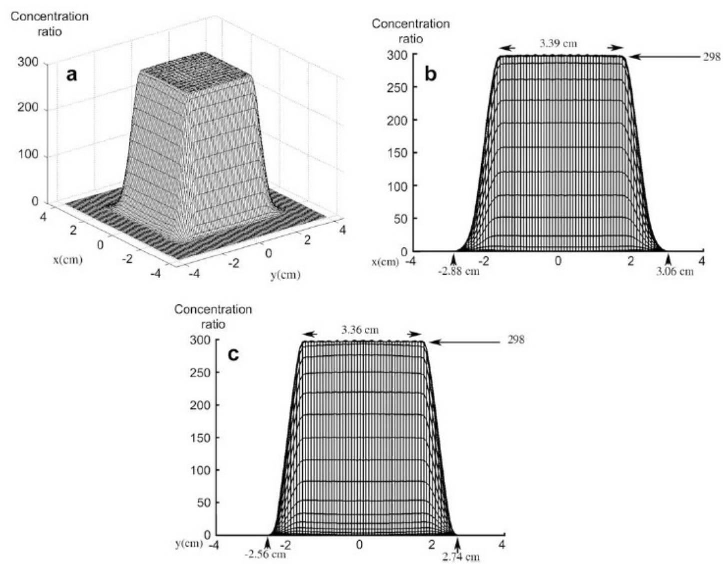

Fig. 6. The optical simulation result of the illumination distribution at the target produced by the non-imaging planar concentrator prototype with the focusing distance of 78 cm. (a) Three-dimensional view of mesh plot, (b) two-dimensional view of mesh plot displaying uniform distribution of concentrated sunlight at the centre of the target (view from x), (c) two-dimensional view of mesh plot displaying uniform distribution of concentrated sunlight at the centre of the target (view from y).

into a size of about 6.0 cm × 6.0 cm. Each sheet is then held horizontally at the hot spot position using an adjustable target holder. Various types of materials such as aluminium (melting point of 660 °C) and copper (melting point of 1084 °C) are employed. We observed that a melted hole is successfully formed in both the aluminium and copper sheets. As an example, an aluminium sheet of 0.12 mm thickness started melting instantly when exposed to concentrated sunlight, and took 5 s to form a hole. This shows that

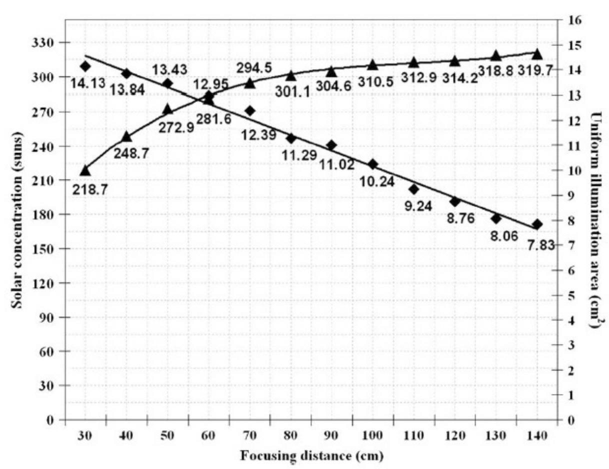

Fig. 7. Graph of the maximum solar concentration (suns) and total uniform illumination area (cm^2) versus focusing distance (cm). Increasing focusing distance can in fact improve the maximum solar concentration but the total uniform illumination area will be sacrificed.

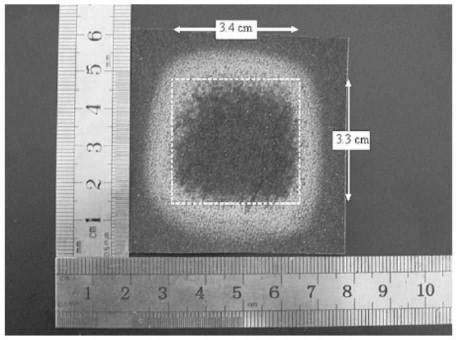

Fig. 8. Solar illumination distribution study has been carried out by exposing a sand paper for a few seconds at the target of the planar concentrator prototype. The concentrated sunlight has generated different grades of burnt mark on the sand paper. The sand paper has shown a reasonably uniform carbonised burnt mark especially at the area of 3.3 cm × 3.4 cm.

the temperature of the prototype has reached the melting point temperature of those materials. These tests have successfully verified that the system can achieve a temperature of at least 1084 °C and thus the solar concentration of 298 suns is possible.

6. Conclusion

As a conclusion, the experiment and simulation results have concurrently confirmed that the non-imaging planar concentrator design can produce a reasonably uniform solar irradiance at the target plane, which is very significant in increasing the efficiency of the CPV system. Consequently, the proposed non-imaging planar concentrator is an optical device that is specially designed for the application in CPV system, especially for CPV cells in a dense-array receiver.

Acknowledgements

The authors would like to express their gratitude to Malaysia Energy Centre, Ministry of Water, Energy and Telecommunication (AAIBE Trust Fund) and Ministry of Science, Technology and Innovation (e-Science Fund) for the financial support.

References

[1] Faiman D, Raviv D, Rosenstreich R. Using solar energy to arrest the increasing rate of fossil-fuel consumption: the southwestern states of the USA as case studies. Energy Policy 2007;35(1):567–76.
[2] Kribus A, Kaftori D, Mittelman G, Hirshfeld A, Flitsanov Y, Dayan A. A concentrating photovoltaic and thermal system. Energy Conversion and Management 2006;47:3582–90.
[3] Luque Antonio, Andreev Viacheslav, editors. Concentrator photovoltaics. Berlin, Heidelberg, New York: Springer; 2007. p. 1–21.
[4] Andreev VM, Grilikhes VA, Rumyantsev VD. Photovoltaic conversion of concentrated sunlight. England: John Wiley & Sons Ltd; 1997. p. 185–259.
[5] Whitfield GR, Bentley RW, Weatherby CK, Hunt AC, Mohring HD, Klotz FH, et al. The development and testing of small concentrating PV systems. Solar Energy 2000;67(1–3):23–34.
[6] Franklin E, Coventry J. Effects of highly non-uniform illumination distribution on electrical performance of solar cells. In: ANZSES solar conference, Newcastle, Australia; 2002.
[7] Luque Antonio, Andreev Viacheslav, editors. Concentrator photovoltaics. Berlin, Heidelberg, New York: Springer; 2007. p. 89–111.
[8] Coventry Joe S. Performance of a concentrating photovoltaic/thermal solar collector. Solar Energy 2005;78:211–22.
[9] Nishioka Kensuke, Takamotob Tatsuya, Agui Takaaki, Kaneiwa Minoru, Uraoka Yukiharu, Fuyuki Takashi. Annual output estimation of concentrator photovoltaic systems using high-efficiency InGaP/InGaAs/Ge triple-junction solar cells based on experimental solar cell's characteristics and field-test meteorological data. Solar Energy Materials and Solar Cells 2006;90:57–67.
[10] Mills DR, Morrison GL. Compact linear Fresnel reflector solar thermal powerplants. Solar Energy 2000;68(3):263–83.
[11] Ryu K, Rhee JG, Park KM, Kim J. Concept and design of modular Fresnel lenses for concentration solar PV system. Solar Energy 2006;80:1580–7.
[12] Chen YT, Chong KK, Bligh TP, Chen LC, Yunus J, Kannan KS, et al. Non-imaging focusing heliostat. Solar Energy 2001;73(3):155–64.
[13] Chen YT, Chong KK, Lim CS, Lim BH, Tan KK, Omar Aliman, et al. Report of the first prototype of non-imaging focusing heliostat and its application in high temperature solar furnace. Solar Energy 2002;72(6):531–44.
[14] Chen YT, Chong KK, Lim BH, Lim CS. Study of residual aberration for non-imaging focusing heliostat. Solar Energy Materials and Solar Cells 2003;79(1):1–20.
[15] Chen YT, Kribus A, Lim BH, Lim CS, Chong KK, Karni J, et al. Comparison of two sun tracking methods in the application of heliostat field. Journal of Solar Energy Engineering 2004;126:638–44.
[16] Chen YT, Chong KK, Lim CS, Tan BK, Lim BH, Lu YF. Report on the second prototype of non-imaging focusing heliostat and its application in food processing. Solar Energy 2005;79:280–9.
[17] Stine WB, Harrigan RW. Solar energy fundamentals and design. 1st ed. New York: Wiley Interscience; 1985. p. 38–69.
[18] Winston R, Minano Juan C, Pablo Benitez. Non-imaging optics. USA: Elsevier Academic Press; 2005. p. 1–6.

APPENDIX B

Sensors **2009**, *9*, 7849-7865; doi:10.3390/s91007849

OPEN ACCESS

sensors

ISSN 1424-8220

www.mdpi.com/journal/sensors

Article

Integration of an On-Axis General Sun-Tracking Formula in the Algorithm of an Open-Loop Sun-Tracking System

Kok-Keong Chong *, Chee-Woon Wong, Fei-Lu Siaw, Tiong-Keat Yew, See-Seng Ng, Meng-Suan Liang, Yun-Seng Lim and Sing-Liong Lau

Faculty of Engineering and Science, Universiti Tunku Abdul Rahman,Off Jalan Genting Kelang, Setapak, 53300 Kuala Lumpur, Malaysia; E-Mails: cheewoon_w@hotmail.com (C.-W.W.); jessiesiaw@gmail.com (F.-L.S.); ytkeat@yahoo.com (T.-K.Y.); ngss@utar.edu.my (S.-S.N.); liangms@utar.edu.my (M.-S.L.); yslim@utar.edu.my (Y.-S.L.); lausl@utar.edu.my (S.-L.L.)

* Author to whom correspondence should be addressed; E-Mails: chongkk@utar.edu.my; kokkeong_c@yahoo.com; Tel.: +603-410 798 02; Fax: +603-410 798 03.

Received: 29 July 2009; in revised form: 19 August 2009 / Accepted: 28 September 2009 / Published: 30 September 2009

Abstract: A novel on-axis general sun-tracking formula has been integrated in the algorithm of an open-loop sun-tracking system in order to track the sun accurately and cost effectively. Sun-tracking errors due to installation defects of the 25 m^2 prototype solar concentrator have been analyzed from recorded solar images with the use of a CCD camera. With the recorded data, misaligned angles from ideal azimuth-elevation axes have been determined and corrected by a straightforward changing of the parameters' values in the general formula of the tracking algorithm to improve the tracking accuracy to 2.99 mrad, which falls below the encoder resolution limit of 4.13 mrad.

Keywords: general sun-tracking formula; azimuth-elevation; sun-tracking accuracy; passive sensors; solar concentrator; solar collector

1. Introduction

Sun-tracking system plays an important role in the development of solar energy applications, especially for the high solar concentration systems that directly convert the solar energy into thermal or electrical energy [1]. Over the past two decades, various types of sun-tracking mechanisms have been proposed to enhance the solar energy harnessing performance of solar collectors. Although the degree of accuracy required depends on the specific characteristics of the solar concentrating system being analyzed, generally the higher the system concentration the higher the tracking accuracy that will be needed [2]. To achieve good tracking accuracy, sun-tracking systems normally employ sensors to feedback error signals to the control system in order to continuously receive maximum solar irradiation on the receiver. The two common types of sensors used for this purpose are closed-loop sensors and open-loop sensors.

Firstly, a closed-loop sensor, such as CCD camera or photo-detector, is used to sense the position of the solar image on the receiver and a feedback signal is sent to the controller if the solar image moves away from the receiver. Sun-tracking systems that employ closed-loop sensors are known as closed-loop sun trackers. Over the past 20 years or so, the closed-loop tracking approach has been traditionally used in the active sun-tracking scheme [3–6]. For example, Kribus *et al*. designed a closed-loop controller for heliostats which improved the pointing error of the solar image up to 0.1 mrad, with the aid of four CCD cameras set on the target [7]. However, this method is rather expensive and complicated because it requires four CCD cameras and four radiometers to be placed on the target. Then the solar images captured by CCD cameras must be analysed by a computer to generate the control correction feedback for correcting tracking errors. In 2006, a sun-tracking error monitoring system that uses a monolithic optoelectronic sensor for a concentrator photovoltaic system was presented by Luque-Heredia *et al*. According to the results from the case study, this monitoring system achieved a tracking accuracy of better than 0.1°. However, the criterion is that this tracking system requires full clear sky days to operate as the incidence light has to be above a certain threshold to ensure that the minimum required resolution is met [8]. That same year, Aiuchi *et al*. developed a heliostat with an equatorial mount and a closed-loop photo-sensor control system. The experimental results showed that the tracking error of the heliostat was estimated to be 2 mrad during fine weather [9]. Nevertheless, this tracking method is not popular and only can be used for sun-trackers with an equatorial mount configuration, which is not a common tracker mechanical structure and is complicated because the central of gravity for the solar collector is far off the pedestal. Furthermore, Chen *et al*. presented studies of digital and analogue sun sensors based on the optical vernier and optical nonlinear compensation measuring principle respectively. The proposed digital and analogue sun sensors have accuracies of 0.02° and 0.2° correspondingly for the entire field of view of ±64° and ±62° respectively [10,11]. The major disadvantage of these sensors is that the field of view, which is in the range of about ±64° for both elevation and azimuth directions, is rather small compared to the dynamic range of motion for a practical sun-tracker that is about ±70° and ±140° for elevation and azimuth directions, respectively. Besides that, it is just implemented at the testing stage in precise sun sensors to measure the position of the sun and has not yet been applied in any closed-loop sun-tracking system so far.

Although closed-loop sun-tracking system can produce a much better tracking accuracy, this type of system will lose its feedback signal when the sensor is shaded or when the sun is blocked by clouds. As an alternative method to overcome the limitation of closed loop sun-trackers, open-loop sun trackers were introduced by using open-loop sensors that do not require any solar image as feedback. The open-loop sensor will ensure that the solar collector is positioned at pre-calculated angles, which are obtained from a special formula or algorithm according to date, time and geographical information. In 2004, Abdallah *et al*. designed a two axes sun tracking system, which is operated by an open-loop control system. A programmable logic controller (PLC) was used to calculate the solar vector and to control the sun tracker so that it follows the sun's trajectory [12]. In addition, Shanmugam *et al.* presented a computer program written in *Visual Basic* that is capable of determining the sun's position and thus drive a paraboloidal dish concentrator (PDS) along the East-West axis or North-South axis for receiving maximum solar radiation [13].

In general, both sun-tracking approaches mentioned above have both strengths and drawbacks, so some hybrid sun-tracking systems have been developed to include both the open-loop and closed-loop sensors. Early in the 21st century, Nuwayhid *et al.* adopted both the open-loop and closed-loop tracking schemes into a parabolic concentrator attached to a polar tracking system. In the open-loop scheme, a computer acts as controller to calculate two rotational angles, i.e., solar declination and hour angles, as well as to drive the concentrator along the declination and polar axes. In the closed-loop scheme, nine light-dependent resistors (LDR) are arranged in an array of a circular-shaped "iris" to facilitate sun-tracking with a high degree of accuracy [14]. In 2006, Luque-Heredia *et al.* proposed a novel *PI* based hybrid sun-tracking algorithm for a concentrator photovoltaic system. In their design, the system can act in both open-loop and closed-loop mode. A mathematical model that involves a time and geographical coordinates function as well as a set of disturbances provides a feedforward open-loop estimation of the sun's position. To determine the sun's position with high precision, a feedback loop was introduced according to the error correction routine which is derived from the estimation of the error of the sun equations that are caused by external disturbances at the present stage based on its historical path [15]. One year later, Rubio *et al.* fabricated and evaluated a new control strategy for a photovoltaic (PV) solar tracker that operated in two tracking modes, i.e., normal tracking mode and search mode. The normal tracking mode combines an open-loop tracking mode that is based on solar movement models and a closed-loop tracking mode which corresponds to the electro-optical controller to obtain a sun-tracking error that is smaller than a specified boundary value and enough for solar radiation to produce electrical energy. Search mode will be started when the sun-tracking error is large or no electrical energy is produced. The solar tracker will move according to a square spiral pattern in the azimuth-elevation plane to sense the sun's position until the tracking error is small enough [16].

As a matter of fact, the tracking accuracy requirement is very much reliant on the design and application of the sun-tracker. In this case, the longer the distance between the solar concentrator and the receiver the higher the tracking accuracy required will be because the solar image becomes more sensitive to the movement of the solar concentrator. As a result, a heliostat or off-axis sun-tracker normally requires much higher tracking accuracy compared to that of on-axis sun-tracker due to the fact that the distance between the heliostat and the target is normally much longer, especially for a central receiver system configuration. In this context, a tracking accuracy in the range of a few miliradians (mrad) is in fact sufficient for an on-axis sun-tracker to maintain its good performance when highly concentrated sunlight is involved [17]. Despite having many existing on-axis sun-tracking methods, the designs available to achieve a good tracking accuracy of a few mrad are complicated and expensive. It is worthwhile to note that conventional on-axis sun-tracking systems normally adopt two common configurations, which are azimuth-elevation and tilt-roll (polar tracking), limited by the available basic mathematical formulas of sun-tracking system. For azimuth-elevation tracking system, the sun-tracking axes must be strictly aligned with both zenith and real north. For a tilt-roll tracking system, the sun-tracking axes must be strictly aligned with both latitude angle and real north. The major cause of sun-tracking errors is how well the aforementioned alignment can be done and any installation or fabrication defects will result in low tracking accuracy. According to our previous study for the azimuth-elevation tracking system, a misalignment of azimuth shaft relative to zenith axis of 0.4° can cause tracking error ranging from 6.45 to 6.52 mrad [18]. In practice, most solar power plants all over the world use a large solar collector area to save on manufacturing cost and this has indirectly made the alignment work of the sun-tracking axes much more difficult. In this case, the alignment of the tracking axes involves an extensive amount of heavy-duty mechanical and civil works due to the requirement for thick shafts to support the movement of a large solar collector, which normally has a total collection area in the range of several tens of square meters to nearly a hundred square meters. Under such tough conditions, a very precise alignment is really a great challenge to the manufacturer because a slight misalignment will result in significant sun-tracking errors. To overcome this problem, an unprecedented on-axis general sun-tracking formula has been proposed to allow the sun-tracker to track the sun in any two arbitrarily orientated tracking axes [18]. In this paper, we would like to introduce a novel sun-tracking system by integrating the general formula into the sun-tracking algorithm so that we can track the sun accurately and cost effectively, even if there is some misalignment from the ideal azimuth-elevation or tilt-roll configuration. In the new tracking system, any misalignment or defect can be rectified without the need for any drastic or labor intensive modifications to either the hardware or software components of the tracking system. In other words, even though the alignments of the azimuth-elevation axes with respect to the zenith-axis and real north are not properly done during the installation, the new sun-tracking algorithm can still accommodate the misalignment by changing the values of ϕ, λ and ζ in the tracking program. The advantage of the new tracking algorithm is that it can simplify the fabrication and installation work of solar collectors with higher tolerance in terms of the tracking axes alignment. This strategy has allowed great savings in terms of cost, time and effort by omitting more complicated solutions proposed by other researchers such as adding a closed-loop feedback controller or a flexible and complex mechanical structure to level out the sun-tracking error [1,19]. To demonstrate the use of general formula for improving sun-tracking accuracy, a prototype solar concentrator has been constructed and tested on the campus of Universiti Tunku Abdul Rahman (UTAR).

2. Methodology of Using General Formula to Improve Sun-Tracking Accuracy

The derivation of the general formula for an on-axis sun-tracking system has been presented in our previous paper [18]. According to the general formula, the sun-tracking accuracy of the system is highly reliant on the precision of the input parameters of the sun-tracking algorithm: latitude angle (Φ), hour angle (ω), declination angle (δ), as well as the three orientation angles of the tracking axes of solar concentrator, i.e., ϕ, λ and ζ. Among these values, local latitude, Φ, and longitude of the sun tracking system can be determined accurately with the latest technology such as a global positioning system (GPS). On the other hand, ω and δ are both local time dependent parameters (please refer to Appendix for the details). These variables can be computed accurately with the input from precise clock that is synchronized with the Internet time server. As for the three orientation angles ϕ, λ and ζ, their precision are very much reliant on the care paid during the on-site installation of solar collector, the alignment of tracking axes and the mechanical fabrication. The following mathematical derivation is attempted to obtain analytical solutions for the three orientation angles based on the daily sun-tracking error results induced by the misalignment of sun-tracking axes.

From our previous study [18], the unit vector of the sun, $[S']$, relative to the solar collector can be obtained from a multiplication of four successive coordinate transformation matrices, i.e., $[\Phi]$, $[\phi]$, $[\lambda]$ and $[\zeta]$ with the unit vector of the sun, $[S]$, relative to the earth and it is written as:

$$[S'] = [\zeta]\,[\lambda]\,[\phi]\,[\Phi]\,[S],$$

$$\begin{bmatrix} \sin\alpha \\ \cos\alpha\sin\beta \\ \cos\alpha\cos\beta \end{bmatrix} = \begin{bmatrix} \cos\zeta & 0 & \sin\zeta \\ 0 & 1 & 0 \\ -\sin\zeta & 0 & \cos\zeta \end{bmatrix} \times \begin{bmatrix} \cos\lambda & -\sin\lambda & 0 \\ \sin\lambda & \cos\lambda & 0 \\ 0 & 0 & 1 \end{bmatrix} \times \begin{bmatrix} 1 & 0 & 0 \\ 0 & \cos\phi & -\sin\phi \\ 0 & \sin\phi & \cos\phi \end{bmatrix} \times \begin{bmatrix} \cos\Phi & 0 & \sin\Phi \\ 0 & 1 & 0 \\ -\sin\Phi & 0 & \cos\Phi \end{bmatrix} \times \begin{bmatrix} \cos\delta\cos\omega \\ -\cos\delta\sin\omega \\ \sin\delta \end{bmatrix}, \tag{1}$$

where α is elevation angle, β is azimuth angle, ω is hour angle, δ is declination angle, Φ is latitude at which the solar collector is located as well as ϕ, λ and ζ are the three orientation angles of two-orthogonal-driving axes of the solar collector. From the Equation (1), let us multiply the first three transformation matrices $[\phi]$, $[\lambda]$ and $[\zeta]$, and then the last two matrices $[\Phi]$ with $[S]$ as to obtain the following result:

$$\begin{bmatrix} \sin\alpha \\ \cos\alpha\sin\beta \\ \cos\alpha\cos\beta \end{bmatrix} = \begin{bmatrix} \cos\zeta\cos\lambda & -\cos\zeta\sin\lambda\cos\phi + \sin\zeta\sin\phi & \cos\zeta\sin\lambda\sin\phi + \sin\zeta\cos\phi \\ \sin\lambda & \cos\lambda\cos\phi & -\cos\lambda\sin\phi \\ -\sin\zeta\cos\lambda & \sin\zeta\sin\lambda\cos\phi + \cos\zeta\sin\phi & -\sin\zeta\sin\lambda\sin\phi + \cos\zeta\cos\phi \end{bmatrix} \times \begin{bmatrix} \cos\Phi\cos\delta\cos\omega + \sin\Phi\sin\delta \\ -\cos\delta\sin\omega \\ -\sin\Phi\cos\delta\cos\omega + \cos\Phi\sin\delta \end{bmatrix}. \tag{2}$$

From Equation (2), we can further dissolve it into Equation (3):

$$\sin\alpha = (\cos\Phi\cos\delta\cos\omega + \sin\Phi\sin\delta)(\cos\zeta\cos\lambda) + (-\cos\delta\sin\omega)(-\cos\zeta\sin\lambda\cos\phi + \sin\zeta\sin\phi) + (-\sin\Phi\cos\delta\cos\omega + \cos\Phi\sin\delta)(\cos\zeta\sin\lambda\sin\phi + \sin\zeta\cos\phi) \tag{3a}$$

$$\cos\alpha\sin\beta = (\cos\Phi\cos\delta\cos\omega + \sin\Phi\sin\delta)(\sin\lambda) + (-\cos\delta\sin\omega)(\cos\lambda\cos\phi) + (-\sin\Phi\cos\delta\cos\omega + \cos\Phi\sin\delta)(-\cos\lambda\sin\phi) \tag{3b}$$

$$\cos\alpha\cos\beta = (\cos\Phi\cos\delta\cos\omega + \sin\Phi\sin\delta)(-\sin\zeta\cos\lambda) + (-\cos\delta\sin\omega)(\sin\zeta\sin\lambda\cos\phi + \cos\zeta\sin\phi) + (-\sin\Phi\cos\delta\cos\omega + \cos\Phi\sin\delta)(-\sin\zeta\sin\lambda\sin\phi + \cos\zeta\cos\phi) \tag{3c}$$

The time dependency of ω and δ can be found from Equation (3). Therefore, the instantaneous sun-tracking angles of the collector only vary with the angles ω and δ. Given three different local times LCT_1, LCT_2 and LCT_3 on the same day, the corresponding three hours angles ω_1, ω_2 and ω_3 as well as three declination angles δ_1, δ_2 and δ_3 can result in three elevation angles α_1, α_2 and α_3 and three azimuth angles β_1, β_2 and β_3 accordingly as expressed in Equation (3a)–(3c). Considering three different local times, we can actually rewrite each of the Equation (3a)–(3c) into three linear equations. By arranging the three linear equations in a matrix form, the Equation (3a)–(3c) can subsequently form the matrices (4a)–(4c):

$$\begin{bmatrix} \sin\alpha_1 \\ \sin\alpha_2 \\ \sin\alpha_3 \end{bmatrix} = \begin{bmatrix} \cos\Phi\cos\delta_1\cos\omega_1+\sin\Phi\sin\delta_1 & -\cos\delta_1\sin\omega_1 & -\sin\Phi\cos\delta_1\cos\omega_1+\cos\Phi\sin\delta_1 \\ \cos\Phi\cos\delta_2\cos\omega_2+\sin\Phi\sin\delta_2 & -\cos\delta_2\sin\omega_2 & -\sin\Phi\cos\delta_2\cos\omega_2+\cos\Phi\sin\delta_2 \\ \cos\Phi\cos\delta_3\cos\omega_3+\sin\Phi\sin\delta_3 & -\cos\delta_3\sin\omega_3 & -\sin\Phi\cos\delta_3\cos\omega_3+\cos\Phi\sin\delta_3 \end{bmatrix} \times \begin{bmatrix} \cos\zeta\cos\lambda \\ -\cos\zeta\sin\lambda\cos\phi+\sin\zeta\sin\phi \\ \cos\zeta\sin\lambda\sin\phi+\sin\zeta\cos\phi \end{bmatrix}. \tag{4a}$$

$$\begin{bmatrix} \cos\alpha_1\sin\beta_1 \\ \cos\alpha_2\sin\beta_2 \\ \cos\alpha_3\sin\beta_3 \end{bmatrix} = \begin{bmatrix} \cos\Phi\cos\delta_1\cos\omega_1+\sin\Phi\sin\delta_1 & -\cos\delta_1\sin\omega_1 & -\sin\Phi\cos\delta_1\cos\omega_1+\cos\Phi\sin\delta_1 \\ \cos\Phi\cos\delta_2\cos\omega_2+\sin\Phi\sin\delta_2 & -\cos\delta_2\sin\omega_2 & -\sin\Phi\cos\delta_2\cos\omega_2+\cos\Phi\sin\delta_2 \\ \cos\Phi\cos\delta_3\cos\omega_3+\sin\Phi\sin\delta_3 & -\cos\delta_3\sin\omega_3 & -\sin\Phi\cos\delta_3\cos\omega_3+\cos\Phi\sin\delta_3 \end{bmatrix} \times \begin{bmatrix} \sin\lambda \\ \cos\lambda\cos\phi \\ -\cos\lambda\sin\phi \end{bmatrix}. \tag{4b}$$

$$\begin{bmatrix} \cos\alpha_1\cos\beta_1 \\ \cos\alpha_2\cos\beta_2 \\ \cos\alpha_3\cos\beta_3 \end{bmatrix} = \begin{bmatrix} \cos\Phi\cos\delta_1\cos\omega_1+\sin\Phi\sin\delta_1 & -\cos\delta_1\sin\omega_1 & -\sin\Phi\cos\delta_1\cos\omega_1+\cos\Phi\sin\delta_1 \\ \cos\Phi\cos\delta_2\cos\omega_2+\sin\Phi\sin\delta_2 & -\cos\delta_2\sin\omega_2 & -\sin\Phi\cos\delta_2\cos\omega_2+\cos\Phi\sin\delta_2 \\ \cos\Phi\cos\delta_3\cos\omega_3+\sin\Phi\sin\delta_3 & -\cos\delta_3\sin\omega_3 & -\sin\Phi\cos\delta_3\cos\omega_3+\cos\Phi\sin\delta_3 \end{bmatrix} \times \begin{bmatrix} -\sin\zeta\cos\lambda \\ \sin\zeta\sin\lambda\cos\phi+\cos\zeta\sin\phi \\ -\sin\zeta\sin\lambda\sin\phi+\cos\zeta\cos\phi \end{bmatrix}. \tag{4c}$$

where the angles Φ, ϕ, λ and ζ are constants with respect to the local time.

In practice, we can measure the sun tracking angles, i.e., (α_1, α_2, α_3) and (β_1, β_2, β_3) during sun-tracking at three different local times via a recorded solar image of the target using a CCD camera. With the recorded data, we can compute the three arbitrary orientation angles ϕ, λ and ζ of the solar collector using the third-order determinants method to solve the three simultaneous equations as shown in Equation (4a)–(4c). From Equation (4b), the orientation angle λ can be determined as follows:

$$\lambda = \sin^{-1}\left(\frac{\begin{vmatrix} \cos\alpha_1\sin\beta_1 & -\cos\delta_1\sin\omega_1 & -\sin\Phi\cos\delta_1\cos\omega_1+\cos\Phi\sin\delta_1 \\ \cos\alpha_2\sin\beta_2 & -\cos\delta_2\sin\omega_2 & -\sin\Phi\cos\delta_2\cos\omega_2+\cos\Phi\sin\delta_2 \\ \cos\alpha_3\sin\beta_3 & -\cos\delta_3\sin\omega_3 & -\sin\Phi\cos\delta_3\cos\omega_3+\cos\Phi\sin\delta_3 \end{vmatrix}}{\begin{vmatrix} \cos\Phi\cos\delta_1\cos\omega_1+\sin\Phi\sin\delta_1 & -\cos\delta_1\sin\omega_1 & -\sin\Phi\cos\delta_1\cos\omega_1+\cos\Phi\sin\delta_1 \\ \cos\Phi\cos\delta_2\cos\omega_2+\sin\Phi\sin\delta_2 & -\cos\delta_2\sin\omega_2 & -\sin\Phi\cos\delta_2\cos\omega_2+\cos\Phi\sin\delta_2 \\ \cos\Phi\cos\delta_3\cos\omega_3+\sin\Phi\sin\delta_3 & -\cos\delta_3\sin\omega_3 & -\sin\Phi\cos\delta_3\cos\omega_3+\cos\Phi\sin\delta_3 \end{vmatrix}} \right) \tag{5a}$$

Similarly, the other two remaining orientation angles, ϕ and ζ can be resolved from Equation (4b) and Equation (4c) respectively as follows:

$$\phi = \sin^{-1}\left(\frac{\begin{vmatrix} \cos\Phi\cos\delta_1\cos\omega_1+\sin\Phi\sin\delta_1 & -\cos\delta_1\sin\omega_1 & \cos\alpha_1\sin\beta_1 \\ \cos\Phi\cos\delta_2\cos\omega_2+\sin\Phi\sin\delta_2 & -\cos\delta_2\sin\omega_2 & \cos\alpha_2\sin\beta_2 \\ \cos\Phi\cos\delta_3\cos\omega_3+\sin\Phi\sin\delta_3 & -\cos\delta_3\sin\omega_3 & \cos\alpha_3\sin\beta_3 \end{vmatrix}}{\begin{vmatrix} \cos\Phi\cos\delta_1\cos\omega_1+\sin\Phi\sin\delta_1 & -\cos\delta_1\sin\omega_1 & -\sin\Phi\cos\delta_1\cos\omega_1+\cos\Phi\sin\delta_1 \\ \cos\Phi\cos\delta_2\cos\omega_2+\sin\Phi\sin\delta_2 & -\cos\delta_2\sin\omega_2 & -\sin\Phi\cos\delta_2\cos\omega_2+\cos\Phi\sin\delta_2 \\ \cos\Phi\cos\delta_3\cos\omega_3+\sin\Phi\sin\delta_3 & -\cos\delta_3\sin\omega_3 & -\sin\Phi\cos\delta_3\cos\omega_3+\cos\Phi\sin\delta_3 \end{vmatrix}} \times \frac{1}{-\cos\lambda} \right) \tag{5b}$$

$$\zeta = -\sin^{-1}\left(\frac{\begin{vmatrix} \cos\alpha_1 \cos\beta_1 & -\cos\delta_1 \sin\omega_1 & -\sin\Phi\cos\delta_1\cos\omega_1 + \cos\Phi\sin\delta_1 \\ \cos\alpha_2 \cos\beta_2 & -\cos\delta_2 \sin\omega_2 & -\sin\Phi\cos\delta_2\cos\omega_2 + \cos\Phi\sin\delta_2 \\ \cos\alpha_3 \cos\beta_3 & -\cos\delta_3 \sin\omega_3 & -\sin\Phi\cos\delta_3\cos\omega_3 + \cos\Phi\sin\delta_3 \end{vmatrix}}{\begin{vmatrix} \cos\Phi\cos\delta_1\cos\omega_1 + \sin\Phi\sin\delta_1 & -\cos\delta_1 \sin\omega_1 & -\sin\Phi\cos\delta_1\cos\omega_1 + \cos\Phi\sin\delta_1 \\ \cos\Phi\cos\delta_2\cos\omega_2 + \sin\Phi\sin\delta_2 & -\cos\delta_2 \sin\omega_2 & -\sin\Phi\cos\delta_2\cos\omega_2 + \cos\Phi\sin\delta_2 \\ \cos\Phi\cos\delta_3\cos\omega_3 + \sin\Phi\sin\delta_3 & -\cos\delta_3 \sin\omega_3 & -\sin\Phi\cos\delta_3\cos\omega_3 + \cos\Phi\sin\delta_3 \end{vmatrix}} \times \frac{1}{\cos\lambda} \right) \quad (5c)$$

Figure 1 shows the flow chart of the computational program designed to solve the three unknown orientation angles of the solar collector: ϕ, λ and ζ using Equation (5a)–(5c). By providing the three sets of actual sun tracking angles, α and β, at different local times for a particular number of day as well as geographical information, i.e., longitude and latitude, the computational program can be executed to calculate the three unknown orientation angles.

Figure 1. The flow chart of the computational program to determine the three unknown orientation angles that cannot be precisely measured by tools in practice, i.e., ϕ, λ and ζ.

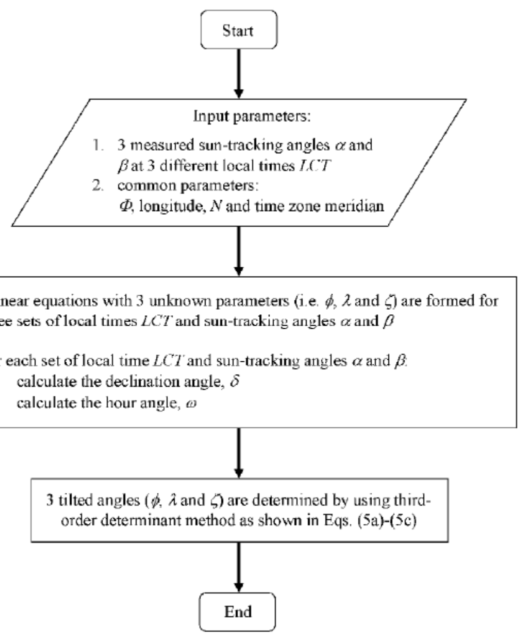

3. Open-Loop Sun-Tracking System Design

To test the aforementioned methodology, a prototype of an on-axis solar concentrator with a total reflective area of 25 m^2 has been constructed in the campus of UTAR, Kuala Lumpur (located at latitude 3.22° and longitude 101.73°; see Figure 2). The prototype consists of 120 sets of mirrors that are arranged into a hexagonal array and the target is placed at a focal point with the distance of 4.5 m from the centre of solar concentrator frame. This solar concentrator is designed to operate on the most common two-axis tracking system, which is the azimuth-elevation tracking system. The drive mechanism for the solar concentrator consists of stepper motors and associated gears. Two stepper motors, with 0.72 degree in full step, are coupled to the shafts, elevation and azimuth shafts, with a gear ratio of 4,400 yielding an overall resolution of 1.64×10^{-4}°/step.

Figure 2. A prototype of on-axis solar concentrator that has been constructed at Universiti Tunku Abdul Rahman (UTAR).

A Windows-based control program has been developed by integrating the general formula into the open-loop sun-tracking algorithm. In the control algorithm, the sun-tracking angles, i.e., azimuth (β) and elevation (α) angles, are first computed according to the latitude (Φ), longitude, day numbers (N), local time (LCT), and the three orientation angles ϕ, λ and ζ. The control program then generates digital pulses that are sent to the stepper motor to drive the concentrator to the pre-calculated angles along azimuth and elevation movements in sequence. Each time, the control program only activates one of the two stepper motors through a relay switch. The executed control program of sun-tracking system is shown in Figure 3.

Figure 3. A Windows-based control program that has been integrated with the on-axis general formula.

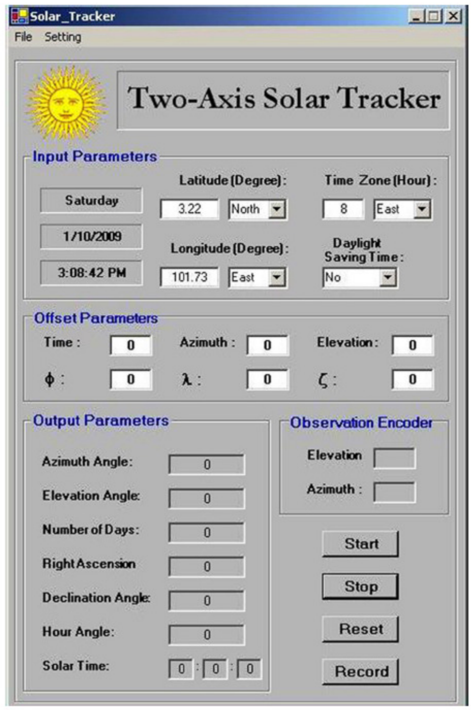

An open-loop control system is preferable for the prototype solar concentrator so as to keep the design of the sun-tracker simple and cost effective. In our design, open-loop sensors, 12-bit absolute optical encoders with a precision of 2,048 counts per revolution, are attached to the shafts along the azimuth and elevation axes of the concentrator to monitor the turning angles and to send feedback signals to the computer if there is any abrupt change in the encoder reading [see the inset of Figure 4(b)]. Therefore, the sensors not only ensure that the instantaneous azimuth and elevation angles are matched with the calculated values from the general formula, but also eliminate any tracking errors due to mechanical backlash, accumulated error, wind effects and other disturbances to the solar concentrator. With the optical encoders, any discrepancy between the calculated angles and real time angles of solar concentrator can be detected, whereby the drive mechanism will be activated to move the solar concentrator to the correct position. The block diagram and schematic diagram for the complete design of the open-loop control system of the prototype are shown in Figure 4 (a),(b), respectively.

Figure 4 (a). Block diagram to show the complete open-loop feedback system of the prototype solar concentrator. **(b).** Schematic diagram to show the detail of the open-loop sun-tracking system of the prototype solar concentrator where AA' is azimuth-axis and BB' is elevation-axis.

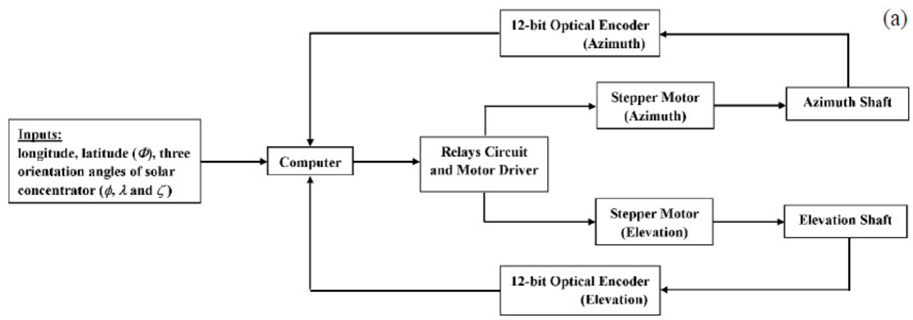

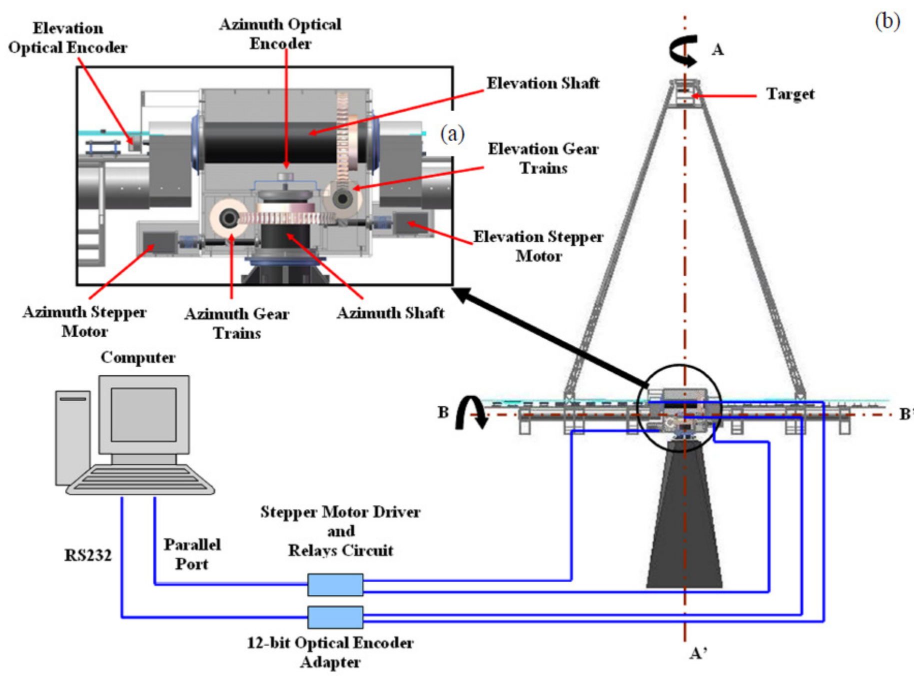

The estimated total electrical energy produced by the prototype solar concentrator and the total energy consumption of the sun-tracking system are also calculated. Taking into account the total mirror area of 25 m^2, optical efficiency of 85%, and the conversion efficiency from solar energy to electrical energy of 30% for direct solar irradiation of 800 W/m^2, we have obtained a generated output energy of 35.7 kW/h/day for seven hours of daily sunshine. Table 1 shows the energy consumption of 1.26 kW/h/day for the prototype includes the tracking motors, motor driver, encoders and computer. It corresponds to less than 3.5% of the rated generated output energy. Among all these components, the computer consumes the most power (more than 100 W) and in the future a microcontroller could be used to replace computer as to reduce the energy consumption.

Table 1. Specification and energy consumption of prototype sun-tracking system.

Total rotational angles of Elevation axis (degree/ day)	240
Total rotational angles of Azimuth axis (degree/ day)	540
Motor's rotational speed (rpm)	120
Gear ratio	1: 4,400
Solar concentrator's angular speed (degree per second)	0.16
Total time for Elevation axis rotation (hour/ day)	0.41
Total time for Azimuth axis rotation (hour/ day)	0.92
Total operating time:10am–5pm (hour/ day)	7
Elevation motor's power consumption (watt)	99
Azimuth motor's power consumption (watt)	66
Power consumption of computer, encoders & motor driver (watt)	165
Energy Consumption of the Elevation motor (kW-h/day)	0.04
Energy Consumption of the Azimuth motor (kW-h/day)	0.06
Energy Consumption of computer, encoder & driver (kW-h/day)	1.16
Total Energy Consumption of the motors (kW-h/day)	1.26

4. Performance Study and Experimental Results

Before the performance of the sun-tracking system was tested, 119 sets of mirrors were covered with black plastic, except the one mirror which is located nearest to the centre of the concentrator frame so that we can analyse the tracking accuracy by only observing the movement of one solar image at the target. To avoid the sun-tracking errors due to wrong estimation of the prototype's geographical location, a GPS was used to determine the latitude (Φ) and longitude of the solar concentrator. Initially, we assume that the alignment of solar concentrator is perfectly done relative to real north and zenith by setting the three orientation angles as $\phi = \lambda = \zeta = 0°$ in the control program. To study the performance of sun-tracking system on 13 January 2009, a CCD camera was employed to capture the solar image cast on the target for every 30 minutes from 10 am. to 5 pm. local time. A CCD camera with 640 × 480 pixels resolution was connected to a computer via a PCI video card to have a real time transmission and recording of solar image. Figure 5 illustrates some of the recorded solar images at different local times. According to the recorded results shown in Figure 6, the recorded tracking errors, ranging from 12.12 to 17.54 mrad throughout the day, have confirmed that the solar concentrator is misaligned relative to zenith and real north.

Figure 5. The recorded solar images on the target of prototype solar concentrator using a CCD camera from 10:07 am. to 4:25 pm. on 13 January 2009 with $\phi = \lambda = \zeta = 0°$.

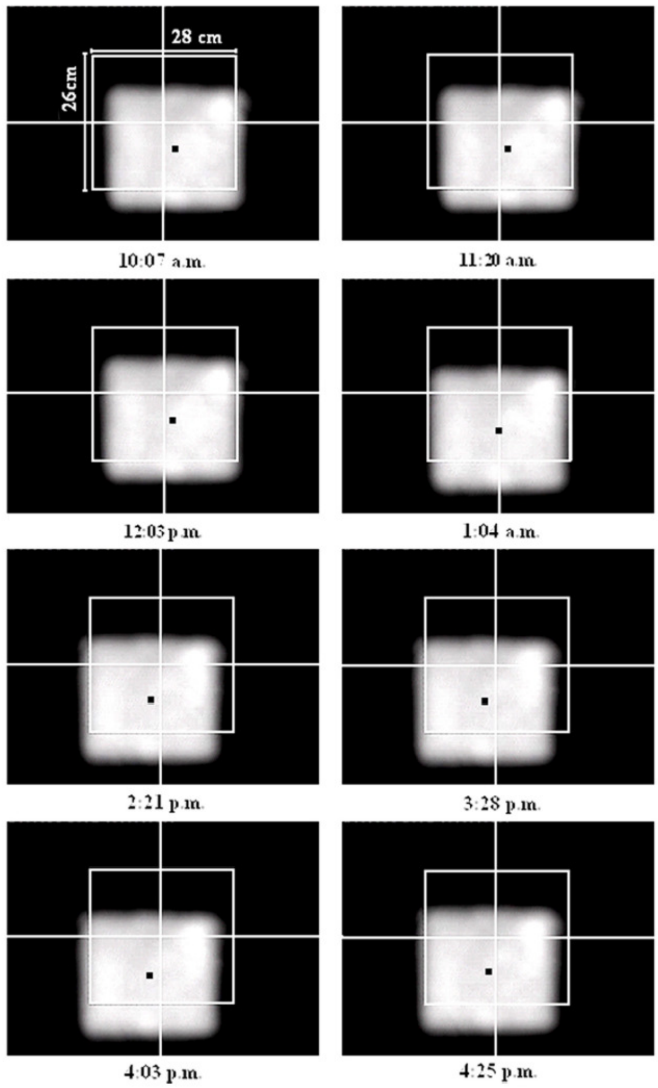

Figure 6. The plot of pointing error (mrad) versus local time (hours) for the parameters, i.e., $\phi = \lambda = \zeta = 0°$, on 13 January 2009.

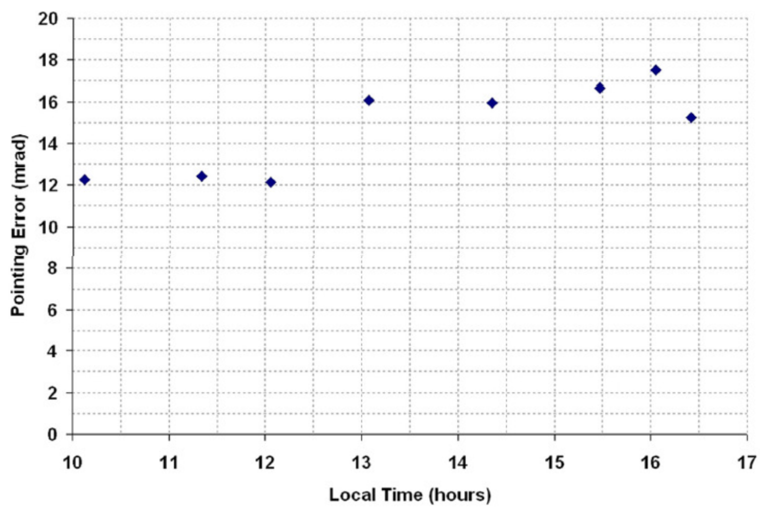

Figure 7. The plot of pointing error (mrad) versus local time (hours) for the parameters, i.e., $\phi = -0.1°$; $\lambda = 0°$; and $\zeta = -0.5°$, on 16 January 2009.

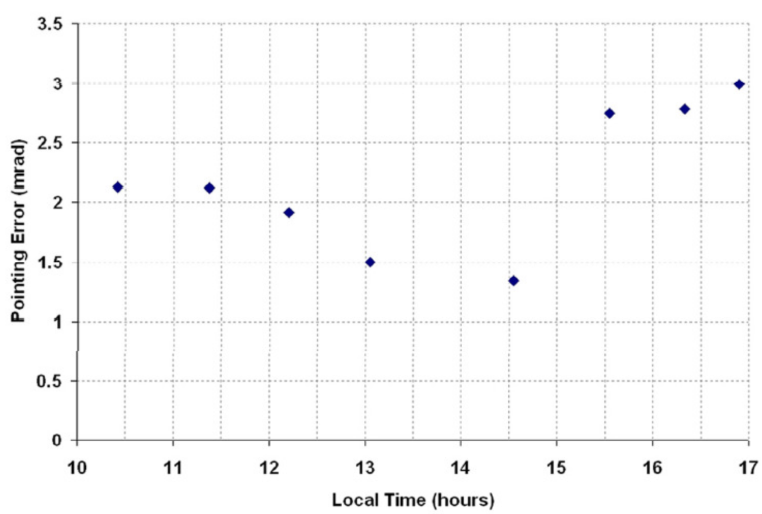

Figure 8. The recorded solar images on the target of prototype solar concentrator using a CCD camera from 10:25 am. to 4:54 pm. on 16 January 2009 with $\phi = -0.1°$; $\lambda = 0°$; and $\zeta = -0.5°$.

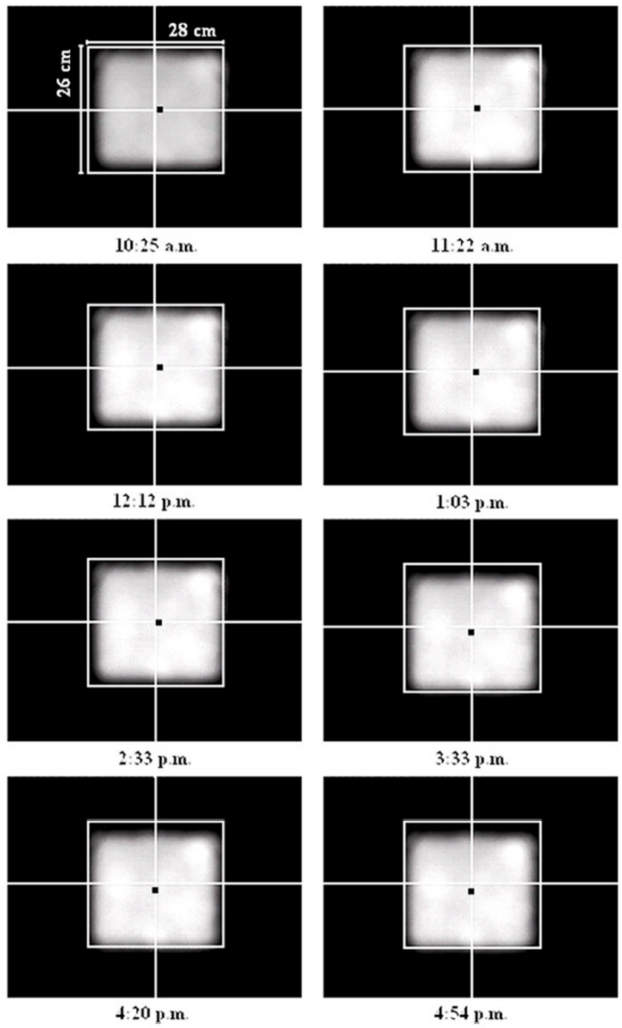

To rectify the problem of the sun-tracking errors due to imperfect alignment of the solar concentrator during the installation, we have to determine the three misaligned angles, i.e., ϕ, λ, ζ, and then insert these values into the edit boxes provided by the control program as shown in Figure 3. Thus, the computational program using the methodology as described in Figure 1 was executed to compute the three new orientation angles of the prototype based on the data captured on 13 January 2009. The actual sun-tracking angles, i.e., α and β, can be determined from the solar image position relative to the central point of the target. Three sets of sun-tracking angles at three different local times from the previous data were used as the input values to the computational program for simulating the three unknown parameters of ϕ, λ and ζ. The simulated results are $\phi = -0.1°$, $\lambda = 0°$, and $\zeta = -0.5°$. To substantiate the simulated results, these values were then used in the next session of sun-tracking that was performed on 16 January 2009 from 10 am. to 5 pm. With the new orientation angles, the performance of the prototype in sun-tracking has been successfully improved to the accuracy of 2.99 mrad, as shown in Figure 7. This result has reached the limit of sun-tracking accuracy due to the resolution of the optical encoder which corresponds to 4.13 mrad, unless higher resolution optical encoders are used as sensors. Figure 8 shows the recorded solar images at the target for different local times ranging from 10 am. to 5 pm. on 16 January 2009. In the experimental results, even though the misalignment on the azimuth axis is in the range of 0.5°, the resulted sun-tracking error is significant, especially for the application in high concentration solar collectors and in particular for dense array concentrator photovoltaic systems [17]. Since then, the prototype has been tested by running it for a period of more than six months to confirm the validation of the sun-tracking results.

5. Conclusions

With the simulated parameter $\phi = -0.1°$; $\lambda = 0°$; and $\zeta = -0.5°$, the performance of a prototype in sun-tracking has been improved to a maximum pointing error of 2.99 mrad, which falls below the encoder resolution, 4.13 mrad. As a result, the general sun-tracking formula is confirmed to be capable of rectifying the installation error of the solar concentrator with a significant improvement in the tracking accuracy. In fact, there are many solutions of improving the tracking accuracy such as adding a closed-loop feedback system to the controller [1], designing a flexible mechanical platform capable of two-degree-of-freedom for fine adjustment of azimuth shaft [19], etc. Nevertheless, all these solutions require a more complicated sun tracker engineering designs, which also make the whole system more costly. Instead of using a complicated sun-tracking method, integration of an on-axis general sun-tracking formula into the open-loop sun-tracking system is a clever method of obtaining a reasonably high precision in sun-tracking with a simple and cost effective design. This approach can significantly improve the performance and reduce the cost of solar energy collectors, especially for high concentration systems.

Acknowledgements

The authors would like to express their gratitude to Malaysia Energy Centre, Ministry of Energy, Green Technology & Water (AAIBE Trust Fund) and Ministry of Science, Technology & Innovation (e-Science Fund) for the financial support.

Appendix

Formula for declination angle:

$$\sin \delta = 0.39795 \cos [0.98563(N - 173)]$$

where N is day number and calendar dates are expressed as the $N = 1$, starting with January 1. Thus March 22 would be $N = 31 + 28 + 22 = 81$ and December 31 means $N = 365$.

The hour angle expresses the time of day with respect to the solar noon: It is the angle between the plane of the meridian containing observer and meridian that touches the earth-sun line. It is zero at solar noon and increases by 15° every hour:

$$\omega = 15\ (t_s - 12)\ \text{(degree)}$$

where t_s is the solar time in hours. A solar time is a 24-hour clock with 12:00 as the exact time when the sun is at the highest point in the sky. The concept of solar time is to predict the direction of the sun's ray relative to a point on the earth. Solar time is location or longitudinal dependent. It is generally different from local clock time (*LCT*) (defined by politically time zones)

The conversion between solar time and local clock time requires knowledge of the location, the day of the year, and the standards to which local clocks are set. The conversion between solar time t_s and local clock time (*LCT*) (in 24-hour rather than AM/PM format) takes the form:

$$t_s = LCT + EOT/60 - LC - D \qquad \text{(hours)}$$

where *EOT* is the equation of time in minutes, *LC* is a longitude correction, and *D* is daylight saving time. Daylight saving time was initiated in the spring of 1918 to "save fuel and promote other economies in a country at war" [20]. According to this concept, the standard time is advanced by 1 hour, usually from 2:00 am. on the last Sunday in April until 2:00 am. on the last Sunday in October.

The difference between mean time and solar time is called the equation of time (*EOT*). An approximation for the equation of time in minutes is given by Woolf (1968) is accurate to within about 30 seconds during daylight hours:

$$EOT = 0.258\cos x - 7.416\sin x - 3.648\cos 2x - 9.228\sin 2x\ \text{(minutes)}$$

where the angle x is a function of the day number N,

$$x = 360(N - 1)/365.242 \quad \text{(degrees)}$$

For example, on February 11, 1981 the day number $N = 42$, $x = 40.41$ degrees and $EOT = -14.35$ minutes. Formula for longitudinal correction:

$$LC = (\text{local longitude} - \text{longitude of standard time zone meridian})/15\ \text{(hours)}$$

References

1. Luque-Heredia, I.; Moreno, J.M.; Magalhaes, P.H.; Cervantes, R.; Quemere, G.; Laurent, O. Inspira's CPV sun tracking. In *Concentrator Photovoltaics*; Luque, A.L., Andreev, V.M., Eds.; Springer: Berlin, Heidelberg, Germany, 2007; Chapter 11, pp. 221–251.
2. Blanco-Muriel, M.; Alarcon-Padilla, D.C.; Lopez-Moratalla, T.; Lara-Coira, M. Computing the solar vector. *Sol. Energy* **2001**, *70*, 431–441.
3. Kalogirou, S.A. Design and construction of a one-axis sun-tracking system. *Sol. Energy* **1996**, *57*, 465–469.
4. Berenguel, M.; Rubio, F.R.; Valverde, A.; Lara, P.J.; Arahal, M.R.; Camacho, E.F.; Lopez, M. An artificial vision-based control system for automatic heliostat positioning offset correction in a central receiver solar power plant. *Sol. Energy* **2004**, *76*, 563–575.

5. Lee, C.D.; Yeh, H.Y.; Chen, M.H.; Sue, X.L.; Tzeng, Y.C. HCPV sun tracking study at INER. In *Proceedings of the IEEE 4th World Conference on Photovoltaic Energy Conversion*, Waikoloa Village, HI, USA, May 7–12, 2006.
6. Arbab, H.; Jazi, B; Rezagholizadeh, M. A computer tracking system of solar dish with two-axis degree freedoms based on picture processing of bar shadow. *Renew. Energy* **2009**, *34*, 1114–1118.
7. Kribus, A.; Vishnevetsky, I.; Yogev, A.; Rubinov, T. Closed loop control of heliostats. *Energy* **2004**, *29*, 905–913.
8. Luque-Heredia, I.; Cervantes, R.; Quéméré, G. A sun tracking error monitor for photovoltaic concentrators. In *Proceedings of the IEEE 4th World Conference on Photovoltaic Energy Conversion*, Waikoloa Village, HI, USA, May 7–12, 2006.
9. Aiuchi, K.; Yoshida, K.; Onozaki, M.; Katayama, Y.; Nakamura, M.; Nakamura, K. Sensor-controlled heliostat with an equatorial mount. *Sol. Energy* **2006**, *80*, 1089–1097.
10. Chen, F.; Feng, J.; Hong, Z. Digital sun sensor based on the optical vernier measuring principle. *Meas. Sci. Technol.* **2006**, *17*, 2494–2498.
11. Chen, F.; Feng, J. Analogue sun sensor based on the optical nonlinear compensation measuring principle. *Meas. Sci. Technol.* **2007**, *18*, 2111–2115.
12. Abdallah, S.; Nijmeh, S. Two axes sun tracking system with PLC control. *Energy Conver. Manage.* **2004**, *45*, 1931–1939.
13. Shanmugam, S.; Christraj, W. The tracking of the sun for solar paraboloidal dish concentrators. *J. Sol. Energy Eng.* **2005**, *127*, 156–160.
14. Nuwayhid, R.Y.; Mrad, F.; Abu-Said, R. The realization of a simple solar tracking concentrator for the university research applications. *Renew. Energy* **2001**, *24*, 207–222.
15. Luque-Heredia, I.; Gordillo, F.; Rodriguez, F. A *PI* based hybrid sun tracking algorithm for photovoltaic concentration. In *Proceedings of the IEEE 19th European Photovoltaic Energy Conversion*, Paris, France, June 7–14, 2004.
16. Rubio, F.R.; Ortega, M.G.; Gordillo, F.; Lopez-Martinez, M. Application of new control strategy for sun tracking. *Energy Conver. Manage.* **2007**, *48*, 2174–2184.
17. Chong, K.K.; Wong, C.W.; Siaw, F.L.; Yew, T.K. Optical characterization of non-imaging planar concentrator for the application in concentrator photovoltaic system. *J. Sol. Energy Eng.* **2009** (accepted for publication).
18. Chong, K.K.; Wong, C.W. General Formula for on-axis sun-tracking system and its application in improving tracking accuracy of solar collector. *Sol. Energy* **2009**, *83*, 298–305.
19. Chen, Y.T.; Chong, K.K.; Bligh, T.P.; Chen, L.C.; Yunus, J.; Kannan, K.S.; Lim, B.S.; Lim, C.S.; Alias, M.A.; Bidin, N.; Aliman, O.; Salehan, S.; Rezan, S.A.H.; Tam, C.M.; Tan, K.K. Non-imaging, focusing heliostat. *Sol. Energy* **2001**, *71*, 155–164.
20. Jesperson, J.; Fitz-Randolph, J. National Bureau of Standards Monograph. In *From sundials to atomic clocks*; 2nd ed.; Harcourts Brace & Company: New York, NY, USA, 1977.

APPENDIX C

ON-AXIS GENERAL SUN-TRACKING FORMULA AND ITS APPLICATION IN IMPROVING SUN-TRACKING ACCURACY OF A 25 kW_{th} NON-IMAGING PLANAR CONCENTRATOR PROTOTYPE

Kok-Keong Chong*, Chee-Woon Wong, Fei-Lu Siaw, Tiong-Keat Yew, Yee-How Chong
Faculty of Engineering and Science, Universiti Tunku Abdul Rahman
Off Jalan Genting Kelang, Setapak, 53300 Kuala Lumpur, Malaysia.
*Corresponding Author. Tel.: (603)-41079802, Fax: (603)-41079803,
E-mail address: chongkk@utar.edu.my, kokkeong_c@yahoo.com

ABSTRACT: A novel on-axis general sun-tracking formula has been integrated in the algorithm of open-loop sun-tracking system in order to track the sun accurately and cost effectively. A $25kW_{th}$ Non-Imaging Planar Concentrator prototype has been constructed in the campus of Tunku Abdul Rahman University, Malaysia. The imperfections in the alignment of azimuth axis relative to the zenith-axis during construction work of the prototype have resulted in significant sun-tracking errors which ranges from 12.12 to 17.54 mrad. Analytical equations based on the general sun-tracking formula and the previous tracking results have been derived and formulated to calculate three misaligned angles. By solving the analytical equations and applying the solutions into the tracking program, the performance of the prototype in sun-tracking has been successfully improved to the daily pointing error below 2.99 mrad. It has reached the accuracy limit due to the optical encoder resolution that corresponds to 4.13 mrad. Hence, the general sun-tracking formula has been demonstrated to be capable of improving sun-tracking accuracy while allowing reduced cost and effort by omitting complicated sun-tracking solutions such as additional closed-loop sensor and complicated alignment work.

Keywords: general sun-tracking formula, sun-tracking accuracy, solar concentrator

1 INTRODUCTION

High concentration solar power system, such as central receiver system, parabolic trough and parabolic dish etc, are the common in the applications of harnessing solar energy. To efficiently collect solar irradiance in high concentration solar power systems, high degree of sun-tracking accuracy is needed to synchronize the movement of solar concentrator with the sun's position. Over the past two decades, various strategies have been proposed and they can be basically classified into the following two categories, i.e. open-loop system and closed-loop system [1].

In the open-loop system, sun-tracking of the solar collector is under computer control. A computer will drive the solar collector to follow the sun path according to pre-calculated sun angles, which are obtained from a special formula or algorithm. In 2005, Shanmugam *et al.* presented a computer program written in *Visual Basic* which is able to determine the sun's trajectory and thus drive a paraboloidal dish concentrator (PDS) along the East-West axis or North-South axis for enhancing the solar energy harnessing performance of solar collector [2]. This type of system is highly reliable as long as the mechanical structure is precisely made. On the contrary, for the closed-loop system, sun-tracking is achieved by rotating the solar collector in accordance with a feedback signal from a variety of sensor devices, such as CCD camera or photo-detector. The closed-loop system has been used in the sun-tracking scheme over the past 20 years [3-6]. For example, Berenguel *et al.* designed an automatic offset correction system closed-loop controller for a heliostat field of a solar tower plant [7]. Black and white (B/W) CCD camera was used to correct the sun-tracking error in an automatic way using the basic threshold-based image processing techniques. This method is costly and complex because it requires a CCD camera to capture the solar image. In, addition, the solar images must be analyzed by a computer to make the control correction feedback for improving the tracking accuracy. In 2006, a sun-tracking system that uses four photo detectors and a DNI detector for a high concentration photovoltaic (HCPV) power generation system was presented by Lee *et al.* [8]. The fine tuning and precision of this sun-tracking system only can be effective in full clear sky days.

In order to avoid the aforementioned complicated and expensive sun-tracking systems, we have integrated a novel on-axis general sun-tracking formula into the sun-tracking control system [9]. The general formula is capable of diminishing any sun-tracking errors that majorly caused by the misalignment of the tracking axes of the solar collector during installation by changing the values of three misaligned angles, i.e. ϕ, λ and ζ. Without adding a closed-loop feedback controller or a flexible and complex mechanical structure, this strategy has allowed the on-axis sun-tracking systems to track the sun accurately and cost effectively. A prototype of solar concentrator has been constructed and tested in the campus of Universiti Tunku Abdul Rahman (UTAR), Kuala Lumpur, Malaysia for demonstrating the integration of general formula into the open-loop control of sun-tracking system to obtain high degree of sun-tracking accuracy cost effectively.

2 DESIGN AND CONSTRUCTION OF PROTOTYPE

A Non-Imaging Planar Concentrator (NIPC) is an on-axis solar concentrator that employs many mirrors with adjustable focal distance to focus the sunlight onto the target [10]. The prototype of NIPC for concentrating sunlight to about 400 suns has been constructed at UTAR (located at latitude 3.22° and longitude 101.73°). The prototype of NIPC consists of 120 sets of mirrors that are arranged into a hexagonal array to form a total reflective area of around 25 m^2 [11]. Each set of mirror is mounted on a specially designed unit frame so that it is expedient for the optical alignment.

The prototype concentrator operates on a conventional method of two-axis sun-tracking system, which is azimuth-elevation. The sun-tracking axes of the azimuth-elevation tracking system must be strictly aligned with both zenith and real north. In order to avoid the complicated alignment work, we have integrated the newly derived general sun-tracking formulas as showed below into the control system to predict the sun's movement and to drive the concentrator towards the sun [9].

$$\alpha = \arcsin\begin{bmatrix} \cos\delta\cos\omega(\cos\zeta\cos\lambda\cos\Phi - \cos\zeta\sin\lambda\sin\phi\sin\Phi - \sin\zeta\cos\phi\sin\Phi) \\ -\cos\delta\sin\omega(\sin\zeta\sin\phi - \cos\zeta\sin\lambda\cos\phi) \\ +\sin\delta(\cos\zeta\cos\lambda\sin\Phi + \cos\zeta\sin\lambda\sin\phi\cos\Phi + \sin\zeta\cos\phi\cos\Phi) \end{bmatrix}$$

when $\cos\beta \geq 0$

$$\beta = \arcsin\left[\frac{\cos\delta\cos\omega(\sin\lambda\cos\Phi + \cos\lambda\sin\phi\sin\Phi) - \cos\delta\sin\omega\cos\lambda\cos\phi + \sin\delta(\sin\lambda\sin\Phi - \cos\lambda\sin\phi\cos\Phi)}{\cos\alpha}\right]$$

when $\cos\beta < 0$

$$\beta = \pi - \arcsin\left[\frac{\cos\delta\cos\omega(\sin\lambda\cos\Phi + \cos\lambda\sin\phi\sin\Phi) - \cos\delta\sin\omega\cos\lambda\cos\phi + \sin\delta(\sin\lambda\sin\Phi - \cos\lambda\sin\phi\cos\Phi)}{\cos\alpha}\right]$$

where

$$\cos\beta = \frac{\begin{bmatrix} \cos\delta\cos\omega(-\sin\zeta\cos\lambda\cos\Phi + \sin\zeta\sin\lambda\sin\phi\sin\Phi - \cos\zeta\cos\phi\sin\Phi) \\ -\cos\delta\sin\omega(\sin\zeta\sin\lambda\cos\phi + \cos\zeta\sin\phi) \\ +\sin\delta(-\sin\zeta\cos\lambda\sin\Phi - \sin\zeta\sin\lambda\sin\phi\cos\Phi + \cos\zeta\cos\phi\cos\Phi) \end{bmatrix}}{\cos\alpha};$$

where α is the elevation angle, β is the azimuth angle, δ is the declination angle; ω is the hours angle, Φ is the latitude angle as well as the three orientation angles of the tracking axes of solar concentrator, i.e. ϕ, λ, ζ.

The newly derived on-axis tracking formula can accommodate the alignment defect of azimuth-axis of the sun-tracker, which cannot be fully removed during the installation work. For this purpose, a tracking program is created using *Visual Basic.net* to include the general formula for correcting any possible misalignment of azimuth-axis relative to zenith. The tracking program is named as Solar_Tracker and it is run on Windows-based Operating System [11]. The program allows us to set latitude (Φ), longitude, time zone meridian and three deviation angles for the misalignment of azimuth-axis (ϕ, λ and ζ). Based on the settings, the program calculate the elevation and azimuth angles and send the pulsing signal to the driving system to move the concentrator along the azimuth (AA') and elevation (BB') axes. The movement of the whole system is directed by a driving system that comprises of stepper motors and their associated gears connected to elevation and azimuth shafts. Two 12-bit absolute optical encoders fixed at the shafts are used to send feedback signals for the azimuth and elevation angles to eliminate tracking errors resulted from mechanical backlash, wind effect or any other external disturbances exerted at the concentrator frame. The schematic diagram for the control system of the prototype is shown in Fig. 1.

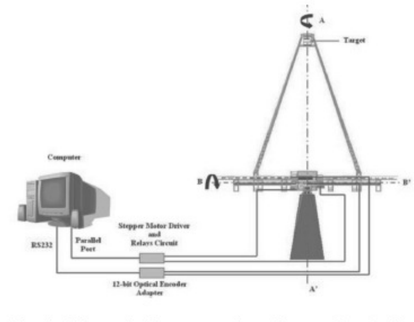

Fig. 1: Schematic diagram to show the complete design of the open-loop control system of the prototype.

3 METHODOLOGY

Referring to the on-axis general sun-tracking formula, the precision of the input parameters (latitude angle (Φ), hour angle (ω), declination angle (δ), as well as the three orientation angles of the tracking axes of solar concentrator, i.e. ϕ, λ and ζ) of the sun-tracking algorithm are the major considerations to achieve high degree of sun-tracking accuracy. The following steps attempt to show the methods in acquiring accurate input parameters of the program.

Step 1: The solar concentrator's geographical location (latitude angle (Φ) and longitude angle) can be determined accurately with global positioning system (GPS).

Step 2: ω and δ are both local time dependent parameters. The local time can be verified precisely by synchronizing the computer system clock with the internet time server.
where
$\delta = \sin^{-1}\{0.39795\cos[0.98563(N - 173)]\}$;
$\omega = 15\,(t_s - 12)$;
N is number of day and t_s is the solar time in hours.

Step 3: The three orientation angles, i.e. ϕ, λ and ζ, can be determined by the derived analytical based on the first attempted tracking error result equations [11]:

$$\lambda = \sin^{-1}\left(\frac{\begin{vmatrix} \cos\alpha_1\sin\beta_1 & -\cos\delta_1\sin\omega_1 & -\sin\Phi\cos\delta_1\cos\omega_1 + \cos\Phi\sin\delta_1 \\ \cos\alpha_2\sin\beta_2 & -\cos\delta_2\sin\omega_2 & -\sin\Phi\cos\delta_2\cos\omega_2 + \cos\Phi\sin\delta_2 \\ \cos\alpha_3\sin\beta_3 & -\cos\delta_3\sin\omega_3 & -\sin\Phi\cos\delta_3\cos\omega_3 + \cos\Phi\sin\delta_3 \end{vmatrix}}{\begin{vmatrix} \cos\Phi\cos\delta_1\cos\omega_1 + \sin\Phi\sin\delta_1 & -\cos\delta_1\sin\omega_1 & -\sin\Phi\cos\delta_1\cos\omega_1 + \cos\Phi\sin\delta_1 \\ \cos\Phi\cos\delta_2\cos\omega_2 + \sin\Phi\sin\delta_2 & -\cos\delta_2\sin\omega_2 & -\sin\Phi\cos\delta_2\cos\omega_2 + \cos\Phi\sin\delta_2 \\ \cos\Phi\cos\delta_3\cos\omega_3 + \sin\Phi\sin\delta_3 & -\cos\delta_3\sin\omega_3 & -\sin\Phi\cos\delta_3\cos\omega_3 + \cos\Phi\sin\delta_3 \end{vmatrix}}\right)$$

$$\phi = \sin^{-1}\left(\frac{\begin{vmatrix} \cos\Phi\cos\delta_1\cos\omega_1 + \sin\Phi\sin\delta_1 & -\cos\delta_1\sin\omega_1 & \cos\alpha_1\sin\beta_1 \\ \cos\Phi\cos\delta_2\cos\omega_2 + \sin\Phi\sin\delta_2 & -\cos\delta_2\sin\omega_2 & \cos\alpha_2\sin\beta_2 \\ \cos\Phi\cos\delta_3\cos\omega_3 + \sin\Phi\sin\delta_3 & -\cos\delta_3\sin\omega_3 & \cos\alpha_3\sin\beta_3 \end{vmatrix}}{\begin{vmatrix} \cos\Phi\cos\delta_1\cos\omega_1 + \sin\Phi\sin\delta_1 & -\cos\delta_1\sin\omega_1 & -\sin\Phi\cos\delta_1\cos\omega_1 + \cos\Phi\sin\delta_1 \\ \cos\Phi\cos\delta_2\cos\omega_2 + \sin\Phi\sin\delta_2 & -\cos\delta_2\sin\omega_2 & -\sin\Phi\cos\delta_2\cos\omega_2 + \cos\Phi\sin\delta_2 \\ \cos\Phi\cos\delta_3\cos\omega_3 + \sin\Phi\sin\delta_3 & -\cos\delta_3\sin\omega_3 & -\sin\Phi\cos\delta_3\cos\omega_3 + \cos\Phi\sin\delta_3 \end{vmatrix}} \times \frac{1}{-\cos\lambda}\right)$$

$$\zeta = -\sin^{-1}\left(\frac{\begin{vmatrix} \cos\alpha_1\cos\beta_1 & -\cos\delta_1\sin\omega_1 & -\sin\Phi\cos\delta_1\cos\omega_1 + \cos\Phi\sin\delta_1 \\ \cos\alpha_2\cos\beta_2 & -\cos\delta_2\sin\omega_2 & -\sin\Phi\cos\delta_2\cos\omega_2 + \cos\Phi\sin\delta_2 \\ \cos\alpha_3\cos\beta_3 & -\cos\delta_3\sin\omega_3 & -\sin\Phi\cos\delta_3\cos\omega_3 + \cos\Phi\sin\delta_3 \end{vmatrix}}{\begin{vmatrix} \cos\Phi\cos\delta_1\cos\omega_1 + \sin\Phi\sin\delta_1 & -\cos\delta_1\sin\omega_1 & -\sin\Phi\cos\delta_1\cos\omega_1 + \cos\Phi\sin\delta_1 \\ \cos\Phi\cos\delta_2\cos\omega_2 + \sin\Phi\sin\delta_2 & -\cos\delta_2\sin\omega_2 & -\sin\Phi\cos\delta_2\cos\omega_2 + \cos\Phi\sin\delta_2 \\ \cos\Phi\cos\delta_3\cos\omega_3 + \sin\Phi\sin\delta_3 & -\cos\delta_3\sin\omega_3 & -\sin\Phi\cos\delta_3\cos\omega_3 + \cos\Phi\sin\delta_3 \end{vmatrix}} \times \frac{1}{\cos\lambda}\right)$$

where ω_1, ω_2 and ω_3 are the hours angles; δ_1, δ_2 and δ_3 are the declination angles; α_1, α_2 and α_3 are the elevation angles as well as β_1, β_2 and β_3 are the azimuth angles at three different local times respectively.

In practice, a CCD camera is used to capture the solar image cast on the target every 30 minutes during sun-tracking. The recorded solar images are used to determine the sun-tracking angles i.e. (α_1, α_2, α_3) and (β_1, β_2, β_3) at three different local times. According to the previous derived analytical formula, a special computational program has been designed to calculate the three arbitrary orientation angles (ϕ, λ and ζ) of the solar concentrator.

4 IMPLEMENTATION AND EXPERIMENTAL RESULTS

By setting the parameters $\phi = \lambda = \zeta = 0°$ in the sun-tracking program, the imperfections in the alignment of azimuth axis relative to the zenith-axis have resulted in significant sun-tracking errors. Fig. 2 shows the sun-tracking result recorded by CCD camera from 10 a.m. to 5 p.m. on 13 January 2009 and the sun-tracking error ranges from 12.12 to 17.54 mrad.

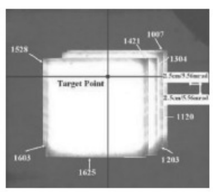

Fig. 2: The sun-tracking result from 10.07 a.m. to 4.25 p.m. on 13 January 2009 ($\phi = \lambda = \zeta = 0°$).

With the initial collected data in the previous tracking, three parameters of misalignment, i.e. ϕ, λ and ζ have been computed using the aforementioned analytical equations and any three recorded data at three different local times. The solutions of the above calculation ($\phi = -0.1°$, $\lambda = 0°$, and $\zeta = -0.5°$) are then applied into the sun-tracking program and the performance of prototype in sun-tracking has been successfully improved to a daily pointing error of below 2.99 mrad from 10 a.m. to 5 p.m. on 16 January 2009 as shown in Fig. 3. It has reached the accuracy limit of the prototype as the optical encoder resolution that corresponds to 4.13 mrad.

5 CONCLUSION

According to the experimental results, the integration of newly derived general sun-tracking formula into the open-loop control system of the prototype has demonstrated a good sun-tracking accuracy even if there is installation error of the solar concentrator. This approach is cost effective because it can work well with only a simple open-loop system without the need of any complicated closed-loop sensor or mechanical alignment system.

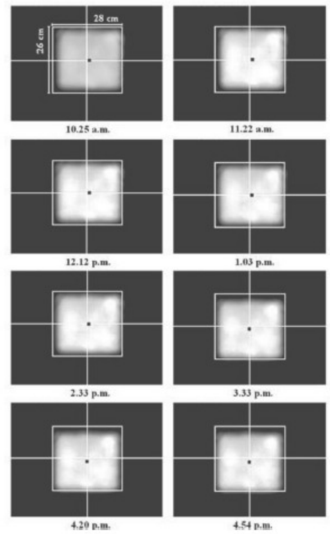

Fig. 3: The graph of sun-tracking pointing error (mrad) versus local time (hours) for the parameters, i.e. $\phi = -0.1°$; $\lambda = 0°$; and $\zeta = -0.5°$, from 10 a.m. to 5 p.m. on 16 January 2009.

ACKNOLEDGEMENT

The authors would like to express their gratitude to Malaysia Energy Centre, Ministry of Energy, Green Technology & Water (AAIBE Trust Fund) and Ministry of Science, Technology & Innovation (e-Science Fund) for the financial support.

REFERENCES

[1] C.Y. Lee, P.C. Chou, C.M. Chiang, C.F. Lin, Sensors 9 (2009) 3875.
[2] S. Shanmugam, W. Christraj, Journal of Solar Energy Engeneering 127 (2005) 156.
[3] F. Chen, J. Feng, Z. Hong, Measurement Science and Technology 17 (2006) 2494.
[4] F. Chen, J. Feng, Measurement Science and Technology 18 (2007) 2111.
[5] S.A. Kalogirou, Solar Energy 57 (1996) 465.
[6] A. Kribus, I. Vishnevetsky, A. Yogev, T. Rubinov, Energy 29 (2004) 905.
[7] M. Berenguel, F.R. Rubio, A. Valverde, P.J. Lara, M.R. Arahal, E.F. Camacho, M. Lopez, Solar Energy 76 (2004) 563.
[8] C.D. Lee, H.Y. Yeh, M.H. Chen, X.L. Sue, Y.C. Tzeng, Proceedings of the IEEE 4th World Conference on Photovoltaic Energy Conversion, (2006) 718.
[9] K.K. Chong, C.W. Wong, Solar Energy 83 (2009) 298.

[10] K.K. Chong, F.L. Siaw, C.W. Wong, G.S. Wong, Renewable Energy 34 (2009) 1364.
[11] Kok-Keong Chong et al., Sensors 9 (2009) (accepted for publication).

APPENDIX D

K. K. Chong[1]
e-mail: chongkk@utar.edu.my
e-mail: kokkeong_c@yahoo.com

C. W. Wong

F. L. Siaw

T. K. Yew

Faculty of Engineering and Science,
Universiti Tunku Abdul Rahman,
Off Jalan Genting Kelang, Setapak,
Kuala Lumpur 53300, Malaysia

Optical Characterization of Nonimaging Planar Concentrator for the Application in Concentrator Photovoltaic System

The design and construction of miniature prototype of nonimaging planar concentrator, which is capable of producing much more uniform spatial irradiance and reasonably high concentration ratio, were presented in the previous paper. In this paper, we further explore the optical characteristics of the new concentrator that is specially designed to be incorporated in concentrator photovoltaic systems. For this study, we have carried out a comprehensive analysis via numerical simulation based on all the important design parameters, i.e., array of facet mirrors, f/D ratio, receiver size, and the effect of sun-tracking error, which lead to the overall optical performance of the new concentrator.
[DOI: 10.1115/1.4000355]

Keywords: nonimaging, solar concentrator, concentrator photovoltaic, uniform illumination, flux distribution, ray-tracing

1 Introduction

Concentrator photovoltaic (CPV) systems not only have the potential in reducing the cost of solar electricity, they are also able to reduce the dependence of the existing power generation systems in fossil and nuclear fuel consumptions. This is mainly due to the newly invented multijunction solar cells that are capable of achieving 40% conversion efficiency. In practice, although the multijunction solar cells assembled into a CPV module has the average efficiency dropped down to around 30%, it is still about double the efficiency of conventional flat plate photovoltaic (PV) module that ranges from 10% to 16% [1–3]. For this application, solar concentrator plays an important role by making use of geometrical optics in the design of reflector or lens to deliver high flux of sunlight onto the CPV module at hundreds to thousands suns with high collection efficiency [4–6].

Generally, solar concentrators can be categorized into two major groups: imaging concentrator and nonimaging concentrator [7–9]. Despite being widely used in optics applications such as astronomical telescope and camera, the imaging concentrator does not aim to produce uniform flux distribution profile at the receiver that is highly required in the dense-array CPV module. For such an array, many small-sized CPV cells (from 0.1 cm^2 to 1 cm^2) are connected together in series and parallel to form a receiver module [10]. When there is nonuniform illumination on the receiver module, the system cannot perform well and will operate at the level of the weakest CPV cell or string of cells. In this context, the receiver module that receives nonuniform illumination will experience a serious drop in efficiency, as opposed to a receiver module under uniform illumination [11–15]. With this reason, various types of nonimaging concentrators have been proposed by researchers to produce more uniform solar illumination. Among them are Mills and Morrison [16] who advocated the use of an advanced form of linear Fresnel reflector that can produce better uniformity of solar irradiation. However, the solar concentration ratio of linear Fresnel reflector is normally lower than 100 suns. To achieve moderate solar concentration ratio (several hundreds of suns), modular Fresnel concentrator has been introduced for the application in CPV system and the results show that the modular Fresnel lenses can provide better uniformity of solar irradiance. However the transmission efficiency is relatively low, which is less than 80% due to the reflection at the lens surface and absorption by the lens material [17–19].

Alternatively, a nonimaging focusing heliostat that is proposed by Chen et al. in 2001 has no fixed geometry but is composed of many small mirror elements to achieve a high solar concentration by overlapping all the mirror images with the use of line-tilting driving mechanism [20–26]. In this scheme, the resulted solar concentration ratio is the algebra sum of the solar energy reflected from the mirrors without creating a specific optical image. Inspired by the previous work, a nonimaging planar concentrator attached to on-axis sun-tracker has been proposed to produce a uniformly illuminated spot through the superposition of all the flat mirror images at the target. To validate the principle of the new proposal, a small prototype of the nonimaging planar concentrator was constructed and the detailed work was presented in the previous publication [27]. In this paper, comprehensive simulations of the solar flux distribution have been carried out to further explore the optical characteristics of the proposed planar concentrator under different design parameters, and we have also analyzed the variables, such as solar concentration ratio, the percentage of energy in the uniform illumination area, spillage loss, deviation from an ideal flux distribution due to sun-tracking error, etc., as to study its optical performance in the dense-array CPV system.

2 Methodology of Optical Analysis

The nonimaging planar concentrator comprised of multifaceted mirrors acts as an optical aperture to collect and focus the incident sunlight at any focal distance along the optical axis. Different from imaging optical devices such as parabolic reflectors, the geometry of nonimaging planar concentrator cannot be explicitly defined by any analytical surface formula, and thus, numerical simulation is a necessary means in optical analysis. For the optical modeling of the nonimaging planar concentrator, coordinate transformations and ray-tracing technique have been employed to express the reflection of sunlight by the planar concentrator as well as to generate the solar flux distribution on the receiver plane.

[1]Corresponding author.
Contributed by the Solar Energy Division of ASME for publication in the Journal of Solar Energy Engineering. Manuscript received February 24, 2009; final manuscript received July 28, 2009; published online January 4, 2010. Assoc. Editor: Akiba Segal.

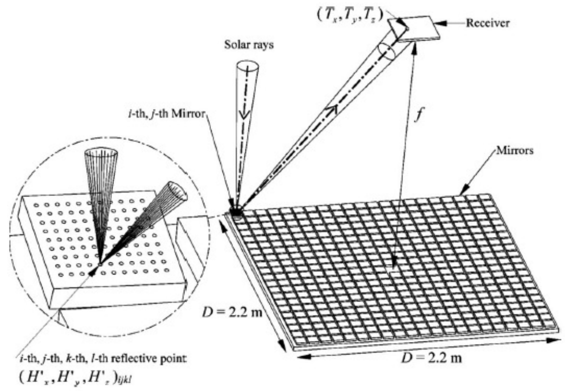

Fig. 1 Conceptual layout design of the nonimaging planar concentrator. Each mirror on the concentrator consists of a finite number of smaller elements called reflective points, and each reflective point is illuminated by a discrete number of subrays arranged in a conic manner (inset).

For the sake of reducing the computing time with negligible effect to the final result, we have included two good assumptions in the optical modeling. First, to account for the spreading of solar irradiation due to solar disk effect upon reflection from the mirror surface, each reflected sunray from the concentrator is spread into P subrays, and each subray carries an amount of energy $1/P$-th of the incident sunray, and these rays uniformly spread in the direction such that it forms a light cone, which subtends to the solar disk half angle of 4.65 mrad. Second, we assume that each facet mirror consists of a finite number of smaller elements called reflective points. Figure 1 depicts the details of how the two assumptions are applied in the optical modeling of the concentrator.

For a geometrical representation, a Cartesian coordinate system (x,y,z) named as the main coordinate system, is defined in the plane of the planar concentrator with its origin located at the center of the planar concentrator, while the subcoordinate system (x',y',z') is defined at the local facet mirror. The x-axis lies along the central column of mirrors, while the y-axis lies along the central row of mirrors, and the z-axis points toward the receiver, as shown in Fig. 2. The coordinates for the central point (or pivot point) of an i,j-mirror are designated as $(H_{Cx},H_{Cy},0)_{ij}$, where i and j denote the mirror location at the ith row and jth column of the concentrator, respectively, and the coordinates of the focal point for the concentrator are $(0,0,f)$. To reflect the sunray toward the receiver, the tilting angles of the i,j-mirror about the axis that is parallel with the x-axis γ, and about the axis that is perpendicular to x-axis σ can be expressed as follows:

$$\gamma = \arctan\left[\frac{H_{Cy}}{f + \sqrt{H_{Cx}^2 + H_{Cy}^2 + f^2}}\right] \tag{1}$$

$$\sigma = \arctan\left[\frac{H_{Cx}}{(H_{Cx}^2 + 2H_{Cy}^2 + 2f^2 + 2f\sqrt{H_{Cx}^2 + H_{Cy}^2 + f^2})^{1/2}}\right] \tag{2}$$

The incident angle of the sunray relative to the i,j-mirror can be obtained as

$$\theta = \frac{1}{2}\arctan\left[\frac{\sqrt{H_{Cx}^2 + H_{Cy}^2}}{f}\right] \tag{3}$$

The initial coordinates of the reflective point for the facet mirror arranged into the i-th row and j-th column are designated as $(H_x,H_y,H_z)_{ijkl}$, where the other two subscripts k and l represent the position of the reflective point at the k-th row and l-th column in the facet mirror, respectively. For the superposition of all the mirror images at the receiver, each individual mirror has to be tilted with its corresponding tilting angles σ and γ to relocate the reflective point in the new coordinates $(H'_x,H'_y,H'_z)_{ijkl}$, as shown in Fig. 1. To ease the mathematical representation of coordinate transformations, we can make the translation a linear transformation by increasing the dimensionality of the space. Thus, the coordinates $(H_x,H_y,H_z)_{ijkl}$ can also be represented by $(H_x,H_y,H_z,1)_{ijkl}$, which is also treated as a vector in matrix form

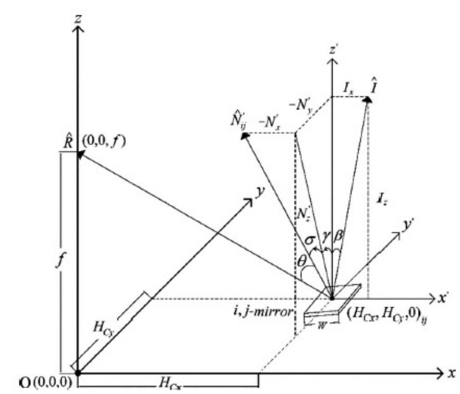

Fig. 2 Cartesian coordinate system (x,y,z), named as the main coordinate system, is defined in the plane of the planar concentrator, with its origin located at the center of concentrator, while the subcoordinate system (x',y',z') is defined at the local facet mirror

$$[H]_{ijkl} = \begin{bmatrix} H_x \\ H_y \\ H_z \\ 1 \end{bmatrix}_{ijkl} \quad (4)$$

The final position of reflective point can also be written in a matrix form as

$$[H']_{ijkl} = \begin{bmatrix} H'_x \\ H'_y \\ H'_z \\ 1 \end{bmatrix}_{ijkl} \quad (5)$$

If the pivot point of the i,j-mirror $(H_{Cx}, H_{Cy}, 0)_{ij}$ is not located at the origin of the main coordinate system, the reflective point will be treated under translation transformation before rotation transformations. The initial coordinates of the reflective point will be first transformed from the main coordinate system that is attached to the concentrator frame to the subcoordinate system that is attached to the local facet mirror via a translation transformation. The translation transformation matrix is

$$[T_1]_{ij} = \begin{bmatrix} 1 & 0 & 0 & -H_{Cx} \\ 0 & 1 & 0 & -H_{Cy} \\ 0 & 0 & 1 & -H_{Cz} \\ 0 & 0 & 0 & 1 \end{bmatrix} \quad (6)$$

Then, it is followed by the first rotation transformation with the angle σ about the y-axis of the subcoordinated system to transform the reflective point from the subcoordinate system to a column-movement coordinate system. The first rotation transformation matrix can be written as

$$[\sigma]_{ij} = \begin{bmatrix} \cos\sigma & 0 & -\sin\sigma & 0 \\ 0 & 1 & 0 & 0 \\ \sin\sigma & 0 & \cos\sigma & 0 \\ 0 & 0 & 0 & 1 \end{bmatrix} \quad (7)$$

The following second rotation transformation with the angle γ about the x-axis of the column-movement coordinate system transforms the reflective point from the column-movement coordinate system to a row-movement coordinate system. The second rotation transformation matrix can be written as

$$[\gamma]_{ij} = \begin{bmatrix} 1 & 0 & 0 & 0 \\ 0 & \cos\gamma & -\sin\gamma & 0 \\ 0 & \sin\gamma & \cos\gamma & 0 \\ 0 & 0 & 0 & 1 \end{bmatrix} \quad (8)$$

Finally, to transform the row-movement coordinate system back to the main coordinate system, we need the last translation matrix that is written as

$$[T_2]_{ij} = \begin{bmatrix} 1 & 0 & 0 & H_{Cx} \\ 0 & 1 & 0 & H_{Cy} \\ 0 & 0 & 1 & H_{Cz} \\ 0 & 0 & 0 & 1 \end{bmatrix} \quad (9)$$

As a result, the matrix for the coordinate transformations from $(H_x, H_y, H_z)_{ijkl}$ to $(H'_x, H'_y, H'_z)_{ijkl}$ can be shortly represented as

$$[\mathrm{H}']_{ijkl} = [\mathrm{M}]_{ij}[\mathrm{H}]_{ijkl} \quad (10)$$

where

$$[\mathrm{M}]_{ij} = [\mathrm{T}_2]_{ij}[\gamma]_{ij}[\sigma]_{ij}[\mathrm{T}_1]_{ij} \quad (11)$$

In the ray-tracing technique, the unit vector of the reflected ray from the mirror element has to be obtained first before we can determine its intersection point on the receiver plane. Considering that the sunray might not be exactly normal relative to the concentrator plane due to the sun-tracking error, we define a unit vector of incident sunray as $\hat{I} = \sin\beta\hat{x} + \cos\beta\hat{z}$, where β is the off-axis angle relative to the concentrator, as shown in Fig. 2. The unit vector of incident sunray can also be described in terms of the sun's position angles as

$$\begin{bmatrix} I_x \\ I_y \\ I_z \\ 1 \end{bmatrix} = \begin{bmatrix} \sin\beta \\ 0 \\ \cos\beta \\ 1 \end{bmatrix} \quad (12)$$

Since all the facet mirrors are oriented in such a way that the normal of their surface are pointing toward $+z$-direction before they are tilted to direct the sunlight toward the receiver, the mirror's normal unit vector in the initial orientation can be described as $\hat{N} = \hat{z}$ and its corresponding matrix form is shown as

$$[N] = \begin{bmatrix} 0 \\ 0 \\ 1 \\ 1 \end{bmatrix} \quad (13)$$

Similar to the case of the reflective point, the initial unit vector normal $[N]$ also undergoes two rotation coordinate transformations when the facet mirror is tilted. Consequently, the new unit vector normal $\hat{N}'_{ij} = N'_x\hat{x} + N'_y\hat{y} + N'_z\hat{z}$ and its corresponding matrix form can be derived as

$$[N']_{ij} = \begin{bmatrix} N'_x \\ N'_y \\ N'_z \\ 1 \end{bmatrix}_{ij} = [\gamma]_{ij}[\sigma]_{ij}\begin{bmatrix} 0 \\ 0 \\ 1 \\ 1 \end{bmatrix}_{ij} \quad (14)$$

From Eqs. (12) and (14), the unit vector of the principal reflected sunray $\hat{R} = R_x\hat{x} + R_y\hat{y} + R_z\hat{z}$ can be obtained as

$$\begin{bmatrix} R_x \\ R_y \\ R_z \end{bmatrix} = \begin{bmatrix} 2(I_xN'_x + I_yN'_y + I_zN'_z)N'_x - I_x \\ 2(I_xN'_x + I_yN'_y + I_zN'_z)N'_y - I_y \\ 2(I_xN'_x + I_yN'_y + I_zN'_z)N'_z - I_z \end{bmatrix} \quad (15)$$

For each principal reflected sunray $\hat{R}$ from the i-th, j-th, k-th, and l-th reflective points, we then generate P subrays within the light cone, which subtend to the solar disk half angle of 4.65 mrad, and each subray is denoted as $\hat{R}_m = R_{mx}\hat{x} + R_{my}\hat{y} + R_{mz}\hat{z}$, where $m = 1, 2, 3, \ldots P$. To determine the intersection point on the receiver plane, we have to solve the line equation of the subray and the surface equation of the receiver plane. The coordinates of the intersection point on the receiver can be calculated as

$$\begin{bmatrix} T_x \\ T_y \\ T_z \end{bmatrix} = \begin{bmatrix} \dfrac{R_{mx}}{R_{mz}}(f - H'_z) + H'_x \\ \dfrac{R_{my}}{R_{mz}}(f - H'_z) + H'_y \\ f \end{bmatrix} \quad (16)$$

Given the coordinates (T_x, T_y), we can plot the solar flux distribution pattern on the receiver plane. In order to achieve a smooth simulation result of illumination distribution on the receiver plane, a fairly high resolution is required in the optical modeling of the reflective point, the solar disk effect, and the receiver plane. In our numerical simulation, each facet mirror of dimension $W \times W$ is subdivided into $S \times S$ reflective points, and the subrays within a cone has a resolution of 65 rays per aperture diameter. Furthermore, the receiver area of $20 \times 20\ \mathrm{cm}^2$ is represented by a matrix with 201 rows and 201 columns of pixels. The solar concentration ratio (number of suns) of each pixel is essen-

Table 1 The specifications used in the simulation of solar flux distribution for the cases of 17×17, 19×19, 21×21, 23×23, and 25×25 arrays of mirrors

Arrays of mirrors	Dimension of facet mirror ($W \times W$)	Total reflective points per facet mirror ($S \times S$)
17×17	12.3×12.3 cm^2	79×79
19×19	11.0×11.0 cm^2	71×71
21×21	10.0×10.0 cm^2	65×65
23×23	9.1×9.1 cm^2	59×59
25×25	8.4×8.4 cm^2	55×55

tially a measure of how much solar irradiation that a pixel receives compared with the direct normal solar irradiation, and it is calculated as

$$C=\sum_{n=1}^{N}\frac{\text{Area of reflective point (cm}^2)}{\text{Area of receiver pixel (cm}^2)}\times\frac{\cos\theta}{P} \tag{17}$$

where the area of reflective point$=(W/S)^2$, area of receiver pixel$=(20/201)^2$ cm/pixel, N is the total counts of subrays hitting on the corresponding pixel on the receiver plane, P is the total number of subrays within the cone, and θ is the incident angle of the principal sunray relative to the normal vector of the corresponding i,j-mirror (refer to Eq. (3)).

3 Characteristics and Performance Study

To quantify the performance of the concentrator photovoltaic system, the maximum solar concentration and the uniformity of solar illumination are the two major considerations that required detailed study. In the study, solar flux distribution at the receiver of the nonimaging planar concentrator has been simulated using aforementioned methodology by varying the f/D ratio (where f is the focal distance and D is the reflector width of the planar concentrator). The simulation results that are based on the f/D ratio can allow us to generalize the study to any concentrator size in future designs.

The optical analysis of nonimaging planar concentrator in our study has included the cases of 17×17, 19×19, 21×21, 23×23, and 25×25 arrays of facet mirrors with their specifications as shown in Table 1. From Table 1, the dimension of the facet mirror and the total reflective points per facet mirror have been selected in such a way that the total reflective area of the concentrator and the area of reflective element (point) remained almost the same for different cases. In overall, the total number of mirrors in the planar concentrator for 17×17, 19×19, 21×21, 23×23, and 25×25 arrays are 288, 360, 440, 528, and 624 pieces, respectively, excluding the central mirror and their total reflective areas are fixed at around 4.4 m^2.

Figures 3(*a*) and 3(*b*) show the simulation results of the solar flux distribution in 3D and 2D plots accordingly for the case of 21×21 array of facet mirrors with a focal distance of 170 cm. For each case, i.e., 17×17, 19×19, 21×21, 23×23, and 25×25 arrays, the same methodology has been adopted to simulate the solar flux distribution for different focal lengths (f) from 100 cm to 300 cm with the increment of 10 cm each time, which is also equivalent to the change in f/D ratio from 0.4545 to 1.3636 with the increment of 0.04545. All the simulated results have shown a similar characteristic, as shown in Fig. 3, which consists of a flat top area in the central region of flux distribution, where the solar concentration ratio is nearly constant and it is named as uniform illumination area.

To facilitate our study, Figs. 4(*a*)–4(*e*) have been plotted to reveal the average solar concentration ratio in the uniform illumination area and percentage of energy in the uniform illumination area versus f/D ratio for different cases, i.e., 17×17, 19×19, 21×21, 23×23, and 25×25 arrays. The average solar concentration ratio in the uniform illumination area is in fact referred to the average value of solar concentration ratio over the entire uniform illumination area of the simulated solar flux distribution. Since ray-tracing is a statistical method of tracing the sunrays from the reflector to the receiver, it is unavoidable that the simulated results obtained in our study are also statistical data. Obviously, average solar concentration ratio in the uniform illumination area curves are much smoother than the percentage of energy in the uniform illumination curves, in which the data are scattered around the best fitted curve. This is because the latter curves are affected by the resolution of the receiver plane, which is ~0.1 cm/pixel (or 20 cm/201 pixels), whereas every increment with focal distance of 10 cm incurs the increase in solar image size due to the solar disk effect of around 0.1 cm as well.

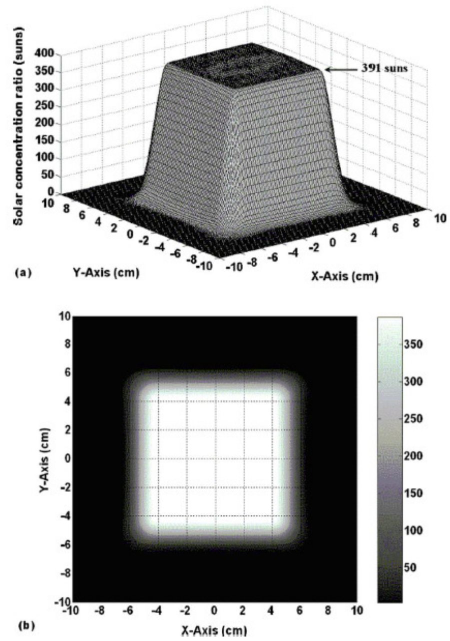

Fig. 3 The simulation results of solar flux distribution for (*a*) 3D and (*b*) 2D plots for the case of 21×21 array of mirrors with a focal distance of 170 cm

Viewing at Figs. 4(*a*)–4(*e*), the change in the average solar concentration ratio in the uniform illumination area with f/D ratio is almost identical for different cases and it basically can be divided into three stages: increase rapidly for f/D ratio below 0.7727, increase moderately for f/D ratio from 0.7727 to 1.0455, and increase marginally for f/D ratio above 0.9091. On the contrary, the relationship between the percentage of energy in the uniform illumination area and f/D ratio is very much case dependant. For the case of 17×17, 19×19, and 21×21 arrays, the percentage of energy in the uniform illumination area shows a slight increase initially to a maximum value and subsequently decreases all the way down with f/D ratio. Referring to Figs. 4(*a*)–4(*c*), the percentage of energy in the illumination area peaks at: f/D ratio=0.6364 for 17×17 array, f/D ratio=0.5000 for 19×19 array, and f/D ratio=0.5455 for 21×21 array. On the

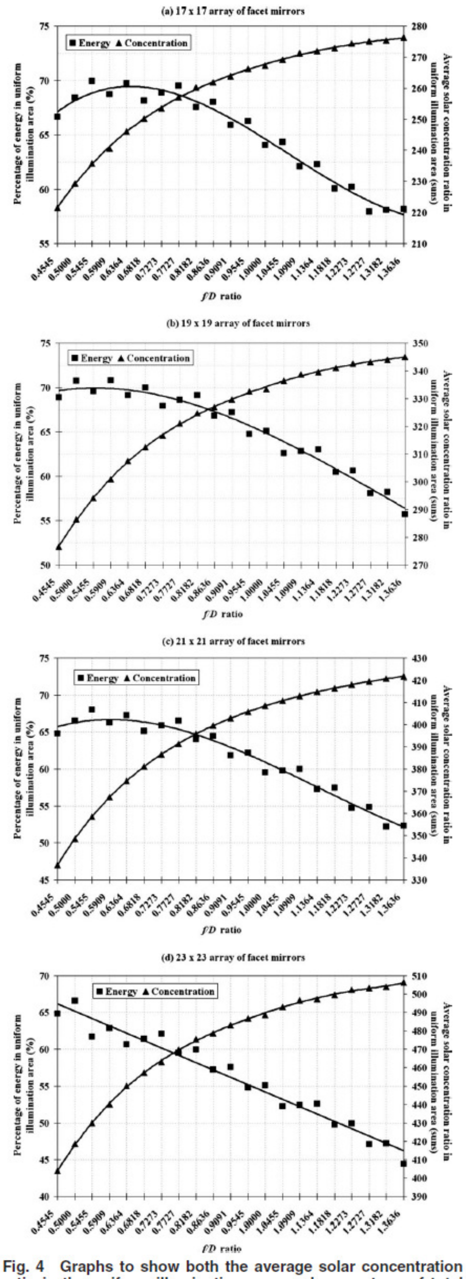

Fig. 4 Graphs to show both the average solar concentration ratio in the uniform illumination area and percentage of total collected energy in the uniform illumination area versus f/D ratio for different cases of (*a*) 17×17, (*b*) 19×19, (*c*) 21×21, (*d*) 23×23, and (*e*) 25×25 arrays of facet mirrors

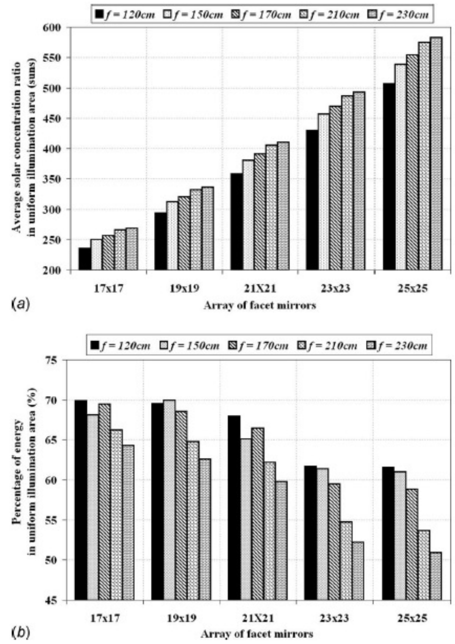

Fig. 5 Bar chart to show the comparisons of (*a*) the average solar concentration ratio in the uniform illumination area and (*b*) percentage of energy in the uniform illumination area for different cases of 17×17, 19×19, 21×21, 23×23, and 25×25 arrays of facet mirrors

other hand, for the cases of 23×23 and 25×25 arrays, the percentage of energy in the illumination area decreases linearly with f/D ratio.

Figures 5(*a*) and 5(*b*) are plotted to show direct comparisons of the average solar concentration ratio in the uniform illumination area and percentage of energy in the uniform illumination area for 17×17, 19×19, 21×21, 23×23, and 25×25 arrays of facet mirrors and five selected focal distances 120 cm, 150 cm, 170 cm, 210 cm, and 230 cm. The charts have shown that different arrays of facet mirrors can cater for different average solar concentration ratios in the uniform illumination area ranging from 236 suns to 583 suns with the focal distances ranging from 120 cm to 230 cm. Besides that, their corresponding percentages of energy in the illumination area that range from 51% to 70% are also shown. Conclusively, increasing focal distance can in fact improve the average solar concentration ratio in the uniform illumination area but most of the time the percentage of energy in uniform illumination area will be sacrificed. Thus, a trade-off between the average solar concentration ratio in the uniform illumination area and total energy in the uniform illumination area has to be sought to obtain the best performance.

For the next study, the size of receiver is fixed and two parameters of the solar flux distribution are simulated, which are the spillage loss and lowest solar concentration ratio at the edge of receiver. This study is very important for the concentrator photovoltaic system designer to optimize the size of receiver by considering both the spillage loss and variation of flux distribution. Spillage loss is defined as the percentage of the solar irradiation falling beyond the boundary of the receiver. Lowest solar concen-

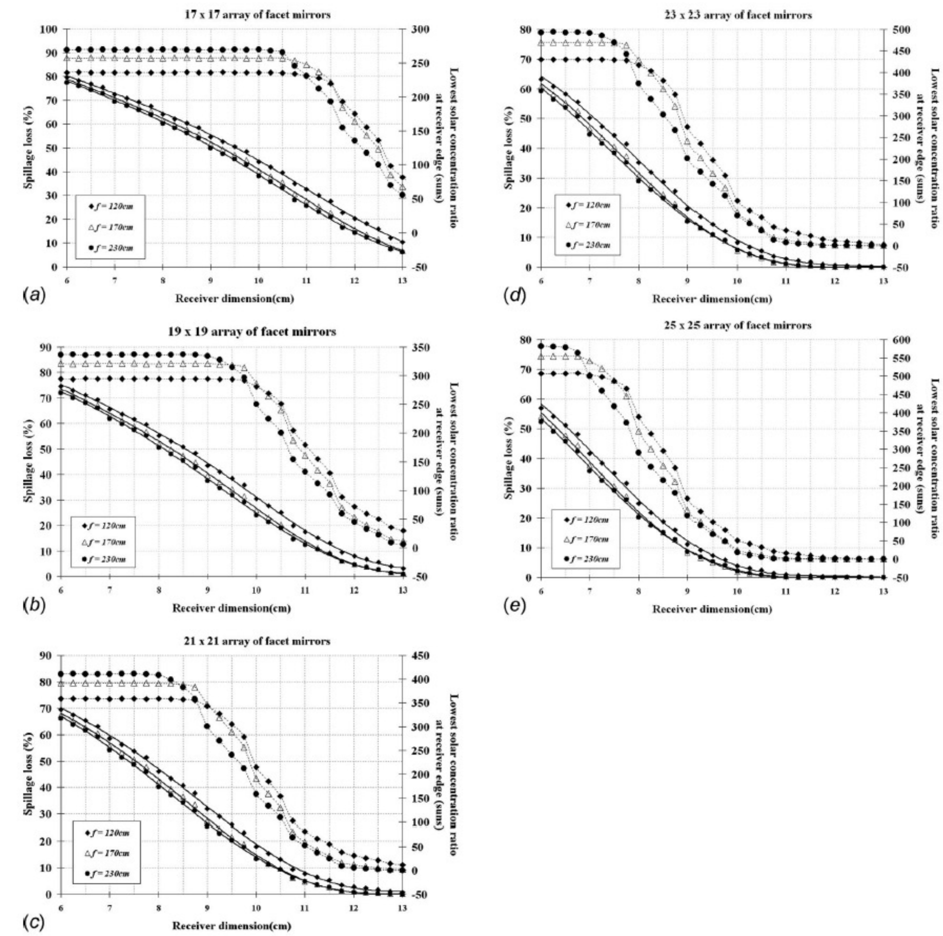

Fig. 6 Spillage loss (solid line) and its corresponding lowest solar concentration ratio at receiver edge (dot line) versus receiver size (square in shape) for the three different focal distances of 120 cm, 170 cm, and 230 cm are plotted in the case of (*a*) 17×17, (*b*) 19×19, (*c*) 21×21, (*d*) 23×23, and (*e*) 25×25 arrays of facet mirrors

tration ratio at the receiver edge is always the lowest solar concentration ratio within the receiver boundary. The variation of flux distribution means the difference between the highest and lowest solar concentration ratios within the receiver boundary in percentage.

Considering the focal distances 120 cm, 170 cm, and 230 cm, we plot the spillage loss (solid line) and its corresponding lowest solar concentration ratio at the receiver edge (dot line) versus receiver size (square in shape) ranging from 6 cm to 13 cm for 17×17, 19×19, 21×21, 23×23, and 25×25 arrays of facet mirrors, as shown in Figs. 6(*a*)–6(*e*). The spillage loss curves for the three different focal distances do not vary much from each other, especially the curves for focal distances 120 cm and 170 cm, which are almost the same with a very minor deviation. From Figs. 6(*a*)–6(*e*), the largest receiver size to reasonably capture the uniform solar flux distribution with the variation of flux distribution at less than 5% and its corresponding spillage loss for different arrays of facet mirrors and focal distances can be listed as follows: In the case of 17×17 array, the optimized receiver sizes (spillage losses) are 11.25 cm (30.1%), 11 cm (27.9%), and 10.5 cm (33.1%) for the focal distances of 120 cm, 170 cm, and 230 cm, respectively. In the case of 19×19 array, the optimized receiver sizes (spillage losses) are 10 cm (30.4%), 9.75 cm (31.4%), and 9.25 cm (34.7%) for the focal distances of 120 cm, 170 cm, and 230 cm, respectively. In the case of 21×21 array, the optimized receiver sizes (spillage losses) are 9 cm (32.0%), 8.75 cm (33.5%), and 8.25 cm (37.2%) for the focal distances of 120 cm, 170 cm, and 230 cm, respectively. In the case of 23×23 array, the optimized receiver sizes (spillage losses) are 8 cm (35.2%), 7.75 cm (37.3%), and 7.25 cm (41.6%) for the focal distances 120 cm, 170 cm, and 230 cm, respectively. In the case of 25×25 array, the

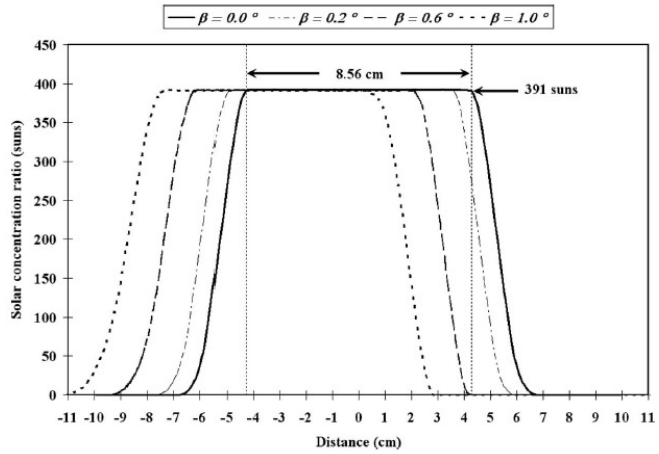

Fig. 7 The simulation results of solar flux distribution to show the solar concentration ratio versus the distance for different off-axis angles of 0 deg, 0.2 deg, 0.6 deg, and 1.0 deg in the case of 21×21 array facet mirrors and f=170 cm

optimized receiver sizes (spillage losses) are 7.25 cm (38.4%), 7 cm (37.7%), and 6.75 cm (42.4%) for the focal distances 120 cm, 170 cm, and 230 cm, respectively.

Another application of Figs. 6(*a*)–6(*e*) is to optimize the size of the receiver and total energy collected by the system, provided that higher tolerance of uniformity in the solar flux distribution is allowed. For instance, if we consider the case of 21×21 array with a focal distance of 170 cm, as shown in Fig. 6(*c*), 8.75 cm is the largest receiver size to contain a reasonably uniform solar irradiation with the variation of flux distribution at less than 2.5% (solar concentration ratio varies from 383 suns to 393 suns) and spillage loss of 33.5%. If the receiver size is increased to 9.5 cm, the lowest solar concentration ratio within the receiver drops to 289 suns and the spillage loss is decreased to 21.6%. In other words even though the variation of flux distribution has increased to 26.5% (varies from 289 suns to 393 suns), the total energy collected by the receiver has been improved to 78.4%. For the receiver size of 10.25 cm, variation of flux distribution is increased to 59.3% with the solar concentration ratio at the receiver edge (160 suns), but its spillage loss is further reduced to 11.7%. Therefore the tolerance in the variation of flux distribution can determine the spillage loss of the system.

For the third study, the effect of off-axis aberration on the solar flux distribution due to the sun-tracking error is also simulated by changing the off-axis angles β from 0 deg to 1 deg. Considering 21×21 array of facet mirrors as our case study, 2D profile of the solar flux distribution displaying the solar concentration ratio versus the distance at a focal distance of 170 cm has been simulated for different off-axis angles. Figure 7 reveals how the solar flux distribution is deviated from the center of the receiver without showing any obvious distortion on the flux distribution profile as the off-axis angle is increased from 0 deg to 1 deg. To be more general, the relationship between the deviation of the solar flux distribution from the center of receiver and focal distances from 100 cm to 300 cm is plotted for β=0.6 deg and 1 deg, as shown in Fig. 8. The graphs show that the deviation from the center of receiver is linearly proportional to the focal distance with the slope dependant on the off-axis angle.

There are three important analyses on the characteristics of solar flux distribution due to the existence of sun-tracking error, which are in terms of spillage loss, nonuniformity, and total acceptance angle where the damage caused is still acceptable. For these analyses, we consider 21×21 array of facet mirrors with a focal distance of 170 cm as our case study. To view at its effect on the spillage loss, Fig. 9 shows the changes in spillage loss curves with the off-axis angles 0 deg, 0.2 deg, 0.4 deg, 0.6 deg, 0.8 deg and 1 deg. For example, if the receiver size is 9.5 cm, the spillage loss can increase significantly from 21.6% at β=0 deg to 23.5% at β=0.2 deg, to 28.2% at β=0.4 deg, to 34.1% at β=0.6 deg, to 40.0% at β=0.8 deg, and finally to 45.9% at β=1 deg. Hence, the accuracy of sun-tracking is very essential to ensure that the spillage loss remained at a minimal level, and subsequently, the performance of a system can be maintained as the sun position varies throughout the day.

To analyze the nonuniformity of the flux distribution due to the sun-tracking error, we define an imaginary boundary with the size of 8.56×8.56 cm^2 to contain the maximum size of uniform illumination area at zero tracking error. For the off-axis angle varying from 0 deg to 1 deg, the ideal flux distribution will shift away

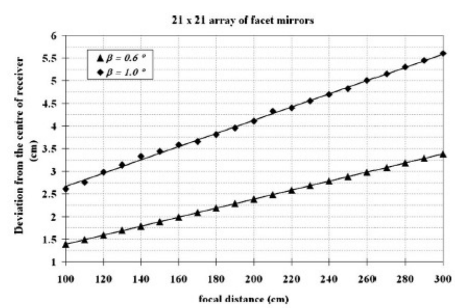

Fig. 8 Deviation from the center of receiver versus focal distance for different off-axis angles of 0.6 deg and 1.0 deg in the case of 21×21 array facet mirrors

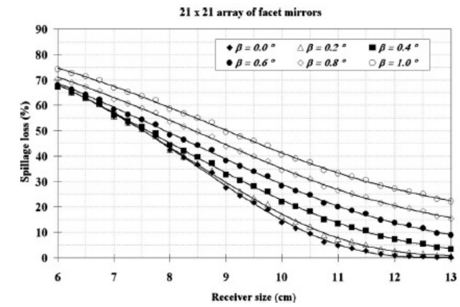

Fig. 9 The spillage loss as a function of the receiver size for different off-axis angles of 0 deg, 0.2 deg, 0.4 deg, 0.6 deg, 0.8 deg, and 1 deg in the case of 21×21 array facet mirrors and f =170 cm

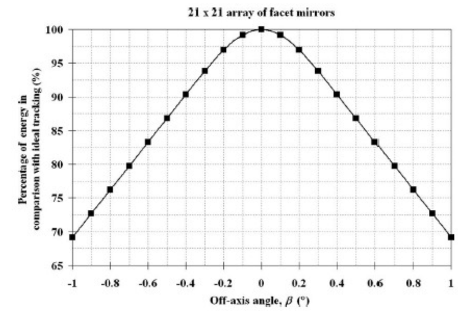

Fig. 11 Percentage of energy falling into the defined area 10.54×10.54 cm² in comparison with ideal tracking versus off-axis angle ranging from −1 deg to 1 deg for the case of 21 ×21 array facet mirrors and f=170 cm

from the center of the defined boundary and the solar concentration ratio at the edge of the boundary will decrease. The seriousness of nonuniformity can be quantified as to how much variation of flux distribution there is within the defined boundary. Figure 10 depicts the variation of flux distribution versus off-axis angle from 0 deg to 1 deg for the case of 21×21 array of facet mirrors with a focal distance of 170 cm

To determine the maximum allowable angular error while keeping the collected energy nearly constant, we define the total acceptance angle of the planar concentrator as a range of allowable angles with less than 5% of the energy lost caused by the sun-tracking error in comparison with ideal tracking. For this purpose, the percentage of energy falling in the defined area of 10.54 ×10.54 cm² in comparison with ideal tracking versus off-axis angle ranging from −1 deg to 1 deg is plotted, as shown in Fig. 11. In this case study, the defined area 10.54×10.54 cm² is chosen based on the common practice in optics known as full width at half maximum (FWHM), in which the solar concentration ratio at the edge of the defined area is half of the maximum solar concentration ratio. According to Fig. 11, the percentages of energy within the receiver in comparison with ideal tracking at the off-axis angles ±0.1 deg, ±0.2 deg, ±0.3 deg, ±0.4 deg, ±0.5 deg, and ±0.6 deg are 99.21%, 96.98%, 93.81%, 90.33%, 86.81%, and 83.29%, respectively. The total acceptance angle of the planar concentrator that receives at least 95% of energy can be determined from Fig. 11 as 0.48 deg.

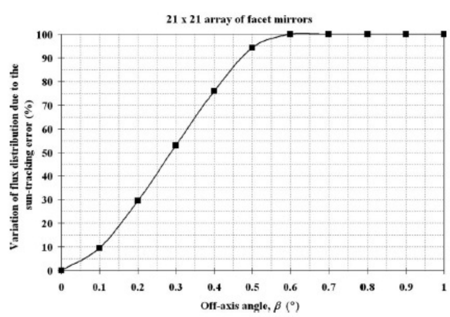

Fig. 10 The variation in flux distribution within the defined boundary area 8.56×8.56 cm² due to the sun-tracking error versus off-axis angles from 0 deg to 1 deg with the increment of 0.1 deg for the case of 21×21 array facet mirrors and f =170 cm

4 Conclusion

The methodology of numerical simulation for plotting solar flux distribution is described in detail and the simulation results are presented. Comprehensive analyses on the simulation results are carried out to study the optical characteristics of the newly proposed nonimaging planar concentrator. In the study, we consider the planar concentrator consisting of various number of mirrors, i.e., 17×17, 19×19, 21×21, 23×23, and 25×25 arrays of facet mirrors, with total reflective area around 4.4 m² and focal distances ranging from 100 cm to 300 cm. In the first part, the average solar concentration ratio and percentage of energy in the uniform illumination area are plotted for different cases. Depending on the array of mirrors (from 17×17 to 25×25) and focal distance (from 100 cm to 300 cm), the average solar concentration ratio in the uniform illumination area can range from 222 suns to 598 suns, and the percentage of energy in the uniform illumination area ranges from 43% to 70%. In the second part, the spillage loss and variation of flux distribution are also analyzed for different cases. If the variation of flux distribution is allowed to be as high as 20–30%, the total energy collected by the receiver can be as high as near to 80%. Alternatively, if it is required, a secondary concentrator can also be added to further improve the total collected energy without much effect on the variation of flux distribution. Finally, the off-axis angle due to sun-tracking error of up to 1 deg is also taken into account in the study of its effect on solar flux distribution. There are three analyses on the characteristics of solar flux distribution due to the existence of sun-tracking error, which are in terms of spillage loss, nonuniformity, and total acceptance angle where the damage caused is still acceptable. In order to collect at least 95% of energy in comparison with ideal tracking, the total acceptance angle of 0.48 deg has been determined. In general, the simulated results have shown a reasonably good uniformity of solar irradiance and high concentration ratio at the receiver plane. All the optical characteristics have strongly recommended that the nonimaging planar concentrator is very suitable for the application in the dense-array CPV system.

Acknowledgment

The authors would like to express their gratitude to Malaysia Energy Centre, Ministry of Energy, Green Technology, and Water (AAIBE Trust Fund), and Ministry of Science, Technology, and Innovation (e-Science Fund) for the financial support.

References

[1] King, R. R., Boca, A., Hong, W., Law, D., Kinsey, G., Fetzer, C., Haddad, M., Edmondson, K., Yoon, H., Pien, P., and Karam, N., 2008, “High-Efficiency Multijunction Photovoltaics for Low-Cost Solar Electricity,” 21st Annual Meeting of The IEEE Lasers and Electro-Optics Society, pp. 2–3.

[2] McConnell, R., and Symko-Davies, M., 2006, “Multijunction Photovoltaic Technologies for High-Performance Concentrators,” Conference Record of the IEEE Fourth World Conference on Photovoltaic Energy Conversion, pp. 733–736.

[3] Nishioka, K., Takamoto, T., Agui, T., Kaneiwa, M., Uraoka, Y., and Fuyuki, T., 2006, “Evaluation of InGaP/InGaAs/Ge Triple-junction Solar Cell and Optimization of Solar Cell’s Structure Focusing on Series Resistance for High-Efficiency Concentrator Photovoltaic Systems,” Sol. Energy Mater. Sol. Cells, **90**, pp. 1308–1321.

[4] Bett, A. W., Burger, B., Dimroth, F., Siefer, G., and Lerchenmuller, H., 2006, “High-Concentration PV Using III-V Solar Cells,” Conference Record of the IEEE Fourth World Conference on Photovoltaic Energy Conversion, pp. 615–620.

[5] Kinsey, G. S., Sherif, R. A., Cotal, H. L., Pien, P., King, R. R., Brandt, R. J., Wise, W. G., Labios, E. L., Wan, K. F., Haddad, M., Lacey, J. M., Fetzer, C. M., Verlinden, P., Lasich, J., and Karam, N. H., 2006, “ Multijunction Solar Cells for Dense-Array Concentrators,” Conference Record of the IEEE Fourth World Conference on Photovoltaic Energy Conversion, pp. 625–627.

[6] Kuo, C. T., Shin, H. Y., Hong, H. F., Wu, C. H., Lee, C. D., Lung, I. T., and Hsu, Y. T., 2009, “Development of the High Concentration III-V Photovoltaic System at INER, Taiwan,” Renewable Energy, **34**, pp. 1931–1933.

[7] 2006, *Energy Technologies Subvolume C: Renewable Energy*, K. Heinloth, ed., Springer, New York, pp. 242–278.

[8] 2007, *Concentrator Photovoltaics*, A. L. Luque and V. M. Andreev, eds., Springer, New York, pp. 113–132.

[9] Winston, R., Minano, J. C., and Benitez, P., 2005, *Non-Imaging Optics*, Elsevier, New York, pp. 1–6.

[10] Verlinden, P. J., Lewandowski, A., Bingham, C., Kinsey, G. S., Sherif, R. A., and Lasich, J. B., 2006, “Performance and Reliability of Multijunction III-V Modules for Concentrator Dish and Central Receiver Applications,” Conference Record of the IEEE Fourth World Conference on Photovoltaic Energy Conversion, pp. 592–597.

[11] Andreev, V., Grilikhes, V., Rumyantsev, V., Timoshina, N., and Shvarts, M., 2003, “Effect of Nonuiform Light Intensity Distribution on Temperature Coefficients of Concentrators Solar Cells,” Third World Conference on Photovoltaic Energy Conversion, pp. 881–884.

[12] Coventry, J. S., 2005, “Performance of a Concentrating Photovoltaic/Thermal Solar Collector,” Sol. Energy, **78**, pp. 211–222.

[13] Franklin, E., and Coventry, J., 2002, “Effects of Highly Non-Uniform Illumination Distribution on Electrical Performance of Solar Cells,” ANZSES Solar Conference, New Castle, Australia.

[14] Nishioka, K., Takamoto, T., Agui, T., Kaneiwa, M., Uraoka, Y., and Fuyuki, T., 2006, “Annual Output Estimation of Concentrator Photovoltaic Systems Using High-Efficiency InGaP/InGaAs/Ge Triple-Junction Solar Cells Based on Experimental Solar Cell’s Characteristics and Field-Test Meteorological Data,” Sol. Energy Mater. Sol. Cells, **90**, pp. 57–67.

[15] Faiman, D., Biryukov, S., and Pearlmutter, K. K., 2002, “PETAL: A Research Pathway to Fossil-Competitive Solar Electricity,” Conference Record of the 29th IEEE Photovoltaic Specialists Conference, pp. 1384–1387.

[16] Mills, D. R., and Morrison, G. L., 2000, “Compact Linear Fresnel Reflector Solar Thermal Powerplants,” Sol. Energy, **68**, pp. 263–283.

[17] Araki, K., Kondo, M., Uozumi, H., Ekins-Daukes, N. J., Egami, T., Hiramatsu, M., Miyazaki, Y., and Yamaguchi, M., 2006, “Packaging III-V Tandem Solar Cells for Practical Terrestrial Applications Achievable to 27% of Module Efficiency by Conventional Machine Assemble Technology,” Sol. Energy Mater. Sol. Cells, **90**, pp. 3320–3326.

[18] Kemmoku, Y., Sakakibara, T., Hiramatsu, M., Miyazaki, Y., and Egami, T., 2003, “Field Test of a Concentrator Photovoltaic System With Flat Fresnel Lens,” Third World Conference on Photovoltaic Energy Conversion, pp. 2379–2382.

[19] Ryu, K., Rhee, J. G., Park, K. M., and Kim, J., 2006, “Concept and Design of Modular Fresnel Lenses for Concentration Solar PV System,” Sol. Energy, **80**, pp. 1580–1587.

[20] Chen, Y. T., Chong, K. K., Bligh, T. P., Chen, L. C., Yunus, J., Kannan, K. S., Lim, B. H., Lim, C. S., Alias, M. A., Bidin, N., Aliman, O., Salehan, S., Shk. Abd. Rezan, S. A. H., Tam, C. M., and Tan, K. K., 2001, “Non-Imaging, Focusing Heliostat,” Sol. Energy, **71**(3), pp. 155–164.

[21] Chen, Y. T., Chong, K. K., Lim, C. S., Lim, B. H., Tan, K. K., Aliman, O., Bligh, T. P., Tan, B. K., and Ismail, G., 2002, “Report of the First Prototype of Non-Imaging Focusing Heliostat and Its Application in High Temperature Solar Furnace,” Sol. Energy, **72**(6), pp. 531–544.

[22] Chen, Y. T., Chong, K. K., Lim, B. H., and Lim, C. S., 2003, “Study of Residual Aberration for Non-Imaging Focusing Heliostat,” Sol. Energy Mater. Sol. Cells, **79**(1), pp. 1–20.

[23] Chen, Y. T., Kribus, A., Lim, B. H., Lim, C. S., Chong, K. K., Karni, J., Buck, R., Pfahl, A., and Bligh, T. P., 2004, “Comparison of Two Sun Tracking Methods in the Application of A Heliostat Field,” ASME J. Sol. Energy Eng., **126**, pp. 638–644.

[24] Chen, Y. T., Chong, K. K., Lim, C. S., Lim, B. H., Tan, B. K., and Lu, Y. F., 2005, “Report on the Second Prototype of Non-Imaging Focusing Heliostat and Its Application in Food Processing,” Sol. Energy, **79**, pp. 280–289.

[25] Lim, C. S., and Li, L., 2009, “Flux Distribution of Solar Furnace Using Non-Imaging Focusing Heliostat,” Sol. Energy, **83**, pp. 1200–1210.

[26] Chong, K. K., 2001, “Characterization of Non-Imaging Focusing Heliostat in University of Technology Malaysia,” Ph.D. thesis, Faculty of Electrical Engineering, Universiti Teknologi Malaysia, Skudai, Malaysia.

[27] Chong, K. K., Siaw, F. L., Wong, C. W., and Wong, G. S., 2009, “Design and Construction of Non-Imaging Planar Concentrator for Concentrator Photovoltaic System,” Renewable Energy, **34**, pp. 1364–1370.

APPENDIX E

SOLAR FLUX DISTRIBUTION ANALYSIS OF NON-IMAGING PLANAR CONCENTRATOR FOR THE APLLICATION IN CONCENTRATOR PHOTOVOLTAIC SYSTEM

Kok-Keong Chong, Chee-Woon Wong, Fei-Lu Siaw and Tiong-Keat Yew
Faculty of Engineering and Science, Universiti Tunku Abdul Rahman,
Off Jalan Genting Kelang, Setapak, 53300 Kuala Lumpur, Malaysia.

ABSTRACT

The design and construction of Non-Imaging Planar Concentrator (NIPC), capable of producing much more uniform spatial irradiance and reasonably high concentration ratio, have been presented in our previous research paper. In this study, we would carry out a comprehensive analysis through the numerical simulation on solar flux distribution at the target by considering all the important criteria to improve the overall performance of dense-array concentrator photovoltaic system, which are the maximum solar concentration, uniform illumination area, spillage loss etc. Maximum solar concentration ratio and percentage of energy in uniform illumination area are plotted for different cases. In general, the simulated results have shown a reasonably good uniformity of solar irradiance and high concentration ratio at the receiver plane.

INTRODUCTION

At present, the development of concentrator photovoltaic (CPV) systems for producing clean, renewable and sustainable energy has grown fleetly as an alternative to replace or complement the existing power generation systems that consume fossil or nuclear fuels. This is mainly due to the encouragement from the advances in state-of-the-art multi-junction solar cells that are capable of achieving 40% conversion efficiency under high solar concentration ratio (300 to 500 suns). In practice, the average efficiency of CPV module that consist of multi-junction solar cells has descended from 40% to 30%, but it is still about two-folds higher than that of conventional flat plate photovoltaic (PV) module ranging from 10% to 16% [1-3].

The higher costs of the multi-junction solar cells compared with silicon or thin-film devices are prohibiting their application in conventional flat-plate modules. Therefore, the solution to this cost-efficiency dilemma is by the application of CPV module in solar concentrator system. Solar concentrators have been developed with either reflecting or refracting optical elements in order to concentrate the sunlight on the multi-junction solar cells for direct electrical conversion. This approach is capable of reducing the expensive solar cell area by increasing the solar concentration ratio and the light intensity.

In general, solar concentrators are classified into two major categories: imaging concentrator and non-imaging concentrator. The imaging concentrator is broadly applied to optics application such as astronomical telescope and camera, but it is not aimed to produce uniform solar flux distribution that is highly required in the dense-array CPV module. Referring to the literatures [4-6], the performance of CPV system will drop badly when there is a non-uniform illumination on the CPV module. With this reason, some researchers have put a lot of effort to design various types of non-imaging concentrators for producing uniform solar illumination. For example, a linear Fresnel reflector with solar concentration ratio of lower than 100 suns has been proposed by Mills *et al.* to produce better uniformity of solar irradiation on the receiver [7]. Although modular Fresnel concentrator has been introduced by Ryu *et al.* for achieving moderate solar concentration ratio of up to 121 suns and better uniform illumination, the reflection at the lens surface and absorption by the lens material have caused the transmission efficiency of less than 80% [8]. Since year 2001, Chen *et al.* and Chong have developed a non-imaging focusing heliostat that is capable of achieving high solar concentration by superposing all of the mirror images into one at a fixed target with the use of line-tilting driving mechanism [9-14]. In this scheme, the resulted solar concentration ratio is the algebra sum of the reflected solar rays without creating a specific optical image, since the sunlight is not coherent.

Inspired by the combined idea from both non-imaging focusing heliostat and the modular Fresnel lens, a Non-Imaging Planar Concentrator (NIPC) has been proposed to achieve a good uniformity of the solar irradiation with a reasonable high concentration ratio. A small prototype of the NIPC consisted of many inexpensive facet mirrors has been designed and constructed in the campus of Universiti Tunku Abdul Rahman (UTAR), Kuala Lumpur, Malaysia to verify the principle of the new proposal [15-16]. In this paper, we would carry out a comprehensive analysis through the numerical simulation on solar flux distribution at the target by considering all the important criteria to improve the overall performance of dense-array concentrator photovoltaic system, which are the maximum solar concentration, uniform illumination area, spillage loss etc.

PRINCIPLE OF OPTICAL ANALYSIS

Instead of using a single piece of parabolic dish, the newly

978-1-4244-5892-9/10/$26.00 ©2010 IEEE

proposed NIPC employs multi-faceted mirrors as the optical aperture to gather and to concentrate the incident sunlight at any focal distance along the optical axis. Since the geometry of NIPC cannot be clearly defined by any analytical surface, numerical simulation is a necessary way for the optical analysis on solar flux distribution at the receiver plane with the use of coordinate transformations and ray-tracing techniques. Two assumptions have been made in the optical modeling for reducing the computer simulation time with negligible effect to the results (see Figure 1):

1. Each reflected sunray from the concentrator is spread into P sub-rays, and each sub-ray carries an amount of energy $1/P$-th of incident sunray. These rays uniformly spread in the direction such that it forms a light cone that subtends to the solar disk half angle of 4.65 mrad.
2. Each facet mirror consists of a finite number of smaller elements called reflective points.

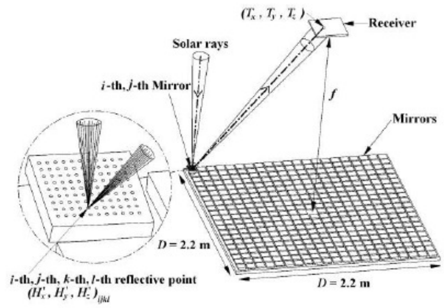

Figure 1 Conceptual layout design of the Non-Imaging Planar Concentrator (NIPC). (Inset) Each facet mirror consists of a finite number of smaller elements called reflective points and each reflective point is illuminated by a discrete number of sub-rays arranged in a conic manner.

A general Cartesian coordinate system is used to represent the main coordinate system (x, y, z) at the plane of the planar concentrator with the origin located at the center of the concentrator. A sub-coordinate system (x', y', z') is defined at the local facet mirror with the origin located at the center of mirror. Referring to Figure 2, the x-axis lies along the central column of mirrors, while the y-axis lies along the central row of mirrors and the z-axis points towards the receiver. The coordinate of the focal point for the concentrator is $(0, 0, f)$. $(H_{Cx}, H_{Cy}, H_{Cz})_{ij}$ represents the coordinate of the central point (or pivot point) for an i, j-mirror, where i and j refer to the mirror location at i-th row and j-th column of the concentrator respectively. The incident angle (θ) of the sunray, relative to i, j-mirror, and the tilted angles of i, j-mirror about x'-axis (γ) and y'-axis (σ) can be expressed as follow:

$$\theta = \frac{1}{2}\arctan\left[\frac{\sqrt{H_{Cx}^2 + H_{Cy}^2}}{f}\right] \tag{1}$$

$$\gamma = \arctan\left[\frac{H_{Cx}}{f + \sqrt{H_{Cx}^2 + H_{Cy}^2 + f^2}}\right] \tag{2}$$

$$\sigma = \arctan\left[\frac{H_{Cx}}{\left(H_{Cx}^2 + 2H_{Cy}^2 + 2f^2 + 2f\sqrt{H_{Cx}^2 + H_{Cy}^2 + f^2}\right)^{1/2}}\right] \tag{3}$$

An initial coordinate of the reflective point on the i, j-mirror is designated as $(H_x, H_y, H_z)_{ijkl}$, where k and l represent the position of the reflective point at k-th row and l-th column of the facet mirror respectively. According to the Figure 1, a new coordinate $(H_x', H_y', H_z')_{ijkl}$ was formed when each individual mirror has to be titled with its corresponding tilted angles (γ and σ) for superposing all the mirror images at the receiver. To ease the mathematical representation of coordinate transformations, a linear translation transformation can be made by increasing the dimensionality of the space. The coordinate transformation starts with the translation transformation from main coordinate system to sub-coordinate system of the planar concentrator. It is then followed by the rotation transformations with the angles σ and γ. Finally it ends with the translation transformation from sub-coordinate system back to main coordinate system of the planar concentrator. As a result, the matrix form for the coordinate transformations from the initial coordinate $(H_x, H_y, H_z)_{ijkl}$ to the final coordinate $(H_x', H_y', H_z')_{ijkl}$ can be simply expressed as follow:

$$[\mathrm{H}']_{ijkl} = [\mathrm{T}_2]_{ij}\,[\gamma]_{ij}\,[\sigma]_{ij}\,[\mathrm{T}_1]_{ij}\,[\mathrm{H}]_{ijkl}$$

$$\begin{bmatrix} H_x' \\ H_y' \\ H_z' \\ 1 \end{bmatrix}_{ijkl} = \begin{bmatrix} 1 & 0 & 0 & H_{Cx} \\ 0 & 1 & 0 & H_{Cy} \\ 0 & 0 & 1 & H_{Cz} \\ 0 & 0 & 0 & 1 \end{bmatrix} \times \begin{bmatrix} 1 & 0 & 0 & 0 \\ 0 & \cos\gamma & -\sin\gamma & 0 \\ 0 & \sin\gamma & \cos\gamma & 0 \\ 0 & 0 & 0 & 1 \end{bmatrix} \times \begin{bmatrix} \cos\sigma & 0 & -\sin\sigma & 0 \\ 0 & 1 & 0 & 0 \\ \sin\sigma & 0 & \cos\sigma & 0 \\ 0 & 0 & 0 & 1 \end{bmatrix} \times \begin{bmatrix} 1 & 0 & 0 & -H_{Cx} \\ 0 & 1 & 0 & -H_{Cy} \\ 0 & 0 & 1 & -H_{Cz} \\ 0 & 0 & 0 & 1 \end{bmatrix} \times \begin{bmatrix} H_x \\ H_y \\ H_z \\ 1 \end{bmatrix}_{ijkl} \tag{4}$$

According to Snell-Descartes law, the incident ray and the normal vector of the mirror are required to obtain the reflected ray. Considering that the incident ray might not be exactly normal relative to the concentrator plane due to the sun-tracking error, the unit vector of incident sunray can be defined in the matrix form as follow:

$$\begin{bmatrix} I_x \\ I_y \\ I_z \\ 1 \end{bmatrix} = \begin{bmatrix} \sin\beta \\ 0 \\ \cos\beta \\ 1 \end{bmatrix} \tag{5}$$

978-1-4244-5892-9/10/$26.00 ©2010 IEEE

where β is the off-axis angle relative to the concentrator that lies in *xz*-plane as shown in Figure 2.

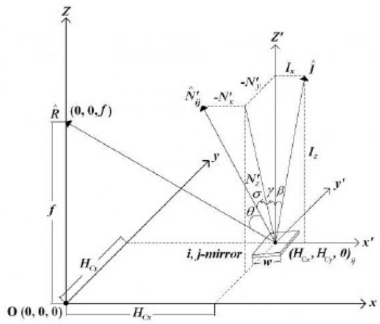

Figure 2 Cartesian coordinate system used to represent the main coordinate system (x, y, z) at the plane of the planar concentrator with the origin located at the center of concentrator, and the sub-coordinate system (x', y', z') at the local facet mirror with the origin located at the center of mirror.

Similar to the case of the reflective point, the initial unit vector normal, $\hat{N} = \hat{z}$ also undergoes two rotation coordinate transformations to form the new unit vector normal when the facet mirror is tilted. Thus, the new unit vector normal can be derived as

$$[N']_{ij} = [\gamma]_{ij}[\sigma]_{ij}[N]_{ij}$$
$$\begin{bmatrix} N'_x \\ N'_y \\ N'_z \\ 1 \end{bmatrix}_{ij} = \begin{bmatrix} 1 & 0 & 0 & 0 \\ 0 & \cos\gamma & -\sin\gamma & 0 \\ 0 & \sin\gamma & \cos\gamma & 0 \\ 0 & 0 & & 1 \end{bmatrix} \times \begin{bmatrix} \cos\sigma & 0 & -\sin\sigma & 0 \\ 0 & 1 & 0 & 0 \\ \sin\sigma & 0 & \cos\sigma & 0 \\ 0 & 0 & 0 & 1 \end{bmatrix} \times \begin{bmatrix} 0 \\ 0 \\ 1 \\ 1 \end{bmatrix}_{ij} \tag{6}$$

Consequently, the unit vector of the principal reflected ray, $\hat{R} = R_x\hat{x} + R_y\hat{y} + R_z\hat{z}$, can be obtained as

$$\begin{bmatrix} R_x \\ R_y \\ R_z \end{bmatrix} = \begin{bmatrix} 2(I_xN'_x + I_yN'_y + I_zN'_z)N'_x - I_x \\ 2(I_xN'_x + I_yN'_y + I_zN'_z)N'_y - I_y \\ 2(I_xN'_x + I_yN'_y + I_zN'_z)N'_z - I_z \end{bmatrix} \tag{7}$$

For each principal reflected ray, $\hat{R}$, from the *i*-th, *j*-th, *k*-th, *l*-th reflective point, *P* sub-rays are generated within the light cone, which subtend to the solar disk half angle of 4.65 mrad, and each sub-ray is denoted as $\hat{R}_m = R_{mx}\hat{x} + R_{my}\hat{y} + R_{mz}\hat{z}$, where $m = 1, 2, 3, \ldots P$. To determine the intersection point on the receiver plane with the use of ray tracing technique, the line equation of the sub-ray and the surface equation of the receiver plane must be solved. The coordinate of the intersection point on the receiver can be calculated as

$$\begin{bmatrix} T_x \\ T_y \\ T_z \end{bmatrix} = \begin{bmatrix} \dfrac{R_{mx}}{R_{mz}}(f - H'_z) + H'_x \\ \dfrac{R_{my}}{R_{mz}}(f - H'_z) + H'_y \\ f \end{bmatrix} \tag{8}$$

The solar flux distribution pattern on the receiver plane can be plotted according to the calculated intersection point (T_x, T_y). In order to achieve a smooth simulation result of illumination distribution at the receiver plane, a reasonably high resolution is required in the optical modeling of the reflective point, the solar disk effect and the receiver plane. In the numerical simulation, each facet mirror of dimension W cm $\times$ W cm is sub-divided into $S \times S$ reflective points and the sub-rays within a cone has a resolution of 65 rays per aperture diameter. In addition, a matrix of 201 rows and 201 columns of pixels represent the receiver area of 20.0 cm × 20.0 cm and hence the solar concentration ratio (number of suns) on each pixel can be calculated as

$$C = \sum_{n=1}^{N} \frac{\text{area of reflective point (cm}^2)}{\text{area of receiver pixel (cm}^2)} \times \frac{\cos\theta}{P} \tag{9}$$

where area of reflective point = $(W/S)^2$, area of receiver pixel = $(20/201)^2$, N is the total count of sub-rays hitting on the corresponding pixel on the receiver plane, P is the total number of sub-rays within the cone and θ is the incident angle as shown in Equation (1).

CHARACTERISTICS AND PERFORMANCE STUDY ON SOLAR FLUX DISTRIBUTION

In this paper, solar flux distribution at the receiver plane of the NIPC has been simulated using the aforementioned methodology by changing of the f/D ratio, where f and D are the focal distance and the width of the planar concentrator respectively. The simulated results that base on f/D ratio can allow us to generalize the study to any concentrator size in future designs. A comprehensive optical analysis of the planar concentrator composed of 21 × 21 facet mirrors with a dimension of 10 cm × 10 cm each to form a total reflective area of 4.4 m^2 and a width of 2.2 m has been carried out through the numerical simulation. Figures 3(a) and (b) show the simulated results of solar flux distribution in 3-D and 2-D plots with a focal distance of 170 cm. All the simulated results have a similar characteristic as shown in Figure 3, which consists of a flat top area in the central region of flux distribution where the solar concentration ratio is nearly constant, and it is named as uniform illumination area. To quantify the performance of CPV system, we have conducted three different performance studies including the maximum solar concentration, the uniformity of solar illumination, spillage loss and the effect of the sun-tracking error.

978-1-4244-5892-9/10/$26.00 ©2010 IEEE

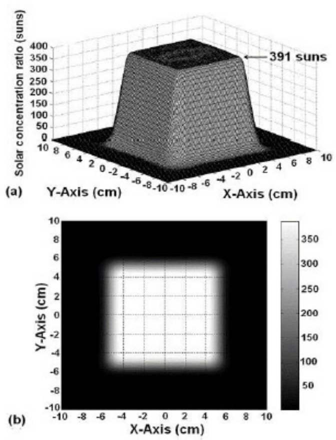

Figure 3 The simulated results of solar flux distribution in (a) 3-D and (b) 2-D plots for 21×21 facet mirrors with a focal distance of 170 cm.

Study I: Figure 4 has been plotted to reveal the maximum solar concentration ratio and percentage of energy in the uniform illumination area for different focal lengths (f) from 100 cm to 300 cm with the increment of 10 cm each time. It is also equivalent to the change of f/D ratio from 0.4545 to 1.3636 with the increment of 0.04545. Due to the resolution of the receiver plane, which is ~ 0.1 cm/pixel (or 20 cm ÷ 201 pixels), the percentage of energy in the uniform illumination curve is not as smooth as solar concentration ratio curve. With the change of the focal distance, maximum solar concentration ratio and percentage of energy in uniform illumination area vary in the range from 336 to 422 suns and from 68 % to 52 % respectively. From the simulated results, we can conclude that the maximum solar concentration ratio improves when the focal distance increases but at the same time the percentage of energy in uniform illumination area will be sacrificed. For that reason, a trade-off between solar concentration ratio and total energy in uniform illumination area has to be sought to obtain the best performance of the concentrator.

Study II: Spillage loss (or percentage of solar irradiance falling beyond the boundary of the receiver) and solar concentration ratio at the edge of receiver were also simulated by adopting different size of receiver. Figure 5 illustrates the spillage loss (solid line) and its corresponding solar concentration ratio at receiver edge (dot line) versus the receiver size (square in shape) from 6 cm to 13 cm for three different focal lengths, i.e. 120 cm, 170 cm and 230 cm. From the graph, the largest receiver size to capture a reasonably uniform solar flux distribution with less than 5 % variation of flux distribution (difference between the highest and the lowest solar concentration

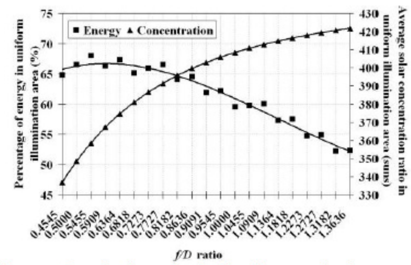

Figure 4 Graph shows both the change of solar concentration ratio and percentage of total collected energy in uniform illumination area versus f/D ratio from 0.4545 to 1.3636 with the increment of 0.04545.

ratios within the receiver in percentage) and its corresponding spillage loss can be summarized as: the optimized receiver size (spillage loss) of the focal distances 120 cm, 170 cm and 230 cm are 9 cm (32.0 %), 8.75 cm (33.5 %) and 8.25 cm (37.2 %) respectively. This study is very useful for the designer to optimize the size of receiver by considering both the spillage losses and variation of flux distribution.

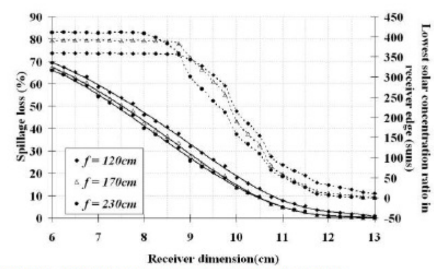

Figure 5 Spillage losses (solid line) and its corresponding solar concentration ratio at receiver edge (dot line) are plotted versus receiver size (square in shape) for the three different focal distances, i.e. 120 cm, 170 cm and 230 cm.

Study III: In this study, we would consider the effect of off-axis aberration to the solar flux distribution due to the sun tracking error. Figure 6 reveals how the solar flux distribution is deviated from the center of the receiver without any obvious distortion to the flux distribution profile at focal distance of 170 cm as the off-axis angle increasing from 0 deg to 1 deg. The same methodology has been applied to simulate the deviation of solar flux distribution from the center of receiver at different focal lengths from 100 cm to 300 cm. The results show that the deviation from the center or receiver is linearly proportional to the focal distance with the slope dependant on the off-axis angle. There are three significant analyses on the characteristics of solar flux distribution due to the and total acceptance angle. For these analyses, we consider 21×21 array of facet mirrors with a focal distance of 170 cm as our case study. To view at its effect on the spillage loss, Figure 7 shows the spillage loss curves varying with the off-axis angles from 0 deg to 1.0 deg with an increment of 0.2 deg for different receiver sizes. According to the simulated results, the accuracy of sun-tracking is very important to maintain the performance of a system since the spillage loss can increase significantly as the off-axis angle varying from 0 deg to 1.0 deg.

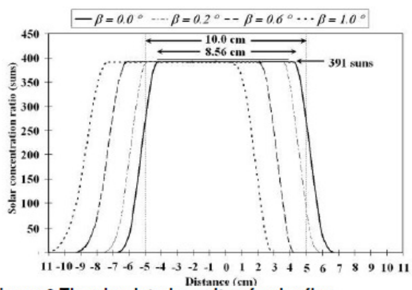

Figure 6 The simulated results of solar flux distribution to show the solar concentration ratio versus the distance for different off-axis angles at a focal distance of 170 cm.

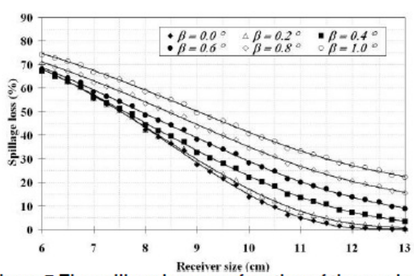

Figure 7 The spillage loss as a function of the receiver size for off-axis angles from 0 deg to 1.0 deg with an increment of 0.2 deg at a focal distance of 170 cm.

An imaginary boundary with a size of 8.56×8.56 cm^2, which is able to contain the maximum size of uniform illumination area at zero tracking error, has been defined to analyze the non-uniformity of the flux distribution caused by the sun-tracking error. The ideal flux distribution will shift away from the center of the defined boundary and the solar concentration ratio at the edge of the boundary will decrease when the off-axis angle varying from 0 deg to 1 deg. We can quantify the seriousness of non-uniformity as how much the variation of flux distribution can exist within the defined boundary. Figure 8 depicts the variation of flux distribution versus off-axis angle from 0 deg to 1 deg. Furthermore, the total acceptance angle of the planar concentrator, which is defined as a range of allowable angles with less than 5% of the energy lost caused by the sun-tracking error in comparison with ideal tracking, has been analyzed as well. Figure 9 illustrates the plot of the percentage of energy falling in the defined area of 10.54×10.54 cm^2 in comparison with ideal tracking versus off-axis angle ranging from −1 deg to 1 deg. In this case study, the defined area 10.54 × 10.54 cm^2 is chosen based on the common practice in optics known as full width at half maximum (FWHM), in which the solar concentration ratio at the edge of the defined area is half of the maximum solar concentration ratio. The percentages of energy within the receiver in comparison with ideal tracking at the off-axis angles ±0.1 deg, ±0.2 deg, ±0.3 deg, ±0.4 deg, ±0.5 deg, and ±0.6 deg are 99.21 %, 96.98 %, 93.81 %, 90.33 %, 86.81 %, and 83.29 % respectively as shown in Figure 9. The total acceptance angle of the planar concentrator that receives at least 95% of energy can be determined from Figure 9 as 0.48 deg.

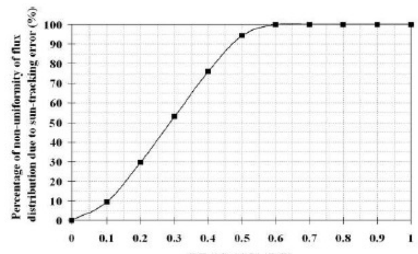

Figure 8 The variation in flux distribution within the defined boundary area 8.56×8.56 cm^2 due to the sun-tracking error versus off-axis angles from 0 deg to 1 deg at a focal distance of 170 cm.

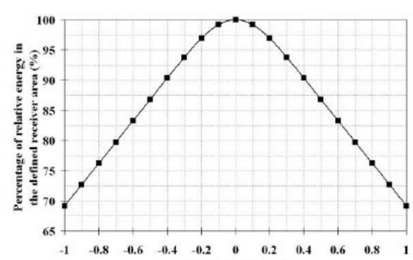

Figure 9 Percentage of energy falling into the defined area 10.54×10.54 cm^2 in comparison with ideal tracking versus off-axis angle ranging from −1 deg to 1 deg at a focal distance of 170 cm.

CONCLUSION

The principle of the non-imaging planar concentrator and the methodology of numerical simulation for plotting solar flux distribution have been described in detail. To study the optical characteristics of the newly proposed planar concentrator, several comprehensive analyses on the simulated results are carried out. According to the simulation results, the designer has to seek a trade-off between solar concentration ratio and total energy in uniform illumination area in order to obtain the best performance for the CPV system. Since the maximum solar concentration ratio increases with the focal distance but at the same time the percentage of energy in uniform illumination area will be surrendered. In addition, the simulated results are very useful for the designer to optimize the size of receiver by considering the spillage losses, variation of flux distribution and the effect of sun-tracking error. As a conclusion, the overall simulated results have strongly recommended that the non-imaging planar concentrator is very suitable for the application in the dense-array CPV system.

ACKNOWLEDGEMENT

The authors would like to express their gratitude to Malaysia Energy Centre, Ministry of Energy, Green Technology & Water (AAIBE Trust Fund) and Ministry of Science, Technology & Innovation (e-Science Fund) for their financial supports.

REFERENCES

[1] R.R. King, A. Boca, W. Hong, D. Law, G. Kinsey, C. Fetzer, M. Haddad, K. Edmondson, H. Yoon, P. Pien and N. Karam, "High-Efficiency Multijunction Photovoltaics for Low-Cost Solar Electricity", *21st Annual Meeting of The IEEE Lasers & Electro-Optics Society*, 2008, pp. 2-3.

[2] R. McConnell and M. Symko-Davies, "Multijunction Photovoltaic Technologies for High-Performance Concentrators", *Conference Record of the IEEE 4th World Conference on Photovoltaic Energy Conversion*, 2006, pp. 733-736.

[3] K. Nishioka, T. Takamoto, T. Agui, M. Kaneiwa, Y. Uraoka and T. Fuyuki,"Evaluation of InGaP/InGaAs/Ge Triple-junction Solar Cell and Optimization of Solar Cell's Structure Focusing on Series Resistance for High-Efficiency Concentrator Photovoltaic Systems", *Solar Energy Materials & Solar Cells* **90**, 2006, pp. 1308-1321.

[4] P.J. Verlinden, A. Lewandowski, C. Bingham, G.S. Kinsey, R.A Sherif and J.B. Lasich, "Performance and Reliability of Multijunction III-V Modules for Concentrator Dish and Central Receiver Applications", *Conference Record of the IEEE 4th World Conference on Photovoltaic Energy Conversion*, 2006, pp. 592-597.

[5] V. Andreev, V. Grilikhes, V. Rumyantsev, N. Timoshina and M. Shvarts, "Effect of Nonuniform Light Intensity Distribution on Temperature Coefficients of Concentrators Solar Cells", *3rd World Conference on Photovoltaic Energy Conversion*, 2003, pp. 881-884.

[6] K. Nishioka, T. Takamoto, T. Agui, M. Kaneiwa, Y. Uraoka and T. Fuyuki, "Annual Output Estimation of Concentrator Photovoltaic Systems Using High-Efficiency InGaP/InGaAs/Ge Triple-Junction Solar Cells Based on Experimental Solar Cell's Characteristics and Field-Test Meteorological Data", *Solar Energy Materials & Solar Cells* **90**, 2006, pp. 57–67.

[7] D.R. Mills and G.L. Morrison, "Compact Linear Fresnel Reflector Solar Thermal Powerplants", *Solar Energy* **68**, 2000, pp. 263-283.

[8] K. Ryu, J.G. Rhee, K.M. Park and J. Kim, "Concept and Design of Modular Fresnel Lenses for Concentration Solar PV System", *Solar Energy* **80**, 2006, pp. 1580-1587.

[9] Y.T. Chen, K.K. Chong, T.P. Bligh, L.C. Chen, J. Yunus, K.S. Kannan, B.H. Lim, C.S. Lim, M.A. Alias, N. Bidin, O. Aliman, S. Salehan, S.A.H. Shk. Abd. Rezan, C.M. Tam and K.K. Tan, "Non-Imaging, Focusing Heliostat", *Solar Energy* **71**, 2001, pp. 155-164.

[10] Y.T. Chen, K.K. Chong, C.S. Lim, B.H. Lim, K.K. Tan, A. Omar, T.P. Bligh, B.K. Tan and I. Ghazally, "Report of the First Prototype of Non-Imaging Focusing Heliostat and Its Application in High Temperature Solar Furnace", *Solar Energy* **72**, 2002, pp. 531-544.

[11] Y.T. Chen, K.K. Chong, B.H. Lim, C.S. Lim, 2003, "Study of Residual Aberration for Non-Imaging Focusing Heliostat", *Solar Energy Material & Solar Cells*, **79**(1), pp. 1-20.

[12] Y.T. Chen, K.K. Chong, C.S. Lim, B.H. Lim, B.K. Tan and Y.F. Lu, "Report on the Second Prototype of Non-Imaging Focusing Heliostat and Its Application in Food Processing", *Solar Energy* **79**, 2005, pp. 280-289.

[13] K. K. Chong "Optimization of Nonimaging Focusing Heliostat in Dynamic Correction of Astigmatism for a Wide Range of Incidence Angles" *Optics Letters* **35**(10), 2010, pp. 1614-1616.

[14] K. K. Chong, "Optical Analysis for Simplified Astigmatic Correction of Non-Imaging Focusing Heliostat" *Solar Energy* **84**, 2010, p. 1356-1365.

[15] K.K. Chong, F.L. Siaw, C.W. Wong and G.S. Wong, "Design and Construction of Non-Imaging Planar Concentrator for Concentrator Photovoltaic System", *Renewable Energy* **34**, 2009, pp. 1364-1370.

[16] K. K. Chong, C. W. Wong, F. L. Siaw, T. K. Yew, "Optical Characterization of Non-Imaging Planar Concentrator for the Application in Concentrator Photovoltaic System", *Journal of Solar Energy Engineering* **132**, 2010, pp. 011011 (9 pages).

APPENDIX F

2012 IEEE Conference on Sustainable Utilization and Development in Engineering and Technology (STUDENT)
Universiti Tunku Abdul Rahman, Kuala Lumpur, Malaysia. 6 - 9 October 2012

Temperature Effects on the Performance of Dense Array Concentrator Photovoltaic System

Fei-Lu Siaw
Faculty of Engineering and Science,
Universiti Tunku Abdul Rahman
Kuala Lumpur, Malaysia
jessiesiaw@gmail.com

Kok-Keong Chong
Faculty of Engineering and Science,
Universiti Tunku Abdul Rahman
Kuala Lumpur, Malaysia
chongkk@utar.edu.my, kokkeong_c@yahoo.com

Abstract—**The performance of dense-array concentrator photovoltaic (CPV) is studied in detail by considering temperature distribution pattern generated from a water-cooled copper cooling block. Using water flow rate 0.400 kg/s and inlet temperature 30°C, the temperature distribution is simulated and the temperature values are used as a means to predict each CPV cell's operating temperature. It is observed that a solar cell located at the central region of the array experiences the highest temperature of 58.3°C, while CPV cells located furthest to the center are operating at 7°C lower than the center region cell. For comparison purpose, we also investigated the effect of uniform temperature distribution for all the cells at 55.2°C. It is found that the output power varies by less than 1W compared to the case of non-uniform temperature distribution where each solar cell is experiencing a different temperature value. On the other hand, the output power increases to 462.70 W when the array temperature is reduced to 40°C, while the output power dropped to 418.60 W when the array temperature is increased to 100°C. Through better understanding of temperature effects to dense array CPV performance, a suitable cooling system can be designed to minimize power loss.**

Keywords- concentrator photovoltaic; nonimaging planar concentrator; Simulink; dense-array; temperature effects

I. INTRODUCTION

High concentration solar energy has attracted increasing attention recently because of great achievement by multi-junction solar cells with conversion efficiencies of over 40%, enabling such systems to become a cost effective alternative to flat-plate photovoltaic (PV) modules [1] [2]. In concentrator photovoltaic (CPV) systems, solar cells that receive high illuminations not only produce high power output but also experience temperature rise which in turn causes a reduction in electrical power conversion. Therefore, an effective heat dissipation system is necessary to ensure that a CPV array is operating within an acceptable temperature range. When the operating temperature is decreased by employing cooling systems, electrical efficiency of solar cells is increased [3] [4] [5].

In this study, an analysis based on different temperature variation is performed using Simulink. Actual sizes of CPV cells and substrates are taken into consideration to embrace practical concerns where packing factor is one of the important parameters in the optimization of overall system performance. This work will complement previous optical system design of the novel concentrator system.

II. DESIGN METHODOLOGY

A. Dense Array Configuration

In view of the importance in correct mapping of concentrated sunlight on each solar cell, this study considers actual limitation in the arrangement of dense-array substrates, CPV cells, as well as wire bonds in the modeling and simulation process. The dimension and specification of substrates, solar cells and wire bonds are referred to direct bonded copper (DBC) from Curamik, high efficiency Concentrating Triple Junction (CTJ) CPV cells (InGaP/InGaAs/Ge) supplied by Emcore, and 10 mil x 1 mil gold ribbon bonds, respectively. Using the aforementioned dimensions, an average solar concentration across the surface of each solar cell is calculated based on the simulated flux distribution as shown Figure 1.

A CPV array that covers a more uniform concentration area is designed and illustrated in Figure 2. In the configuration, only one of the busbars located on top of the solar cells, which is the negative terminal, is utilized for electrical connection. To form a series-connected string, the electrical connections of ribbon bonds are extended from solar cells' top contact to the bottom contact of the next set of solar cells by connecting to the copper surface of DBC substrate. CPV cells that are subjected to non-uniform solar irradiation are protected with schottky bypass diode. As this simulation assumes that all CPV cells have the same characteristics, bypass diodes are not connected to the cells located at the middle of the array. In the event where CPV cells are measured to have different characteristics, or when solar irradiation is not uniform at the centre, bypass diodes need to be added to the circuit. Further study on array arrangement design is not included in this paper and will be covered in future papers. The array from Figure 2 consists of twenty-six sets of two parallel-connected solar cells which are mounted together to form an array of fifty-two cells. The solar concentration level throughout the array ranges from 353× to 391×, and all CPV cells are assumed to have similar characteristics. Since this configuration covers a relatively

978-1-4673-1705-4/12/$31.00 ©2012 IEEE

uniform solar distribution area, the variation of average concentration level on each solar cell is small.

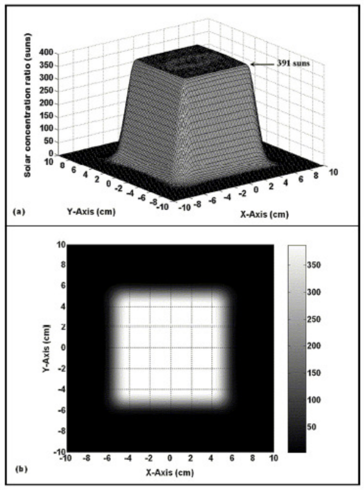

Figure 1. Simulation results using ray-tracing method for the case of 21 × 21 array of mirrors with a focal distance of 170 cm displayed in (a) 3D and (b) 2D plots.

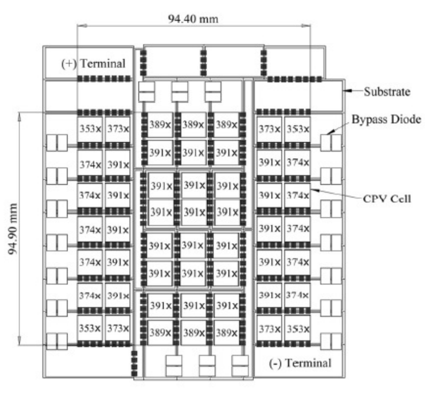

Figure 2. This diagram presents a dense array of fifty-two cells, connecting twenty-six CPV modules in series. Each module consists of two parallel-connected solar cells on a substrate.

The authors would like to express their gratitude to AAIBE Trust Fund by the Ministry of Energy, Green Technology & Water in supporting the project entitled: "Pre-commercialized project on grid connected dense array concentrator photovoltaic system".

B. *Modelling and Simulation of Electrical Performance*

A comprehensive equivalent circuit model for triple-junction solar cell can be represented by three current sources connected in series [8]. Nevertheless, not all of the parameters can be readily collected from field measurements nor obtained from a standard manufacturer's datasheet. Therefore the two-diode model, which is also capable of representing the CPV cells well, is applied in this study as a representation of solar cell. The simulation is done by arranging solar cells into the configuration as showed in Figure 2. Solar cell blocks representing single solar cells as a current source with two exponential diodes, a parallel resistor (R_p), and connected with a series resistance (Rs) are arranged into subsystems in Simulink to form the array. The output current I can be represented by the equation

$$I = I_{ph} - I_{o1}(exp^{(V+IRs)/(N_1 Vt)} - 1) - I_{o2}(exp^{(V+IRs)/(N_2 Vt)} - 1) - (V+IRs)/R_p \quad (1)$$

where I_{ph} is the solar-induced current, I_{o1} is the saturation current of the first diode, I_{o2} is the saturation current of the second diode, Vt is the thermal voltage, N_1 is the diode ideality factor of the first diode, N_2 is the diode ideality factor of the second diode, and V is the voltage across a solar cell. In Simulink, it is possible to choose between the eight-parameter model and the five parameter model. For the five-parameter model, two simplifying assumptions are made: the first assumption is that saturation current of the second diode is zero in value and the second assumption is that the impedance of its parallel resistor is infinite.

For the simulation of this study, the five-parameter model is chosen and applied to solar cell blocks from SimElectronics. Dense-array solar cells are parameterized individually in terms of short-circuit current and open circuit voltage based on its respective location. Both of these values are common parameters which are readily available in a manufacturer's datasheet or measured as field data. In addition to that, this study considers solar power input at direct solar irradiance of 800W/m^2 with 19% of optical losses contributed by limitations from mirror quality and reflectivity. To complete the modeling of the entire array, parameters including short-circuit current (Isc), open-circuit voltage (Voc), diode ideality factor (N), irradiation, and series resistance (Rs) are entered into solar cell blocks. When all parameters are transferred into each cell of the array, this circuit is ready for simulation. Results such as the array current, array voltage and output power are stored into Matlab workspace and then exported to excel for data analysis. Referring to Figure 3, a simulated IV curve using the method described above is presented and is superimposed to the experimental IV curve of a CPV cell operating at 321× concentration. This shows that a close match is possible using matlab simulation.

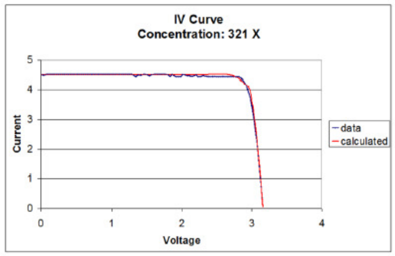

Figure 3. Fitted data superimposed upon experimental data

C. *Temperature Distribution on Cooling Block*

The dense array from Figure 2 is cooled using a copper block (0.146 m width× 0.180 m length × 0.20 m height) machined with multiple water channels and water circulation to maintain the solar cells' temperature (Figure 4). For temperature simulation, the solar flux intensity applied is 2000 W (70% of concentrated solar power input) into a 0.1 m × 0.1 m CPV area at the center region of the cooling block. Theoretical modeling is established on the cooling block with defined solar heat flux input, water mass flow rate, and water inlet temperature. Using NX6, a Computational Fluid Dynamic (CFD) program, flow and hear transfer analysis is performed to the designed cooling block. A simulated temperature distribution on the cooling block for water flow rate of 0.400 kg/s is showed in Figure 5, with water inlet temperature set at 30°C. From Figure 5, the highest temperature of 49.2°C is observed at the center of cooling block surface.

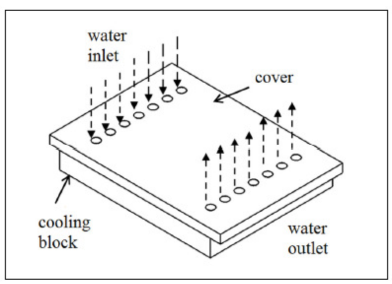

Figure 4. Cooling block assembly, showing water inlet and water outlet locations. CPV array is attached to the cooling block surface

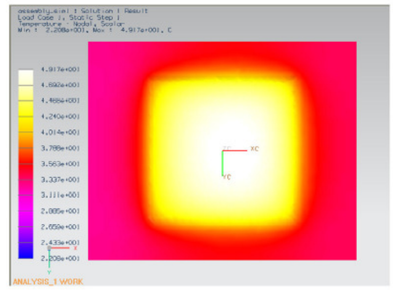

Figure 5. Temperature discribution on CPV dense array for the flow rate of 0.400 kg/s wiith water inlet temperature of 30°C. The maximum temperature observed at the center is 49.2°C

In a dense array, CPV cells are located at differen positions on the cooling block, and hence each solar cel experiences a different localized temperature. To get the CFI simulated temperature value, the center point coordinate o each solar cell is determined and its respective temperature i recorded. The total thermal resistance from cooling block t CPV cell consists of the following material and thickness 0.1mm of Arctic Silver thermal adhesive, 0.3 mm of coppe layer in direct bond copper (DBC) substrate, 0.38 mm alumin layer in DBC substrate, 0.3 mm of copper layer in DBC substrate, 0.15 mm of solder and 0.2 mm of CPV cell. A sketc of the material stack is presented in Figure 6. The temperatur at the surface of the solar cell is derived from temperature o the surface of copper heat sink. Thermal conductivity values o the different materials are listed in Table I. The table shows total thermal resistance of 3.65 × 10^{-5} Km^2W^{-1} from solar cel to copper cooling block. To determine solar cell temperature the following equation is applied:

$$T_{CPV} = (P_{solar} \times R_{tot} \times (1/A_{CPV})) + T_{CB} \qquad (2)$$

where T_{CPV} is the temperature of CPV cell, P_{solar} is the solar thermal power input, R_{tot} is the total thermal resistance from cooling block to CPV cell, A_{CPV} is the total CPV area, and T_{CB} is the temperature of cooling block. Replacing all values of P_{solar}, R_{tot} and A_{CPV} into equation (2), the temperature on CPV surface is calculated for each solar cell in the array.

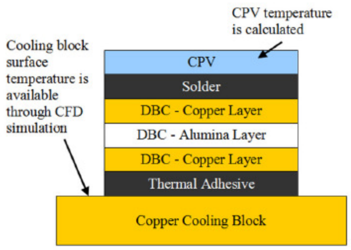

Figure 6. A sketch of the material stack used in the calculation of CPV cell temperature. The temperature at the surface of solar cell is derived from the temperature obtained on the surface of cooling block through CFD simulation.

TABLE I. THERMAL CONDUCTIVITY OF DIFFERENT MATERIALS

Material	Thickness, l (mm)	Thermal Conductivity, k ($Wm^{-1}K^{-1}$)	Thermal Resistance, R (Km^2W^{-1})
CPV	0.20	55	3.64×10^{-6}
Solder	0.15	50	3.00×10^{-6}
Copper Layer of DBC	0.30	400	7.50×10^{-7}
Alumina Layer of DBC	0.38	24	1.58×10^{-5}
Arctic Silver Thermal Adhesive	0.10	7.5	1.33×10^{-5}
R_{tot}			3.65×10^{-5}

III. RESULTS AND DISCUSSION

In concentrator systems, the temperature distribution across a CPV array is far from uniform, and hence each CPV cell will be subjected to different temperatures. A solar cell that is located at the center will be operating at a higher temperature, while the cells that are further from the center will experience lower temperatures. To understand the temperature effects on a dense array, two cases have been investigated. In the first case, temperature value of each solar cell is calculated based on the information from Figure 5 and Figure 6. The solar cell temperature varies from as low as 50.6°C till 51.9°C at the corners to the highest value of 58.3°C at the middle region of copper cooling block. With fifty-two different temperature values, each corresponding solar cell's characteristics are calculated to be used for array simulation. In Figure 7, it is shown that the array maximum power (*Pm*) is 450.57 W.

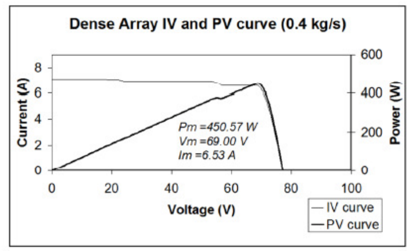

Figure 7. A maximum power of 450.57 W is possible with cooling water flow rate of 0.4 kg/s.

It is also interesting to compare the array output power if a designed cooling block can remove heat while maintaining uniform distribution of surface temperature. Therefore, in the second case, a simulation based on uniform temperature on each solar cell value is also conducted. In the second case, a calculated average temperature from the first case (55.2°C) is applied to each solar cell of the array. The simulated output power from Matlab is 450.5 W, which is very close to the output power for Figure 7.

To investigate the relationship of increased or reduced average temperature across the arrray, simulations based on a lower temperature of 40°C is also compared to an array at 100°C (Figure 8). Having reduced the average temperature from 55.2°C to 40°C, the maximum power obtained has increased by about 12 W to become 462.7 W. However, when the array is operating at 100°C, the CPV dense array would produce a lower output power of as much as 32 W to become 418.60 W. In fact, the array voltage at maximum power point has dropped tremendously to become 62.20 V (100°C) as compared the first case that had 69 V. Conversely, if the operating temperature could be lowered to 40°C, the array voltage at maximum power point is 71. 07 V.

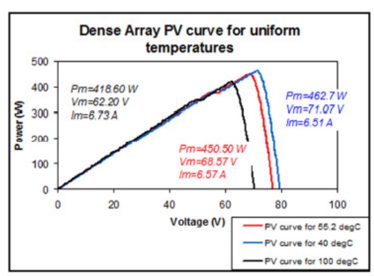

Figure 8. Power-Voltage (PV) curves simulated using uniform temperature on each solar cell in the dense-array for the case of 40°C, 55.2°C and 100°C

IV. Conclusion

This paper has presented a follow-up study on temperature effects to the electrical performance of CPV dense-array incorporated in a nonimaging planar concentrator. By comparing simulation results, it is revealed that temperature uniformity is less significant in affecting the maximum power output, as compared to lowering the average temperature. It is found that the difference between using average temperature as an input parameter in simulation as compared to using all fifty-two different individual temperatures is less than 1 W. In contrast, lowering the average CPV temperature to 40°C improves the maximum output power to 462.7 W, while increasing the average temperature to 100°C yields a reduced output power of 418.6 W. It is predicted that for a larger scale dense-array system, this increased output power will be even more significant when system operating temperature is lowered. Hence, by understanding temperature effects to the performance of CPV dense array, system designers can optimize the cooling system by lowering the average cooling block temperature instead of focusing on temperature uniformity.

Acknowledgment

The authors would like to thank Mr. Tan Woei Chong for his contribution in CFD simulation results of the nonimaging planar concentrator. The authors would also like to express their gratitude to AAIBE Trust Fund by the Ministry of Energy, Green Technology & Water in supporting the project entitled: "Pre-commercialized project on grid connected dense array concentrator photovoltaic system".

References

[1] A. P. Kirk, "Proposal for a high voltage AlGaAs/AlGaAs/GaAs triple junction photovoltaic cell," Solar Energy Materials & Solar Cells, vol. 94, pp. 2242-2445, 2010.

[2] S. Pasovani, A. Del Negro, M. Antonipieri, S. Sinesi, R. Campesato, M. C. Casale, G. Gabetta, and G. Gori, " Triple junction InGaP/InGaAs/Ge solar cells for high concentration photovoltaics application: Degradation tests of solar receivers," Microelectronics Reliability, vol. 50, pp. 1894-1898, 2010.

[3] H. G. Teo, P. S. Lee, and M. N. A. Hawlader, "An active cooling system for photovoltaic modules," Applied Energy, vol. 90, pp. 309-315, 2012.

[4] L. Zhu, R. F. Boehm, Y. Wang, C. Halford, and Y. Sun, "Water immersion cooling of PV cells in a high concentration system," Solar Energy Materials & Solar Cells, vol. 95, pp. 538-545, 2011.

[5] A. Royne, C. J. Dey, and D. R. Mills, "Cooling of photovoltaic cells under concentrated illumination: a critical review," Solar Energy Materials & Solar Cells, vol. 86, pp. 451-483, 2005.

[6] K.K. Chong, F.L. Siaw, C.W. Wong and G.S. Wong, "Design and construction of non-imaging planar concentrator for concentrator photovoltaic system" Renewable Energy, vol. 34, pp.1364-1370, 2009.

[7] K. K. Chong, C. W. Wong, F. L. Siaw, and T. K. Yew, "Optical characterization of nonimaging planar concentrator for the application in concentrator photovoltaic system," Journal of Solar Energy Engineering, vol. 132, pp. 011011.1-011011.9, 2010.

[8] Y. Ota, Y. Sakurada, and K. Nishioka, " Temperature characteristics analysis of InGaP/InGaAs/Ge triple junction solar cell under concentrated light using spice diode model," 35th IEEE Photovoltaic Specialists Conference (PVSC) 2010; Honolulu, pp. 002093-002096

APPENDIX G

ELECTRICAL CHARACTERIZATION OF DENSE-ARRAY CONCENTRATOR PHOTOVOLTAIC SYSTEM

Kok-Keong Chong*, Fei-Lu Siaw
Faculty of Engineering and Science, Universiti Tunku Abdul Rahman,
Off Jalan Genting Kelang, Setapak, 53300 Kuala Lumpur, Malaysia

ABSTRACT: In this paper, we explores various arrangement of solar cells in dense-array configuration for optimizing the electrical performance of Concentrator Photovoltaic (CPV) system. Three different configurations of dense-array layouts are proposed to be analyzed in our study using numerical simulation method aided by Simulink and taking into account of module bypass diodes. The simulated results of different dense-array configurations in terms of current-voltage (I-V) and power-voltage (P-V) curves are presented and discussed based on the irradiance profile of the non-imging planar concentrator. The mismatch effects due to non-uniform irradiance for the solar cells located at the peripheral of the receiver module are illustrated and discussed. When an I-V curve contains many mismatch steps, the maximum power output is greatly affected and then leads to a lower fill factor (FF) value. Power loss can be minimized to enhance the overall performance and hence to obtain the best design with more cost-effective solution via better understanding of the importance in proper arrangement of CPV cells with reference to the irradiance profile of the concentrator, which is to avoid low concentration and non-uniform solar concentration area at the receiver target.
Keywords: Multijunction Solar Cell, Concentrator Cells, Concentrators, Electrical Properties, Energy Performance

1 INTRODUCTION

Mismatch losses caused by soiling, non-uniform irradiance, shading, temperature variations, cell quality and aging of solar cell, all contribute to the serious power reduction in the real site testing of concentrator photovoltaic system. When the current-voltage (*I-V*) curves of solar cells are not identical, the output power of that array or string of cells decreases considerably. The system cannot achieve good performance and will operate at the level of the weakest CPV cell or string of cells. Therefore, receiver modules that receive non-uniform illumination will experience a serious drop in efficiency, as opposed to receiver modules under reasonably uniform illumination [1][2]. Most available papers discuss on single CPV module and its performance under Fresnel lens system, whereby the non-uniformity of concentrated light is identical in each cell of the array. On the other hand, study in dense array CPV systems is rare due to the complication in the mismatch loss and hence the drive towards commercialization for this type of CPV technology is less encouraged. The novel non-imaging planar concentrator, as presented in previous publication [3][4], is capable of producing much more uniform spatial irradiance and at reasonably high concentration ratio for the application in dense-array CPV system. The cells in the array are subjected to solar flux distribution pattern that greatly differs to that of the Fresnel System.

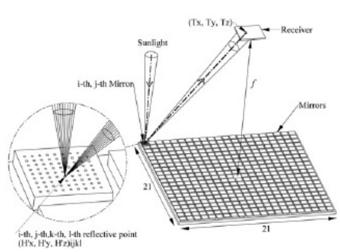

Figure 1: The Non-Imaging Planar Concentrator (NIPC)

Several solutions for reducing mismatch losses have been proposed by other authors to modify array interconnections or utilizing alternative topologies such as total-crossed tied (TCT) and bridge-link (BL) configurations. However, such solutions cannot be directly applied to densely-packed CPV arrays due to limitation of available space in the receiver module. As all the concentrated irradiance is focused onto a relatively small receiver module, a good packing factor will be sacrificed if intricate connection methods requiring more circuit interconnect space are employed. It will further increase the complexity in the assembly process of CPV dense-array that is comparatively much smaller than a regular PV array of the same power rating.

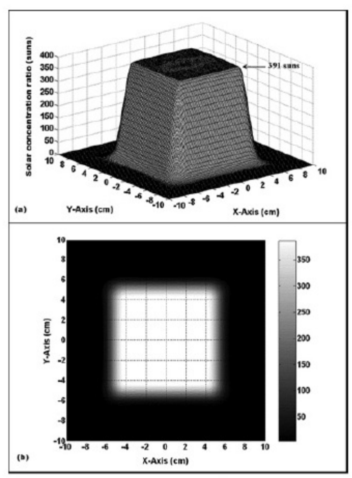

Figure 2: The optimized result of solar illumination distribution in both (a) 3-D and (b) 2-D views.

2 RESULTS

2.1 Non-imaging planar concentrator

The non-imaging planar concentrator comprises of multifaceted mirrors, and uses mirror arrays as an optical aperture to collect and focus the incident sunlight at any focal distance along its optical axis as shown in Fig. 1. To study the spatial irradiance of the concentrator system in evaluating its overall optical performance, numerical simulations were applied based on parameters such as array of facet mirrors, *f/D* ratio, receiver size, and the effect of sun-tracking error.

The optimized result of solar illumination distribution is defined by Figs. 2(a)-(b), which is simulated based on the case of 21 × 21 array of facet mirrors with the dimension of 10 cm × 10 cm each and focal distance of 170 cm excluding the central mirror. The flux pattern consists of a flat top area in the central region of flux distribution where the solar concentration ratio is constant and it is named as uniform illumination area with peak intensity of 391 suns.

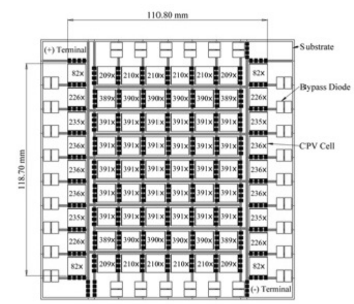

Figure 3: Diagram showing an array of seventy-two series-connected solar cells, labeled with the average concentration level on each cell. The minimum average solar concentration level is calculated to be 82×.

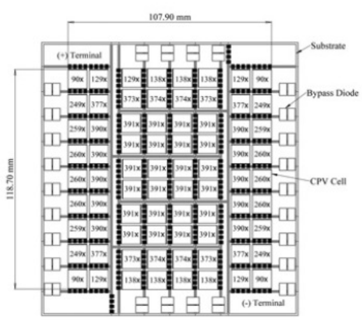

Figure 4: Dense array consisting thirty-eight sets of two parallel-connected modules totaling up to seventy-six CPV cells for the whole configuration. Each cell's average concentration ratio is calculated and mapped on its respective location.

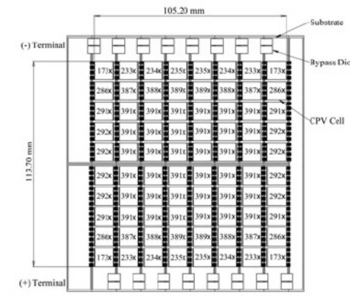

Figure 5: Eighty cells arranged into an assembly and packed into the area of target receiver under relatively high solar concentration ratio, due to the reason of space saving because lesser substrates are used in this configuration. Each module set consists of five parallel-connected solar cell and bypass diodes.

2.2 Concentrator photovoltaic cell arrays

In view of the importance in the correct mapping of concentrated sunlight level on each CPV cell, this paper proposes a practical modelling and simulation approach by considering actual limitation in the arrangement of substrates, CPV cells and wire bonds. Four different configurations are selected for the various combination in series and parallel connection of high-efficiency triple-junction solar cells to cover most of the practical mismatch problems. Figures 3, 4 and 5 show three different configuration to be considered in our case study.

3 ANALYSIS OF THE RESULTS, CLEAR EXPOSITION OF THE MAIN FINDINGS

The *FF* values for Figures 6(a), (b) and (c) are 46%, 51% and 67% respectively. This finding further supports the importance of uniform solar irradiance in a concentrator solar system. The maximum power is lowest for the curve from Figure 6(a) with P_{max}= 567.18W, followed by the curve from Figure 6(b) with P_{max}= 647.94W and the highest for the curve from Figure 6(c) with P_{max} = 852.03W.

The high output power for Figure 6(c), which corresponds to the arrangement in Figure 5, can be directly linked to its high packing factor because each of the sixteen modules contains five CPV cells to form an eighty-cell array. As the modules are packed closely together, CPV cells located at the outer corners have relatively higher concentration level (173×), and this reduces the mismatch effect as compared to the arrays from Figures 6(a)-(b).

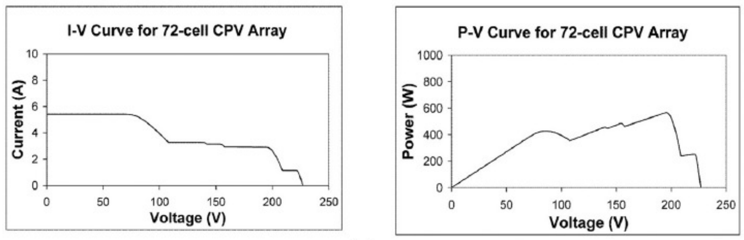

(a)

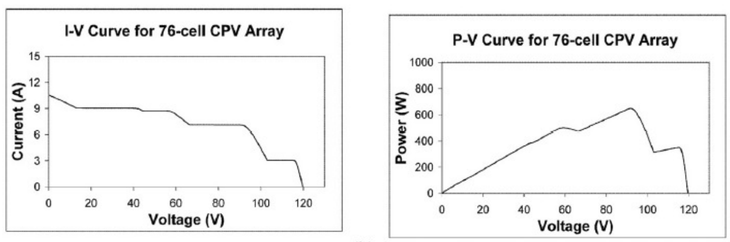

(b)

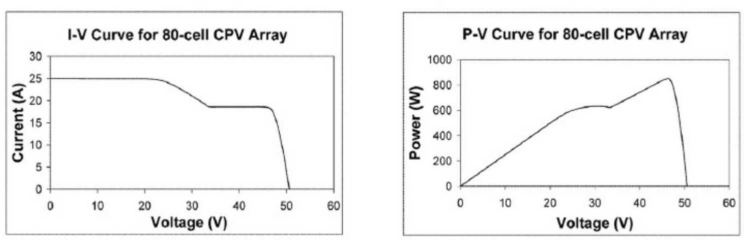

(c)

Figure 6: Various *I-V* and *P-V* curves of four separate configurations subjected to different solar concentration designed for the NIPC.

Table I: Key parameters for the *I-V* curves in Figure 10 (a) to (d) showing values of short-circuit current (I_{SC}), open-circuit voltage (V_{OC}), maximum power ($P_{\max}$) and fill factor (*FF*)

Curve	I_{SC}(A)	V_{OC}(V)	P_{max}(W)	FF(%)
(a)	1.86	226.82	567.18	46
(b)	0.32	119.66	647.94	51
(c)	3.78	50.58	852.03	67

4 ACKNOLEDGEMENT

The authors would like to express their gratitude to Ministry of Energy, Green Technology & Water (AAIBE Trust Fund) for the financial support.

5 REFERENCES

[1] E. Franklin, J. Coventry, ANSES Solar Conference New Castle, Australia (2002).

[2] V. Andreev, V. Grilikhes, V. Rumyantsev, N. Timoshina, M. Shvarts, Third World Conference on Photovoltaic Energy Conversion (2003) 881-884.

[3] K.K. Chong, C.W. Wong, F.L. Siaw, T.K. Yew, Journal of Solar Energy Engineering Vol 132 (2010) 011011.1-011011.9.

[4] K.K. Chong, F.L. Siaw, C.W. Wong and G.S. Wong, Renewable Energy Vol. 34 (2009) 1364-1370

APPENDIX H

An Interconnection Reconfiguration Method for Concentrator Photovoltaic Array

Fei Lu Siaw, Kok Keong Chong

Faculty of Engineering and Science, Universiti Tunku Abdul Rahman, Off Jalan Genting Kelang, Setapak, Kuala Lumpur, 53300, Malaysia.

***Abstract* — This paper reports on the application of heuristic algorithms for one-dimensional bin-packing problems in solving current mismatch of concentrator photovoltaic (CPV) arrays that is caused by non-uniform solar flux distribution. As a case study, actual flux profile for a non-imaging planar concentrator (NIPC) is measured based on CPV cells' location in a dense array. Then, forty-four solar cells are reconfigured according to heuristic algorithm results. From the study, current mismatch is minimized from 1.03A to 0.07A resulting an increase in output power from 83.99W to 116.36 W. This reconfiguration method is tested by comparisons with Simulink current-voltage (*I-V*) curve results.**

***Index Terms* — arrays, current-voltage characteristics, heuristic algorithms, photovoltaic systems, optimal matching, optimization methods**

I. Introduction

The one-dimensional bin-packing problem (BPP) consists of finding a packing of the objects using a minimum number of bins of pre-sized capacity with a given list of objects and their respective sizes. Conventionally, the bin-packing models are applied in several areas such as storage allocation of computer networks, assigning commercial breaks on television, packing boxes into shipping containers, copying a collection of files to magnetic tapes and floppy disks, etc. As BPP is an NP-hard problem which can be tedious and time-consuming to solve, various heuristics are reported in previous literature for solving the classical bin-packing problem [1] [2].

In this paper, we investigate BF and BFD heuristics for one-dimensional bin-packing problem to solve current-mismatch problem that is faced in concentrator photovoltaic (CPV) systems. The results generated have been compared with those obtained with conventional array configuration method. This approach is free from the limitation of conventional array topologies which are the series-parallel (SP), bridge-link (BL) and total-cross-tied (TCT), as the bin-packing method proposes new arrangements based on heuristics results.

II. Solar flux distribution of non-imaging planar concentrator (NIPC)

We often find that delivered electrical power in field conditions is much lower than array ratings because mismatch losses have affected current-voltage (*I-V*) and power-voltage (*P-V*) curves of dense-array solar cells. Mismatch factors such as soiling, non-uniform irradiance, shading, temperature variations, cell's quality as well as aging of solar cells, all contribute to serious array power reduction in real site testing. Non-uniform distribution of concentrated solar irradiance is one of the significant problems faced by most of concentrator systems, especially around receiver edges.

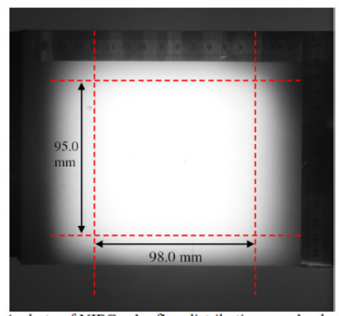

Fig. 1. A photo of NIPC solar flux distribution on a lambertian target that was taken with a CCD camera.

Over the recent years, many studies can be found discussing on the improvement of solar concentrator optical design to produce more uniform solar illumination at high concentrations [3-5]. Nevertheless, the overall output current of CPV cells connected in a dense array arrangement is very much dependent on the solar flux distribution of a solar concentrator. Despite the employment of flat mirrors in the non-imaging planar concentrator (NIPC), the resultant flux distribution from simple super-positioning of all flat mirror images is inevitably non-uniform near the peripheral zone.

An NIPC prototype located in Universiti Tunku Abdul Rahman (UTAR) Kuala Lumpur (3.22° North, 101.73° East) is chosen for this study, and its solar flux distribution on the receiver is measured. This prototype is capable of producing reasonably high concentration using 192 flat mirrors with dimension 10 cm × 10 cm each. An optical scanner using a row of calibrated triple-junction solar cells (InGaP/InGaAs/Ge) as sensors with the resolution of 1.0 cm × 1.0 cm is designed to scan along the column direction for acquiring a 2-D flux distribution of concentrated solar irradiance at the receiver. Using the flux profile, current values

1

of CPV cells are calculated and used as objects for packing. Details of this optical scanner device setup has been published by Chong et al. except the sensor used in previous work is photodiode which has lower limit of irradiance level [6].

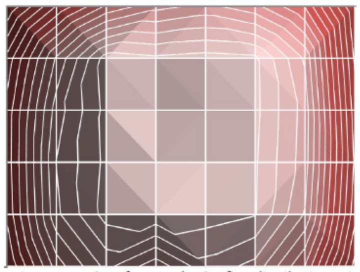

Fig. 2. A contour plot of scanned solar flux distribution using an optical scanner with triple-junction solar cells.

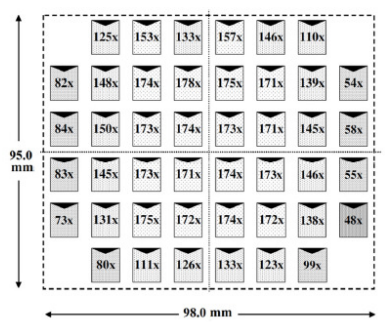

Fig. 3. By using measured flux distribution from an optical scanner that is fixed at the receiver plane, the solar concentration ratio of each CPV cell was determined and mapped to its respective position.

III. RESULTS AND DISCUSSIONS

In this section, results are provided to demonstrate the effectiveness of the proposed bin-packing heuristic method. Bin capacity is defined as 2A, as a starting point and this value is swept until 20A. From the generated results, only solutions which give current mismatch of less than 0.45A are chosen and presented in Fig. 4. This chart allows a system designer to decide on the array current that fits this CPV system while having minimal mismatch losses. The optimal solution with the least current mismatch is a BFD 9.4A, which consists of five series-connected strings, as displayed in Figure 5 & 6. Each string has a unique color and the CPV cells that are grouped into the same string have similar color.

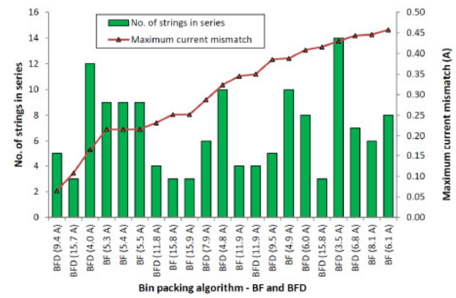

Fig. 4. Bin-packing configurations with maximum current mismatch of less than 0.50A

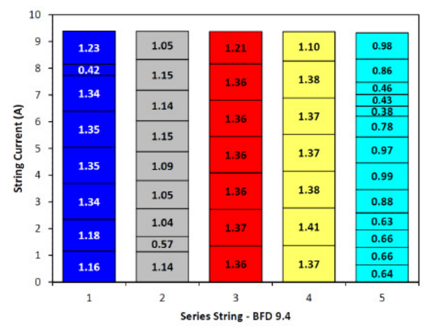

Fig. 5. A representation of a dense-array consisting of 5 strings connected in series and minimum current mismatch of 0.07A.

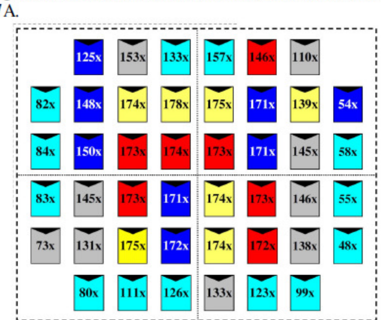

Fig. 6. Solar cells that are grouped into the same string are labeled with similar color

IV. Conclusion

We have explored the performance of BF and BFD heuristic of the classical bin-packing problem in an NIPC dense-array subjected to non-uniform flux distribution. Mismatch losses caused by non-uniform irradiance is a crucial drawback that affects the electrical performance of CPV systems as maximum output power of the array is considerably reduced. Layout reconfiguration using bin-packing method is an expeditious and cost effective approach to optimize any dense-array layout for any solar concentrator, by minimizing current mismatch of its *I-V* and *P-V* curve. This method allows automatic reconfiguring of new array topologies optimally, and is a breakthrough concept as compared to the conventional array topologies such as the SP, BL and TCT. As a case study, the actual flux profile for an NIPC is measured and tabulated based on the position of forty-four CPV cells in the dense array. Using the flux profile, current values of each solar cell is calculated and used as objects for packing. From the findings of this study, current mismatch can be minimized from 1.03A to as low as 0.07A, when operating at DNI: 604.19 W/m^2. This improvement enhances output power to 116.36W, an increase of 30.28W as compared to the conventional configuration of 22 × 2 - TCT with only 86.08W. When compared to a 6 × 8 – TCT* dense array configuration, the new optimized configuration is also superior by 32.37W in output power, as presented in Table I. The bin-packing reconfiguration method is validated by testing and comparing with *I-V* curve results in Simulink using solar cell blocks. The results from bin-packing and Simulink simulation are in close agreement with each other.

TABLE I
AN ELECTRICAL PERFORMANCE COMPARISON OF THE OPTIMIZED ARRAY TO TWO OTHER ARRAYS WITH CONVENTIONAL ARRANGEMENTS

Array configuration	P_{mp} (W)	Fill factor (FF) (%)	V_{mp} (V)	I_{mp} (A)
22 × 2 - TCT	86.08	49.84	58.65	1.47
6 × 8 - TCT*	83.99	55.14	15.87	5.29
Optimised array using BFD 9.4A arrangement – TCT	116.36	85.45	12.75	9.13

* each string consists of all of the eight CPV cells within the same row, except for the top and bottom strings that only has six CPV cells

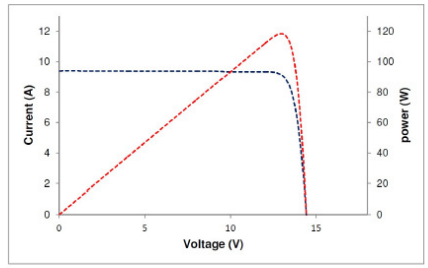

Fig. 7. The optimized NIPC dense-array *I-V* and *P-V* curves are plotted in Simulink using the configuration results from BFD 9.4A, plotted at DNI: 604 W/m^2.

Acknowledgement

The authors would like to express their gratitude to the Ministry of Energy, Green Technology and Water (AAIBE Trust Fund), the Ministry of Science, Technology and Innovation (e-Science Fund with project number 03-02-11-SF0143), and the Ministry of Higher Education (Fundamental Research Grant Scheme with project no.: FRGS/1/11/TK/UTAR/03/4) for their financial support.

References

[1] E. G. Coffman, Jr. J. Galambos, S. Martello, and D. Vigo, "Bin packing approximation algorithms: combinatorial analysis," in *Handbook of Combinatorial Optimization, D-Z. Du and P. Pardalos, Eds. Kluwer Academix Publishers*, 1998.

[2] D. L. Applegate, L. S. Buriol, N. L. Dillard, D. S. Johnson, and P.W. Shor, "The cutting-stock approach to bin-packing: theory and experiments," in *Proceedings of the 5th Workshop on Algorithm Engineering and Experiments (ALENEX03), Maryland, R. E. Ladner, Ed. SIAM*, pp. 1-15, 2003.

[3] D. R. Mills, G. Morrison, "Compact linear Fresnel reflector solar thermal powerplants", *Sol. Energy*,68, 2000, pp. 263-283.

[4] Y. T. Chen, K. K. Chong, T. P. Bligh, L. C. Chen, J. Yunus, K. S. Kannan, B. H. Lim, C. S. Lim, M. A. Alias, N. Bidin, O. Aliman, S. Salehan, S. A. H. Shk. Abd. Rezan, C. M. Tam, K. K. Tan, "Non-Imaging, focusing heliostat", *Sol. Energy*, vol. 71, pp. 155-164, 2001.

[5] K. K. Chong, F. L. Siaw, C. W. Wong, G. S. Wong, "Design and construction of non-imaging planar concentrator for concentrator photovoltaic system", *Renewable Energy*, vol. 34, pp. 1364-1370, 2009.

[6] K. K. Chong, T. K. Yew, "Novel optical scanner using photodiodes array for two-dimensional measurement of light flux distribution", *IEEE Transactions on Instrumentation and Measurement*, pp. 2918-2925, 2011.

APPENDIX I

28th European Photovoltaic Solar Energy Conference and Exhibition

A DENSE-ARRAY RECONFIGURATION METHOD TO MINIMIZE MISMATCH LOSSES IN A NON-IMAGING PLANAR CONCENTRATOR SYSTEM FOR THE 28th EU PVSEC 2013

Fei-Lu Siaw*, Kok-Keong Chong
Faculty of Engineering and Science, Universiti Tunku Abdul Rahman,
Off Jalan Genting Kelang, Setapak, 53300 Kuala Lumpur, Malaysia.

ABSTRACT: In this paper, a systematic interconnection optimization method for dense-array concentrator photovoltaic system is presented. By analyzing all possible array configurations, it is possible to determine the most optimal dense-array configuration. The proposed fast-prediction method is very useful as a preliminary assessment because it is systematic, simple and reasonably accurate. As a case-study, *I-V* curve predictions are simulated for a non-imaging planar concentrator prototype to find all possible array configurations. From the results, the configuration which yields the highest output power is determined. A dense-array based on the best configuration is then simulated with detail using Matlab modeling. The acquired *I-V* curve from Matlab was found to closely resemble the simulated FPM *I-V* curve predictions, and output power variation is only 1.88%
Keywords: Multijunction Solar Cell, Concentrator, Performance

1 INTRODUCTION

All solar concentrators face the common problem of non-uniform flux distribution, which is mainly contributed by factors such as the design of concentrator optics, slope errors in concentrator profile, tracking error, misalignment of concentrator, as well as the condition of refractive lens and reflecting mirrors. While some of the mentioned causes such as the concentrator optics design and tracking error could be minimized by implementing improved optical design and more accurate tracking methods, factors like the imperfections of refractive lens or reflecting mirrors are inevitable [1-3].

When an array of series-connected solar cells is subjected to non-uniform irradiation, current mismatch will occur, which leads to a degradation of output power. To avoid mismatch losses, a CPV dense-array's interconnection should be designed according to its concentrator's flux distribution pattern. Optical and electrical design considerations were first introduced by Tallent in 1963, as a basic guideline to predict the performance of a CPV panel operating under low concentration [4]. However, that study did not discuss non-uniformity matters. Therefore, a systematic optimization method for dense-array concentrator systems is proposed in this paper. In our optimization approach, a new fast-prediction method (FPM) of CPV cell using three-point model (TPM) is introduced to analyze large dense-array. Using this method, the performance of dense-array CPV system can be optimized via best interconnection for any type of solar concentrator such as parabola, lens and non-imaging planar concentrator, using standard-sized CPV cells in the market. As a case-study we have chosen to optimize the dense-array configuration of a non-imaging planar concentrator (NIPC) prototype in the campus of Universiti Tunku Abdul Rahman (UTAR), Malaysia. (Figure 1)

2 MATERIALS AND METHODS

Conventionally, designing CPV dense-array for solar concentrator system is a trial and error exercise that is fairly complex, time consuming, and very dependent on a designer's approach and experience. This process starts with an initial design based on a designer's preference and if results are not satisfactory, the design will be discarded and another trial design process is restarted from the beginning. This process is repeated for a few times to find further possible trial designs, and finally all trial designs are analyzed to find the most optimum one that yields the best power output. This exhaustive process takes a long time until a good dense-array design is established. Differing to that approach, we are proposing a novel FPM that is systematic, fairly accurate and comprehensive. A summary of the whole process from the start up till a satisfactory result is obtained (Figure 2).

Figure 1: A non-imaging planar concentrator (NIPC) prototype.

For solar concentrators, it is essential to measure its solar flux distribution on the receiver after any alignment of optical components. An optical scanner equipped with a row of calibrated InGaP/InGaAs/Ge cells of the size 1.0 cm × 1,0 cm is installed at the receiver to retrieve a 2-D solar flux distribution. The device setup information for the optical scanner is similar to our previous publication except the sensors used there were photodiodes with lower limit of irradiance [5-6]. When the focused image is well at the center of the receiver, measurements of flux distributions were made and the data is later correlated to absolute irradiance level across each CPV cell location on the array.

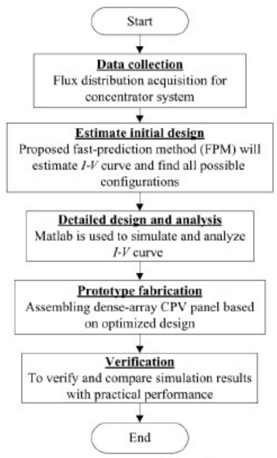

Figure 2: A systematic approach in designing dense-array

Referring to the Figure 3, it can be observed that the solar cells that are near to the corners are exposed to low solar concentration, mainly due to solar disc effect. Since the current of an array will follow the lowest current of a series-connected assembly, the mentioned cells will cause higher current mismatch, which leads to more power losses.

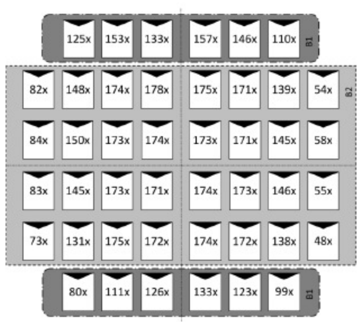

Figure 3: The solar concentration ratio at each CPV cell's location is determined using measured flux distribution data.

The next step after completing flux distribution data measurements is the initial design estimation stage. In this paper, we are introducing a new approach to formulate the initial design, which is by TPM *I-V* curve. The basic principle of the TPM *I-V* curve prediction is presented in Figure 4 where the nonlinear *I-V* curve is predicted using three critical points for each solar cell. The three points consist of the parameters short-circuit current (I_{sc}), open-circuit voltage (V_{oc}), and voltage of the maximum power point (V_{mp}). Since ΔI is very small as the current value at the maximum power point, (I_{mp}) is usually very close (97% - 98%) to I_{sc}. Therefore the TPM model approximates maximum power point to (V_{mp}, I_{sc}) instead of (V_{mp}, I_{mp}). The rationale of this fast modeling approach is to use lesser parameters to save on computing time, while still producing reasonably accurate approximation modelling results.

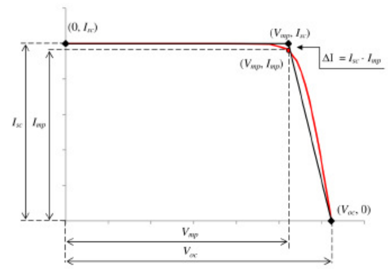

Figure 4: An *I-V* curve of a solar cell (red line) is superimposed with TPM prediction model (black line), consisting three critical points, namely (0, I_{sc}), (V_{mp}, I_{sc}) and (V_{oc}, 0)

For a large array consisting of *x* rows and *y* column of elements, it is critical to know all possible dense-array configurations so that no possible solutions are left-out. The process of determining all possible dense-array configurations starts by checking the number of cells that are present at the corresponding row and calculating the number of cells in a basic module, *p*:

$$p = N_{cell} / d \tag{1}$$

where *d* is the number of basic modules per row (integer number: 1, 2, 3, etc.) and N_{cell} is the total number of cells per row. In this study, only integer whole numbers of cells are accepted to be used as a basic module. The minimum value of *p* is 1, which means that only one CPV cell form a basic module, and this is the smallest basic module size.

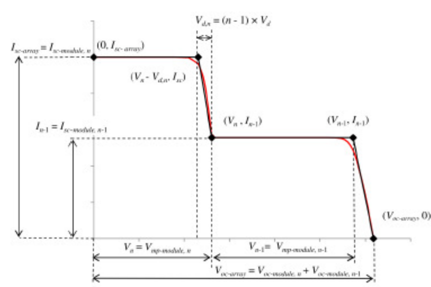

Figure 5: This figure shows critical points of the new approximation model (black line), with two series-connected string in an array ($n = 2$).

In Figure 5, an example array consisting two modules is presented. In this figure, the output power of each critical point in the array can be calculated by multiplying the voltage to its respective current value. The maximum output power (P_{mp}) of a well-designed array of minimal current mismatch normally occurs on the point (V_1, I_1). For a large series-connected array, some points may appear in the negative voltage, and in these cases y-axis is realigned while the value of $I_{sc\text{-}array}$ is revised to be the array current that crosses the y-axis instead of the highest array current.

The next stage of FPM is to determine the best configuration. In this section, careful analysis is carried out to determine the best option that gives the highest output power, from the sixteen possible configurations using the modes method (Figure 6). Based on the results of FPM, the best configuration is 2 × 6 (B1) and 8 × 4 (B2). Besides having the highest output power, power density of this configuration is also the highest at 2.58 W /cell.

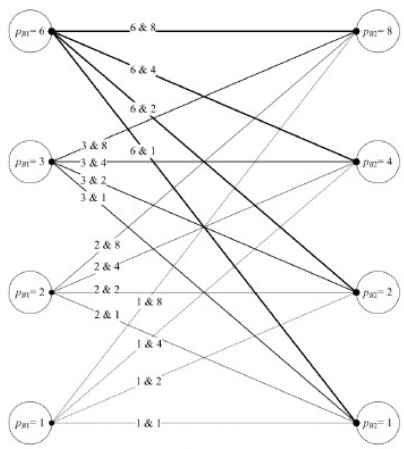

Figure 6: In total, there are sixteen possible configurations using nodes method

3 RESULTS

After carrying out initial design process, a more comprehensive computer simulation is carried out using Matlab Simulink. This detailed simulation includes effects of non-uniform solar distribution as well as solar cells' operating temperature to achieve more accurate *I-V* and *P-V* plots. In our previous publications, a special modeling method using Simulink in Matlab have been developed [7]. For this study, the most optimum dense-array layout configuration is built in Simulink and the simulation results are presented in Figure 7, based on direct normal irradiance (DNI) 641 W/m^2 and operating temperature 55 °C. It was found that the estimation of maximum output power that was computed from FPM which is 113.64 W is very close to a simulation result from Simulink which is 111.54 W.

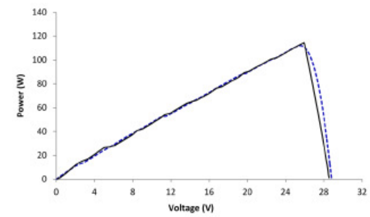

Figure 7: The Matlab simulated *P-V* curve of optimized array (blue dashed line) is compared to FPM simulation curve (black line)

4 DISCUSSION AND CONCLUSION

Conventionally, CPV dense-array design is an exhaustive iterative process to achieve a preset output power requirement based on a trial design. Nevertheless, target-based design approach is not comprehensive because not all dense-array configuration possibilities are explored and analysed. In this study a systematic method is introduced in achieving the most optimal dense-array design using the newly proposed FPM at the initial design phase.

By optimizing a dense-array layout configuration, the best configuration of 2 × 6 (B1) and 8 × 4 (B2) is found. Once the initial design of dense-array has been completed, detailed computer simulations are carried out to check the prediction. Comprehensive simulation using Matlab has verified the proposed FPM prediction with the value of P_{mp} having only 1.88 % in error. The next step of this work is to proceed with an actual assembly of dense-array based on the optimised interconnection configuration and to install the optimised dense-array assembly on the NIPC prototype for verification purpose. The results from actual field measurements will be presented in our future publications to complete our findings.

5 REFERENCES

[1] D. Faiman, S. Biryukov, K.K. Pearlmutter, PETAL: A Research Pathway to Fossil-competitive Solar Electricity. In Proceedings of the 29th IEEE Photovoltaic Specialist Conference, New Orleans, USA (2002) 1384-1387.

[2] K.K. Chong, C.W. Wong, F.L. Siaw, T.K. Yew, Optical Characterization of Nonimaging Planar Concentrator for the Application in Concentrator Photovoltaic System. J. Sol. Energy Eng., Vol. 132 (2010) 011011.1-011011.9

[3] H. Baig, K.C. Heasman, T.K. Mallick, Non-uniform Illumination in Concentrating Solar Cells, Renew. Sustainable Energy Rev., Vol. 16 (2012) 5890-5909.

[4] R.J. Tallent, Optical Electrical Design Considerations for Concentrating Solar Cell Panels, IEEE Trans. Appl. Ind., Vol. 82 (1963) 169-174.

[5] K.K. Chong, K.K, T.K. Yew, Novel Optical Scanner using Photodiodes Array for Two-dimensional Measurement of Light Flux Distribution. IEEE Trans. Instrum. Meas., Vol. 60, (2011) 2918-2925.

[6] K.K. Chong, T.K. Yew, C.W. Wong, S.L. Lau, Study of Image Quality of Mirror via Solar Flux Distribution Measurement Using a Novel High Speed Optical Scanner. Appl. Optic, Vol. 50, (2011) 4927-4935.

[7] F.L. Siaw, K.K. Chong, C.W. Wong, A Comprehensive Study of Dense-array Concentrator Photovoltaic System Using Non-imaging Planar Concentrator, Renewable Energy (2014) 542-555.

APPENDIX J

Hindawi Publishing Corporation
The Scientific World Journal
Volume 2013, Article ID 275169, 11 pages
http://dx.doi.org/10.1155/2013/275169

Research Article

A Systematic Method of Interconnection Optimization for Dense-Array Concentrator Photovoltaic System

Fei-Lu Siaw and Kok-Keong Chong

Faculty of Engineering and Science, Universiti Tunku Abdul Rahman, Off Jalan Genting Kelang Setapak, 53300 Kuala Lumpur, Malaysia

Correspondence should be addressed to Fei-Lu Siaw; jessiesiaw@gmail.com and Kok-Keong Chong; chongkk@utar.edu.my

Received 23 September 2013; Accepted 4 November 2013

Academic Editors: A. Atimtay, A. Durmus, and A. Greco

This paper presents a new systematic approach to analyze all possible array configurations in order to determine the most optimal dense-array configuration for concentrator photovoltaic (CPV) systems. The proposed method is fast, simple, reasonably accurate, and very useful as a preliminary study before constructing a dense-array CPV panel. Using measured flux distribution data, each CPV cells' voltage and current values at three critical points which are at short-circuit, open-circuit, and maximum power point are determined. From there, an algorithm groups the cells into basic modules. The next step is *I-V* curve prediction, to find the maximum output power of each array configuration. As a case study, twenty different *I-V* predictions are made for a prototype of nonimaging planar concentrator, and the array configuration that yields the highest output power is determined. The result is then verified by assembling and testing of an actual dense-array on the prototype. It was found that the *I-V* curve closely resembles simulated *I-V* prediction, and measured maximum output power varies by only 1.34%.

1. Introduction

Nonuniform flux distribution is a common problem that can be found in all solar concentrator systems [1, 2]. Some of the main contributors to nonuniform illumination are limitation in the design of concentrator optics, slope errors in concentrator profile, tracking error, misalignment of concentrator, and the condition of refractive lens or reflecting mirrors. Some of the causes mentioned such as concentrator optics design and improper tracking could be minimized by implementing new optical design and using improved tracking methods, other causes such as the condition of refractive lens or reflecting mirrors are inevitable defects that are introduced while manufacturing and installation or due to aging. The defects include discoloration of concentrator optics, shape changing, and mechanical fatigue, buckling, and warping [3].

A concentrator photovoltaic (CPV) system performance is affected when there is nonuniform illumination especially for densely packed CPV cells array. When the array is operating under nonuniform illumination, current mismatch will happen among the cells that are connected in series, causing degradation to output power [4]. In single optic/single cell CPV systems that have optical units that are all reasonably well aligned and hence produce the same incident power to all individual CPV cells, current mismatch problem is less critical. In a large array of CPV receivers, usually Fresnel lens system, an additional secondary optical element (SOE) such as flux homogenizer is added to produce uniform illumination [5, 6]. The optical homogenizers that produce uniform flux distribution over solar cells minimize conversion losses caused by chromatic aberration and surface voltage variation. Nevertheless, the additional SOE increases manufacturing cost and the complexity of solar concentrator system [7, 8].

Another method of improving system performance is by adopting nonconventional geometry of CPV cells, in an attempt to improve optical mismatch. For example, a radial large area Si-cell receiver uses custom-shaped cells that divide the incident flux evenly between the cells, as discussed by Vivar et al. [9]. It was presented that the losses from nonuniformity and misalignment decrease by nearly

6 times lesser as compared to a full series connection [10]. However, this method is still vulnerable to tracking errors and optical misalignment. On the other hand, AZUR SPACE Solar Power GmbH also developed custom-sized dense-array modules for the application in parabolic concentrator systems. In their design, dense-array modules consisting of four different geometries of solar cells are arranged in a manner that compensates inhomogeneous illumination. As an example, the outer section of the array that receives lesser light is compensated by using wider segments of CPV module. To avoid higher investment cost from having too many uniquely-sized CPV modules, it is finally reduced from four to two different solar cell types throughout a dense-array [11]. Needless to say, this approach compromised optical matching of the modules. Segev and Kribus introduced High-Voltage silicon Vertical Multijunction (VMJ) cells that were designed for parallel connection in a dense-array [12]. With a parallel connection, voltage matching rather than series matching is attempted to reduce mismatch losses under nonuniform illumination. The new VMJ modules exhibit greater tolerance to nonuniform illumination and tracking errors. Despite the advantages of the new cells, a dense-array that is interconnected in parallel rather than in series will yield a high array current because current from each CPV module is added up. The effect of high array current to resistive losses needs to be further studied to ensure that the overall system efficiency is not jeopardized.

For a CPV system to be cost effective, the whole system should be designed to operate optimally. In fact, a CPV dense-array's interconnection should be arranged according to solar flux distribution pattern of solar concentrator system. In 1963, optical and electrical design considerations were first introduced by Tallent as a basic guideline to predict the performance of a CPV panel for V-trough systems [13]. Nevertheless, this study only covers dense-array CPV panel operating under low concentration and does not discuss nonuniform ity problem. Addressing this need, a systematic method of optimizing performance of dense-array concentrator photovoltaic system under nonuniform illumination is proposed. In addition, this paper also introduces a new fast prediction model of CPV cell using three-point model (TPM) to analyze large and complicated interconnected dense-array cells. The TPM approximation method is fast, and reasonably accurate for optimization purposes, before we go for the comprehensive *I-V* curve simulation. In our method, we can optimize the performance of dense-array CPV system via best electrical interconnection of solar cells for any concentrator such as parabola, lens, and nonimaging concentrator with the use of any standard CPV cells in the market. The procedure of our method is described as follows. First, a dense-array size of any standard sized CPV cells available in the market is estimated based on the flux distribution of a solar concentrator. The array of cells then goes through a computer algorithm that can automatically reconfigure the array of CPV cells in all possibilities and then estimating the output power for each possible configuration. By comparing the output power predicted by the algorithm, a dense-array is selected for assembly. As a case-study, we applied this systematic approach to design and develop an optimized dense-array for a nonimaging planar concentrator. The finalized assembly is installed onto a concentrator prototype, and results such as current-voltage (*I-V*) curve, maximum power (P_{mp}) and fill factor (FF) are compared to the TPM prediction model.

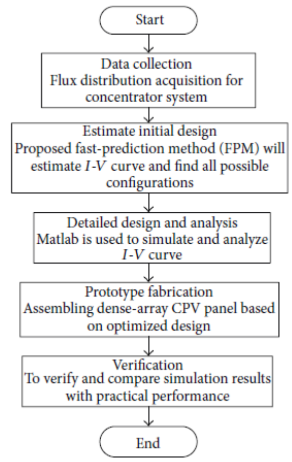

Figure 1: An algorithm to show systematic and complete approach in achieving high-performance dense-array using a newly proposed fast prediction method (FPM) at the second process, which is initial design phase.

2. Materials and Methods

Designing CPV dense-array for a concentrator system is a fairly complex process. Conventionally, a trial and error practice that is very dependent on a designer's approach is used to estimate initial design. After first estimation it is necessary to carry out a comprehensive and detailed design to get preliminary results. If the results are not satisfactory, the first design is discarded and another trial design is started from initial design stage again [14]. This process is repeated for a few times based on the system designer's experience to find other possible trial designs. Finally, the trial designs are analyzed to deterimine the best and most optimized one. The optimized design is then verified by experiments. This iterative process is exhaustive and it takes a long time to come up with a good and optimal dense-array design that suits a solar concentrator system. In this paper, a novel fast-prediction method (FPM) that is both systematic and fairly accurate is proposed to replace conventional trial and error practice based on a system designer's experience, intuition and mathematical analysis. An algorithm of the whole process from start until a satisfactory design is presented in flow chart as shown in Figure 1, while four stages of the newly proposed FPM approach for optimizing dense-array design are shown in Figure 2.

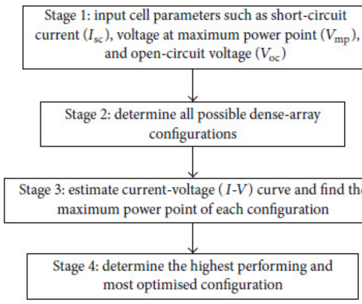

FIGURE 2: A detailed description showing all four stages of FPM.

FIGURE 3: A prototype of nonimaging planar concentrator (NIPC) in the campus of Universiti Tunku Abdul Rahman (UTAR), Malaysia.

2.1. Flux Distribution Measurement. Referring to Figure 1, a dense-array design process starts with data collection of the solar concentrator. An NIPC prototype located in Universiti Tunku Abdul Rahman (UTAR) (3.22° North, 101.73° East) is chosen as a case study for this research paper [15]. Using azimuth-elevation sun-tracking method, the concentrator orientation is driven by stepper motors for maintaining its tracking position throughout the day, as presented by Chong and Wong [16]. The concentrator frame holds 192 flat mirrors that are individually prealigned to focus sunlight towards the target. Three outer rings of mirrors as well as some mirrors at the center of the concentrator were not included in this study due to serious blocking between mirrors and shading by the receiver (refer to Figure 3).

After the alignment of optical components is completed, it is essential to measure solar flux distribution on the receiver. An optical scanner equipped with a row of calibrated InGaP/InGaAs/Getriple-junction cells of the size 1.0 cm × 1.0 cm is installed on the receiver to scan along the column direction for retrieving a 2D solar flux distribution. The device setup information of the optical scanner has been presented in our previous publications except the sensors used earlier which were photodiodes with lower limit of irradiance level [17, 18]. During sun-tracking, measurements of flux distribution were made when the image is well focused at the center of the receiver. The measured data are then correlated to absolute irradiance level and presented in Figure 4. Looking at the concentration levels of cells in the Figure 4(a), it is observed that corner cells are exposed to very low solar concentration due to solar disc effect. Since the current of an array follows the lowest current of a series-connected assembly, the corner cells contribute to higher current mismatch, which leads to greater power loss. Hence, current mismatch can be minimized by omitting the corner cells and it might lead to better performance of the overall dense-array. As a comparison between the array with corner cells and array without corner cells, two CPV array arrangements are investigated, namely, (a) array arrangement A with flux distribution A and (b) array arrangement B with flux distribution B.

2.2. Development of FPM. After completing flux distribution data measurements, we proceed to the second process which is to estimate initial design. In this section, we introduce a new approach to formulate the initial design by analyzing TPM *I-V* curve that is useful for the application in a solar concentrator system. The basic principle of the TPM *I-V* curve prediction is to approximate the nonlinear *I-V* curve by using three critical points of each solar cell as presented in Figure 5. In stage 1 of the TPM prediction model, *I-V* curve of each solar cell is represented by three points which are $(0, I_{sc})$, (V_{mp}, I_{sc}), and $(V_{oc}, 0)$. The three points consist of the parameters short-circuit current (I_{sc}), open-circuit voltage (V_{oc}), and voltage of the maximum power point (V_{mp}). As observed from the figure mentioned, ΔI is very small as the current value at the maximum power point (I_{mp}) is usually very close (97%-98%) to I_{sc}. Hence, the TPM model approximates maximum power point to (V_{mp}, I_{sc}) instead of (V_{mp}, I_{mp}). The rationale of this fast modeling approach is to produce a reasonably accurate approximation model with lesser parameters to save on computing time.

In a large array consisting of x rows and y columns of elements, the location of each element/solar cell is represented by $S_{x,y}$ in total-crosstied (TCT) connection (Figure 6). To accurately predict the *I-V* characteristics, solar concentration value (C) of each CPV cell is required for retrieving the corresponding parameters such as I_{sc}, V_{oc}, and V_{mp}. These values are then stored in three different matrix files in Matlab environment to be used for sorting.

2.3. Determining All Possible Dense-Array Configurations. In our analysis, all solar cells in a basic module are deemed to be connected in parallel and the connection between basic modules is in series. The process of determining all possible dense-array configurations starts by checking the number of

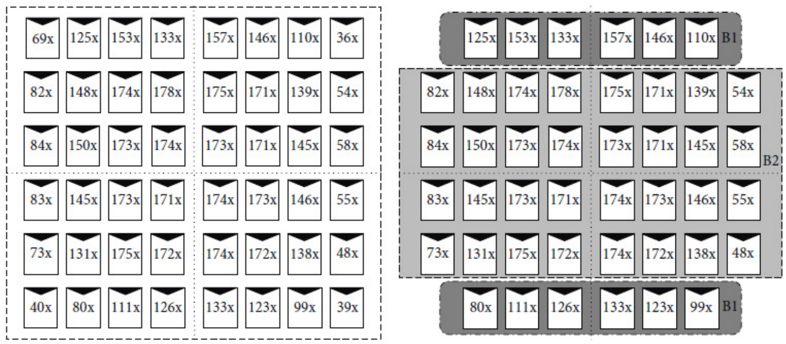

(a) Array arrangement A with flux distribution A (b) Array arrangement B with flux distribution B

Figure 4: By using measured flux distribution data, the solar concentration ratio at each CPV cell's location is determined. In this study, two dense-array arrangements for two flux distributions are considered, namely, (a) array arrangement A with flux distribution A and (b) array arrangement B with flux distribution B.

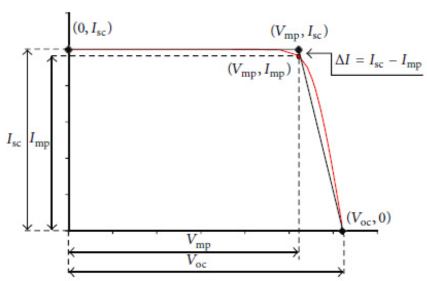

Figure 5: An I-V curve of one solar cell (red line) is superimposed with a new TPM prediction model (black line), consisting three critical points, namely, $(0, I_{sc})$, (V_{mp}, I_{sc}), and $(V_{oc}, 0)$.

Figure 6: A general network connection of solar cells in an assembly comprising x rows and y columns of elements.

cells that are present at the corresponding row. The number of cells in a basic module (p) can be calculated as follows:

$$p = \frac{N_{cell}}{d}, \quad (1)$$

where d is the number of basic modules per row (integer number: 1, 2, 3, etc.) and N_{cell} is the total number of cells per row. In this study, we have set that only integer whole numbers of cells are accepted to be used as a basic module. The minimum value of p is 1, which means that only one CPV cell forms a basic module and this is the smallest basic module size.

Referring to Figure 4(a), every row in the array consists of eight cells. Using (1), we can calculate every possible number of cells in a basic module for different array configurations. All possible values of p for Figure 4(b) are listed in Table 1. From that table, we can see that the cells in region B1 can be connected in four parallel configurations as a basic module, which are six solar cells in parallel ($p_{B1} = 6$), 3 solar cells in parallel ($p_{B1} = 3$), 2 solar cells in parallel ($p_{B1} = 2$), and only one cell in a basic module ($p_{B1} = 1$). On the other hand, the region B2 consists of eight solar cells in parallel ($p_{B2} = 8$), 4 solar cells in parallel ($p_{B2} = 4$), 2 solar cells in parallel ($p_{B2} = 2$), and 1 solar cell in a basic module ($p_{B2} = 1$). As for array arrangement A, the total number of cells in a row is the same throughout the array and thus the values of calculated p are similar.

In flux distribution A, the array consists of equal number of cells in every row. Due to this, series connection is straightforward which are 48×1 cells ($p = 1$), 24×2 cells ($p = 2$), 12×4 cells ($p = 4$), and 6×8 cells ($p = 8$). With the configurations mentioned, I-V prediction is made. However, flux distribution B (refer to Figure 4(b)) shows that regions B1 and B2 consist of different number of cells in a row. Hence,

Table 1: Calculation of p for flux distribution B.

Integer (d)	$p_{B1} = N_{cell}/d$ (In region B1, $N_{cell} = 6$)	$p_{B2} = N_{cell}/d$ (In region B2, $N_{cell} = 8$)
1	6	8
2	3	4
3	2	—
4	—	2
5	—	—
6	1	1
7	—	—
8	—	1

it is recommended to break the array into two groups which are the arrays that consist of 6 cells in region B1 (top row and bottom row that consists of six cells), and B2 (rows located at the center that consist of 8 cells each). Using the nodes method, a total of sixteen possible configurations are found for array arrangement B (see Figure 7).

2.4. Dense-Array Current-Voltage (I-V) Characteristics Prediction. From Figure 8, the flow chart starts by initializing counting parameters that will be used throughout the algorithm. Based on calculated p, new values of module short-circuit current ($I_{\text{sc-module}}$), module open-circuit voltage ($V_{\text{oc-module}}$), and module voltage at maximum power point ($V_{\text{mp-module}}$) are calculated row by row until the whole array is completed (see Figure 8). The equations used to calculate the three new parameters can be found in the flow chart, where (x, y) represents the position of cell at xth row and yth column of array arrangement as shown in Figure 6, N_{row} is the total number of rows, and N_{column} is the total number of columns in a CPV array.

Next, module values of the entire solar cell array, that is, $I_{\text{sc-module}}$ and $V_{\text{oc-module}}$, are sorted based on decreasing order of $I_{\text{sc-module}}$ value. The module that produces the highest $I_{\text{sc-module}}$ is reassigned to $I_{\text{sc-module},n}$, while its corresponding module open-circuit voltage and module voltage at maximum power point are also reassigned accordingly to $V_{\text{oc-module},n}$ and $V_{\text{mp-module},n}$, respectively. Here, n is defined as the total number of basic modules in the array configuration. Besides that, this modeling assumes that each basic module is protected with a parallel-connected bypass diode in the opposite polarity. When a basic module receives lower solar irradiance, bypass diode(s) will be forward biased so that the current of the array can safely pass through. When array current passes through bypass diodes, the diodes will turn on and hold its corresponding group of cells to a small negative voltage which will limit any further drop in the total voltage of the array. Bypass diode's forward voltage ($V_{d,n}$) is calculated with the equation

$$V_{d,n} = (n-1) \times V_d, \tag{2}$$

where n is also the total number of series-connected basic module in an array. $I_{\text{sc-module},1}$ is the lowest in the string when $n = 1$ and $V_{d,1} = 0$. To complete the I-V curve, array open-circuit voltage and array short-circuit current are calculated. At short-circuit condition, array current is equivalent to the highest current value, when voltage is zero $(0, I_{\text{sc-array}})$; at open-circuit condition, array current is zero and the array voltage is $(V_{\text{oc-array}}, 0)$ as shown in (3). The value of

$$V_{\text{oc-array}} = \sum_{i=1}^{n} V_{\text{oc-module},i}. \tag{3}$$

With all of the values mentioned, critical points of the new array are found. In Figure 9, an example of an array with two modules is presented. In this figure, the output power of each critical point in the array can be calculated by multiplying the voltage to its respective current value. The maximum power (P_{mp}) of a well-designed array of minimal current mismatch normally occurs on the point (V_1, I_1). For a dense-array with more series-connected modules, an illustration of the I-V critical points is presented in Figure 10. For a large series-connected array, some points may appear in the negative voltage, and in these cases y-axis is realigned while the value of $I_{\text{sc-array}}$ is revised to be the array current that crosses the y-axis (Figure 11) instead of the highest array current.

The fourth stage of FPM (refer to Figure 2) is to determine the best configuration with the highest performance. In this section, careful analysis is carried out to determine the best option. A summary of simulated I-V curve results for both flux distributions based on FPM approach is shown in Table 2. From column P_{mp} in the table, it can be observed that the maximum output power from simulation 4 and 6 is the highest among all configurations. Since both output power values are similar, further analysis is necessary. Despite fill factor (FF) being commonly used to evaluate the performance of single solar cell, it does not work the same for dense-array solar cells with I-V curve containing multiple current mismatch steps. According to Vorster and Dyk, although FF typically depends on the series and shunt resistance of the cells in the module to relatively reflect the performance quality of the module, the FF does not consider the presence of reverse-bias steps and hence is not useful for measuring the quality of the array I-V curve that consists of current mismatched cells [19, 20]. Furthermore, array current cannot be precisely determined using FPM if there is any serious current mismatch in the circuitry.

Power density is another important evaluation criterion when finalizing the initial design of dense-array, and its equation is presented in the following:

$$\text{Power density} = \frac{P_{\text{mp}}}{(\text{total cells in dense-array})}. \tag{4}$$

Referring to the last column of Table 2, power density of simulation 6 is 2.58 W/cell and it is higher than power density of simulation 4 which yields only 2.37 W/cell. This directly indicates that, in average, each solar cell in simulation 6 generates more output power than simulation 4. In fact, the total number of cells in simulation 6 is lesser (44 cells) than that in simulation 4 (48 cells). As simulation 6 is superior in power density while achieving the highest output power among all configurations, it is finally selected.

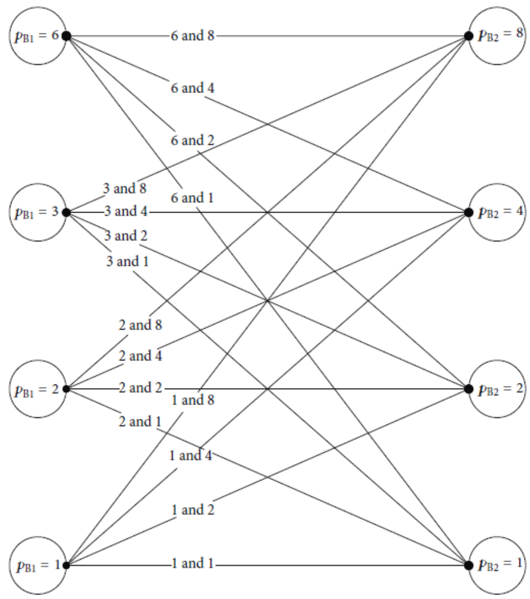

Figure 7: In total, there are sixteen possible configurations for flux distribution B using nodes method.

Table 2: Comparison of different array configurations at DNI: 641 W/m^2.

Simulation no.	Array configuration	Flux distribution	P_{mp} (W)	Fill factor (FF) (%)	V_{mp} (V)	I_{mp} (A)	V_{oc} (V)	I_{sc} (A)	Power density P_{mp}/no. cells (W/cell)
1	48 × 1	*A*	79.36	39.74	77.77	1.02	137.71	1.45	1.65
2	24 × 2	*A*	82.09	41.82	52.98	1.55	68.88	2.85	1.71
3	12 × 4	*A*	91.24	54.96	30.72	2.97	34.44	4.82	1.90
4	6 × 8	*A*	113.62	68.95	15.36	7.4	17.22	9.57	2.37
5	2 × 6 (B1) and 4 × 8 (B2)	*B*	86.01	53.15	15.4	5.58	17.27	9.37	1.95
6	2 × 6 (B1) and 8 × 4 (B2)	*B*	113.64	57.71	25.68	4.43	28.79	6.84	2.58
7	2 × 6 (B1) and 16 × 2 (B2)	*B*	71.63	20.2	46.22	1.55	51.83	6.84	1.63
8	2 × 6 (B1) and 32 × 1 (B2)	*B*	71.09	10.62	61.86	1.42	97.9	6.84	1.62
9	4 × 3 (B1) and 4 × 8 (B2)	*B*	81.69	38.14	9.07	9	23.03	9.3	1.86
10	4 × 3 (B1) and 8 × 4 (B2)	*B*	85.63	51.33	19.35	4.43	34.54	4.83	1.95
11	4 × 3 (B1) and 16 × 2 (B2)	*B*	79.58	40.29	51.36	1.55	57.58	3.43	1.81
12	4 × 3 (B1) and 32 × 1 (B2)	*B*	76.99	21.66	66.99	1.15	103.65	3.43	1.75
13	6 × 2 (B1) and 4 × 8 (B2)	*B*	76.29	28.29	8.47	9	28.78	9.37	1.73
14	6 × 2 (B1) and 8 × 4 (B2)	*B*	82.97	42.64	18.75	4.43	40.29	4.83	1.89
15	6 × 2 (B1) and 16 × 2 (B2)	*B*	87.53	47.17	56.49	1.55	63.33	2.93	1.99
16	6 × 2 (B1) and 32 × 1 (B2)	*B*	82.88	31.44	72.12	1.15	109.4	2.41	1.88
17	12 × 1 (B1) and 4 × 8 (B2)	*B*	60.09	13.93	6.67	9	46.03	9.37	1.37
18	12 × 1 (B1) and 8 × 4 (B2)	*B*	75.01	26.99	16.95	4.43	57.55	4.83	1.70
19	12 × 1 (B1) and 16 × 2 (B2)	*B*	61.7	26.13	60.47	1.02	80.58	2.93	1.40
20	12 × 1 (B1) and 32 × 1 (B2)	*B*	80.58	42.99	78.97	1.02	126.66	1.48	1.83

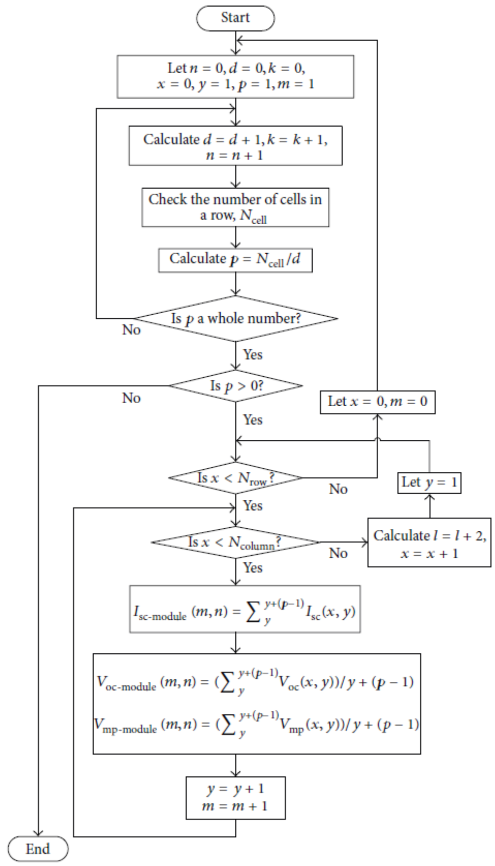

FIGURE 8: Flowchart of a systematic way of I_{sc}, V_{oc}, and V_{mp} grouping.

3. Comprehensive Computer Simulations in Matlab

After the initial design process using FPM approach, a more comprehensive computer simulation is carried out. This detailed simulation includes effects of nonuniform solar distribution and temperature to achieve more accurate *I-V* and *P-V* plots. In our previous publications, a special modeling method using solar cell block from SimElectronics is developed in Matlab to analyze the electrical performance of dense-array [21–23]. For this study, a dense-array with layout configuration of simulation 6 (Table 2) is built in Simulink, and the simulation results are presented in Figures 12 and 13. The simulation was performed for direct normal irradiance (DNI) 641 W/m^2 and operating temperature 55°C. It was found that the estimation of P_{mp} computed from FPM which is 113.64 W is very close to a simulation result from Simulink which is 111.54 W with an error of 1.88%.

4. Results and Discussion

Using the optimized dense-array configuration, a CPV dense-array is designed and constructed accordingly to confirm our computational modeling results. The dense-array is attached onto a copper cooling block so that operating temperature of the CPV cells can be regulated at about 55°C (refer to Figure 14). Using N3300A configurable DC electronic load mainframe installed with two units of N3305A 500 Watts electronic load modules, real time data acquisition of *I-V*

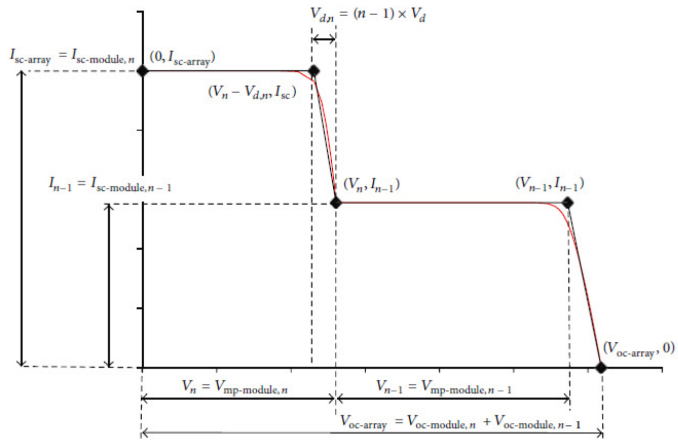

Figure 9: This figure shows critical points of the new approximation model (black line), with two series-connected string in an array ($n = 2$).

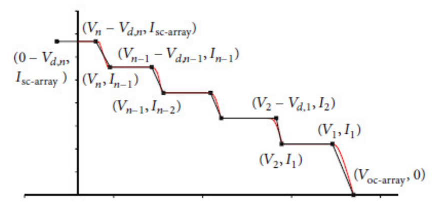

Figure 10: This figure shows the critical points of an array consisting n series-connected basic modules.

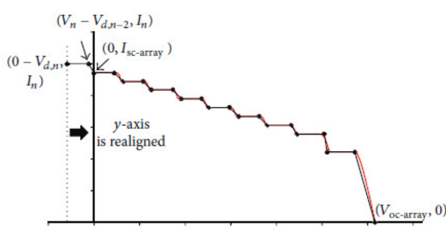

Figure 11: When some critical points lie in the negative voltage region, y-axis should be realigned, and $I_{sc\text{-}array}$ is updated as a current value that crosses the axis.

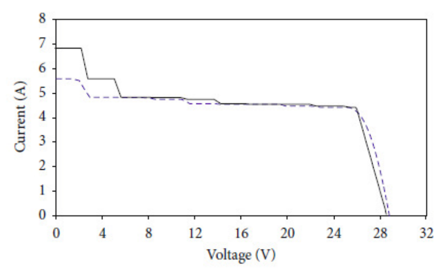

Figure 12: Matlab simulated I-V curve (blue dashed line) of the optimized dense-array is superimposed on FPM simulation curve (black line).

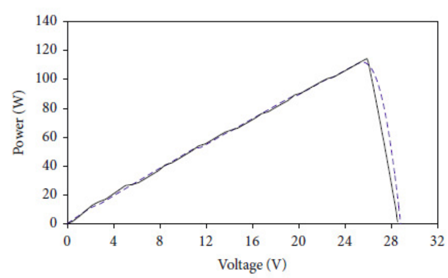

Figure 13: Matlab simulated P-V curve of optimized array (blue dashed line) is compared to P-V curve of FPM simulation curve (black line).

plots was carried out. During I-V data acquisition, supporting information such as dense-array operating temperature, direct normal irradiance (DNI), and global irradiance were measured. This study was performed based on real time measured parameters such as DNI and dense-array operating

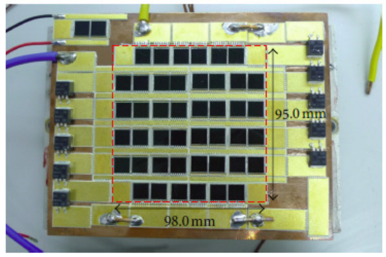

FIGURE 14: A dense-array CPV assembly of proposed optimized configuration from simulation 6 in Table 2, using triple-junction solar cells [24].

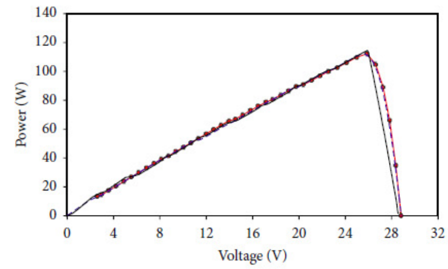

FIGURE 16: *P-V* curve of the optimized array's measured data (red line with dots) is superimposed on FPM simulation curve (black line) and Matlab simulation curve (blue dashed line).

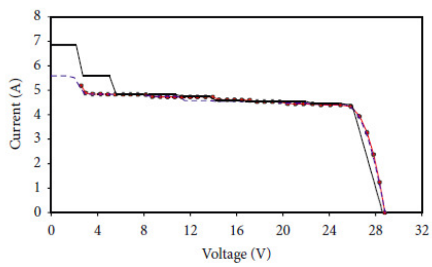

FIGURE 15: *I-V* curve of measured data (red line with dots) acquired during field test is superimposed on FPM simulation curve (black line) and Matlab simulation curve (blue dashed line).

TABLE 3: Comparison between simulated (Matlab) and measured results of the dense-array CPV assembly is presented in terms of maximum output power P_{mp}, maximum voltage V_{mp}, maximum current I_{mp}, array efficiency, and error of maximum output power P_{mp}.

	DNI: 641 W/m^2		
	P_{mp} (W)	V_{mp} (V)	I_{mp} (A)
Measured results	112.14	25.87	4.33
FPM simulated results	113.64	25.68	4.43
Efficiency measured (%)		34.19	
Efficiency simulated (%)		34.64	
Error, P_{mp} (%)		−1.34	

temperature, as well as taking into consideration 15% of optical losses. For comparison purpose, the measured data is superimposed onto simulated *I-V* curve. From Figures 15 and 16, a very close match between measured data and simulated curve is observed, which is only 1.34% of error for P_{mp} (refer to Table 3).

Referring to Figures 15 and 16, the *I-V* curve of measured data acquired during field test matches fairly well with FPM prediction curve. The only obvious difference lies around the area from 0 V to 5.6 V. The presence of steps in the prediction curve indicates that current mismatch happened around that voltage region. These steps are not evident in the measured curve as compared to the prediction curve because the combined string current has reduced when some cells are operating at reverse biased condition [25]. As the calculation from the FPM process is a straight-forward addition of current from parallel-connected cells, a clear indication of current mismatch can be seen and this is very helpful for system designers to evaluate the severity of mismatch in a dense-array design. Furthermore current mismatch at the 0 V to 5.6 V range has negligible effect to the *P-V* curve (see Figure 16). Hence, it will not affect the calculation of P_{mp} of a well-designed dense-array panel, which normally occurs near to V_{oc} region of a *P-V* curve.

5. Conclusion

Conventionally, CPV dense-array design is an exhaustive iterative process to achieve a preset output power requirement. This design approach is not comprehensive because designers do not explore all dense-array configuration possibilities. In this study a systematic and complete method is introduced in achieving the most optimal dense-array design using the newly proposed FPM at the initial design phase. The FPM consists of four stages and is developed to optimize dense-array configurations through a systematic approach instead of conventional trial and error method. The first stage is where cell parameters such as I_{sc}, V_{mp}, and V_{oc} are calculated from measured flux distribution data. After that, every possibility of array configurations is predicted at the second stage of FPM. The third stage deals with *I-V* curve prediction using critical points of solar cells and bypass diodes that are connected across each basic module. Finally, the *I-V* prediction curve is analyzed by comparing with the calculated P_{mp}. This four-stage approach is very systematic, fast and capable to explore all possibilities of dense-array configurations, while maintaining reasonable accuracy. From this method, an optimized configuration in simulation 6 (Table 2) was found to have the highest output power, together with simulation 4. Upon further evaluation, simulation 6 was selected because its power density is superior (2.58 W/cell) as compared to the calculated power density in simulation 4 (2.37 W/cell). By optimizing dense-array layout configuration, simulation 6 with only 44 cells can achieve the same output power as simulation 4 with 48 cells. When lesser solar cells are used, a system designer is able to reduce installation cost while increasing the competitiveness of concentrator solar technology. This finding highlights a new important factor that affects power density which is layout configuration, in addition to the influence of solar concentration. At the same time, it was found that FF is not a conclusive benchmark when evaluating dense-array solar cells. While FF is commonly used to evaluate the quality and performance of a single solar cell, it can only act as a guideline and not a deciding factor when finalizing dense-array design. This can be confirmed when we compare the results of simulation 6 and simulation 4 listed in Table 2. While the FF of simulation 4 is higher (68.95%) as compared to simulation 6 (57.71%), simulation 4 requires more CPV cells to generate the same amount of power as simulation 6. Once the initial design of dense-array has been completed, detailed computer simulations are carried out to verify the prediction. Comprehensive simulation using Matlab has verified the proposed FPM prediction as presented in Section 3 with the value of P_{mp} having only 1.88% in error. Last but not least, an actual assembly of the dense-array was built and installed on an NIPC prototype. The modeling method had been successfully validated with the NIPC prototype to achieve practical conversion efficiency of 34.19% with similar *I-V* curve characteristics. Comparing the results obtained from field measurement with FPM simulated results by evaluating *I-V* and *P-V* curves, a very close match can be observed. It was found that the estimation of P_{mp} by computational modeling is only 1.34% in error.

Conflict of Interests

The authors declare that they have no conflict of interests.

Acknowledgments

The authors would like to express their gratitude to the Ministry of Energy, Green Technology and Water (AAIBE Trust Fund) and the Ministry of Science, Technology and Innovation (e-Science Fund with Project no. 03-02-11-SF0143) for their financial support. The authors would also like to thank the project advisor Ir. Dr. Philip Tan Chee Lin, for his support, encouragement, and many insightful suggestions.

References

[1] D. Faiman, S. Biryukov, and K. K. Pearlmutter, "PETAL: a research pathway to fossil-competitive solar electricity," in *Proceedings of the 29th IEEE Photovoltaic Specialists Conference*, pp. 1384–1387, New Orleans, La, USA, May 2002.

[2] K. K. Chong, C. W. Wong, F. L. Siaw, and T. K. Yew, "Optical characterization of nonimaging planar concentrator for the application in concentrator photovoltaic system," *Journal of Solar Energy Engineering*, vol. 132, no. 1, Article ID 011011, 9 pages, 2010.

[3] H. Baig, K. C. Heasman, and T. K. Mallick, "Non-uniform illumination in concentrating solar cells," *Renewable & Sustainable Energy Reviews*, vol. 16, pp. 5890–5909, 2012.

[4] D. Nguyen and B. Lehman, "An adaptive solar photovoltaic array using model-based reconfiguration algorithm," *IEEE Transactions on Industrial Electronics*, vol. 55, no. 7, pp. 2644–2654, 2008.

[5] K. Araki, M. Kondo, H. Uozumi, N. J. Ekins-Daukes, Y. Kemmoku, and M. Yamaguchi, "Achievement of 27% efficient and 200 Wp concentrator module and the technological roadmap toward realization of more than 31% efficient modules," *Solar Energy Materials and Solar Cells*, vol. 90, no. 18-19, pp. 3312–3319, 2006.

[6] K. K. Chong, S. L. Lau, T. K. Yew, and P. C. L. Tan, "Design and development in optics of concentrator photovoltaic system," *Renewable & Sustainable Energy Reviews*, vol. 19, pp. 598–612, 2013.

[7] P. Benítez, J. C. Miñano, P. Zamora et al., "High performance fresnel-based photovoltaic concentrator," *Optics Express*, vol. 18, no. 9, pp. A25–A40, 2010.

[8] M. Victoria, C. Dominguez, I. Anton, and G. Sala, "Comparative analysis of different secondary optical elements: effective concentration, acceptance angle and light distribution," in *Proceedings of the 24th European Photovoltaic Solar Energy Conference*, pp. 755–759, Hamburg, Germany, September 2009.

[9] M. Vivar, C. Morilla, I. Anton, and G. Sala, "Si-cells radial parquet for parabolic dish receivers," in *Proceedings of the 24th European Photovoltaic Solar Energy Conference*, pp. 141–144, Hamburg, Germany, September 2009.

[10] M. Vivar, I. Antón, and G. Sala, "Radial CPV receiver," *Progress in Photovoltaics: Research and Applications*, vol. 18, no. 5, pp. 353–362, 2010.

[11] R. Lockenhoff, T. Kubera, and K. D. Rasch, "Water cooled TJ dense-array modules for prabolic dishes," in *Proceedings of the 6th International Conference on Concentrating Photovoltaic Systems (CPV '10)*, pp. 43–46, Freiburg, Germany, September 2010.

[12] G. Segev and A. Kribus, "Performance of CPV modules based on vertical multijunction cells under non-uniform illumination," *Solar Energy*, vol. 88,, pp. 120–128, 2013.

[13] R. J. Tallent, "Optical electrical design considerations for concentrating solar cell panels," *IEEE Transactions on Industry Applications*, vol. 82, pp. 169–174, 1963.

[14] J. S. Arora, *Introduction to Optimum Design*, chapter 1, Elservier Academic Press, 2nd edition, 2004.

[15] K. K. Chong and W. C. Tan, "Study of automotive radiator cooling system for dense-array concentration photovoltaic system," *Solar Energy*, vol. 86, pp. 2632–2643, 2012.

[16] K. K. Chong and C. W. Wong, "General formula for on-axis sun-tracking system and its application in improving tracking accuracy of solar collector," *Solar Energy*, vol. 83, no. 3, pp. 298–305, 2009.

[17] K. K. Chong and T. K. Yew, "Novel optical scanner using photodiodes array for two-dimensional measurement of light flux distribution," *IEEE Transactions on Instrumentation and Measurement*, vol. 60, no. 8, pp. 2918–2925, 2011.

[18] K. K. Chong, T. K. Yew, C. W. Wong, and S. L. Lau, "Study of image quality of mirror via solar flux distribution measurement using a high speed optical scanner," *Applied Optics*, vol. 50, no. 25, pp. 4927–4935, 2011.

[19] F. J. Vorster and E. E. Van Dyk, "Current-voltage characteristics of high-concentration, photovoltaic arrays," *Progress in Photovoltaics: Research and Applications*, vol. 13, no. 1, pp. 55–66, 2005.

[20] F. J. Vorster, E. E. Van Dyk, and A. W. R. Leitch, "Investigation on the I-V characteristics of a high concentration, photovoltaic array," in *29th IEEE Photovoltaic Specialists Conference*, pp. 1604–1607, May 2002.

[21] F. L. Siaw and K. K. Chong, "Temperature effects on the performance of dense-array concentrator photovoltaic system," in *Proceedings of the IEEE Conference on Sustainable Utilization and Development in Engineering and Technology (STUDENT '12)*, pp. 140–144, Kuala Lumpur, Malaysia, October 2012.

[22] K. K. Chong and F. L. Siaw, "Electrical characterization of dense array concentrator photovoltaic system," in *Proceedings of the 27th European Photovoltaic Solar Energy Conference and Exhibition*, pp. 224–227, Frankfurt, Germany, September 2012.

[23] F. L. Siaw, K. K. Chong, and C. W. Wong, "A comprehensive study of dense-array concentrator photovoltaic system using non-imaging planar concentrator," *Renewable Energy*, vol. 62, pp. 542–555, 2014.

[24] EMCORE Corporation, "Triple-junction high efficiency solar cells for terrestrial concentrated photovoltaic applications," EMCORE Photovoltaics, August 2008.

[25] C. S. Solanki, *Solar Photovoltaics: Fundamentals, Technologies and Applications*, chapter 12, PHI Learning, 2nd edition, 2011.

APPENDIX K

Renewable Energy 62 (2014) 542–555

Contents lists available at ScienceDirect

Renewable Energy

journal homepage: www.elsevier.com/locate/renene

A comprehensive study of dense-array concentrator photovoltaic system using non-imaging planar concentrator

Fei-Lu Siaw*, Kok-Keong Chong, Chee-Woon Wong

Faculty of Engineering and Science, Universiti Tunku Abdul Rahman, Off Jalan Genting Kelang, Setapak, Kuala Lumpur 53300, Malaysia

ARTICLE INFO

Article history:
Received 29 January 2013
Accepted 16 August 2013
Available online 11 September 2013

Keywords:
Non-uniform irradiance
I–V characteristics
Non-imaging planar concentrator
Concentrator photovoltaic
Dense array
Simulink

ABSTRACT

A special modeling method using Simulink has been developed to analyze the electrical performance of dense-array concentrator photovoltaic (CPV) system. To optimize the performance of CPV system, we have adopted computational modeling method to design the best configuration of dense-array layout specially tailored for flux distribution profile of solar concentrator. It is an expeditious, efficient and cost effective approach to optimize any dense-array configuration for any solar concentrator. A prototype of non-imaging planar concentrator (NIPC) was chosen in this study for verifying the effectiveness of this method. Mismatch effects in dense array solar cells caused by non-uniform irradiance as well as sun-tracking error normally happens at the peripheral of the array. It is a crucial drawback that affects the electrical performance of CPV systems because maximum output power of the array is considerably reduced when a current–voltage (I–V) curve has many mismatch steps and thus leads to lower fill factor (FF) and conversion efficiency. The modeling method is validated by assembling, installing and field testing on an optimized configuration of solar cells with the NIPC prototype to achieve a conversion efficiency of 34.18%. The measured results are in close agreement with simulated results with a less than 3% deviation in maximum output power.

1. Introduction

Solar power generation systems, including concentrator photovoltaic (CPV) installations, usually incur a substantial amount of initial investment cost. To offset the cost of expensive semiconductor material and encourage CPV installations, these systems employ comparatively inexpensive optical elements such as mirrors or lenses acting as solar concentrator together with high-efficiency multi-junction solar cells. To further reduce the cost of generated electricity, optimal system design is necessary so that maximum solar energy can be harnessed from CPV cells [1,2]. However, we often find that the delivered electrical power in field conditions is much lower than the array ratings because mismatch losses have affected the current–voltage (I–V) and power–voltage (P–V) curves of the solar cells. Mismatch factors such as soiling, non-uniform irradiance, shading, temperature variations, cell's quality as well as aging of solar cells, all contribute to serious array power reduction in real site testing [3,4].

Non-uniform distribution of concentrated solar irradiance is one of the significant problems faced by most of concentrator systems, especially around the receiver edges, mainly caused by optical design limitations, structure misalignment, and low tracking accuracy. Over the recent years, many studies can be found discussing on the improvement of solar concentrator optical design to produce more uniform solar illumination at high concentrations [5–10]. Nevertheless, the overall output current of CPV cells connected in a dense array arrangement is very much dependent on the solar flux distribution of a solar concentrator. Due to factors such as sunshape, circumsolar effect, aberration, imperfection of mirror's geometry etc., it is impossible to produce perfect uniform illumination on the dense-array CPV receiver and hence causing a significant loss in the overall output power and average conversion efficiency [11–16]. Despite the employment of flat mirrors in the non-imaging planar concentrator (NIPC), the resultant flux distribution from simple super-positioning of all flat mirror images is inevitably non-uniform near the peripheral zone. Hence, a specially designed algorithm has been developed to analyze I–V curve of different dense-array configurations in order to optimize conversion efficiency and improve overall output power. In our study, the measured solar flux distribution of NIPC prototype is matched to every solar cell's location at the receiver. The measured solar flux distribution shows deviation from a perfect uniform distribution

* Corresponding author. Tel.: +60 3 41079802; fax: +60 3 41079803.
E-mail addresses: jessiesiaw@gmail.com (F.-L. Siaw), chongkk@utar.edu.my (K.-K. Chong), wcwoon@utar.edu.my (C.-W. Wong).

0960-1481/$ – see front matter © 2013 Elsevier Ltd. All rights reserved.
http://dx.doi.org/10.1016/j.renene.2013.08.014

owing to various imperfections in practical installation such as mechanical structure and mirror alignment. There are considerable efforts in the study of partially shaded PV array for minimizing mismatch losses through the use of different interconnection methods [17–19]. In this paper, a new approach of Simulink-based computational modeling is proposed to accurately simulate *I–V* and *P–V* curves of CPV dense-array. Various possible configurations have been simulated and analyzed based on real flux distribution of the solar concentrator to obtain the best array configuration. An optimized configuration of CPV array has been constructed for the purpose of verification with an NIPC prototype. The methodology and practical demonstration of CPV dense-array performance optimization are reported in detail.

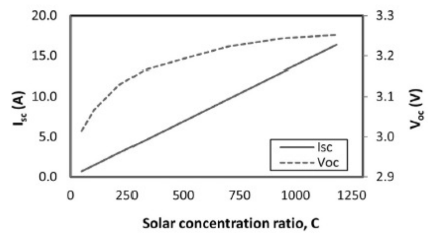

Fig. 2. The relationship of short-circuit current (I_{SC}) and open-circuit voltage (V_{OC}) versus solar concentration ratio from 50× to 1182× for high-efficiency CTJ solar cell.

2. Modeling and simulation of dense array CPV system

2.1. Concentrator photovoltaic (CPV) cell modeling

A comprehensive equivalent circuit model for a triple-junction solar cell can be represented by three current sources connected in series [20]. Nonetheless, not all of the parameters that are required by the model can be readily collected from field measurements nor obtained from a standard manufacturer's datasheet. Therefore the two-diode model, a model that is capable of representing CPV cells, is chosen for this study (Fig. 1). The temperature of solar cell was measured as 55 °C using a k-type thermocouple, and this value is applied in our circuit simulation to improve modeling accuracy.

Solar cell block represented by a single solar cell as current source with two exponential diodes, a parallel resistor (R_P), and connected in series with a series resistance (R_S) are arranged into subsystems in Simulink to form an array. The output current, *I*, can be represented by the equation

$$I = I_{ph} - I_{o1} \times \left(e^{(V+IR_S)/(N_1V_t)} - 1\right) - I_{o2} \times \left(e^{(V+IR_S)/(N_2V_t)} - 1\right) - (V + IR_S)/R_P \quad (1)$$

where I_{ph} is the solar-induced current, I_{o1} is the saturation current of the first diode, I_{o2} is the saturation current of the second diode, V_t is the thermal voltage, N_1 is the diode ideality factor of the first diode, N_2 is the diode ideality factor of the second diode, and V is the voltage across the solar cell. In Simulink, it is possible to choose either an eight-parameter model in which the preceding equation describes the output current or a five-parameter model. In the five-parameter model, two simplifying assumptions are made: the first assumption is that saturation current of the second diode is zero in value and the second assumption is that the impedance of its parallel resistor is infinite. The five-parameter model is good enough to perform a reasonably accurate analysis and we have successfully verified it in the field test that will be presented in the later section.

For this study, the five-parameter model is applied to solar cell blocks from SimElectronics, and therefore solar cells are parameterized in terms of short-circuit current (I_{SC}) and open-circuit voltage (V_{OC}). Both short-circuit current and open-circuit voltage values are common parameters which are readily available in a manufacturer's datasheet or measured as field data. To complete the modeling of the entire array, parameters such as short-circuit current (I_{SC}), open-circuit voltage (V_{OC}), diode ideality factor (N), the series resistance (R_S) and irradiance level of each CPV cell are keyed-in to the program.

2.2. Electrical characteristics of solar cell under high concentration

Main electrical parameters of EMCORE's high efficiency Concentrating Triple Junction (CTJ) cells are extracted from the *I–V* curves of increasing concentration ratios (from 50× to 1182×) from the manufacturer's datasheet using graph digitizing method [21]. This can be achieved by employing WebPlotDigitizer v2.5, or other similar software that are able to automatically follow data lines on a scanned image of high resolution *I–V* curve (refer to Fig. 23 in Appendix) to extract digitized current, voltage and concentration values. Once the axis limits were set, all necessary data points can

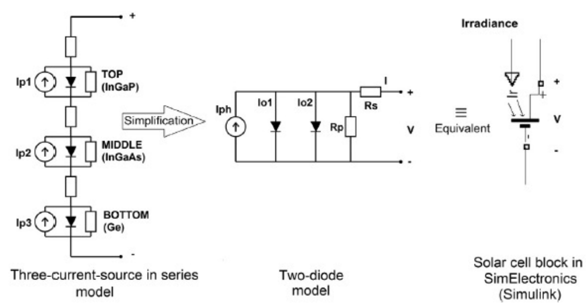

Fig. 1. A schematic diagram to show the representation of a triple-junction solar cell which is simplified from three-current-source in series model to the two-diode model, which is equivalent to a solar cell block in SimElectronics, Simulink.

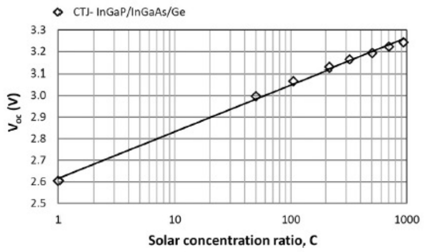

Fig. 3. Linear relationship is shown in a graph plotted between V_{OC} and logarithm of solar concentration ratio (ln C).

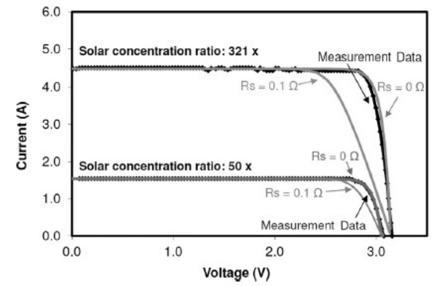

Fig. 4. I–V curves plotted for AM 1.5D, 25 °C conditions, with a comparison to data points extracted from I–V curves in EMCORE datasheet [21]. Note that the introduction of series resistance at solar concentration of 50× and 321× for a triple-junction InGaP/InGaAs/Ge CPV can significantly reduce the performance of solar cell.

be acquired. These data points were selectively checked and confirmed its accuracy with experimental observation on the real solar cell. From there, data were transferred into excel spreadsheets for obtaining the correlation equations of I_{SC} and V_{OC} versus solar concentration ratio (C) with R^2 value of 0.99. For EMCORE's high efficiency CTJ cells, the extracted I_{SC} and V_{OC} data points at varying solar concentration levels are presented in Fig. 2. From Fig. 2, we can find a linear relationship between short-circuit current I_{SC} and solar concentration ratio C whilst open circuit voltage V_{OC} has a logarithmic relation with C. Other electrical parameters such as series resistance (R_S), and diode ideality factor (N) are calculated values from the database of I–V curve.

From the plot of V_{OC} versus C in logarithmic scale as shown in Fig. 3, it can be seen that V_{OC} is gradually rising as ln C increases. At operating temperature T, the curve will follow equation (2) that allows us to find the value of V_{OC}, which is open-circuit voltage of CPV cell at solar concentration ratio C,

$$V_{OC} \cong V_{OC}^1 + N(kT/q)\ln C \tag{2}$$

where N is the effective diode ideality factor, T is the operating temperature (Kelvin), V_{OC}^1 is the open-circuit voltage of the CPV cell under one sun, k is the Boltzmann constant and q is the electron charge. Since the I–V curve data extracted from EMCORE datasheet correspond to current and voltage values at 25 °C, the following equations are applied when the cells are operating at other temperatures [22]:

$$I_{SC,T} = I_{SC-STC} + K_i \Delta T \tag{3}$$

$$V_{OC,T} = V_{OC-STC} + K_v \Delta T \tag{4}$$

where for equation (3), $I_{SC,T}$ is the operating short-circuit current, $I_{SC\text{-}STC}$ is the short-circuit current at Standard Test Conditions (STC), K_i is the short-circuit current temperature coefficient that is provided by the manufacturer (A/°C), $\Delta T = T - T_{STC}$ (°C). On the other hand, in equation (4), $V_{OC,T}$ is the operating open-circuit voltage, $V_{OC\text{-}STC}$ is the open-circuit voltage at STC, and K_v is the temperature coefficient of open-circuit voltage (V/°C).

Referring to Fig. 3, the effective diode ideality factor $N = 3.01$ is derived from curve fitting plots from medium to high solar concentration ratio using equation (2). It agrees with Vossier et al. and King et al. that diode ideality factor for triple-junction CPV is close to 3 which can be derived from V_{OC} versus solar concentration plots from medium to high solar concentration [23,24]. According to Kinsey et al., the diode ideality factor is considered not to be affected by moderate temperature changes [25]. Therefore, diode ideality factor of $N = 3.01$ can still be used when CPV cells are operating at 55 °C during field test.

2.2.1. Series resistance (R_S)

Several methods are well known to be capable of extracting series resistance from solar cell effectively. Generally, it is possible to estimate series resistance (R_S) from two approaches: firstly, obtained from illuminated I–V data; and secondly calculated from I–V data under dark condition. In the illuminated state, electrons are generated homogenously over the whole cell area and also diffuse almost homogenously over to the emitter. As a result, in the illuminated method, a larger lateral electron flow in the emitter is observed and this will provide a more accurate value of series-resistance as compared to the value obtained from the dark I–V data [26]. Therefore, we have adopted the method of estimating series resistance using the slopes of the I–V curves at the point of open-circuit voltage (V_{OC}) under illuminated condition. The estimation of series resistance in our case is done according to the I–V curves at various solar concentration ratios provided by the datasheet and thus it can better characterize CPV cells for our modeling. As illustrated in Fig. 4, an increase in series resistance can degrade the electrical performance of the CPV cell at solar concentration ratios ranging from 50× to 321×. By applying $R_S = 0.1\ \Omega$ to I–V curves at both solar concentration ratios i.e. 50× and 321× as illustrated in Fig. 4, the electrical performance at 321× is much worse than that of 50×. It also concluded that the effect of series resistance to I–V curve is dependent on solar concentration ratio.

2.3. Bypass diode

To protect CPV cells from reverse-bias breakdown that could cause permanent damage to the cells, every solar cell must be connected in parallel with bypass diode in opposite polarity. When the cell is shaded or receives lower solar irradiance, the bypass diode is forward biased so that the current of the array can safely pass through the combination of cell-bypass-diode. For an array exposed to non-uniform solar irradiance, the role of bypass diode is very vital to avoid those CPV cells receiving low irradiance become the load of other CPV cells receiving high irradiance. The bypass diode creates an alternative path for the current so that the underperforming CPV cell is protected. When the array current passes through the bypass diode, the diode will turn on and hold the corresponding cell or group of cells to only a small negative voltage which can help to limit any further drop in the total voltage of the whole array [27]. From Fig. 5, the simulated maximum power point for an array of CPV cells could be greatly deviated from the actual value if bypass diode parameters, i.e. forward voltage V_d and turn-on resistance R_d, are not appropriately estimated. For the case study, we simulate the I–V and P–V curves using 12 × 4 Total Cross Tied array configuration for three different values of V_d and R_d as shown in Fig. 5. In our dense array, the MBRB4030 Schottky diode from "On Semiconductor" is selected with $V_d = 0.3$ V and $R_d = 0.1\ \Omega$ operating at the temperature 55 °C.

2.4. Dense-array modeling

The combination of CPV cell and bypass diode is referred as first stage of modeling and it acts as the lowest layer of sub-system in our modeling for ease of array connection as revealed in Fig. 6. For second stage modeling, the full connection consists of forty-eight sub-systems, which are labeled from C1 to C48, and they are connected together in a circuit to represent a complete dense-array CPV cells (see Fig. 7).

The manner of computing both I–V and P–V curves is summarized in block diagram for computational modeling under Simulink environment, which is known as the last stage implementation. The last stage of the dense-array solar cells modeling is depicted in Fig. 8, while all other stages are masked as sub-systems under 'CPV array' block. Upon completing the above step, this model is ready for simulation with a selected simulation time that will affect the resolution of I–V curve. Results generated from simulation, such as the current, voltage and output power values are stored to Matlab workspace and can be exported to excel for further analysis. The flow chart to illustrate the procedure of dense array solar cells modeling is shown in Fig. 9. After simulation, mismatch conditions of each array can be investigated by evaluating the I–V characteristics of the array configurations and the variation of their maximum output power.

3. Methodology of optimizing electrical performance

In the methodology of optimizing electrical performance of dense array CPV system, different possible configurations of CPV arrays are first simulated using the aforementioned modeling method in order to obtain the best configuration. Then, hardware installation is conducted and tested in the field for data collection. Finally, a comparison between measured data and simulated data is carried out to validate our modeling method.

3.1. Non-imaging planar concentrator (NIPC) prototype

To verify our modeling method, the optimized design of CPV array is assembled and installed to a NIPC prototype located in Universiti Tunku Abdul Rahman (UTAR) Kuala Lumpur (3.22° North, 101.73° East) [28,29]. This prototype is capable of producing reasonably high concentration using 192 flat mirrors with dimension 10 cm × 10 cm each. Azimuth-elevation sun-tracking method is engaged to drive the concentrator, whereby each of the axes is driven by a stepper motor connected to worm gear reducer. Since material of structural frame is aluminum, the whole concentrator is light and hence low rating power of stepper motor can be used. A Windows-based program implemented using Microsoft Visual Basic.net was developed to control the sun-tracking mechanism according to the day number, the local time, time zone, latitude and longitude of the site test. Using the aforementioned information, the program calculates both azimuth and elevation angles of the sun so that the stepper motors are triggered to drive the concentrator frame to the correct orientation [30]. As the apparent position of the sun changes with time throughout the day, a computer continuously send signals via parallel port to a driver to maneuver the orientation of concentrator frame appropriately about the azimuth and elevation axes for maintaining its tracking position.

At the receiver of the concentrator, copper cooling block is installed for the purpose of optical alignment as well as investigation of solar flux distribution. Due to serious blocking between mirrors and shading caused by the receiver, the outer three rings of mirrors as well as some mirrors at the center are omitted in this study as illustrated in Fig. 10

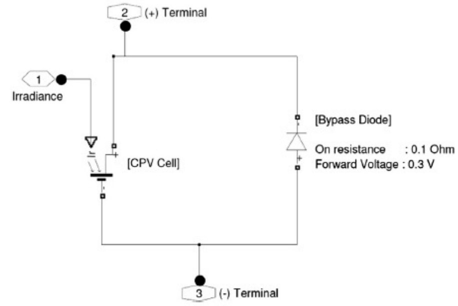

Fig. 6. The first stage modeling is a sub-system consisting of a CPV cell and bypass diode. For a circuit of 24 × 4 cells, there are 48 sub-systems.

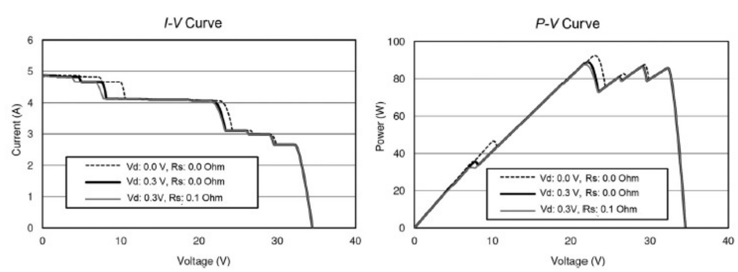

Fig. 5. I–V and P–V curves plotted for comparison between different bypass diode parameters, which has shown the importance of selecting correct bypass diode parameters for accurate modeling of an actual CPV array.

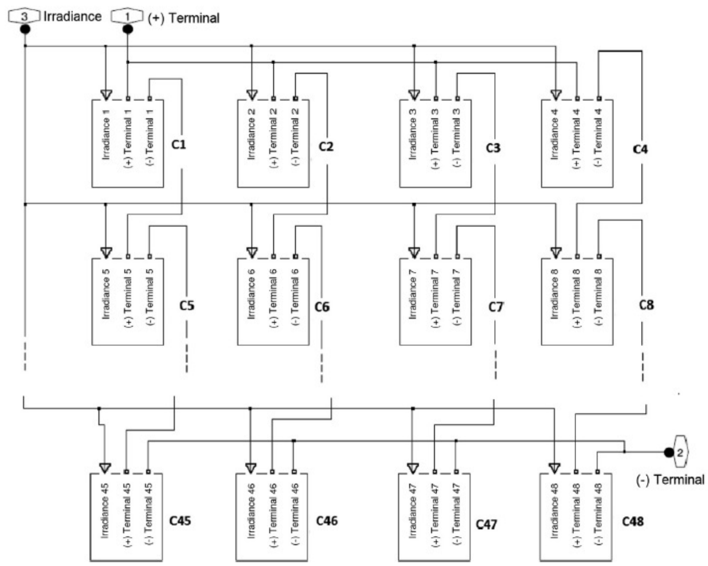

Fig. 7. The second stage modeling is a Simulink sub-system assembly. In this example, 12 × 4 CPV cells are connected using Series–Parallel configuration to form a full array.

3.2. Flux distribution measurement

The determination of solar flux distribution on the receiver is essential after any alignment of optical components in a concentrator system. For CPV systems, it is well known that non-uniform solar flux distribution can deteriorate electrical performance and even cause failure in some solar cells via local overheating. For the installed NIPC prototype, an optical scanner using a row of calibrated triple-junction cells (InGaP/InGaAs/Ge) as sensors with the resolution of 1.0 cm × 1.0 cm is designed to scan along the column direction for acquiring a 2-D flux distribution of concentrated solar irradiance at the receiver. Details of this optical scanner device setup has been published by Chong et al. except the sensor used in previous work is photodiode which has lower limit of irradiance

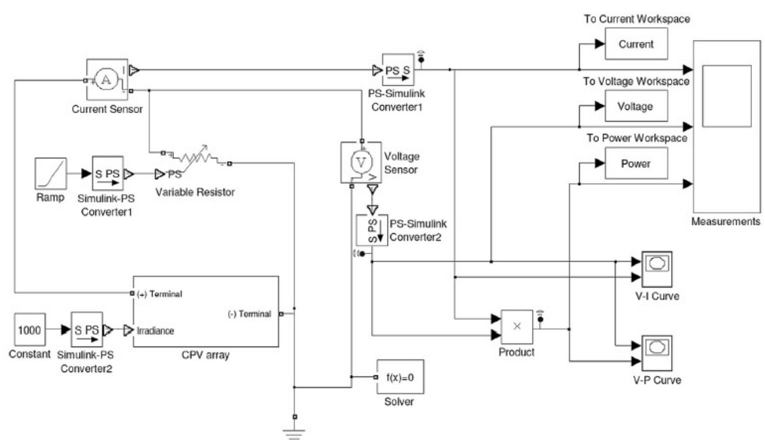

Fig. 8. Overall Simulink implementation of dense-array solar cells simulation with block diagram.

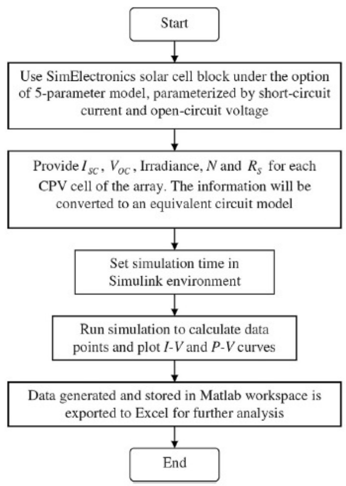

Fig. 9. Flow chart showing dense-array modeling and simulation approach using Simulink.

level [10,31]. The optical scanner is placed at the receiver plane of NIPC prototype in such a way that sensors' surface is always normal to the optical-axis of the concentrator. Measurements of flux distribution using the optical scanner were made during sun-tracking

Fig. 10. . A prototype of non-imaging planar concentrator (NIPC) located in the campus of Universiti Tunku Abdul Rahman (UTAR), Kuala Lumpur, Malaysia, is tested for the application of dense-array CPV cells.

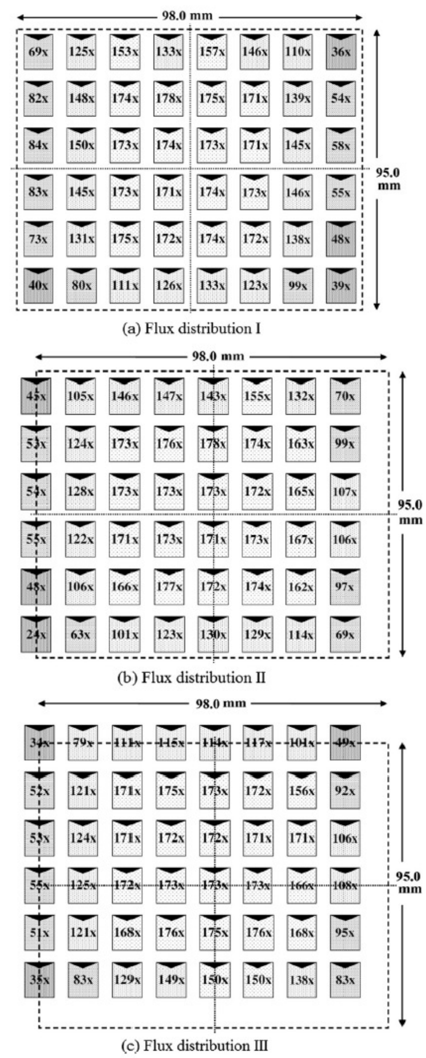

Fig. 11. Using an optical scanner fixed at the receiver plane, a solar concentration distribution was acquired and the solar concentration ratio of each CPV cell was mapped to its respective position on the receiver plane. There are three conditions of flux distribution: (a) Flux distribution I: no tracking error, (b) Flux distribution II: 5.0 mm off-tracking to the right, and (c) Flux distribution III: 5.0 mm off-tracking to the right and 5.0 mm to the bottom.

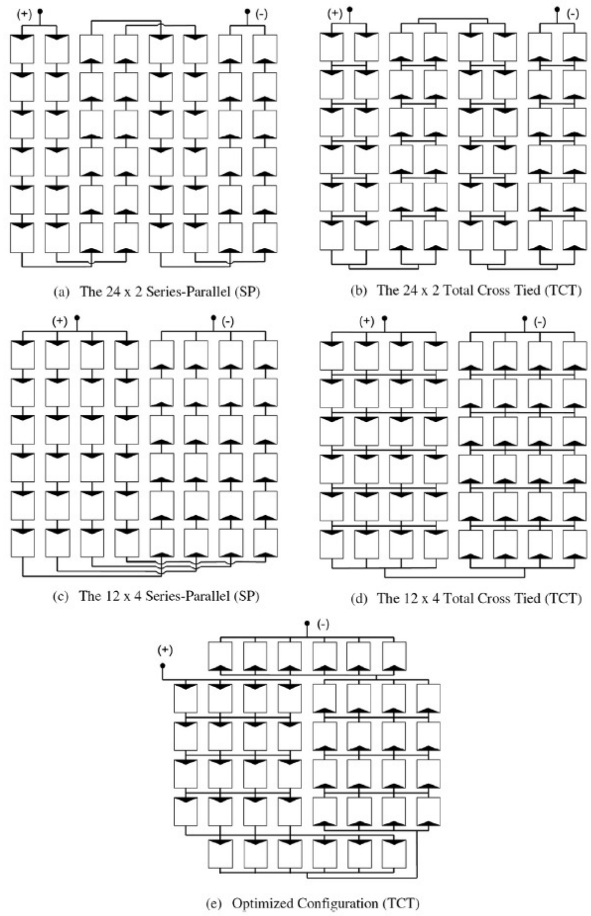

Fig. 12. Schematic diagram of five different array configurations. (a) 24 × 2 Series–Parallel (SP), (b) 24 × 2 Total Cross Tied (TCT), (c) 12 × 4 SP, (d) 12 × 4 TCT, and (e) Optimized configuration in TCT, which is a novel approach in array connection to minimize current-mismatch.

when the image was well focused at the center of receiver, as well as with off-tracking condition of as much as 2.94 mrad which is 5 mm for this system. The high speed scanning method of about 5 s across the receiver allows mapping of solar concentration distribution pattern with a total coverage area of about 95 cm × 98 cm. With the calibrated information, measurement results can be correlated with absolute irradiance level. Fig. 11 shows the solar flux distribution profile that is superimposed on each CPV cell within the dense-array in term of solar concentration ratio. In view of the importance in correct mapping of concentrated irradiance level on each solar cell, this paper proposes a practical modeling approach by considering constraints in the packing factor of dense array solar cells. The specification of materials used in the NIPC dense array consists of Direct-Bonded-Copper (DBC) substrates manufactured by Curamik, high efficiency CTJ CPV solar cells (InGaP/InGaAs/Ge) supplied by EMCORE and 10 mil × 1 mil ribbon bonds.

3.3. Dense-array configuration

Five different common configurations including an optimized configuration that is specially tailored to achieve high conversion efficiency are investigated and analyzed under three different flux distributions as described in Fig. 11. Referring to Fig. 12, the array

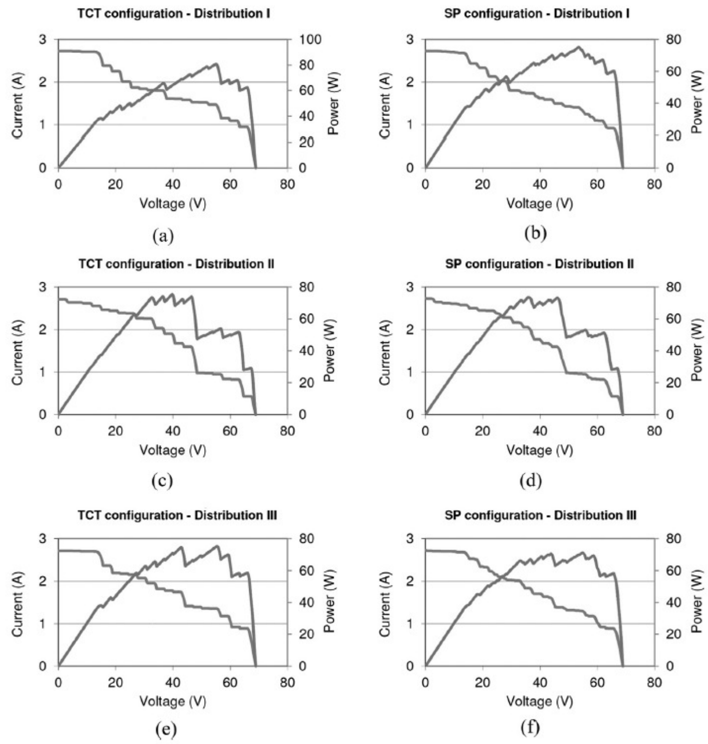

Fig. 13. Simulated I–V and P–V curves of 24 × 2 array under three different flux distributions of concentrated solar irradiance, which are (a) TCT configuration – Distribution I, (b) SP configuration – Distribution II, (c) TCT configuration – Distribution II, (d) SP configuration – Distribution II, (e) TCT configuration – Distribution III, and (f) SP configuration – Distribution III.

configurations are (a) 24 × 2 Series–Parallel (SP), (b) 24 × 2 Total Cross Tied (TCT), (c) 12 × 4 SP, (d) 12 × 4 TCT, and (e) Optimized configuration in TCT. To accurately model these dense-arrays, CPV modules consisting of both CPV cells and DBC substrates are arranged based on real dimensions. The dual-bus bar solar cells employed in this study have an overall external dimension of 10.68 mm × 10.075 mm with a 10 mm × 10 mm designated aperture area and two 0.255 mm wide bondable bus bars. In all the configurations, only one of the two bus bars that acts as the negative terminal on each solar cells is utilized for electrical connection. The electrical connection is done via ribbon bonding method by connecting the top contact of a solar cell to the DBC substrate of the next solar cell to form a series-connected string of cells.

3.4. Dense array simulation

To understand the overall performance of a photovoltaic system, it is generally accepted that I–V graphs remain as one of the most common and important tools [32–35]. When a photovoltaic array is subjected to non-uniform irradiance, its I–V and P–V curves will show common characteristics of multiple steps and multiple peaks. The appearance of multiple steps in an I–V curve and multiple peaks in a P–V curve is associated to reverse characteristics of some reverse biased solar cells. The graphs in Figs. 13–15 reveal simulated results for five CPV configurations under three different flux distributions. The profiles of I–V and P–V curves for dense-array CPV cells are dependent on both the flux distribution pattern and the array configuration. Moreover, bypass diodes also affect the I–V curve significantly which can lead to the appearance of one or more local maximum power point (MPP) for the case of substantial current mismatch.

The I–V and P–V curves from Figs. 13 and 14 have significant mismatch steps and low value of maximum output power. On the contrary, the I–V and P–V curves of the optimized array as shown in Fig. 15 only displays small mismatch steps as well as having the highest maximum output power. A summary of important simulated parameters from Simulink modeling is compiled in Table 1. As opposed to the optimized array ranging from 59.85% to 71.90%, fill factor (FF) value is significantly lower for the other array

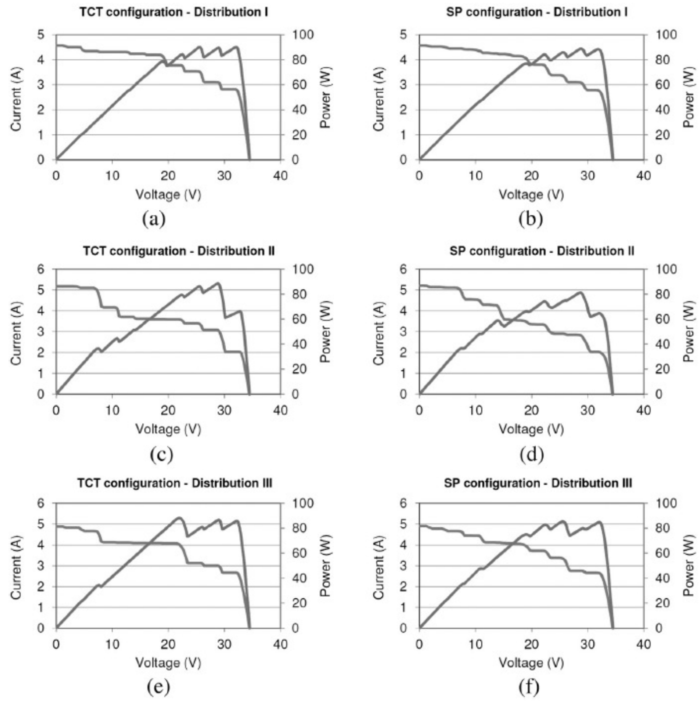

Fig. 14. Simulated I–V and P–V curves of 12 × 4 array under three different flux distributions of concentrated solar irradiance, namely: (a) TCT configuration – Distribution I, (b) SP configuration – Distribution II, (c) TCT configuration – Distribution II, (d) SP configuration – Distribution II, (e) TCT configuration – Distribution III, and (f) SP configuration – Distribution III.

configurations only ranging from 39.93% to 57.23%.where DNI is the measured direct normal irradiance, A_{mirror} is total mirror area, PF is packing factor of solar cells in the dense-array receiver module, and $\eta_{optical}$ is the optical efficiency of the solar concentrator. This approach is selected because packing factor is not yet fully optimized in this study due to limitation in our current DBC design and it can be further improved when better die-attach and ribbon bond technologies are available. As illustrated in Fig. 16, the proposed optimized array has undeniably surpassed all conventional configurations in terms of maximum output power and fill factor. By considering current-matching, we have grouped six CPV cells with lower concentration levels at the top and bottom of the array (Fig. 12(e)), to match with the current of four CPV cells that are exposed to higher solar concentration, hence achieving an attractive conversion efficiency of as high as 33.79%.

3.5. Assembling process of dense array CPV cells

The assembling process of the CTJ solar cells into modules and then complete assembly is a critical step for dense-array cells. The interconnect design has to be made according to machinery limitations while not compromising on overall electrical performance. As CPV cells are thinner than flat-plate photovoltaic (PV) cells, some areas require special attention, including low-impact cell handling and more stringent heat dissipation requirements.

Before going into the assembly, cell testing and classification are important to enable sorting and grouping of CPV cells. Essentially, the underperforming cell within a series string will limit the output current and subsequently reduce total power produced by the array. This effect can be reduced by selecting solar cells with the most similar characteristics in order to minimize losses from module mismatching. In our case, bare cells were sorted based on the observation of I–V curves under illumination as well as the dark condition using Keithley's 4200-SCS semiconductor characterization system.

Next, a selected group of solar cells is attached to DBC substrates to form individual modules through solder reflow process. The solder reflow process provides low-void-content bonding and excellent thermal conductivity between the solar cell and its substrate. The DBC substrates from Curamik consist of a ceramic isolator Al_2O_3 that is sandwiched in between two copper layers. These DBC substrates are ideally suited for CPV application due to its high thermal conductivity of 24 Wm^{-1} K^{-1}, high voltage isolation, and adjusted coefficient of thermal expansion. To ensure that CPV modules will not experience hot-spot problem, X-ray scanning is carried out on all modules. The filtered ones that have very little

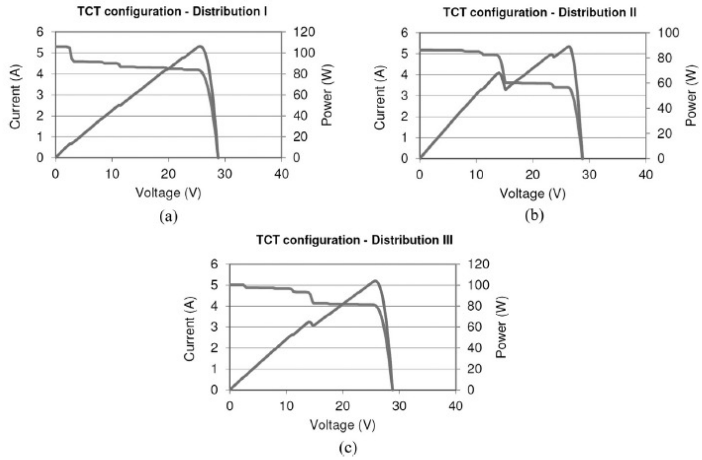

Fig. 15. Simulated *I–V* and *P–V* curves of optimized configuration for (a) TCT configuration – Distribution I, (b) TCT configuration – Distribution II, and (c) TCT configuration – Distribution III.

voids are selected for further assembling into dense-array assembly (Fig. 17).

Using Arctic Silver thermal adhesive with thickness of about 0.1 mm, each module consisting two solar cells in parallel, is attached manually onto a copper cooling block. The thermal adhesive requires a small pressure for 5-minutes to cure. This method is preferred due to its simplicity and ease of rework in case array rearrangement is required. After the thermal adhesive process has been completed, ribbon-bonding process begins. Front-side bus bar contact of the triple-junction solar cell is connected using aluminum ribbon to the next solar module's DBC copper layer, which is electrically isolated to the first module to form a series connection. Finally, bypass diodes and cables are fixed to the assembly using electrically conductive epoxy.

3.6. Temperature measurement

A cross sectional sketch of various materials for the CPV assembly in stack is presented in Fig. 18. The solar cell temperature (T_{CPV}) is derived from the temperature measured at copper cooling block, using a k-type thermocouple located 2.0 mm from the cooling block's top surface. The thermal conductivity of the

Table 1
Comparison of the five array configurations under three flux distributions in terms of maximum output power P_{mp}, electrical conversion efficiency, and fill factor (FF), simulated at DNI: 604.19 W/m^2.

$$\text{Efficiency}(\%) = P_{mp}/\left(\text{DNI} \times A_{\text{mirror}} \times \text{PF} \times \eta_{\text{optical}}\right) \times 100\% \tag{5}$$

Array configuration	Flux distribution	P_{mp} (W)	Efficiency (%)	Fill factor (FF) (%)	V_{mp} (V)	I_{mp} (A)
24 × 2 – SP	I	75.15	23.86	39.93	53.55	1.40
	II	75.52	23.34	39.01	36.01	2.04
	III	71.10	22.57	37.90	54.88	1.30
12 × 4 – SP	I	80.81	28.83	56.37	28.83	3.08
	II	81.12	25.75	45.15	28.77	2.82
	III	85.32	27.08	50.49	25.60	3.33
24 × 2 – TCT	I	80.81	25.65	42.97	55.09	1.47
	II	75.43	23.95	40.37	39.80	1.90
	III	75.19	23.87	40.19	55.39	1.36
12 × 4 – TCT	I	90.19	28.63	57.23	32.06	2.81
	II	88.58	28.12	49.67	28.79	3.08
	III	88.06	27.96	52.38	22.05	3.99
Optimized array – TCT	I	106.43	33.79	69.80	25.52	4.17
	II	89.15	28.30	59.85	26.37	3.38
	III	103.84	32.96	71.90	25.70	4.04

In any photovoltaic system, the electrical conversion efficiency is the ultimate benchmark to judge the overall electrical performance. To offset the effect of packing factor of the dense-array receiver module that can be improved in the future, we apply the following formula in our calculation of conversion efficiency.

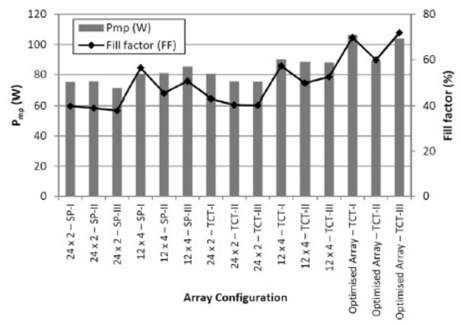

Fig. 16. Graphs to show comparisons in terms of maximum output power (P_{mp}) and fill factor (FF) for five different layout configurations under three flux distributions.

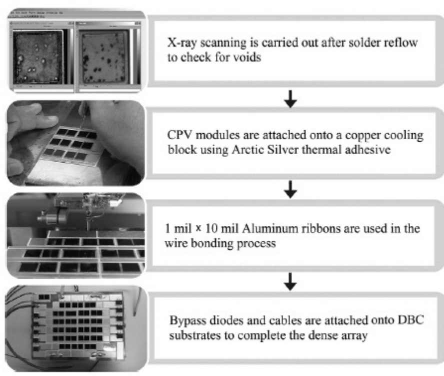

Fig. 17. Flow chart showing the assembly process of dense-array.

different materials is listed in Table 2. The table shows a total thermal resistance of 4.22×10^{-5} Km^2 W^{-1} from solar cell to the measurement point. To determine the temperature of solar cell, the following equations are applied [36]:

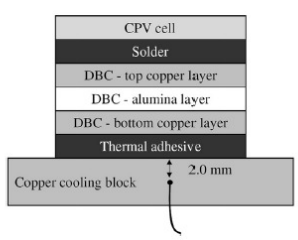

Fig. 18. Cross-sectional sketch of different materials in stack for the calculation of CPV cell temperature: the temperature at the surface of solar cell is derived from the temperature measured by k-type thermocouple located at 2.0 mm from top surface of cooling block.

Table 2
The thickness, thermal conductivity and thermal resistance of different materials for CPV cell temperature calculation are presented.

Material	Thickness, l (mm)	Thermal conductivity, k (Wm^{-1} K^{-1})	Thermal resistance, R (Km^2 W^{-1})
CPV Cell	0.20	55	3.64×10^{-6}
Solder	0.15	50	3.00×10^{-6}
DBC, top copper layer	0.30	400	7.50×10^{-7}
DBC, alumina layer	0.38	24	1.58×10^{-5}
DBC, bottom copper layer	0.30	400	7.50×10^{-7}
Thermal adhesive	0.10	7.5	1.33×10^{-5}
Copper layer from thermocouple location to cooling block surface	2.00	400	5.00×10^{-6}
R_{tot}			4.22×10^{-5}

$$P_{CPV,\ in} = \eta_{CPV} \times \mathrm{DNI} \times A_r \times (A_{CPV}/A_{image}) \tag{6}$$

$$T_{CPV} = P_{CPV,\ in} \times R_{tot} \times (1/A_{CPV}) \times (1 - \eta_{CPV}) + T_{CB} \tag{7}$$

where $P_{CPV,\ in}$ is the solar power input received by CPV assembly, η_{CPV} is the electrical conversion efficiency of CPV assembly, A_r is the total area of mirrors which reflect solar flux to the target of NIPC, A_{CPV} is the total active area of CPV assembly, A_{image} is the total image area of concentrated sunlight on the cooling block, T_{CB} is the temperature of cooling block, and R_{tot} is the total thermal resistance from cooling block to CPV cell consisting of the following materials: copper (cooling block), arctic silver thermal adhesive, bottom copper layer in DBC substrate, alumina layer in DBC substrate, top copper layer in DBC substrate, solder, and CPV cell that can be computed as:

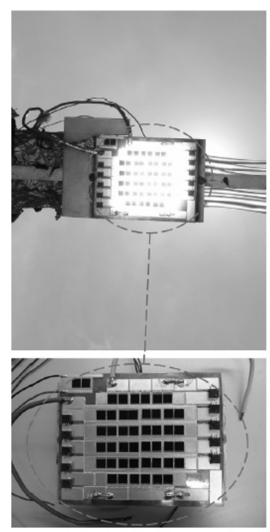

Fig. 19. Completed dense-array CPV assembly with a proposed optimized configuration for TCT: (Top) Fixed at the receiver plane under concentrated sunlight (Bottom) Front view of the CPV assembly.

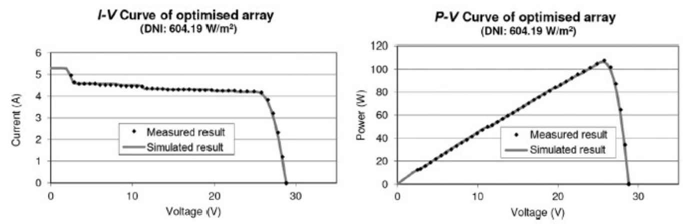

Fig. 20. Measured data (black dot) acquired during field test superimposed on simulation curve for comparison in I–V and P–V plots at direct normal irradiance (DNI) = 604.19 W/m^2, operating without tracking error (Flux distribution I).

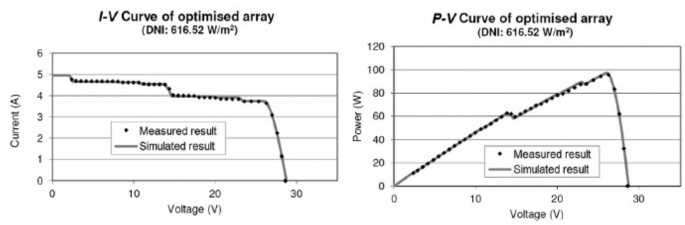

Fig. 21. Measured data (black dot) acquired during field test superimposed on simulation curve for comparison in I–V and P–V plots at direct normal irradiance (DNI) = 616.52 W/m^2, operating with tracking error 5.0 mm to right (Flux distribution II).

$$R_{tot} = R_{CPV} + R_{solder} + R_{DBC-copper} + R_{DBC-alumina} + R_{DBC-copper} + R_{arctic\ silver} + R_{copper} \tag{8}$$

provided that

$$R_{CPV} = l_{CPV}/k_{CPV}$$

$$R_{solder} = l_{solder}/k_{solder}$$

$$R_{DBC-copper} = l_{DBC-copper}/k_{DBC-copper}$$

$$R_{DBC-alumina} = l_{DBC-alumina}/k_{DBC-alumina}$$

$$R_{arctic\ silver} = l_{arctic\ silver}/k_{arctic\ silver}$$

$$R_{copper} = l_{copper}/k_{copper}$$

in which l_{CPV}, l_{solder}, $l_{DBC-copper}$, $l_{DBC-alumina}$, $l_{arctic\ silver}$, and l_{copper} were the thicknesses of different materials measured as 0.2 mm, 0.15 mm, 0.3 mm, 0.38 mm, 0.1 mm and 2.0 mm respectively; k_{CPV}, k_{solder}, $k_{DBC-copper}$, $k_{DBC-alumina}$, $k_{arctic\ silver}$, and k_{copper} are referred as the thermal conductivity of different materials with the values 55 Wm^{-1} K^{-1}, 50 Wm^{-1} K^{-1}, 400 Wm^{-1} K^{-1}, 24 Wm^{-1} K^{-1}, 7.5 Wm^{-1} K^{-1}, 400 Wm^{-1} K^{-1} respectively, which are provided by Luque and Andreev (2007) [37]. Substituting all of the values into equation (7), the temperature on CPV surface can be calculated. This temperature value is applied in our computational modeling to achieve more accurate simulation results.

4. Results and discussion

To validate our computational modeling, a CPV assembly is designed and constructed according to an optimized configuration. The temperature of dense-array assembly that was attached onto a copper cooling block was regulated at about 55 °C. This optimized dense-array assembly was installed on the NIPC prototype, and

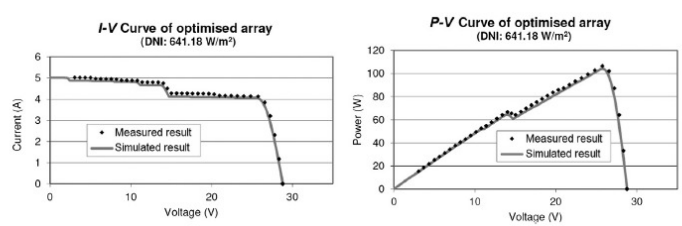

Fig. 22. Measured data (black dot) acquired during field test is superimposed on simulation curve for comparison in I–V and P–V plots at direct normal irradiance (DNI) = 641.18 W/m^2, operating with tracking error 5.0 mm to right + 5.0 mm to bottom (Flux distribution III).

Table 3
Comparison between simulated and measured results of the dense-array CPV assembly is presented in terms of maximum output power P_{mp}, maximum voltage V_{mp}, maximum current I_{mp}, measured array efficiency, simulated array efficiency, and error of P_{mp}.

I–V curve: Fig. 20	DNI: 604.19 W/m^2		
	P_{mp} (W)	V_{mp} (V)	I_{mp} (A)
Measured results	107.67	25.77	4.18
Simulated results	106.45	25.52	4.17
Efficiency – measured (%)	34.18		
Efficiency – simulated (%)	33.80		
Error, P_{mp} (%)	−1.13		
I–V curve: Fig. 21	DNI: 616.52 W/m^2		
	P_{mp} (W)	V_{mp} (V)	I_{mp} (A)
Measured results	95.76	26.05	3.73
Simulated results	97.23	25.75	4.04
Efficiency – measured (%)	29.79		
Efficiency – simulated (%)	30.25		
Error, P_{mp} (%)	1.53		
I–V curve: Fig. 22	DNI: 641.18 W/m^2		
	P_{mp} (W)	V_{mp} (V)	I_{mp} (A)
Measured results	106.49	25.75	4.14
Simulated results	104.01	25.75	4.04
Efficiency – measured (%)	31.86		
Efficiency – simulated (%)	31.12		
Error, P_{mp} (%)	−2.32		

measured data is then superimposed onto simulated *I–V* curve for comparison purposes. Real time *I–V* data acquisition was carried out using N3300A Configurable DC electronic load mainframe installed with two units of N3305A 500 Watt electronic load modules. At the same time, supporting information such as operating temperature, direct normal irradiance (DNI) and global irradiance were also measured.

The simulation was performed based on the real time measured parameters such as DNI, operating temperature, as well as taking into consideration 15% of optical loss. From the results in Figs. 19–22, a very close match between measured data and simulated curve with 3% of error for P_{mp} (refer to Table 3) is observed.

Furthermore, the effect of 2.94 mrad sun-tracking error to the conversion efficiency is also observed for two cases: (a) tracking error with 5.0 mm to right and (b) tracking error with 5.0 mm to right +5.0 mm to bottom. It was found that the effect of tracking error to the electrical performance is manageable for the tolerance of ±5 mm along up-down and left-right directions. According to Table 3, the measured conversion efficiencies for tracking error with 5.0 mm to right and tracking error 5.0 mm to right +5.0 mm to bottom are 29.79% and 31.86% respectively which are not much lower than 34.18% in the case of without tracking error.

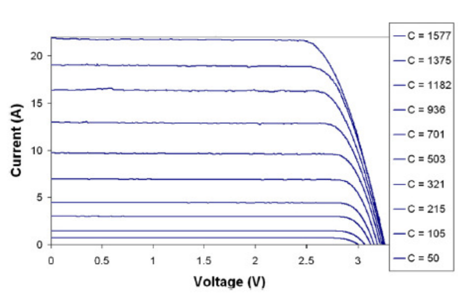

Fig. 23. Typical *I–V* curves from EMCORE 2008 datasheets of InGaP/InGaAs/Ge CPV cells at varying concentration levels and 25 °C.

5. Conclusion

A comprehensive modeling method has been developed for analyzing dense-array CPV cells with five different cell connection configurations: 24 × 2 SP, 24 × 2 TCT, 12 × 4 SP, 12 × 4 TCT and optimized configuration using TCT. This analysis includes the effects of non-uniform solar flux distribution that falls onto the NIPC prototype receiver. Using an optical scanner, solar flux distributions were acquired under three conditions, i.e. flux distribution I: no tracking error, flux distribution II: off-tracking with 5.0 mm to the right, and flux distribution III: off-tracking with 5.0 mm to the right +5.0 mm to the bottom. From simulated results, an optimized configuration in TCT was found to have the least mismatch steps with the highest output power for all the three flux distributions. The FF value of 24 × 2 SP, 24 × 2 TCT, 12 × 4 SP, 12 × 4 TCT are significantly lower, only ranging from 39.93% to 57.23%, while the proposed optimized array is capable of maintaining good performance with FF = 59.85%–71.90%. By considering current-matching in the optimized array configuration, we have grouped six CPV cells with lower concentration levels at the top and bottom of the array to match with the current of four CPV cells that are exposed to higher solar concentration, and hence achieving an attractive conversion efficiency of as high as 33.79%. With the support of computational modeling result, an actual assembly of the dense-array CPV cells was built and installed on the NIPC prototype for verification purpose. The modeling method has been successfully validated with the NIPC prototype to achieve practical conversion efficiency of 34.18%. Comparing the results obtained from field measurement with simulated results by evaluating their *I–V* and *P–V* curves, a very close match can be observed. It was found that the estimation of P_{mp} by computational modeling is less than 3% in error.

Acknowledgments

The authors would like to express their gratitude to the Ministry of Energy, Green Technology and Water (AAIBE Trust Fund), the Ministry of Science, Technology and Innovation (e-Science Fund with project number 03-02-11-SF0143), and the Ministry of Higher Education (Fundamental Research Grant Scheme with project no.: FRGS/1/11/TK/UTAR/03/4) for their financial support.

Appendix

The solar cells that are used in this study are EMCORE's high efficiency CTJ cells with n-on-p polarity on a Germanium substrate. The *I–V* curve of a CPV cell for different solar concentration ratio is provided in the datasheet as shown in Fig. 23 [21]. These cells' multi-layer antireflective coatings enable low reflectance over the wavelength range of 300 nm–1800 nm to absorb more solar energy.

References

[1] Nishioka K, Takamoto T, Agui T, Kaneiwa M, Uraoka Y, Fuyuki T. Evaluation of InGaP/InGaAs/Ge triple-junction solar cell and optimization of solar cell's structure focusing on series resistance for high-efficiency concentrator photovoltaic systems. Sol Energy Mater Sol Cells 2006;90:1308–21.
[2] Luque A, Sala G, Luque-Heredia I. Photovoltaic concentration at the onset of its commercial deployment. Prog Photovolt 2006;14:413–28.

[3] Kaushika ND, Rai AK. An investigation of mismatch losses in solar photovoltaic cell networks. Energy 2007;32:755–9.

[4] Picault D, Raison B, Bacha S, Casa J, Aguilera J. Forecasting photovoltaic array power production subject to mismatch losses. Sol Energy 2010;84:1301–9.

[5] Mills DR, Morrison G. Compact linear Fresnel reflector solar thermal powerplants. Sol Energy 2000;68:263–83.

[6] Chen YT, Chong KK, Bligh TP, Chen LC, Yunus J, Kannan KS, et al. Non-imaging, focusing heliostat. Sol Energy 2001;71:155–64.

[7] Chen YT, Chong KK, Lim BH, Lim CS. Study of residual aberration for non-imaging focusing heliostat. Sol Energy Mater Sol Cells 2003;79:1–20.

[8] Chong KK, Siaw FL, Wong CW, Wong GS. Design and construction of non-imaging planar concentrator for concentrator photovoltaic system. Renew Energy 2009;34:1364–70.

[9] Chong KK, Wong CW, Siaw FL, Yew TK. Solar flux distribution analysis of non-imaging planar concentrator for the application in concentrator photovoltaic system. In: 35th IEEE Photovoltaic Specialist Conference. Honolulu, HI 2010. p. 003013–8.

[10] Chong KK, Yew TK, Wong CW, Lau SL. Study of image quality of mirror via solar flux distribution measurement using a novel high speed optical scanner. Appl Opt 2011;50:4927–35.

[11] Faiman D, Biryukov S, Pearlmutter KK. PETAL: a research pathway to fossil-competitive solar electricity. In: 29th IEEE Photovoltaic Specialist Conference 2002. p. 1384–7.

[12] Franklin ET, Coventry JS. Effects of highly non-uniform illumination distribution on electrical performance of solar cells. In: ANSES Sol. Conference. New Castle, Australia 2002.

[13] Andreev V, Grilikhes V, Rumyantsev V, Timoshina N, Shvarts M. Effect of nonuniform light intensity distribution on temperature coefficients of concentrator solar cell. In: Third World Conference on Photovoltaic Energy Conversion 2003. p. 881–4.

[14] Coventry JS. Performance of a concentrating photovoltaic/thermal solar collector. Sol Energy 2005;78:211–22.

[15] Nishioka K, Takamoto T, Agui T, Kaneiwa M, Uraoka Y, Fuyuk T. Annual output estimation of concentrator photovoltaic systems using high-efficiency InGaP/InGaAs/Ge triple-junction solar cells based on experimental solar cell's characteristics and field-test meteorological data. Sol Energy Mater Sol Cells 2006;90:57–67.

[16] Sherif R, Cotal H, Paredes A. High concentration tests of a dense PV array using GaInP/GaAs/Ge triple-junction cells in the high flux solar furnace. In: 3rd World Conference on Photovoltaic Energy Conversion, Osaka, Japan 2003. p. 829–32.

[17] Kajihara A, Harakawa AT. Model of photovoltaic cell circuits under partial shading. In: IEEE International Conference on Industrial Technology. Hong Kong 2005. p. 866–70.

[18] Alonso-Garcia MC, Ruiz JM, Chenlo F. Experimental study of mismatch and shading effects in the I–V characteristics of a photovoltaic module. Sol Energy Mater Sol Cells 2006;90:329–40.

[19] Sullivan CR, Awerbuch J, Latham AM. Decrease in photovoltaic power output from ripple: simple general calculation and effect of partial shading. In: Twenty-Sixth Annual IEEE Appl. Power Electronics Conference and Exposition (APEC). Fort Worth, TX 2011. p. 1954–60.

[20] Chong KK, Wong CW. General formula for on-axis sun-tracking system and its application in improving tracking accuracy of solar collector. Sol Energy 2009;83:298–305.

[21] EMCORE Corporation. Triple-junction high efficiency solar cells for terrestrial concentrated photovoltaic applications. EMCORE Photovoltaics; August 2008.

[22] Ishaque K, Salam Z, Syafaruddin. A comprehensive MATLAB Simulink PV system simulator with partial shading capability based on two-diode model. Sol Energy 2011;85:2217–27.

[23] Vossier A, Chemisana D, Flamant G, Dollet A. Very high fluxes for concentrating photovoltaics: considerations from simple experiments and modeling. Renew Energy 2012;38:31–9.

[24] King RR, Bhusari D, Boca A, Larrabee D, Liu XQ, Hong W, et al. Band gap-voltage offset and energy production in next-generation multijunction solar cells. In: 5th World Conference on Photovoltaic Energy Conversion and 25th Eur. Photovoltaic Sol. Energy Conference. Valencia, Spain 2010.

[25] Kinsey GS, Hebert P, Barbour KE, Krut DD, Cotal HL, Sherif RA. Concentrator multijunction solar cell characteristics under variable intensity and temperature. Prog Photovolt 2008;16:503–8.

[26] Pysch D, Mette A, Glunz SW. A review and comparison of different methods to determine the series resistance of solar cells. Sol Energy Mater Sol Cells 2007;91:1698–706.

[27] Karatepe E, Boztepe M, Colak M. Development of a suitable model for characterizing photovoltaic arrays with shaded solar cells. Sol Energy 2007;81: 977–92.

[28] Chong KK, Wong CW, Siaw FL, Yew TK. Optical characterization of nonimaging planar concentrator for the application in concentrator photovoltaic system. J Sol Energy Eng 2010;132:011011.1–9.

[29] Chong KK, Tan WC. Study of automotive radiator cooling system for dense-array concentration photovoltaic system. Sol Energy 2012;86:2632–43.

[30] Chong KK, Wong WC. Application of on-axis general sun-tracking formula in open-loop sun-tracking system for achieving tracking accuracy of below 1 mrad. Int J Energy Eng 2011;1:25–32.

[31] Chong KK, Yew TK. Novel optical scanner using photodiodes array for two-dimensional measurement of light flux distribution. IEEE Trans Instrum Meas 2011:2918–25.

[32] Cotal H, Fetzer C, Boisvert J, Kinsey G, King R, Hebert P, et al. III-V multi-junction solar cells for concentrating photovoltaics (review). Energy Environ Sci 2009;2:174–92.

[33] Vorster FJ, van Dyk EE, Leitch AWR. Investigation on the I–V characteristics of a high concentration, photovoltaic array. In: 29th IEEE Photovoltaic Specialists Conference (PVSC) 2002. p. 1604–7.

[34] Vorster FJ, van Dyk EE. Current-voltage characteristics of high concentration, photovoltaic arrays. Prog Photovolt 2005;13:55–66.

[35] Quaschning V, Hanitsch R. Numerical simulation of current-voltage characteristics of photovoltaic systems with shaded solar cells. Sol Energy 1996;56: 513–20.

[36] Peharz G, Rodriguez JPF, Siefer G, Bett AW. A method for using CPV modules as temperature sensors and its application for rating procedures. Sol Energy Mater Sol Cells 2011;95:2734–44.

[37] Luque AL, Andreev VM. Concentrator photovoltaics. 1st ed. Springer Berlin Heidelberg New York; 2007. Reference to: Chapter 7.

APPENDIX L

Schematic diagrams for interconnection configurations

Simulation No.			Configuration
1	48 × 1	A	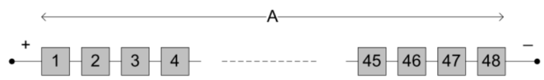
2	24 × 2	A	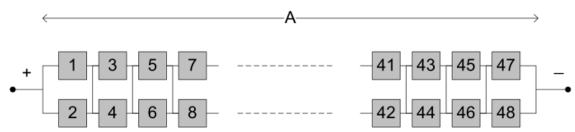
3	12 × 4	A	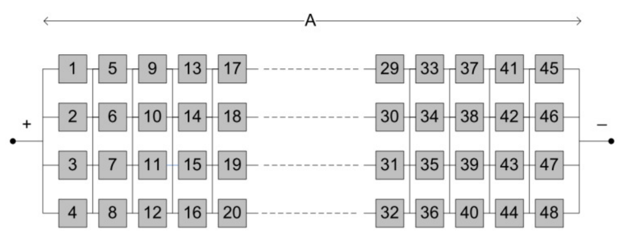
4	6 × 8	A	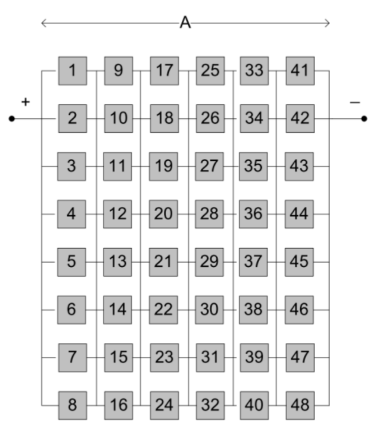

5	2×6 (B1) and 4×8 (B2)	B	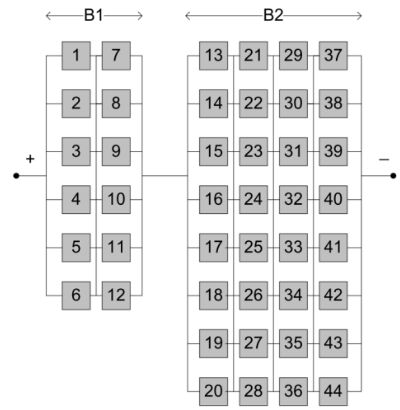
6	2×6 (B1) and 8×4 (B2)	B	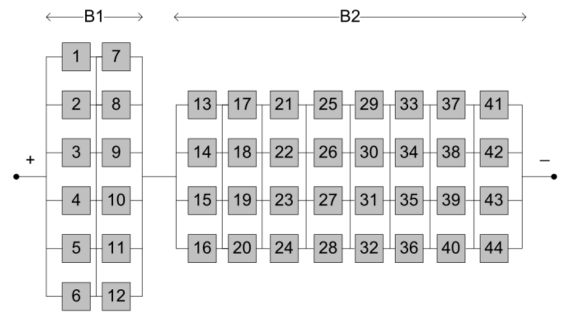
7	2×6 (B1) and 16×2 (B2)	B	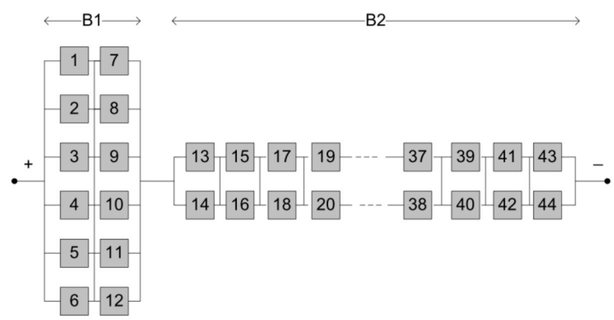
8	2×6 (B1) and 32×1 (B2)	B	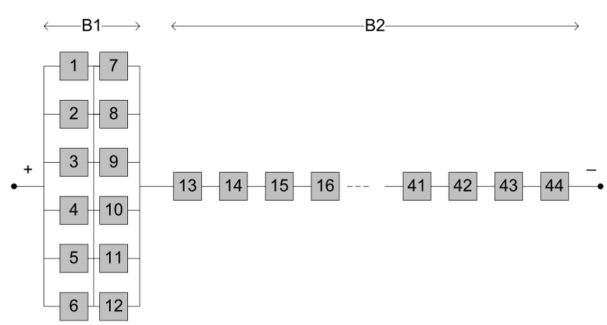

9	4 × 3 (B1) and 4 × 8 (B2)	B	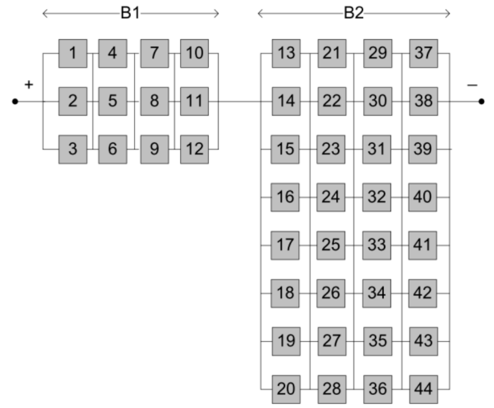
10	4 × 3 (B1) and 8 × 4 (B2)	B	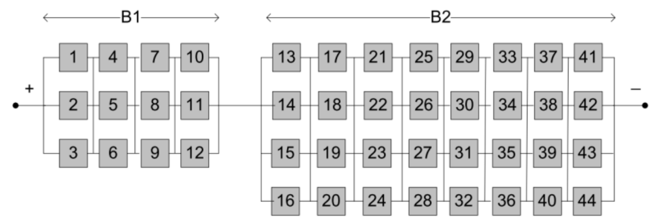
11	4 × 3 (B1) and 16 × 2 (B2)	B	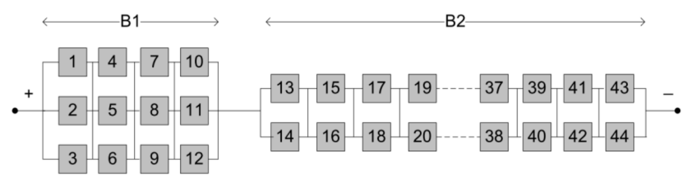
12	4 × 3 (B1) and 32 × 1 (B2)	B	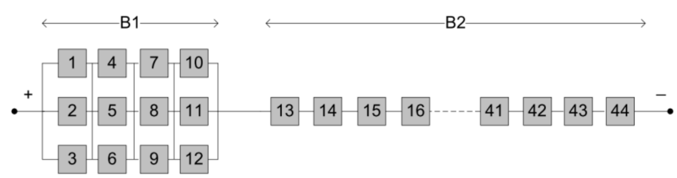

13	6 × 2 (B1) and 4 × 8 (B2)	B	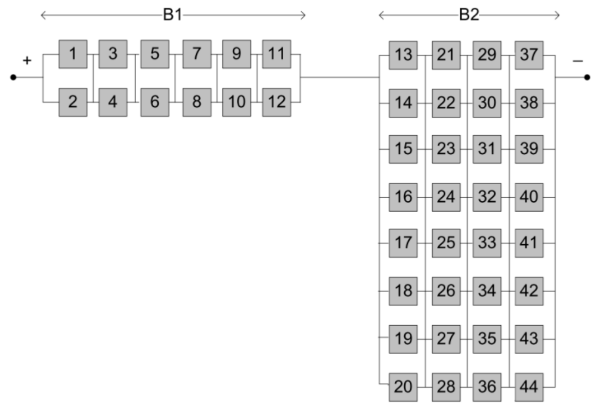
14	6 × 2 (B1) and 8 × 4 (B2)	B	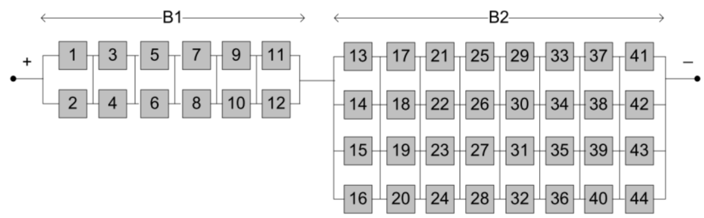
15	6 × 2 (B1) and 16 × 2 (B2)	B	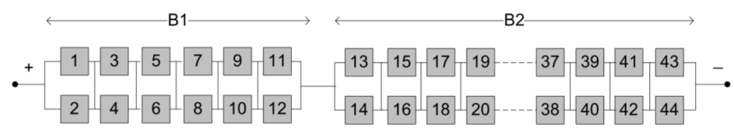
16	6 × 2 (B1) and 32 × 1 (B2)	B	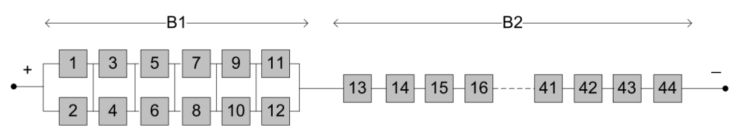

17	12 × 1 (B1) and 4 × 8 (B2)	B	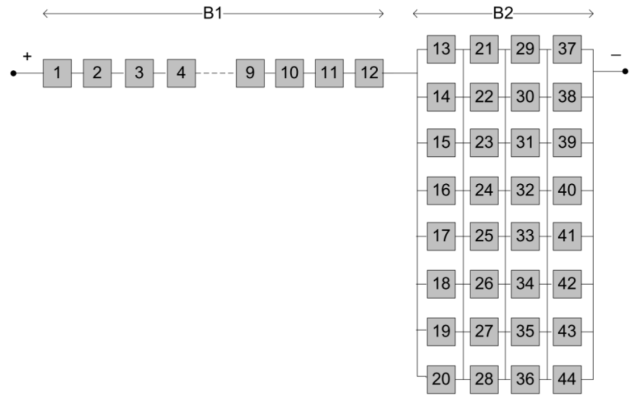
18	12 × 1 (B1) and 8 × 4 (B2)	B	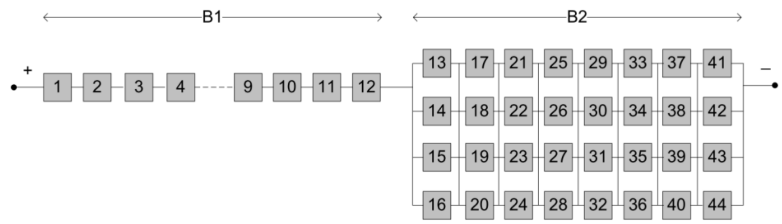
19	12 × 1 (B1) and 16 × 2 (B2)	B	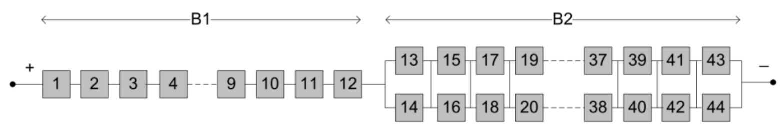
20	12 × 1 (B1) and 32 × 1 (B2)	B	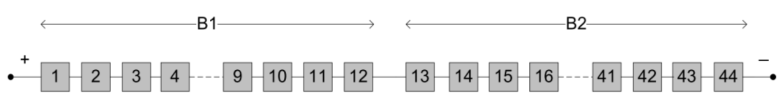

APPENDIX M

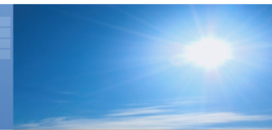

August 2008

Triple-Junction High Efficiency Solar Cells for Terrestrial Concentrated Photovoltaic Applications

Over 38% Efficiency under Concentrated Illumination

Features and Characteristics

- Triple-Junction Heritage InGaP/InGaAs/Ge Solar Cells with n-on-p Polarity on Germanium Substrate
- Multi-Layer Antireflective Coating Providing Low Reflectance over Wavelength Range 0.3 to 1.8µm
- Characterized for Terrestrial Applications Under Concentrated Illumination (Over 1500 Suns)
- Weldable or Solderable Contacts, Front and Back
- Standard 1x1 cm^2 (Designated Aperture Area) and Customer-Specific Sizes Available
- Available in Cell and Application-Specific Configurations
- Application-Specific Grid Design Service to Optimize Power Output
- 4" Ge Manufacturing Operation with >300MW Annual Capacity

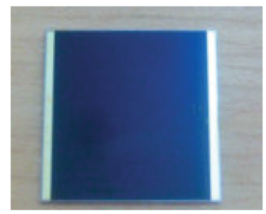

Standard Cell Dimensions

10.68 mm x 10.075 mm External Dimensions
10 mm x 10 mm Designated Aperture Area
100 mm^2 Total Nominal Active Area
0.255 mm Wide Bondable Perimeter Busbar
~ 0.2 mm Total Cell Thickness

Performance Data

Solar Cell Electrical Output Parameters @ AM1.5D, low-AOD Illumination, 25°C

1X Concentration		503X Concentration		1182X Concentration	
Efficiency	31.4%	Efficiency	38.4%	Efficiency	36.3%
Voc:	2.605 V	Voc:	3.193 V	Voc:	3.251 V
Jsc:	13.85 mA/cm^2	Jsc:	6.96 A/cm^2	Jsc:	16.37 A/cm^2
Vmp:	2.33 V	Vmp:	2.84 V	Vmp:	2.68 V
Jmp:	13.4 mA/cm^2	Jmp:	6.8 A/cm^2	Jmp:	16.04 A/cm^2
Pmp	31.4 mW/cm^2	Pmp	19.3 W/cm^2	Pmp	42.9 W/cm^2

EMCORE Photovoltaics
10420 Research Road SE
Albuquerque, New Mexico 87123
Phone: 505.332.5000
Fax: 505.332.5100
www.emcore.com

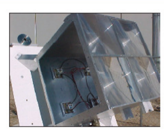

Application Example. On-sun testing at EMCORE at 520 suns

ISO 9001-2000 Registered

emcore
empower with light™

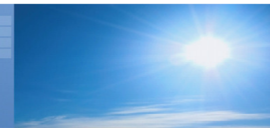

August 2008

Quantum Efficiency

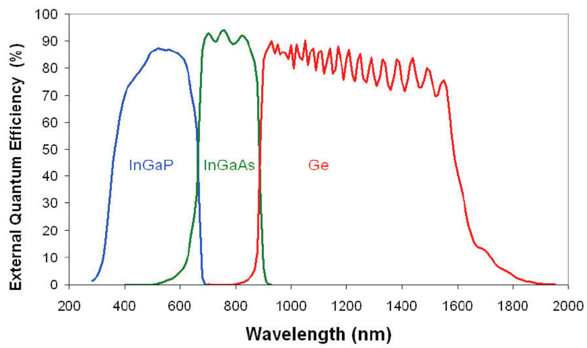

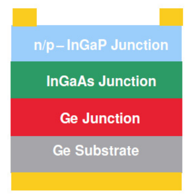

Cell Structure
(Tunnel diodes not shown)

Temperature Dependence at 800 Suns (20°C - 70°C)

ΔVoc = -5.9 mV/°C
ΔJsc = 7.2 mA/°C
Δefficiency = -0.06% (absolute)/°C

Efficiency vs. Concentration

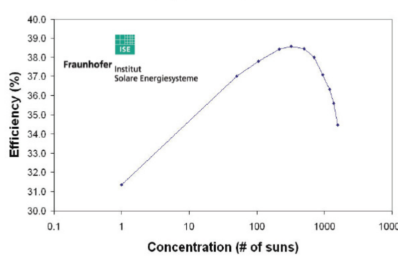

Typical IV Curves at Varying Concentration Levels, 25° C

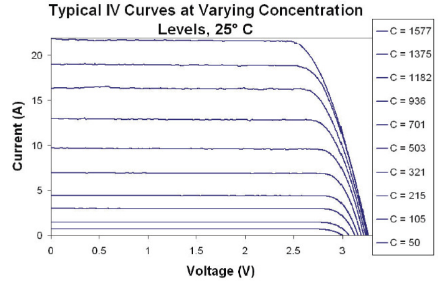

Information contained herein is deemed to be reliable and accurate as of issue date. EMCORE reserves the right to change the design or specifications of the product at any time without notice. EMCORE and the EMCORE logo are trademarks of EMCORE Corporation.

EMCORE Photovoltaics
10420 Research Road SE
Albuquerque, New Mexico 87123
Phone: 505.332.5000
Fax: 505.332.5100
www.emcore.com

Application Example.
On-sun testing at
EMCORE at 520 suns

ISO 9001-2000 Registered

REFERENCES

Alonso-Garcia, M.C., Ruiz, J.M. and Chenlo, F., 2006. Experimental study of mismatch and shading effects in the *I-V* characteristic of a photovoltaic module. *Solar Energy Materials and Solar Cells*, 90 (3), pp. 329-340.

Andreev, V., Grilikhes, V., Rumyantsev, V., Timoshina, N. and Shvarts, M., 2003. Effect of nonuniform light intensity distribution on temperature coefficients of concentrator solar cell. *Third World Conference on Photovoltaic Energy Conversion,* 18 May, Osaka, Japan, pp. 881-884.

Applegate, D.L., Buriol, L.S., Dillard, N.L., Johnson, D.S. and Shor, P.W., 2003. The cutting-stock approach to bin-packing: theory and experiments. *Proceedings of the 5th Workshop on Algorithm Engineering and Experiments,* 11 January, Baltimore, MD, USA, pp. 1-15.

Araki, K., Kondo, M., Uozumi, H., Ekins-Daukes, N.J., Kemmoku, Y. and Yamaguchi, M., 2006. Achievement of 27% efficient and 200Wp concentrator module and the technological roadmap toward realization of more than 31% efficient modules. *Solar Energy Materials and Solar Cells,* 90 (18-19), pp. 3312-3319.

Araki, K., Kondo, M., Uozumi, H., Ekins-Daukes,N.J., Egami, T., Hiramatsu, M., Miyazaki, Y. and Yamaguchi, M., 2006. Packaging III-V tandem solar cells for practical terrestrial applications achievable to 27% of module efficiency by conventional machine assembly technology. *Solar Energy Materials and Solar Cells,* 90 (18-19), pp. 3320-3326.

Arora, J.S., 2004. *Introduction to Optimum Design*. 2nd ed.; Elservier Academic Press, USA, Chapter 1, pp. 1-12.

Benitez, P., Minano, J.C., Zamora, P., Mohedano, R., Cvetkovic, A., Bujian, M. and Hernandez, M., 2010. High performance Fresnel-based photovoltaic concentrator. *Optics Express,* 18 (S1), pp. A25-A40.

Baig, H., Heasman, K.C. and Mallick, T.K., 2012. Non-uniform illumination in concentrating solar cells. *Renewable and Sustainable Energy Reviews,* 16 (8), pp. 5890-5909.

Castro, M., Anton, I. and Sala, G., 2008. Pilot production of concentrator silicon solar cells: Approaching industrialization. *Solar Energy Materials & Solar Cells*, 92, pp. 1697-1705.

Chen, Y.T., Chong, K.K., Bligh, T.P., Chen, L.C., Yunus, J., Kannan, K.S., Lim, B.H., Lim, C.S., Alias, M.A., Bidin, N., Aliman, O., Salehan, S., Shk. Abd. Rezan, S.A.H., Tam, C.M. and Tan, K.K., 2001. Non-imaging, focusing heliostat. *Solar Energy,* 71(3), pp. 155-164.

Chen, Y.T., Chong, K.K., Lim, B.H. and Lim, C.S., 2003. Study of residual aberration for non-imaging focusing heliostat, *Solar Energy Materials and Solar Cells,* 79 (1), pp. 1-20.

Chong, K.K., Siaw, F.L., Wong, C.W. and Wong, G.S., 2009. Design and construction of non-imaging planar concentrator for concentrator photovoltaic system, *Renewable Energy*, 34 (5), pp. 1364-1370.

Chong, K.K. and Wong, C.W., 2009. General formula for on-axis sun-tracking system and its application in improving tracking accuracy of solar collector, *Solar Energy*, 83 (3), pp. 298-305.

Chong, K.K., Wong, C.W., Siaw, F.L. and Yew, T.K., 2010. Solar flux distribution analysis of non-imaging planar concentrator for the application in concentrator photovoltaic system, *35th IEEE Photovoltaic Specialist Conference*, Honolulu, HI, pp. 003013-003018.

Chong, K.K., Wong, C.W., Siaw, F.L. and Yew, T.K., 2010. Optical characterization of nonimaging planar concentrator for the application in concentrator photovoltaic system. *Journal of Solar Energy Engineering,* 132 (1), pp. 011011.1-011011.9

Chong, K.K. and Wong, C.W., 2011. Application of on-axis general sun-tracking formula in open-loop suntracking system for achieving tracking accuracy of below 1 mrad. *International Journal of Energy Engineering,* 1, pp. 25-32.

Chong, K.K and Yew, T.K., 2011. Novel optical scanner using photodiodes array for two-dimensional measurement of light flux distribution. *IEEE Transactions on Instrumentation and Measurement,* 60 (8), pp. 2918-2925.

Chong, K.K., Yew, T.K., Wong, C.W. and Lau, S.L., 2011. Study of image quality of mirror via solar flux distribution measurement using a novel high speed optical scanner. *Applied Optics,* 50 (25), pp. 4927-4935.

Chong, K.K. and Siaw, F.L., 2012. Electrical characterization of dense array concentrator photovoltaic system. *In Proceedings of the 27th European Photovoltaic Solar Energy Conference and Exhibition*, Frankfurt, Germany, September 2012, pp.224-227.

Chong, K.K. and Tan, W.C., 2012. Study of automotive radiator cooling system for dense-array concentration photovoltaic system. *Solar Energy,* 86 (9), pp. 2632-2643

Chong, K.K., Lau, S.L., Yew, T.K. and Tan, P.C.L., 2013. Design and development in optics of concentrator photovoltaic system. *Renewable and Sustainable Energy Reviews,* 19, pp. 598-612.

Coffman, E.G., Galambos, Jr.J., Martello, S. and Vigo, D., 1999. Bin packing approximation algorithms: combinatorial analysis. *Handbook of Combinatorial Optimization,* Du, D.-Z. and Pardalos P. (Eds.), Kluwer Academic Publishers.

Cotal, H., Fetzer, C., Boisvert, J., Kinsey, G., King, R., Hebert, P., Yoon, H. and Karam, N., 2009. III-V multijunction solar cells for concentrating photovoltaics (Review). *Energy & Environmental Science*, 2, pp. 174-192.

Coventry, J.S., 2005. Performance of a concentrating photovoltaic/thermal solar collector. *Solar Energy*, 78, pp. 211-222.

EMCORE Corporation, 2008. Triple-junction high efficiency solar cells for terrestrial concentrated photovoltaic applications, *EMCORE Photovoltaics*, pp. 1-2.

Faiman, D., Biryukov, S., and Pearlmutter, K.K., May 2002. PETAL: A research pathway to fossil-competitive solar electricity. *29th IEEE Photovoltaic Specialist Conference,* New Orleans, USA, pp. 1384-1387.

Franklin, E.T., and Coventry, J.S., 2002. Effects of highly non-uniform illumination distribution on electrical performance of solar cells. *ANSES Sol. Conference.* New Castle, Australia, pp. 1-8.

Ishaque, K., Salam, Z. and Syafaruddin, 2011. A comprehensive MATLAB Simulink PV system simulator with partial shading capability based on two-diode model. *Solar Energy*. 85 (9), pp. 2217-2227.

Kajihara, A. and Harakawa A.T., 2005. Model of photovoltaic cell circuits under partial shading. *IEEE International Conference on Industrial Technology*, Hong Kong, pp. 866-870.

Karatepe, E., Boztepe, M. and Colak, M., 2007. Development of a suitable model for characterizing photovoltaic arrays with shaded solar cells. *Solar Energy*, 81(8), pp. 977-992.

Kaushika, N.D. and Rai, A.K., 2007. An investigation of mismatch losses in solar photovoltaic cell networks, *Energy*, 32 (5), pp. 755-759.

Kemmoku, Y., Sakakibara, T., Hiramatsu, M., Miyazaki, Y., and Egami, T., 2003. Field test of a concentrator photovoltaic system with flat Fresnel lens. *Third World Conference on Photovoltaic Energy Conversion*, Osaka, Japan, 3, pp. 2379 – 2382.

King, R.R., Bhusari, D. Boca, A. , Larrabee, D., Liu, X.Q., Hong, W., Fetzer, C.M., Law, D.C., Karam, N.H.,2010. Band gap-voltage offset and energy production in next-generation multijunction solar cells, *5th World Conference on Photovoltaic Energy Conversion and 25th European Photovoltaic Solar Energy Conference*, Valencia, Spain, 19 (7), pp. 797 – 812.

Kinsey, G.S., Hebert, P., Barbour, K.E., Krut, D.D., Cotal, H.L. and Sherif, R.A., 2008. Concentrator multijunction solar cell characteristics under variable intensity and temperature, *Progress in Photovoltaics*, 16(6), pp. 503-508.

Kovach, A., Schmid, J., 1996. Determination of energy output losses due to shading of building-integrated photovoltaic arrays using a raytracing technique. *Solar Energy*, 57 (2), pp. 117–124.

Kreske, K., 2002. Optical design of a solar flux homogenizer for concentrator photovoltaics. *Applied Optics*, 41(10), pp. 2053–2058.

Lovegrove, K., Burgess, G. and Pye J., 2011. A new 500m^2 paraboloidal dish solar concentrator. *Solar Energy*, 85, pp. 620-626.

Lockenhoff, R., Kubera, T. and Rasch, K.D., 2010. Water cooled TJ dense-array modules for parabolic dishes. *6th International Conference on Concentrating Photovoltaic Systems (CPV-6)*, Freiburg, Germany, pp. 43-46.

Luque Antonio and Andreev Viacheslav (Eds.) Concentrator Photovoltaics. Springer Berlin Heidelberg, New York, 2006, pp. 89-111.

Mills, D.R. and Morrison, G., 2000. Compact linear Fresnel reflector solar thermal powerplants. *Solar Energy*, 68 (3), pp. 263-283.

Nguyen, D.; Lehman, B., 2008. An adaptive solar photovoltaic array using model-based reconfiguration algorithm. *IEEE Transactions on Industrial Electronics*, 55(7), pp. 2644-2654.

Nishioka, K., Takamoto, T., Agui, T., Kaneiwa, M., Uraoka, Y. and Fuyuki T., 2006. Evaluation of InGaP/InGaAs/Ge triple-junction solar cell and optimization of solar cell's structure focusing on series resistance for high-efficiency concentrator photovoltaic systems. Solar Energy Materials and *Solar Cells*, 90 (9), pp. 1308-1321.

Nishioka, K., Takamoto, T., Agui, T., Kaneiwa, M., Uraoka, Y. and Fuyuki, T., 2006. Annual output estimation of concentrator photovoltaic systems using high-efficiency InGaP/InGaAs/Ge triple-junction solar cells based on experimental solar cell's characteristics and field-test meteorological data. *Solar Energy Materials and Solar Cells*, 90 (1), pp. 57-67.

Peharz, G., Rodriguez, J.P.F., Siefer, G. and Bett, A.W., 2011. A method for using CPV modules as temperature sensors and its application for rating procedures. *Solar Energy Materials and Solar Cells*, 95 (10), pp. 2734-2744.

Perez, M.V., Dominguez, C., Anton, I. and Sala, G., 2009. Comparative analysis of different secondary optical elements: effective concentration, acceptance angle and light distribution. *24th European Photovoltaic Solar Energy Conference*, Hamburg, Germany, pp. 755-759.

Picault, D., Raison, B., Bacha, S., Casa, J. and Aguilera, J., 2010. Forecasting photovoltaic array power production subject to mismatch losses, *Solar Energy*, 84 (7), pp. 1301-1309.

Pysch, D., Mette, A. and Glunz, S.W., 2007. A review and comparison of different methods to determine the series resistance of solar cells. Solar *Energy Materials and Solar Cells*, 91 (18), pp. 1698-1706.

Quaschning, V. and Hanitsch, R., 1996. Numerical simulation of current-voltage characteristics of photovoltaic systems with shaded solar cells. *Solar Energy*, 56 (6), pp. 513-520.

Reddy, K.S. and Veershetty, G., 2013. Viability analysis of solar parabolic dish stand-alone power plant for Indian conditions. *Applied Energy*, 102, pp. 908-922.

Ryu, K., Rhee, J.G., Park, K.M. and Kim, J., 2006. Concept and design of modular Fresnel lenses for concentration solar PV System. Solar Energy, 80 (12), pp. 1580-1587.

Sater, B.L. and Sater, N.D., 2002. High voltage silicon VMJ solar cells for up to 1000 suns intensities. *29th IEEE Photovoltaic Specialists Conference*, pp. 1019–1022.

Segev, G. and Kribus, A., 2013. Performance of CPV modules based on vertical multi-junction cells under non-uniform illumination. *Solar Energy,* 88, pp. 120-128.

Sherif, R., Cotal, H., Paredes, A., Lewandowski, A., Bingham, C. and Mehos, M., 2003. High concentration tests of a dense PV array using GaInP/GaAs/Ge triple-junction cells in the high flux solar furnace. *3rd World Conference on Photovoltaic Energy Conversion*, Osaka, Japan, pp. 829-832.

Siaw, F.L. and Chong, K.K., 2012. Temperature effects on the performance of dense array concentrator photovoltaic system. *IEEE Conference on Sustainable Utilization and Development in Engineering and Technology (STUDENT)*, Kuala Lumpur, Malaysia, pp. 140-144.

Siaw, F.L., Chong, K.K. and Wong, C.W., 2014. A Comprehensive study of dense-array concentrator photovoltaic system using non-imaging planar concentrator. *Renewable Energy*, 62, pp. 542 -555.

Solanki, C.S., 2011. *Solar Photovoltaics: Fundamentals, Technologies and Applications*; 2nd ed.; PHI Learning Pvt. Ltd, Chapter 12, pp. 324-329.

Sullivan, C.R., Awerbuch, J. and Latham AM., 2011. Decrease in photovoltaic power output from ripple: simple general calculation and effect of partial shading, *Twenty-Sixth Annual IEEE Applied Power Electronics Conference and Exposition (APEC),* Fort Worth, TX, pp. 1954-1960.

Tallent, R.J., 1963. Optical electrical design considerations for concentrating solar cell panels. *IEEE Transactions on Applications and Industry,* 82 (67), pp. 169-174.

Vivar, M., Morilla, C., Anton, I. and Sala, G., 2009. Si-cells radial parquet for parabolic dish receivers. *24th European Photovoltaic Solar Energy Conference*, Hamburg, Germany, 21-September 2009, pp. 141-144.

Vivar, M., Anton, I. and Sala, G., 2010. Radial CPV Receiver. *Progress in. Photovoltaics: Research and. Applications,* 18, pp. 353-362.

Vorster, F.J., van Dyk, E.E. and Leitch, A.W.R., 2002. Investigation on the *I-V* characteristics of a high concentration, photovoltaic array. *29th IEEE Photovoltaic Specialists Conference*, pp. 1604-1607.

Vorster, F.J. and van Dyk, E.E., 2005. Current-voltage characteristics of high-concentration, photovoltaic arrays. *Progress in Photovoltaics: Research and Applications*, 13 (1), pp. 55-66.

Vossier, A., Chemisana, D. and Flamant, G. and Dollet, A., 2012. Very high fluxes for concentrating photovoltaics: considerations from simple experiments and modeling, *Renewable Energy*, 38 (1), pp. 31-39.

Zubi, G., Bernal-Agustin, J.L. and Fracastoro G.V., 2009. High concentration photovoltaic systems applying III-V cells. *Renewable and Sustainable Energy Reviews*, 13, pp. 2645-2652.